

NORTHWESTERN UNIVERSITY

Assembly and transport in complex and confined environments

A DISSERTATION

SUBMITTED TO THE GRADUATE SCHOOL
IN PARTIAL FULFILLMENT OF THE REQUIREMENTS

for the degree

DOCTOR OF PHILOSOPHY

Field of Applied Physics

By

Ali Ehlen

EVANSTON, ILLINOIS

March 2024

© Copyright by Ali Ehlen 2024

All Rights Reserved

ABSTRACT

Assembly and transport in complex and confined environments

Ali Ehlen

In this work, we look closely the feedback between a nanoscale object and its environment and how it determines how the object behaves. In Part 2, I will focus on ions in confined spaces, particularly accounting for cases when the confining interfaces are polarizable due to dielectric mismatch. In this case, the induced polarization charge changes how ions move and distribute themselves in very narrow slits and near undulating interfaces. In Part 3, I will shift focus to nanoparticle self-assembly. In this case, we examine the competition between energy and entropy in determining the symmetry of an assembled nanoparticle crystal. I will present projects that examined the conditions under which binary systems of functionalized nanoparticles self-assemble into various crystal types, some of which allow the smaller of the two nanoparticle types to delocalize, even while the large particle lattice stays intact. In both Parts, we learn that in situations where ions are close to a wall or nanoparticles are very close to each other, the balance between different components of each interaction can play a large role in determining overall structure.

Acknowledgements

Thank you to every single person who has put up with me over the past 6.5 years! My family (Mom, Dad, Sophie and Bron) and Hector, you weird, smart, wonderful people. Grandparents (Grandma and Opa, Grammie, Grandie, and Duncan, Nana and Papa) and aunts and uncles (Bridget and Marty, Tom, Kristin and Alf, Emily and Boyd, Marc and Allie, Trav and Kira) — I can't imagine a better set of people to grow up looking up to. Thank you always for your advice and support. Cousins (Liz, Kentin, Briley, Lindsay, Jesse, Ella, Anni, Henry, Nic, Christian, Sadie, Dominique, and Donovan) — you *all* are amazing, inspiring humans and I am so lucky to have grown up around and with you and to be able to spend time together as adults. You've also brought some fantastic +1s (and, lately, very cute babies) into our lives, so thank you for that. Family that has entered my life recently (Leticia, Cris, Paola, Zoë, Héctor, Alondra, and Sofia, más los tíos y las tías y primos y primas y las abuelitas Irma y Mamamyr)— thank you for being so patient and welcoming. Childhood friends (Monica and Hannah Joy, everything would be incomplete with you). Friends in the applied physics program (2017 cohort - I'm so glad we had each other during first year, also Saugat, Katherina, Sajid of course), Carleton people (what would I have done without being able to vent to and hear from the Emma, Anna, Jaelyn, and Lindsay? And thank you for the continued conversations, Leaf), NREL people (Dheepak, Tarek, Ivonne, Lilly - you all still inspire me), and Chicago people: Abi and Karen (may the Trivial Ideas Factory live on forever, thanks for being a solid COVID

bubble, great roommates, and hotdish providers), Nick (I have no sufficient words, you bring fun and intellectual engagement and creativity to our lives), Cecile (another woman in science, so glad you came to live with us, keep up the fight because I know you can), Chloe (we have been exchanging to-do lists, venting, and supporting each other for years and I am so grateful), Gaby (you lent not only your friendship but a beautiful space from which to write on Wednesdays), Khat (we came to Chicago together, I admire so much about you, and I hope we get to live in a 3rd city together someday) and so many others (Ramya, Sarah, Helena, Rogan). Several of you talked me down from quitting multiple times. I suppose you were right, in the end.

Salsa team - you kept me sane, distracted, and exercising for the past several months. Thanks for that. I miss this already.

The rest of the Olvera de la Cruz group that has joined and left while I've been here: what a pleasure to know all of you, and I wish you all the best with your careers and lives! Of course, could not have started or finished any of this without Professor Monica Olvera de la Cruz – thank you for your support and enthusiasm over the years.

Dedication

This work is dedicated to two members of my family we've lost in the past year and a half: Papa and Tom. They were both unwavering examples of how intellectual curiosity can be fun, rewarding, and a lifelong project. Tom always had brainteasers for us when we were kids, and both Tom and Papa would often come to family gatherings with questions (how can there have been nothing before there was something? What are the subtle differences between 'mistaken,' 'unintentional,' and 'inadvertent'?). Neither of them were particularly interested in science, but both were ready to learn about anything if they came across it. Tom was a professor of philosophy and avid bridge player, yet when Hector and I published our first paper about colloidal crystals, he immediately read the "colloids" wikipedia page and starting asking questions. Papa was a lover of literature, music, and languages, and yet one of the last times I spent time with him, he was agitated and excited by the fact that he could not understand the Big Bang. I dedicate this work to them, because they both missed this moment by a matter of months, and I wish I had been able to tell them now how much I am driven to learn because of them.

Table of Contents

ABSTRACT	3
Acknowledgements	4
Dedication	6
Table of Contents	7
List of Tables	9
List of Figures	10
Part 1. Introduction	17
Chapter 1. Brief overview of crowded and confined environments at the nanoscale	18
Part 2. Electrostatics in strong confinement: impacts of confinement material and geometry on ion distribution and transport	20
Chapter 2. Introduction to ions in confinement	21
Chapter 3. Ion transport in nanoslits of constant charge or constant potential	47
Chapter 4. Confined ion current modulation by slit material and polarization plane location	71

	8
Chapter 5. Geometry effects	89
Chapter 6. Conclusion: outlook and future direction	98
Part 3. Symmetry in crowded environments: colloidal crystal metallicity	100
Chapter 7. Introduction	101
Chapter 8. BCC assembly and transition to "metallic" state	107
Chapter 9. Metallicity transition in other crystal types	140
Chapter 10. Conclusion: outlook and future directions	177
Part 4. Conclusion	178
Chapter 11. Review and outlook	179
Bibliography	184
Appendix A. Supplementary information for Chapter 3	199
Appendix B. Supplementary information for Chapter 4	212
Appendix C. Supplementary information for Chapter 8	218
Appendix D. Supplementary information for Chapter 9	228

List of Tables

8.1	Simulation parameters.	115
9.1	Observed lattices, their properties, and the systems in which they occur.	148
9.2	Simulation parameters.	174
A.1	Number of water molecules and ions in each simulation.	200
C.1	Temperature of onset of delocalization, melting, and existence of crystal lattices for varying number of small particle chains.	219
D.1	Comparison of potential energy landscape (theory) and interactive nead distribution (simulation) for all observed lattices.	239

List of Figures

2.1	Polarization of an interface represented as an image charge or surface charge.	29
2.2	Polarization of interfaces due to ions in a slit.	32
2.3	Particle distribution across a slit of width $4.2a$, varying particle charge and concentration. Reproduced with permission from AIP Publishing.	36
2.4	Ion density across a slit, varying wall charge and polarizability. Reproduced with permission from AIP Publishing.	38
2.5	Ion density and mobility across a slits with different dielectric contrast. Reproduced with permission from the American Physical Society.	41
2.6	Ionic current as a function of electric field in slits of varying material types. Reproduced with permission from AIP.	42
3.1	Simulation setup.	52
3.2	Induced charge on multiple planes of constant potential; force between two ions between plates of either constant charge or constant potential.	57

3.3	Distribution of surface charge for gated or ungated constant potential electrodes; distribution of water across a gated or ungated slit of constant potential or constant charge electrodes.	60
3.4	Dielectric response of water confined by polarizable and non-polarizable surfaces.	61
3.5	Ionic current through constant charge or constant potential slit for mono-, di-, and trivalent salts.	65
3.6	Ionic current through constant charge or constant potential slit for mono-, di-, and trivalent salts, separated into the contribution from positive and negative particles.	66
3.7	Cation-cation pair correlation function for varying electric field strength and salt in constant charge or potential slits.	67
4.1	System setup; potential due to an ion in slits of different polarizability; convergence of the infinite sum.	77
4.2	Ion distribution and pair correlation functions for a 1:1 electrolyte confined in nanoslits of various polarizable materials.	81
4.3	Ionic current and conductivities for a 1:1 electrolyte confined in nanoslits of various polarizable materials.	82
4.4	Diagram of different polarization plane placements; ion distribution across slits of different materials using multiple methods.	84
4.5	Ionic current and pair correlation function within slits of different materials using multiple methods.	87

		12
5.1	Induced polarization on an oscillating and flat surface due to an external field.	92
5.2	Charge density heatmap for different electric fields E_z .	94
5.3	Net ion charge density as a function of distance from the peak or trough.	96
7.1	Cartoon of a polymer-grafter nanoparticle in an electrolyte solution. Reproduced with permission from the American Chemical Society.	102
7.2	A wide array of tunable colloidal crystal assemblies. Reproduced with permission from AAAS.	104
7.3	Transition from ionic to metallic bonding in a colloidal crystal. Reproduced with permission from AAAS.	105
8.1	System setup.	111
8.2	Definition of BCC lattice sites; comparison of energy landscape and interactive bead visitation frequency in simulation.	123
8.3	Visitation frequency of small particles in a BCC unit cell for low and high temperatures.	124
8.4	Lattice properties as a function of temperature and number of small particle linkers.	125
8.5	Lattice properties as a function of temperature and number of small particle linkers, compared between simulations with lattices that are and are not allowed to vibrate.	131

8.6	Visitation frequency of small particles in a BCC unit cell with suppressed lattice fluctuations for low and high temperatures.	132
8.7	Interaction potential energy from theory and simulation for linearly and exponentially expanding systems; theoretical free energy values for linearly and exponentially expanding systems.	133
9.1	System setup.	145
9.2	Phase diagrams, showing crystal type as determined by small:large particle number ratio, number of small particle chains, and temperature.	147
9.3	Average interaction energy as a function of lattice type.	154
9.4	Lattice properties as a function of temperature for 3:1 and 4:1 lattices.	156
9.5	Lattice properties as a function of temperature for 5:1, 6:1, 9:1, and 10:1 lattices.	161
9.6	Example of BCC/FCC phase coexistence in a 7:1 system.	163
9.7	Fraction of large particles in each phase as a function of temperature for 7:1 and 8:1 systems.	164
9.8	Lattice properties as a function of lattice composition for systems showing no phase transition.	167
9.9	Lattice properties as a function of lattice composition for systems showing phase transitions.	168

A.1	System setup for equilibration with bulk water reservoir; system setup for transport property simulations	202
A.2	Charge distribution on each polarizable electrode for different salt types and applied electric fields.	203
A.3	Ionic density profiles for constant potential and constant charge simulations for different salts and applied electric fields.	204
A.4	Cation-anion pair correlation function for varying electric field strength and salt in constant charge or potential slits.	205
A.5	Anion-anion pair correlation function for varying electric field strength and salt in constant charge or potential slits.	206
A.6	Ionic current through constant charge or constant potential <i>gated</i> slit for mono-, di-, and trivalent salts	207
A.7	Ionic density profiles for constant potential and constant charge simulations for different <i>gated</i> salts and applied electric fields.	208
A.8	Diagram accompanying the derivation of the potential due to a charge between two conductors.	209
B.1	Ionic number density in a conductor nanoslit as a function of wall softness.	214
B.2	Deviation of ionic current results of <i>explicit polarization</i> methods from results using the PGF method, for different <i>explicit polarization</i> mesh types.	216

B.3	Ionic number density in a conductor nanoslit as a function of Gaussian charge distribution width in the <i>explicit polarization</i> model.	217
C.1	Pair distribution function at the minimum and maximum temperatures at which BCC lattices were observed, for different numbers of small particle chains.	221
C.2	Fits for ΔG as a function of number of small particle chains.	222
C.3	Lattice density as a function of temperature for different numbers of small particle chains.	223
C.4	Average number of large particles interacting with each small particle as a function of temperature for different numbers of small particle chains.	227
D.1	More detailed crystal phase diagrams for 3:1 and 4:1 systems.	233
D.2	Distances between nearest neighbors in a BCT lattice as a function of c/a .	238
D.3	Number of large particle neighbors of each small particle for all systems.	241
D.4	Lattice vibration components for different observed lattices.	242
D.5	Large particle number density for all systems.	243
D.6	Average small particle chain end-to-end distance for all systems.	244
D.7	Vibrational density of states for two different sublattice transitions.	245
D.8	Grain boundaries in a 7:1 system.	247

D.9	Velocity cross-correlation function for two different sublattice transitions.	249
D.10	Thermodynamic quantities for all 3:1 crystals systems as a function of temperature.	251
D.11	Thermodynamic quantities for all 4:1 crystals systems as a function of temperature.	252
D.12	Thermodynamic quantities for all 6:1 crystals systems as a function of temperature.	253

Part 1

Introduction

CHAPTER 1

**Brief overview of crowded and confined environments at the
nanoscale**

Nanoscale objects like ions, proteins, synthesized nanoparticles, often exist in environments that are confined and crowded, both in our bodies and in engineered devices. Understanding how they operate specifically with respect to other objects and barriers around them can help us predict more specifically the properties of the devices of which they are components.

In this dissertation, I will discuss work done on two specific ways in which the environment of a nanoscale object influences its behavior. In Part 2, I will discuss the effect of strong confinement on the interaction of ions in an electrolyte. We will see that the electronic properties (specifically polarizability expressed as a dielectric mismatch) and the shape of a confining wall will change how ions enclosed by the wall conduct and interact with each other. In Part 3, I will explore the self-assembly of functionalized nanoparticles into "metallic" colloidal crystals. We will look at the way that manipulating the strength and symmetry of interaction between two types of functionalized nanoparticles can affect the symmetry of the structures formed by these nanoparticles when assembled, pitting attractive energy against translational entropy in a crowded environment.

All of the work presented here is the result of molecular simulation, mostly coarse-grained, though there is some contribution from all-atom simulations and theory. While

the simulation does not purport to represent reality exactly—we know that real systems have many more layers of chemical and physical complexity—it does allow us to separate the influences of various effects, electrostatic polarization or nanocrystal lattice vibration, for example. The following work is meant to provide a physical piece to each puzzle, with the hopes that others will find something motivating in it and continue to explore.

Part 2

Electrostatics in strong confinement: impacts
of confinement material and geometry on ion
distribution and transport

CHAPTER 2

Introduction to ions in confinement

2.1. Motivation: the power of ion-driven devices

The motion and arrangement of ions drives the functionality of many current and nascent technologies. Small charged particles generate large electric fields near their surfaces, and their freedom to move within liquid media near room temperature results in reconfigurable electrostatic systems with a wide range of abilities. For example, proteins can selectively capture and bind ions, and the presence of the bound ions alters the protein in a way that drives a significant amount of biochemical activity [1]. Electric double layer supercapacitors are a variant of capacitors that rely on an electric field to drive the rearrangement of ions, which stores energy in the very thin layer between the ions and the plates. This enables significantly higher capacitance values than normal capacitors and a faster charging and discharging response than batteries, and supercapacitors are already paired with batteries in electric vehicles for fast braking and accelerating. Their drawback is a low energy density, though it has been shown that changing the geometry of graphene plates can improve this [2]. Iontronic devices also take advantage of ion configuration near surfaces: electric double layer transistors use gated electrolytes that use the ions to change the carrier density of nearby surfaces, which opens up a wide range of sensing and other applications [3]. Organic versions use electronically conducting polymers whose conductivity can be enhanced or suppressed by proximity to ions [4], and this ability to

tailor and manipulate ion interactions with a surface is leading rapidly to the development of iontronic neuromorphic devices [5]. The common thread in all of these technologies and biological mechanisms is the interaction between electric fields, ion configuration, and the materials in and near which the ions are moving.

The motion of ions and the electric fields they produce in nearby materials are key to functionality in all of these applications, so important characteristics for device design are therefore the speed of ion transport and the ion concentration distribution near walls. Both of these properties are likely to be impacted by the presence of confining walls, and this is what I will focus on in Part 2 of this thesis. There are many nuanced components of the interaction between ions and confining walls, including steric effects, electrostatic attraction or repulsion, charge transfer, other quantum or chemical effects, degree of confinement, shape of the confinement, etc. Here, we narrow our focus to classical electrostatic and steric effects: how do the shape and material of walls that confine an electrolyte determine the distribution of ion concentration and the mobility of the ions? We generally consider very strong confinement—less than two ion diameters—or surface deformations on the order of an ion diameter. We specifically add electrostatic interactions not only between the ions but between them and the materials they are in and near: we account for dielectric contrast between the electrolyte and the confining walls, which will result in induced surface charge on the interface between the two. This has only been starting to be included in studies, and it turns out to impact ion behavior significantly, especially in very narrow slits.

First, the remainder of this chapter will review some foundational background on the topic and briefly review what has been studied recently. Then, in Chapter 3, I will present

work originally published in Royal Society of Chemistry’s Faraday Discussions that uses all-atom simulations to show that ionic current through a nanoslit is higher when the nanoslit walls are conducting than when they are non-polarizable. In Chapter 4, which presents work originally published in Physical Review Research, we extend this to other slit materials and focus narrowly on the electrostatics effects by using a coarse-grained model with implicit solvent modeled as a homogeneous isotropic dielectric constant. We see that ions travel faster in conducting confinement than non-polarizable confinement, and slower in dielectric confinement, and we explore the mechanism underlying this nonlinear effect. We also see that the location of the surface polarization is an important piece of this puzzle. In Chapter 5, we look at how an undulating surface (rather than a flat one) will modify the induced surface polarization and therefore open doors to more types of charge patterning.

2.2. Background: Ions in polarizable media

2.2.1. Point charge in different uniform media and associated fields

A point charge q_0 in a vacuum and located at the origin of our coordinate system generates an electrostatic potential ϕ , radial electric field \vec{E} , and force \vec{F} on a test charge q at point \vec{r} of the form:

$$(2.1) \quad \phi(\vec{r}) = \frac{q_0}{4\pi\epsilon_0|r|}$$

$$(2.2) \quad \vec{E}(\vec{r}) = -\nabla\phi(\vec{r}) = \frac{q_0}{4\pi\epsilon_0|r|^2}\hat{r}$$

$$(2.3) \quad \vec{F}(\vec{r}) = q\vec{E}(\vec{r}) = \frac{q_0q}{4\pi\epsilon_0|r|^2}\hat{r}$$

where ε_0 is the permittivity of free space and all equations are in SI units. If the charge q_0 is embedded in a dielectric medium, the material around it will respond to and screen the electric field produced by q_0 . This happens through the rearrangement of charges within the material: by shifting electron density, deforming electron clouds, molecular bending or rotation, and other microscopic mechanisms determined by the specific chemistry of the material. The material's response to an external electric field is summarized by the value of its relative dielectric constant ε_r , which in general is a tensor, but we will treat it as a scalar for most of this work. The relative dielectric constant enters the previous equations as follows:

$$(2.4) \quad \phi(\vec{r}) = \frac{q_0}{4\pi\varepsilon_0\varepsilon_r|\vec{r}|}$$

$$(2.5) \quad \vec{E}(\vec{r}) = -\nabla\phi(\vec{r}) = \frac{q_0}{4\pi\varepsilon_0\varepsilon_r|\vec{r}|^2}\hat{r}$$

$$(2.6) \quad \vec{F}(\vec{r}) = q\vec{E}(\vec{r}) = \frac{q_0q}{4\pi\varepsilon_0\varepsilon_r|\vec{r}|^2}\hat{r}$$

The higher the value of the relative dielectric constant, the more a material screens an electric field.

This microscopic rearrangement of charges within a medium in response to an external electric field is referred to as polarization, and the field describing the net displacement of the charges is referred to as $\vec{P}(\vec{r})$ (qualitatively, \vec{P} points in the direction of net displacement of positive charges). Following Zangwill [6], \vec{P} is most appropriately quantified as the time integrated sum of the current that flows through a microscopic volume in response to an external field (rather than the sum of microscopically averaged dipoles, see sections 6.2.2 and 6.2.3 of Zangwill). \vec{P} can also be thought of as a volume density

of (fictitious) point dipoles, and when integrated over all space, it gives the total dipole moment \vec{p} of the polarized material:

$$(2.7) \quad \int_V \vec{P}(\vec{r}) d\vec{r} = \vec{p}$$

It should be noted that \vec{P} is nonzero only inside the volume and on the surface of the dielectric material and is zero in a vacuum. Anywhere in space where \vec{P} is not uniform, a net induced polarization charge will develop. This net induced polarization charge will contribute to the overall electric field of the system. A summary of important equations for the electrostatic fields are as follows, with the addition of auxiliary field $\vec{D}(\vec{r})$, which will be described further later. Here, we follow the notation of Zangwill, where a subscript P means induced polarization charge and F means "free" charge (or, any charges that are fixed and produce a net field).

$$(2.8) \quad -\nabla \cdot \vec{P}(\vec{r}) = \rho_P(\vec{r})$$

$$(2.9) \quad \nabla \cdot \vec{D}(\vec{r}) = \rho_F(\vec{r})$$

$$(2.10) \quad \epsilon_0 \nabla \cdot \vec{E}(\vec{r}) = \rho(\vec{r}) = \rho_P(\vec{r}) + \rho_F(\vec{r}) = -\nabla \cdot \vec{P}(\vec{r}) + \nabla \cdot \vec{D}(\vec{r})$$

where $\rho(\vec{r})$ is always the total (free and induced) charge in the system and \vec{E} is always the total electric field due to the total charge density $\rho(\vec{r})$.¹ Note here the negative sign in Eq. 2.8, which is present because the electric field due to the polarization charge \vec{E}_P is the opposite direction of the polarization field \vec{P} (\vec{P} points in the direction of the net displacement of the positive charges, while \vec{E} always points away from positive charges).

¹With external fields often written as \vec{E} and some relationships between fields quite simple, it is easy to confuse the total and external fields. I try here to use \vec{E} exclusively to indicate the total electric field.

We have also included the auxiliary field \vec{D} , which is defined as

$$(2.11) \quad \vec{D}(\vec{r}) = \epsilon_0 \vec{E}(\vec{r}) + \vec{P}(\vec{r})$$

An important note is that, even though $\vec{P}(\vec{r})$ for a given material is zero outside of that material, it is not the case that $\vec{D} = \epsilon_0 \vec{E}_F$ outside of that material. This is because, while the divergence of \vec{D} is only dependent on the free charge in the system, the actual value of \vec{D} is dependent on both the free charge distribution *and* the spatial variations of \vec{P} , see Eq. 6.30 in Zangwill [6]. So, even for points \vec{r} in a vacuum outside a dielectric material, both $\vec{D}(\vec{r})$ and $\vec{E}(\vec{r})$ in Eq. 2.11 are different from what they would be in a different system with the same ρ_F but no dielectric material.

The boundary conditions between two regions, labeled region 1 and region 2, separated by an interface comprised of points \vec{s} with (optional) fixed charge $\sigma_F(\vec{s})$, for all these fields are as follows:

$$(2.12) \quad \hat{n}_2(\vec{s}) \cdot (\vec{E}_1(\vec{s}) - \vec{E}_2(\vec{s})) = \sigma(\vec{s}) = \sigma_P(\vec{s}) + \sigma_F(\vec{s})$$

$$(2.13) \quad \hat{n}_2(\vec{s}) \times (\vec{E}_1(\vec{s}) - \vec{E}_2(\vec{s})) = 0$$

$$(2.14) \quad \hat{n}_2(\vec{s}) \cdot (\vec{D}_1(\vec{s}) - \vec{D}_2(\vec{s})) = \sigma_F(\vec{s})$$

$$(2.15) \quad \hat{n}_2(\vec{s}) \times (\vec{D}_1(\vec{s}) - \vec{D}_2(\vec{s})) = \hat{n}_2(\vec{s}) \times (\vec{P}_1(\vec{s}) - \vec{P}_2(\vec{s}))$$

where \vec{s} is any point on the boundary, $\sigma(\vec{s})$ is the total surface charge density at that point, and \hat{n}_2 is the normal vector that points *from* region 2 into region 1. We will see the significance of these normal-dependent boundary conditions in Chapt. 5.

The preceding equations would be sufficient to describe the system if we knew both ρ_F (including σ_F) and the induced polarization field \vec{P} . However, in the most general case, \vec{P} is challenging to calculate from scratch and depends on lots of microscopic details of the material. However, for many materials, \vec{P} and \vec{E} are related in the following way (using Einstein notation):

$$(2.16) \quad P_i = \varepsilon_0 \chi_{ij} E_j + \varepsilon_0 \chi_{ijk}^{(2)} E_j E_k + \dots$$

where the susceptibility χ is a tensor that relates the total electric field \vec{E} to \vec{P} . This relationship can be very complicated, so for most of this work, we will take the extremely simplifying assumption that any polarizable materials are linear, homogeneous, and isotropic. The result of that assumption is that each material has a constant, scalar-valued susceptibility χ that is uniform except at the boundary of materials, at which point it changes sharply from one material to the other. This allows the following simplified relationships, drawing from a simplified Eq. 2.16 and plugging the result into Eq. 2.11 and Eq. 2.14:

$$(2.17) \quad \vec{P} = \varepsilon_0 \chi \vec{E}$$

$$(2.18) \quad \vec{D}(\vec{r}) = \varepsilon_0 \vec{E}(\vec{r}) + \vec{P}(\vec{r}) = \varepsilon_0 \vec{E}(\vec{r}) + \varepsilon_0 \chi \vec{E} = \varepsilon_0 (1 + \chi) \vec{E} = \varepsilon_0 \varepsilon_r \vec{E}$$

$$(2.19) \quad \hat{n}_2(\vec{s}) \cdot (\vec{D}_1(\vec{s}) - \vec{D}_2(\vec{s})) = \varepsilon_0 \hat{n}_2(\vec{s}) \cdot (\varepsilon_1 \vec{E}_1(\vec{s}) - \varepsilon_2 \vec{E}_2(\vec{s})) = \sigma_F(\vec{s})$$

where we have defined the relative dielectric constant $\varepsilon_r = (1 + \chi)$ and \vec{E} , as usual, is the total \vec{E} field, not just the externally applied one. These equations mean: \vec{P} and \vec{D} are

always larger than and in the same direction is \vec{E} , and \vec{P} is always subtracted from \vec{D} to construct the final total field \vec{E} .

2.2.2. Induced charge on dielectric interfaces

The studies presented in this Part all use simplified linear, homogeneous, and isotropic materials with sharp boundaries between them. This means that $\nabla \cdot \vec{P} \neq 0$ only at the boundary, and therefore there is induced polarization charge only there, per Eq. 2.8. The physical intuition for why a net charge develops at any point of change in dielectric constant is that different materials respond more or less strongly to an external field due to free charges \vec{E}_F . Because the material on one side of the boundary is more enthusiastically opposing the external field than the other, there is a higher charge contribution from one side than the other, resulting in a non-zero net charge.

This induced surface polarization charge can be calculated using the above equations and boundary conditions. For a single ion a distance d above an infinite planar interface, it looks qualitatively like the cartoon on the left-hand side of Fig. 2.1. However, for a very narrow set of simple geometries, like the planar case, it is also possible to obtain an identical solution for the potential ϕ and electric field \vec{E} on the ion side of the interface using a construct called the "method of images," shown on the right-hand side of Fig. 2.1. This technique assumes that the ion q induces an "image charge" of charge q' a distance d away from the interface, but on the other side. Start from that, one can use the boundary conditions for \vec{D} and \vec{E} to solve for the value of q' . The solution turns out to be:

$$(2.20) \quad q' = \frac{\epsilon_s - \epsilon_w}{\epsilon_s + \epsilon_w} q$$

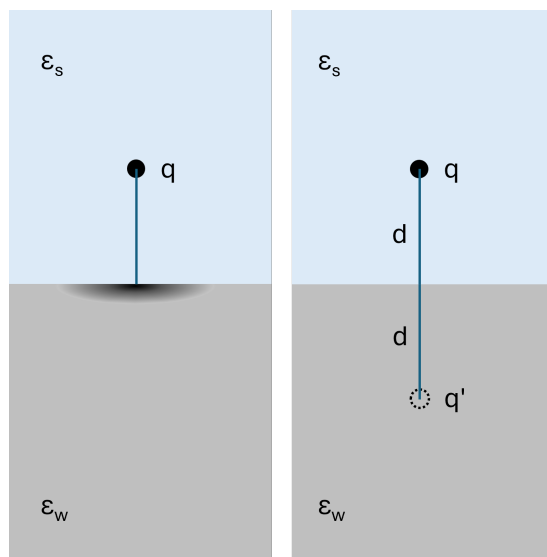


Figure 2.1. Polarization of an interface represented as actual induced surface charge (right) or a fictitious image charge (left). The interface is between a solvent with dielectric constant ϵ_s and a wall with dielectric constant ϵ_w . (The charge here is spread out across the surface and it does not extend into the material.)

Equation 2.20 implies a few things: first, if the relative dielectric constant of the wall is smaller than that of the solvent, $\epsilon_w < \epsilon_s$, then the overall sign of the prefactor is positive and therefore q and q' have the same sign: the induced charge is repulsive. In the opposite case, if the relative dielectric constant of the wall is greater than that of the solvent, $\epsilon_w > \epsilon_s$, then the image charge has the opposite sign charge as q , and therefore the induced charge is attractive. Note that if the wall is a perfect conductor, the electrons of the material rearrange such that they perfectly screen all electric fields and none enter the material. To model conductors, we use an infinite relative dielectric constant, in which limit the prefactor of equation 2.20 goes to -1 and therefore the image charge in a

conductor is exactly equal and opposite of q :

$$(2.21) \quad q' = -q$$

Note: repulsive or attractive force between an ion and its induced surface charge is:

$$(2.22) \quad \vec{F}_{q-q'} = \frac{\varepsilon_s - \varepsilon_w}{\varepsilon_s + \varepsilon_w} \cdot \frac{q^2}{4\pi\varepsilon_0\varepsilon_s(2d)^2}$$

It scales as the charge squared, meaning that multivalent ions feel a disproportionately strong attraction or repulsion relative to monovalent ions, and it falls off as $1/d^2$. For contained electrolytes whose containers are very large and therefore most ions are very far from the walls, the impact of surface polarization can be small. However, when electrolytes are strongly confined, all or most ions are close to the interfaces, and the interfaces may even electrostatically interact with each other. These are the cases we focus on in this work, and we will show qualitatively how the walls interact with each other in the next section.

2.2.3. Ions between two polarizable interfaces

As discussed in Sect. 2.2.2, when an ion is near a polarizable surface (i.e. an interface between two materials of different dielectric constant), its presence will induce charge on the interface, the magnitude and distribution of which will depend on the ion's charge and position relative to the wall, as well as the relative dielectric constants of both materials. If an ion is between two polarizable interfaces, the induced charge on each interface is a result of both the interactions between the ion and each surface and the interaction of the surfaces with each other. Fig. 2.2 shows this schematically: Fig. 2.2a shows this in terms

of (fictitious) image charges. The ions in the slit induces an image in each wall, each of which in turn induce images in the opposite walls, which in turn induce images in the original walls, and so on infinitely. Figs. 2.2b-2.2e show this in terms of real induced charge on the interface, calculated from simple simulations using the DIELECTRIC package [7] in LAMMPS [8]. Figs. 2.2b and 2.2c show the case when the relative dielectric constant in the slit is higher than that of the polarizable wall(s), and Figs. 2.2d and 2.2e show the case when the dielectric in the slit is lower than that of the polarizable wall(s).² Consistently with Eq. 2.20, ions induce same-sign image charges in the former case and opposite-sign image charges in the latter. Comparing the cases where only one wall is polarizable (Figs. 2.2b and 2.2d) with those where both walls are polarizable (Figs. 2.2c and 2.2e) shows the interaction between induced charge in narrow slits, which is related to the sign of the induced charge. When the solvent dielectric constant is higher than that of the polarizable walls (same-sign induced charge), a second polarizable wall results in enhanced induced charge in both walls. When the solvent dielectric constant is lower than that of the polarizable walls (opposite-sign induced charge), a second polarizable wall will reduce the total induced charge on each interface.

For slits narrow enough that a) ions are constrained to be close enough to the interface to interact strongly with their induced charges and b) interfaces can interact with each other, the induced charge on the slit interfaces will non-negligibly impact the arrangement

²To word this carefully: the *wall* is not polarizable—the interface is. Polarization due to a nearby ion will occur on any interface between two regions of different relative dielectric constant because of the difference in the way each material reacts to an external electric field. In this work, a "nonpolarizable wall" refers to a wall with the same dielectric constant as the solvent it confines. This is a simulation construct that is useful for isolating the impact of polarization.

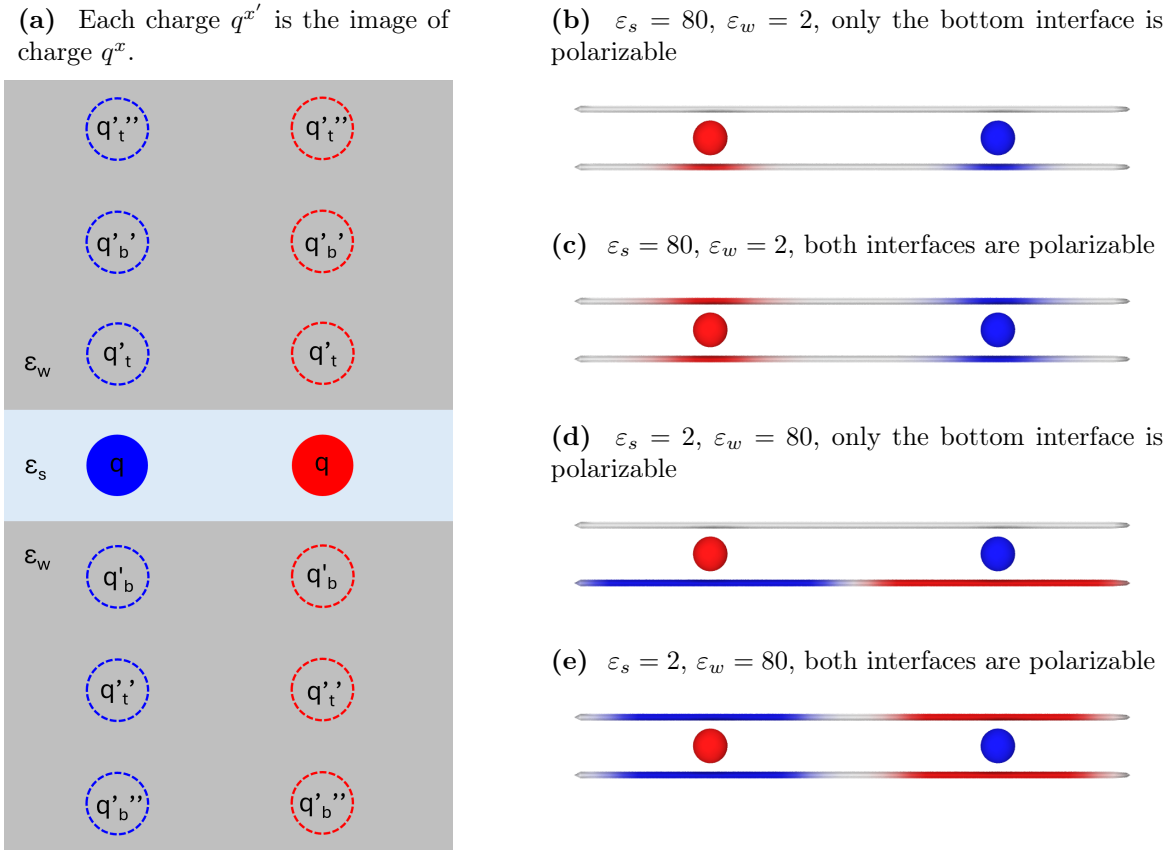


Figure 2.2. Induced polarization charge due to ions in a nanoslit. Fig. 2.2a shows a schematic of the first three images charges on each side of the slit (in this case, the image charges are colored as if $\epsilon_s > \epsilon_w$). The remaining figures show actual induced surface charge due to the pictured ions, in environments with slit width $2a$ and solvent dielectric constant ϵ_s is higher or lower relative to the wall dielectric constant ϵ_w , and either one or both walls is polarizable. When the wall has a lower dielectric constant than the solvent, induced charge is enhanced when both walls are polarizable; when the wall has a higher dielectric constant, the induced charge is slightly suppressed.

and interaction of ions within the slit. This has been shown by various authors and various techniques, which I will briefly summarize in Sect. 2.4.

2.3. Relevant energy and length scales for ions in solution

Generally, the scales relevant to problems that we will explore there are as follows. Energy scales are the thermal energy scale $k_B T$ and the electrostatic energy scale, $e^2/(4\pi\epsilon_0\epsilon_r a)$. Length scales are the diameter of a typical ion a ; the Bjerrum length ℓ_B , which is the distance between two unit charges at which the electrostatic and thermal energy are equal, dependent on the relative dielectric constant ϵ_r and the temperature T ; and the Debye length λ_D , which represents the charge screening length in a solution and is dependent on relative dielectric constant, temperature, and ion concentration. These are expressed as follows:

Energy scales:

$$(2.23) \quad \text{Electrostatic energy: } \frac{e^2}{4\pi\epsilon_0\epsilon_r a}$$

$$(2.24) \quad \text{Thermal energy: } k_B T$$

Length scales:

$$(2.25) \quad \text{Ion diameter: } a$$

$$(2.26) \quad \text{Bjerrum length: } \ell_B = \frac{e^2}{4\pi\epsilon_r\epsilon_0 k_B T}$$

$$(2.27) \quad \text{Debye length: } \lambda_D = \kappa^{-1} = \sqrt{\frac{\epsilon_r\epsilon_0 k_B T}{2e^2 I}}$$

where I is the ionic strength of solution with n ionic species $I = \frac{1}{2} \sum_{i=1}^n c_i z_i^2$, where c_i is the concentration and z_i is the valence of ion species i . Both ℓ_B and λ_D are between 7 and 8 Å at room temperature in water with 150 mM of a 1:1 salt ($\epsilon_r = 78$, $T = 293$ K). Ionic

diameters are typically in the range of 0.2-0.3 nm, though often coarse-grained simulations use a hydrated ionic diameter, which can be closer to 0.5 nm, to represent the size of the ion. Energy scales are around 10^{-21} J: the thermal energy at room temperature is 4.11×10^{-21} J, and the electrostatic energy can vary between 10^{-18} and 10^{-21} J, depending on the value of ionic diameter and dielectric constant. For hydrated ions in water, the value is 5.77×10^{-21} J.

In many applications, the properties of bulk ionic solutions are sufficient. Mean field theories like Poisson-Boltzmann will predict that ions will be distributed, on average, uniformly throughout the bulk (in the absence of walls with fixed charge), and that each point in the bulk is on average charge neutral. However, at low enough ion concentrations, low enough relative dielectric constants, and low temperatures, ion-ion correlations become impossible to ignore. Similarly, not accounting for the impact of the edge of the electrolyte container is reasonable in large systems, but when the electrolyte is confined to any length scale close to the Debye lengths, the effects of the edges become important, as we shall see in the next section.

2.4. Ions confined in narrow slits

When an electrolyte is confined in nanoscale slits, the distribution of ions is impacted in several ways. In this section, I will briefly detail the influences on ion structure that are *not* due to polarization of the slit walls, and then I will discuss work that has been done on narrow slits in which both walls are polarizable and how this changes ion behavior.

2.4.1. Neutral walls

Jing, et al. [9] studied the structure of neutral particles and ions in nanoconfined solutions and found two primary effects that determine the distribution of particles between neutral, non-polarizable walls, confirming the results of Zwanikken and Olvera de la Cruz [10]. They used molecular dynamics simulations, combined with liquid state theory when possible, to calculate the distribution of particles of diameter a in a slit of width $4.2a$, in different concentrations and particle charges. One effect they identified is steric. At higher concentrations, particles will tend to order in layers. They will also be pushed toward the edges of the slit due to an imbalance of collision forces, since particles near either wall will be bumped by other particles much more from the center of the slit than the wall. This can be seen in Fig. 2.3a, which shows the distribution of several concentrations of neutral particles in the slit. At higher concentrations, both the ordering of the "bulk" particles and the strong push towards the walls become more prominent. When the particles are charged, a competing effect arises due to electrostatic attraction. Configurations with non-charge-neutral areas tend to be unfavorable; therefore, the deformation of an ion's neutralizing cloud caused by the presence of a wall is also unfavorable. This effect tends to push ions away from the wall, and Zwanikken and Olvera de la Cruz show this effect nicely for monovalent ions in Fig. 2 of [10]. Additionally, higher valency ions show this effect more strongly, and this can be seen in Fig. 2.3b, which shows the ion distribution deforming away from the wall for higher valency (but also lower concentration) ions.

(a) Neutral particle distribution across as neutral slit of width $4.2a$. Larger concentrations result in a higher density close to the walls. This is Fig. 5 in [9]. Note that the inset of this is the neutral particle version of the red line of Fig. 2.3b.

(b) Ion distribution across as neutral slit of width $4.2a$ for different ion valency. Here, the concentration of anions is kept constant at 0.1 M, while the valency of the cations is changed. Higher valency salt tends to be pushed from the walls. This is Fig. 2 in [9].

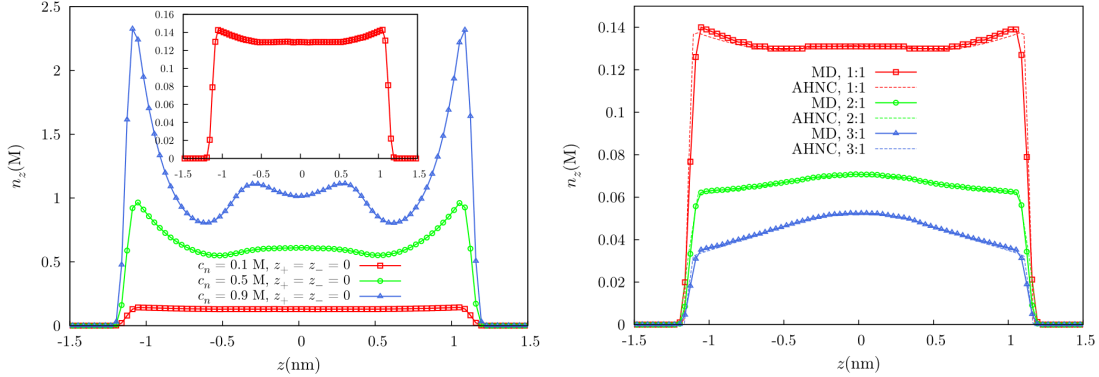


Figure 2.3. Particle distribution across a slit of width $4.2a$ for different particle charges and concentrations. In both cases, the z variable is in nm, and the ions have diameter $a = 0.714$. Reprinted from *Jing, Jadhao, Zwanikken, and Olvera de la Cruz. "Ionic structure in liquids confined by dielectric interfaces." Journal of Chemical Physics 143, 194508 (2015)*, with permission from AIP Publishing. These appear as Figs. 5 and 2 in the original [9].

2.4.2. Charged walls

Of course, ion distribution will be affected if one or both slit walls is electrically charged: ions of the same sign charge will be repelled from the wall and ions of the opposite sign charge will be attracted to it. Quite a bit of work has been done to characterize the electric double layer, which is the region of electrolyte near a charged wall where the presence of the charged wall changes the ion concentrations from the bulk value. The structure and net charge can also become quite complicated due to the presence of complex solvent, polymers, and other effects. For example, Bagchi et al. showed that polyelectrolytes can interact with charged walls by overcharging (attracting like-charged species to the wall),

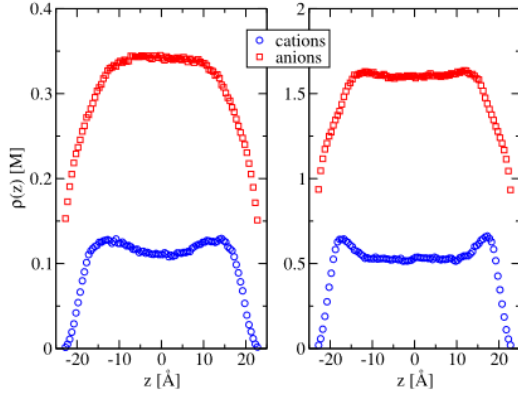
charge inversion (overcompensating the wall's charge), and other interesting effects [11]. In this work, we will restrict our discussion to simple electrolytes and neutral walls, though polarizable slits will exhibit electrostatic behavior that impacts ion distribution. As we will see in the next section, the proximity of ions changes the state of charge on polarizable walls and therefore adds another aspect of complexity to the systems.

2.4.3. Polarizable walls and static structure

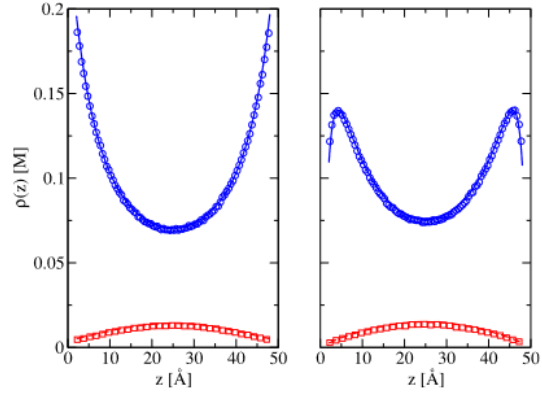
Several studies have been done to confirm, particularly for slits of medium width, that dielectric walls have the expected impact on ion distribution: repulsion for $\varepsilon_w < \varepsilon_s$ and attraction for $\varepsilon_w > \varepsilon_s$. The interplay between steric forces, dielectric mismatch, and fixed charge is interesting and depends on many factors. A few examples are mentioned here, using a few different techniques to incorporate the slit wall polarizability.

Zwanikken and Olvera de la Cruz also showed using liquid state theory that the interplay between anisotropic forces, which push ions towards slit walls, and electrostatic forces that resist counterion cloud deformation, which push ions away from slit walls, can be impacted by attractive or repulsive wall polarizability [10]. They incorporated polarizability by solving the infinite summation of image charges in Fourier space. dos Santos and Levin 2015 [12] later developed an analytical method to treat ions in periodic boxes in molecular dynamics simulations. See results in Fig. 2.4a, which shows the competition between ion cloud and steric effects in non-polarizable slits, and 2.4b, which shows the competition between wall charge attraction and repulsive polarizability. They later improved upon this developing a fast converging solution to the Poisson equation

(a) Ion density profiles for 3:1 salt across a slit of width $12.5a$ for $\epsilon_s = 80$ and $\epsilon_w = 2$ for 100 mM salt (left) and 500 mM salt (right). Ions are repelled from the walls in both cases to avoid counterion cloud deformations, but the higher concentration system has a stronger effect of anisotropic collision forces pushing ions toward the wall. Reprinted from *dos Santos and Levin*. "Electrolytes between dielectric charged surfaces: simulations and theory." *Journal of Chemical Physics* 142, 194104 (2017), with permission from AIP Publishing. This appears as Fig. 5 in the original [12].



(b) Ion density profiles for 1:1 salt (and positive counterions) across a slit of width $12.5a$ between negatively charged plates, for $\epsilon_s = 80$ and $\epsilon_w = 80$ (left) and $\epsilon_w = 2$ (right). In both cases, the anions are repelled from the wall and the cations are attracted to it, but the repulsive dielectric contrast on the right competes with the attraction of the charged wall to shift ions away. Reprinted from *dos Santos and Levin*. "Electrolytes between dielectric charged surfaces: simulations and theory." *Journal of Chemical Physics* 142, 194104 (2017), with permission from AIP Publishing. This appears as Fig. 3 in the original [12].



(c) Ion distribution across a slit of width $4.2a$ where a is the ion diameter with different dielectric contrast. This is a 1:1 electrolyte of concentration 0.2 M. a) $\epsilon_{w1} = 20$, $\epsilon_s = 80$, $\epsilon_{w2} = 20$, b) $\epsilon_{w1} = 40$, $\epsilon_s = 80$, $\epsilon_{w2} = 10$ c) $\epsilon_{w1} = 20$, $\epsilon_s = 80$, $\epsilon_{w2} = 160$. Reprinted from *Jing, Jadhao, Zwanikken, and Olvera de la Cruz*. "Ionic structure in liquids confined by dielectric interfaces." *Journal of Chemical Physics* 143, 194508 (2015), with permission from AIP Publishing. This appears as Fig. 8 in the original [9].

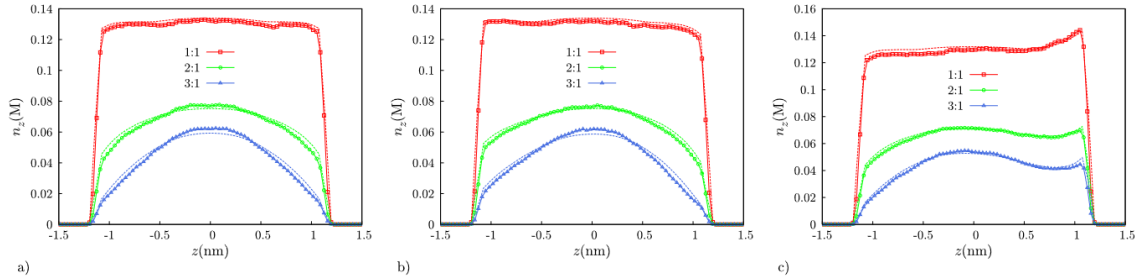


Figure 2.4. Ion distribution across a slit from two recent publications.

using periodic Green functions applicable for more dielectric contrast values and found consistent results [13].

Jing, et al. 2015 not only showed the effects of neutral walls as previously described, but also explored the impacts on ion distribution if the walls are polarizable, showing a deformation in ion concentrations near the walls using Car-Parinello molecular dynamics simulations to incorporate polarization. As expected, ion density is lower near walls with repulsive dielectric contrast ($\epsilon_w < \epsilon_s$) and higher near walls with attractive dielectric contrast ($\epsilon_w > \epsilon_s$), as shown in Fig. 2.4c. It is helpful to see that all these work show consistent results.

Others have started to extend the exploration of polarization effects past ion density and into other properties. Schlaich, et al. model an interface's induced charge as a virtual fluid of partially charged particles, mimicking Thomas-Fermi theory and the idea that charge induction extends into a material in a real system. They can vary the partial charge of the particles to allow the virtual Thomas-Fermi fluid to screen more or less strongly (tuning between a perfect metal and an insulator) and they show that properties of a molten salt contained by two Thomas-Fermi metals are influenced by the strength of the screening, such as capacitance, capillary freezing, and wetting [14].

2.4.4. Polarizable walls and ion transport

Additional studies that examine ion motion in a polarizable slit, which is useful property for a broader range of iontronic devices. The transport of ions, too, can be changed by the polarizability of nearby interfaces.

Antila, et al. noted that classic Debye-Hückel-Onsager theory says that the mobility of an electrolyte is proportional to the negative square root of ion concentration, meaning that higher density electrolytes should show lower ion mobility due to the ion-ion correlations [15]. However, in simulations in which one slit wall was polarizable, they found that mobility and concentration varied in the opposite manner near dielectric surface [15]. This was later confirmed by Ma, et al., who incorporated dielectric boundary conditions into a solution for the potential due to an ion in a planar slit [16]. Their results are shown in Fig. 2.5, which demonstrates that ion density and mobility are both higher near conducting walls.

Modulations due to polarization can lead to other interesting behavior. Robin et al. described the electric field lines due to an ion in a slit of repulsive walls ($\epsilon_w < \epsilon_s$) as repelled from the interfaces and therefore approximately parallel to the slit walls for some characteristic distance. They find the potential $\phi_{ij}(r)$ between two ions q_i and q_j in a slit by solving Poisson's equation with an asymmetric dielectric tensor (this is a good description of confined water) and dielectric contrast at the interfaces [5]. They use approximations to make the solution tractable, including expansion for longer distances from the ion, strong dielectric contrast, and the restriction that the ion must be in the center of the slit. They come up with the expression

$$(2.28) \quad \beta\phi_{ij}(r) = -\frac{q_i q_j}{T^*} \log \frac{r}{r + \xi}$$

where $\beta = \frac{1}{k_B T}$ as usual, r is the distance between them (parallel to the slit wall), and ξ is the characteristic distance over which the ion's electric field lines are approximately parallel to the slit walls. For reasonable values of ξ (their results show $\xi = 14$ nm at room

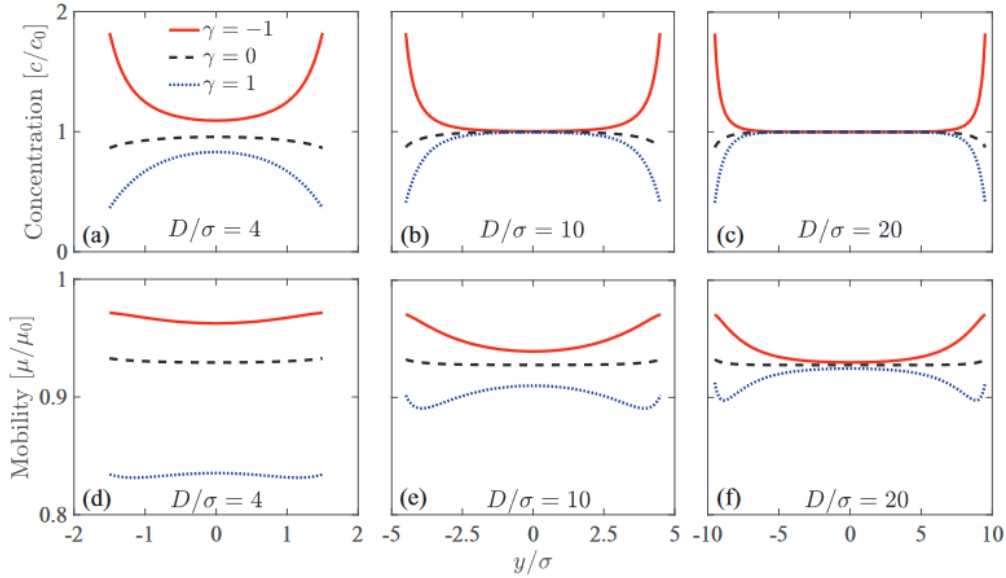


Figure 2.5. Ion distribution and mobility across slits of varying widths ($4a$, $10a$, and $20a$) showing that ion concentration and mobility are positively correlated in systems with dielectric contrast. Their $\gamma = \frac{\epsilon_s - \epsilon_w}{\epsilon_s + \epsilon_w}$, which is the prefactor of an image charge in Eq. 2.22. Thinner slits show a much larger deviation from bulk behavior. Reprinted figure with permission from *Ma, Xu, and Zhang*. "Ion transport in electrolytes of dielectric nanodevices." *Physical Review E*, 104, 3, 035307, 2021. <http://dx.doi.org/10.1103/PHYSREVE.104.035307>. Copyright 2021 by the American Physical Society. This appears as Fig. 2 in the original [16].

temperature for their slit height), this expression for the potential is much longer range than the unconfined electrostatics $\frac{1}{r}$ potential, consistent with the idea that confinement by dielectrics where $\epsilon_w < \epsilon_s$ strengthens the interactions between ions. Robin et al. go on to show interesting applications of this potential: because this potential is strong and between rearrangeable ions, applying a varying electric field parallel to the slit can result in ion current with hysteresis effects. This occurs due to the difference in timescales of ion pairing and release and can result in memory and neuromorphic effects [5].

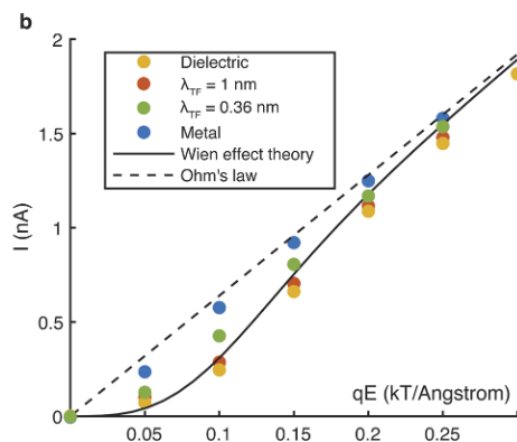


Figure 2.6. Ionic current as a function of electric field in slits of varying material types. The slit is 0.7 nm high and ion motion is restricted to the center of the slit. Reprinted from *Kavokine, Robin, and Bocquet. "Interaction confinement and electronic screening in two-dimensional nanofluidic channels." Journal of Chemical Physics 157, no. 11, 114703 (2022)*, with permission from AIP Publishing. This appears as Fig. 4 in the original [17].

Kavokine et al. [17] later followed up on this work to use approximations for analytical results of the potential due to an ion in exactly the center of a slit of perfect metal, dielectric insulator, or Thomas-Fermi imperfect metal [17]. They show that the ionic current in all materials limits to the same linear trend, but for lower fields, there is some variation based on slit material, as seen in Fig. 2.6.

These works together show us that the material of a slit (or, more specifically, the dielectric mismatch between a solvent and the walls of a slit) impacts ion distribution and transport behavior. There has been a need for simulations that use potentials that are more exact or that allow ions more free reign in much narrower slits. This will be explored in Chap. 3, which looks at ionic current in slits made of inert (non-polarizable) walls or conducting walls for ions of different valency in all-atom simulations, and Chap. 4, which

isolates the electrostatic interactions of this system and shows the impact to ionic current of slit wall material as well as the image plane position.

2.4.5. When the polarizable surface isn't planar

So far, we have discussed only the polarization of planar surfaces in response to the presence of ions. However, most surfaces are not exactly planar. In fact, porosity is quite important in several of the applications discussed in Sect. 2.1. Some simple cases have been studied: different geometries do change the polarization response of a material. For example Duplantier, et al. calculated the free energy of arbitrarily shaped surfaces using linearized Debye-Hückel theory and boundary conditions representing constant potential or dielectric surfaces [18]. Solis and Olvera de la Cruz showed that a sinusoidal interface has a different dielectric response than a planar one for two reasons. The first is modulation of the surface height relative to a nearby ion: points at peaks are closer to slit center than points in the troughs and so will have a stronger response. The second is the change of curvature: the negative curvature of trough regions results in a higher density of surface normals facing nearby both ions and other polarizable parts of the surface, so the dielectric response is stronger than that at the peaks [19]. Wu et al. showed via molecular dynamics simulation that this results in a modified ion distribution near the surface: for asymmetric salts (2:1), the divalent cations were more repelled from the surface than monovalent anions, resulting in a net negative ion charge density near the surface—and that this effect is much stronger near troughs than peaks [20]. However, the study of distribution and transport of ions near surfaces more complex than a plane is young and there is quite a bit of space to explore.

Given that polarization effects are so different between simple planar surfaces and undulating ones, and given that many of the applications motivating this work do rely rough surfaces (like activated carbon), we need to understand how properties like capacitance, ion arrangement, and ion transport, are affected by geometries more complex than simple planes. Additional geometry effects will be discussed in more detail in Chap. 5.

2.5. Limitations of the polarization-only framework and next steps

In this chapter, we have focused quite precisely how the distribution and motion of ions is impacted by two related properties: confinement and polarizability of the confining walls. However, there are other contributors to ion behavior in these systems. These include the following

- Ions themselves are polarizable. This has been accounted for by Levin [21] and is especially relevant when ions are crossing interfaces, though may also play a role in transport or when counterion clouds are deformed. We do not include any ion polarizability.
- Quantum interactions between the ion and the surface, some of which can be incorporated as a force field, or which might be need to be included in more detail [22]. This is still an emerging field due to computational complexity of solving for quantum effects. We focus only on electrostatic interactions here.
- Confinement can impact the solvent itself. Water, a highly polar and asymmetric molecule, has a high dielectric constant (80) due to its ability to bend, rotate, etc., in response to an external electric field. However, when it is confined to near a surface or between two very close surfaces, its degrees of freedom are restricted.

This substantially lowers the perpendicular component of the dielectric constant of water to about 2 for the layer of water next to the surface [23]. This is not isotropic—the component of the dielectric constant parallel to the surface remains around 80 [24, 25]. Robin et al. and Kavokine et al. have incorporated some of this tensor nature of the dielectric constant of confined water, which tends to enter equations as $\sqrt{\varepsilon_{\perp}\varepsilon_{\parallel}}$ [5, 17], but we will not do this. In most of the following studies, we will treat the solvent as a background medium with a certain isotropic relative dielectric constant. The exception is the all-atom modeling work in Chapt. 3. However, this does not hamper the utility of our work completely. Knowing that, for example, water’s relative dielectric constant can change so dramatically under strong confinement will influence the choice of relative dielectric constant in our calculations. However, for any more detailed study, solvent effects should be included.

Even without the inclusion of all of these effects, we believe there is value in studying the simplified electrostatics of complex nanoscale systems. There are so many forces at play: steric ordering at high concentrations, depletion-like forces that push ions towards the walls, ion-ion correlations and resistance to neutralizing cloud deformations that tend to pull ions from the walls, and charge-based attraction and repulsion all are acting with varying degrees of importance, based on the properties of the electrolyte and the walls that contain it. Steric effects are less important at low concentrations or if the slit is so narrow that ions cannot interact in three dimensions, ion cloud deformation is easier when the ions are of lower valency, charged surfaces may or may not be present. In the next three chapters, we will explore these effects in the context of ion transport in

very narrow slits, as well as ion distribution near an undulating surface in response to an external electric field. We hope these insight will contribute to the field's understanding of how ions behave when they are confined to small spaces, with the end goal of improving supercapacitor energy density, functionality of iontronic devices, and more.

CHAPTER 3

Ion transport in nanoslits of constant charge or constant potential

While the response of one perfect conductor to a nearby ion has been long known [26], the ability to incorporate induced charge on both conducting walls of a narrow slit into molecular simulations is relatively new [13, 16, 17] and has been limited to wider slits or situations where ions sit exactly in the middle of the slit. The work presented in this chapter uses a constant potential boundary method to compare the behavior of ions being transported by external electric field in a slit whose boundaries are either constant charge or constant potential. The all-atom simulations allow us to understand both the behavior of ions and also the response of confined water, and how these interact with one another. For the simulation and analysis in this paper, Felipe Jiménez-Ángeles's focus was studying the modulation of the potential between electrodes of constant potential and calculating the dielectric response of water. My primary contribution was simulation and analysis of ionic current.

The following was originally published in the Faraday Discussions ("Iontronics: from fundamentals to ion-controlled devices") in 2023. It is reproduced here with permission of Felipe Jiménez-Ángeles, Monica Olvera de la Cruz, and the Royal Society of Chemistry.

Supplementary material associated with this chapter can be found in Appendix A.

Surface polarization enhances ionic transport and correlations in electrolyte solutions nanoconfined by conductors

Felipe Jiménez-Ángeles, Ali Ehlen, Monica Olvera de la Cruz

Reprinted with permission from:

Faraday Discussions, 2023, **246**, 576-591, DOI: 10.1039/D3FD00028A

<https://pubs.rsc.org/en/content/articlehtml/2023/fd/d3fd00028a>

ABSTRACT: Layered materials that perform mixed electron and ion transport are promising for energy harvesting, water desalination, and bioinspired functionalities. These functionalities depend on the interaction between ionic and electronic charges on the surface of materials. Here we investigate ion transport by an external electric field in an electrolyte solution confined in slit-like channels formed by two surfaces separated by distances that fit only a few water layers. We study different electrolyte solutions containing monovalent, divalent, and trivalent cations, and we consider walls made of non-polarizable surfaces and conductors. We show that considering the surface polarization of the confining surfaces can result in a significant increase in ionic conduction. The ionic conductivity is increased because the conductors' screening of electrostatic interactions enhances ionic correlations, leading to faster collective transport within the slit. While important, the change of water's dielectric constant in confinement is not enough to explain the enhancement of ion transport in polarizable slit-like channels.

3.1. Introduction

Ions transport in strongly confined fluids plays a key role in biological processes and nanoscale applications, including ion exchange between cells and their surrounding aqueous medium, nanofluidic energy conversion, and water desalination [27–29]. Slit-like pores fabricated of layered materials allow studying thin liquid films of thicknesses down to the nanometre scale [30], leading to the discovery of new properties of water and ions, such as the suppression of the dielectric permittivity in water films consisting of two or three molecular layers [23], and room-temperature phase transitions [31–33]. Studies of ion transport in slit-like channels show that an applied voltage acts as a gate of a pressure-driven current [34]. Interestingly, in that work, slit-like channels of graphite and hexagonal boron nitride (hBN) exhibit marked differences in the ion transport attributed solely to the properties of the confining surfaces. Specifically, hBN is an insulator, whereas graphite has properties of dielectrics and conductors due to its anisotropy [35]. In the basal plane’s normal direction, the electric conductivity is at least four orders of magnitude lower than along the directions of the basal plane. As a consequence, while graphite conducts in-plane, a dielectric constant in the basal plane’s normal direction can be measured in graphitic materials, and its value is similar to that of hBN [36, 37].

The phenomena described in the previous paragraph underscore the need to consider the coupling between the electrons on a surface interacting with atoms and molecules from another material. The coupling between the electronic and atomic interactions occurs because atomic charges induce interfacial polarization charges on nearby surfaces. To consider the surface polarization charges induced by charges near interfaces, it is necessary to impose distinct electrostatic boundary conditions on dielectrics and conductors.

In conductors, the surface electrostatic potential is maintained constant [38, 39], whereas dielectrics require the continuity of the displacement field [40, 41]. The image charge method is employed to solve the electrostatic boundary condition equations [42–44], but it is difficult to extend to non-planar interfaces and can be computationally expensive. The fluctuating charges methods [7, 39, 45, 46] consist of adjusting the surface polarization charges on-the-fly to minimize the electrostatic energy. A recent method employs periodic Green functions to consider the surface polarization [13]. Atomistic models consider the atomic polarizability in dielectrics using the Drude model of fluctuating induced dipoles [47]. However, this approach is not extensible to conductors.

The metallic nature of conductors leads to different degrees of electronic screening [48]. The Thomas-Fermi (TF) model is suggested to explain the degree of electronic screening in non-perfect conductors [14]. In the TF model, the charges in a solid are envisioned as an electron gas in a neutralizing background. The quantum effects are considered using a finite screening length λ_{TF} of the interactions between polarization charges. The TF theory [49] considers that the charge density in an electron gas is approximated by $q_{\text{TF}}\rho^P(r) = -\varepsilon_0\varepsilon_r k_{\text{TF}}^2 \Psi_\beta(r)$, similar to the Debye-Hückel theory for electrolytes; ε_0 is the vacuum permittivity, ε_r is the dielectric constant of the medium, $k_{\text{TF}} = \lambda_{\text{TF}}^{-1}$ is the inverse screening length, and $\Psi_\beta(r)$ is the electrostatic potential in the conductor. In perfect conductors $\lambda_{\text{TF}}^{-1} \rightarrow \infty$. The TF approximation, however, is only valid in the limit of infinite nuclear charge [50].

The electronic screening affects the properties of a nearby ionic fluid. To consider the electronic screening of conductors next to an ionic fluid, a TF fluid is considered as an ionic mixture within a region of width d_{TF} inside the conductor [14]. It is found that

the screening from the TF fluid shifts the wetting and phase transition points of confined ionic liquids.

Water and ions in confinement play a key role in numerous applications. Therefore, it is of paramount importance to understand how water and electrolyte solutions are affected by the properties of the confining materials. Recently, we showed that the water polarization near an interface breaks the symmetry of electrostatic interactions [25]. The symmetry breaking implies that the potential of mean force between two oppositely charged ions near a liquid-solid interface, interacting along the interface's normal direction, differs by $5 k_B T$ when exchanging the ions' position with respect to the surface. Here, we use molecular dynamics simulations to investigate ionic transport in aqueous solutions confined in slit-like-channels formed by conductors. To account for the interaction between conductive surfaces, ions, and water, we assign fluctuating polarization charge on the atoms of the conductors with a spatial Gaussian distribution [38, 39]. We propose using the width of the Gaussian distributions κ^{-1} to model the electronic screening in non-perfect conductors.

3.2. Methods

3.2.1. Molecular Dynamics

We consider an ion solution consisting of N_w water molecules, N_+ cations, and N_- anions confined between two surfaces modelled using graphene sheets. The surfaces are parallelly placed on the x - y plane separated by a distance h in the z -direction (see Figure 3.1). We use graphene sheets made of 1008 carbon atoms each. The system is placed in a

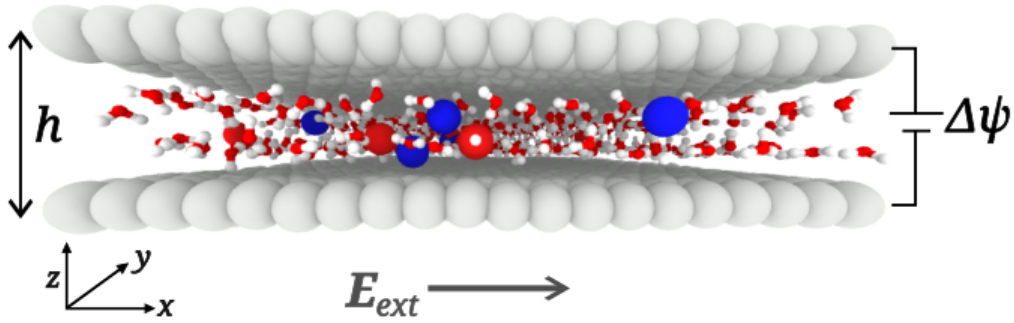


Figure 3.1. Simulation setup consisting of an electrolyte solution confined by a slit-like channel formed by two surfaces with separation distance h measured from the carbon atoms' center. The particles size is reduced in this image to visualize the ions. Polarizable surfaces of conductors are maintained at constant potentials Ψ_t and Ψ_b at the top and bottom electrodes, respectively. The potential difference is $\Delta\Psi = \Psi_t - \Psi_b$. Non-polarizable surfaces are assigned constant surface charge densities, σ_t and σ_b at the top and bottom electrodes, respectively. An external electric field E_x is applied in parallel surfaces' direction to induce the ions' transport.

simulation box of dimensions $L_x = 5.065$ nm and $L_y = 5.104$ nm, in the x - and y -directions, respectively. The box length in the z -direction is $L_z \gg h$. To mimic two-dimensional (2D) periodicity in the x - and y - directions, we use the slab correction [51] in three-dimensional boundary conditions (3DC). We set $h = 0.97$ nm to study the dielectric response of water and an electrolyte solution. The water layer is made of 580 water molecules. The electrolyte solution is made of 560 water molecules, 10 cations, and 10 anions. Water is represented using the extended simple point charge [52] (SPC/E) model, and the AA-OPLS force field parameters are employed to represent the van der Waals interactions of graphene and the ions [53].

We study the systems when the surfaces are conductors and non-polarizable. In conductors, the surface potential at the top and bottom surfaces (see Figure 3.1) is kept constant at Ψ_t and Ψ_b , respectively, and the potential difference is $\Delta\Psi = \Psi_t - \Psi_b$. In non-polarizable electrodes, the surface charge density at the top and bottom surfaces are constant at σ_t and σ_b , respectively. We study the cases when the surfaces are at zero charge and zero surface potential and are asymmetrically charged. In general, the potentials in conductors are assigned as $\Psi \equiv \Psi_t = -\Psi_b$, whereas in the non-polarizable surfaces, the charges are assigned as $\sigma \equiv \sigma_t = \sigma_b$. The system formed by conductors are referred to as constant potential systems (Ψ), whereas the non-polarizable systems are referred to as constant charge density (σ) systems. In the constant charge systems, each atom on the bottom and top electrodes has a charge q_b and q_t , respectively. The charges are assigned using the average simulation values at a constant potential. In the next section, we outline the method to maintain a constant potential on the surfaces.

To induce the ionic transport, the external electric field is applied tangentially to the surface in the x -direction and designated as \mathbf{E}_x . The force due to the external field on each charged atom or ion is $\mathbf{f}_i = q_i \mathbf{E}_x$. The magnitude of the effective field experienced by any charge in the system $|\mathbf{E}|$ is smaller than $|\mathbf{E}_x|$ due to the polarization of water and other charged particles in the system in response to \mathbf{E}_x . Later, we discuss the implications of polarization in water and how our results could be related to experimental measurements.

The ions' equations of motion are integrated using the standard molecular dynamics algorithms implemented in LAMMPS [8]. The system temperature is maintained at $T = 298$ K. We compared the cases when the slit surfaces are made of conductors and non-polarizable materials.

3.2.2. Constant Potential

We use the model introduced by Siepmann and Sprik [38, 39] that consists in assigning a Gaussian distribution of the polarization charge on each of the electrode's atoms

$$(3.1) \quad \rho_P(\mathbf{r}) = \sum_{i=1}^{N_e} q_i \left(\frac{\eta^2}{\pi} \right)^{\frac{3}{2}} e^{-\eta^2(\mathbf{r}-\mathbf{R}_i)^2}$$

where κ is the inverse width of the distribution centered at the position \mathbf{R}_i of each one of the N_e atoms forming the electrodes. The charge of the water atoms and the ions is considered using a Dirac delta function for each atomic position \mathbf{r}_i containing a point charge

$$(3.2) \quad \rho_F(\mathbf{r}) = \sum_i q_i \delta(\mathbf{r} - \mathbf{r}_i)$$

where the summation is performed over the charges of the atoms in the liquid. The electrostatic energy of the system is expressed as

$$(3.3) \quad U_C = \frac{1}{8\pi\epsilon_0} \int \int \frac{\rho(\mathbf{r}')\rho(\mathbf{r}'')}{|\mathbf{r}'' - \mathbf{r}'|} d\mathbf{r}' d\mathbf{r}''$$

where $\rho(\mathbf{r})$ is the total charge density including the polarization charges of the electrode, and the charges from water molecules, and ions. The potential Ψ_j on a charge q_j is obtained by taking the derivative of U_C with respect to this charge, keeping all the other charges constant

$$(3.4) \quad \Psi_j = \left(\frac{dU_C}{dq_j} \right)_{q_i, i \neq j}$$

The charge of each electrode atom is obtained by imposing the potential constant on each atom, $\Psi_j = V_{0j}$. This condition is achieved minimizing the constrained electrostatic energy function

$$(3.5) \quad U_E = U_C(q_i) - \sum_j \Psi_j q_j$$

where the summation is performed over the charges of the electrodes. By writing the charge density as $\rho(\mathbf{r}) = \rho_F(\mathbf{r}) + \rho_P(\mathbf{r})$, where $\rho_F(\mathbf{r})$ includes the charges in the fluid and $\rho_P(\mathbf{r})$ includes the polarization charges in the electrode. Employing this definition, Eq. 3.3) is cast as

$$(3.6) \quad U_C = U_{FF} + U_{PF} + U_{PP}$$

where U_{FF} is the Coulombic interaction between the charges in the liquid, U_{PF} is the interaction between the liquid and the polarization charges, and U_{PP} is the interaction between the polarization charges. Setting the derivative of U_E equal to zero, and using Eq. 3.6, the potential on each atom of the electrode can be written as

$$(3.7) \quad \Psi_j = \sum_k A_{jk} q_k + b_j$$

A_{jk} includes the interaction terms of all the charges q_k on the electrode with the site j , whereas b_j includes the interaction term of the fluid particles with the site j . Because the positions of the electrode charged sites remain fixed in the simulation, the components of the matrix A_{jk} remain constant during the simulation, while the components of b_j are

updated at each time step. Using matrix notation, the solution of Eq. 3.7 is written as

$$(3.8) \quad \mathbf{q} = \mathbf{A}^{-1}(\Psi - \mathbf{b})$$

where \mathbf{q} is a vector that contains the charges of the electrodes, and Ψ contains the potential at the electrodes' charged sites. The computation of the polarization charges at each time step is necessary to perform molecular dynamics simulations. By using a Gaussian distribution the calculation of the electrostatic energy is performed using the available P3M algorithm to calculate long-range electrostatic interactions [45]. In our study $\eta = 18 \text{ nm}^{-1}$.

3.3. Results

First, we study the polarization charge induced by ions located at the center of the simulation box in the x and y directions and 0.3 nm from the conductors separated by h (See inset of Figure 3.2a). It is well known in electrostatics that near the surface of single conductor, an ion of charge q induces an image charge of the same magnitude as its own but of the opposite sign $-q$. However, when an ion is confined by two conductors, the polarization charge is induced on both conductors and depends on the surfaces' separation distance and the ion's position with respect to the surfaces. We consider the configuration in the inset of Figure 3.2a that contains two oppositely charged ions placed symmetrically at $(L_x/2, L_y/2, \pm(h/2 - 0.3 \text{ nm}))$. We see that the magnitude of the total induced charge on a given conductor is lowered by the presence of the other parallel conducting surface. In this configuration, the magnitude of the induced charge on the conductor is equal to that of the nearby ion only when the separation h is in the range of 1000 nm.

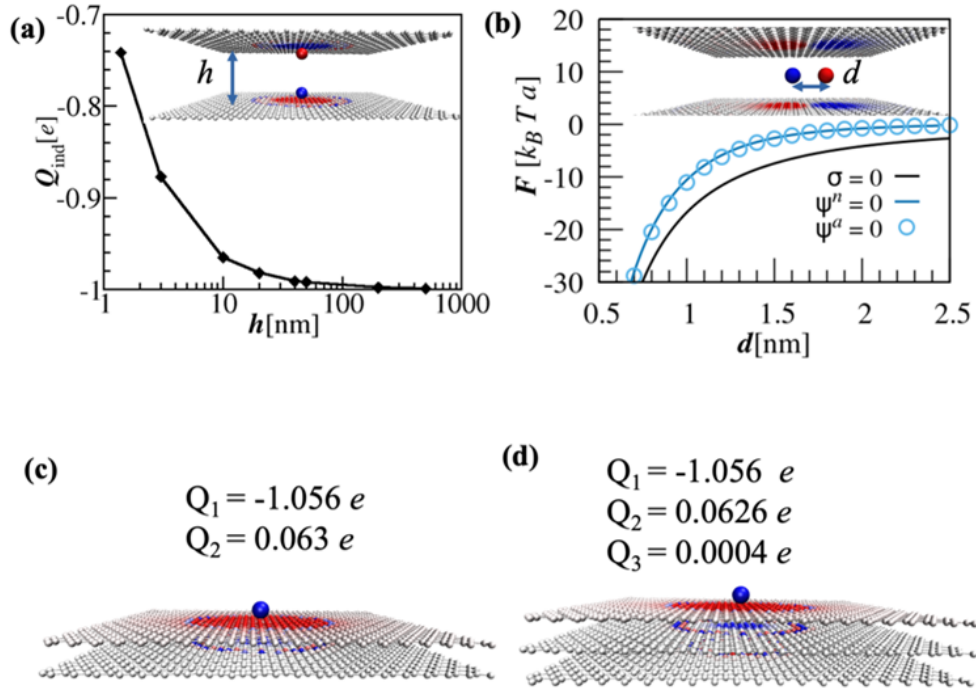


Figure 3.2. Polarization of conductive materials maintained at $\Psi_t = \Psi_b = \Psi = 0$. (a) Induced polarization charge Q_{ind} on the conductor as a function of the surface-surface separation distance h when an ion is placed at 0.3 nm from each surface. The inset shows the ions' configuration between the two surfaces. Blue and red colors on the surface of conductors are assigned based on the magnitude and sign of the polarization charge; positive charges are colored in blue, and negative charges are in red. (b) Interaction force between a monovalent cation and a monovalent anion placed at the middle plane between the two conductors separated by a distance of $h = 1.3$ nm; the black line is calculated by neglecting the surface polarization ($\sigma = 0$); the light blue line ($\Psi^n = 0$) is the force that includes the contributions from the polarization charges obtained by numerically solving Equation 3.8. The open circles represent ($\Psi^a = 0$) the force calculated using the analytical image charge method (see Supporting Information). Polarization charges (showing only the bottom electrode) in slit-like channels formed surfaces of (c) two and (d) three layers. The surfaces' separation distance is $h = 50$ nm. The induced charges Q_1 , Q_2 , and Q_3 are numbered from the closest layer to the ion.

We now investigate how the interaction between two ions is changed by the presence of the two surfaces. For that, we calculate the interaction force between two oppositely charged ions placed at the middle plane between the two surfaces separated by $h = 1.3$ nm. Figure 3.2b shows the interaction forces between the two ions confined between polarizable and unpolarizable surfaces as a function of their separation distance d (see inset of Figure 3.2b). We observe that the magnitude and range of the attraction are reduced between ions confined by conductors with respect to the interaction between non-polarizable surfaces. The reduction is caused by the polarization charges on the conductors that screen the interaction between the confined charges.

Now we investigate the induced surface charge in multi-layered surfaces separated by $h = 50$ nm. In single-layered conductors at $h = 50$ nm, the absolute value of the induced charge $|Q_{\text{ind}}|$ is approximately $0.992e$. In multi-layered conductors, the polarization charge is induced as far as three layers from the closest surface to the ion. We find that the absolute value of the induced charges on the closest layer to the ion Q_1 is larger than $1e$, while a charge of the opposite sign is induced on the second layer Q_2 . The induced charge in the third layer is negligible and is similar in surfaces made of three or more layers. The overall charge in single-layer and multi-layer conductors is similar. However, the polarization is distributed differently depending on the number of layers. Our results imply that the induced charge fluctuations on single-layered materials are affected by the induced polarization of a supporting substrate [54].

3.3.1. Static properties of confined water and ions

Given that the presence of conductors impacts charged interactions, we are interested in how this effects a more realistic system. We investigate the behavior of a water layer confined between two surfaces separated by $h = 0.97$ nm. The polarization charge on the conductors is induced by the charges of oxygen and hydrogen atoms from water. Oxygen is negatively charged and induces positive polarization charges, whereas hydrogen bears a positive charge and induces negative polarization charges. In Figure 3.3a, we observe that the polarization charge on the conductors is distributed in a non-uniform way due to different conformations of the water molecules. Therefore, the total charge density σ on the surface of conductors is not constant. Figure 3.3b shows the probability distribution of the induced charge densities on the surfaces at $\Psi = 0$ and 0.5 V. Figure 3.3b shows the results of water with no ions. We observe that the charge density fluctuates around a mean value σ_V that depends on the potential. We find that $\sigma_V = 0.00$ and $0.187 e/\text{nm}^2$ for potentials of $\Psi = 0$ and 0.5 V, respectively. By plotting the distribution around the mean value σ_V the two curves overlap. An applied electric field in the surface parallel direction slightly changes the value of σ_V and the presence of different ion type too (see Figure S2 in the Supporting Information). The distribution width remains unchanged by the presence of ions, gating potential, and an applied electric field in the surface parallel direction (see Figure S2 in the Supporting Information). Therefore, while the mean value of the surface charge density changes with the potential, the width of the distribution is independent of the applied potential. This indicates that the fluctuations of the polarizations are regulated by the thermal fluctuations of the water molecules.

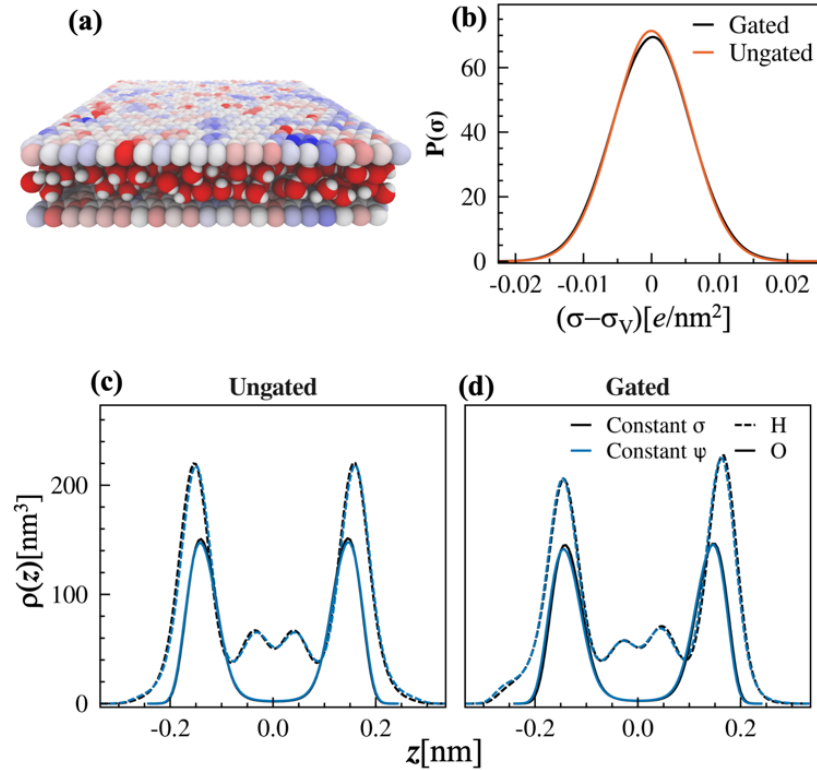


Figure 3.3. Effect of the surface polarization on confined water. (a) Snapshot of an instantaneous configuration of water confined between two conductive surfaces separated by $h = 0.97$ nm. The surface atoms are colored by their charge; blue and red represent positive and negative charges, respectively; the intensity represents the magnitude. (b) Probability distribution $P(\sigma)$ of the induced charge density $\rho(z)$ plotted around the mean value σ that depends on the potential difference between the two surfaces. Density profiles $\rho(z)$ of hydrogen and oxygen atoms from water between (c) uncharged non-polarizable ($\sigma = 0$) and conductive ($\Psi = 0$) surfaces, and (d) charged non-polarizable ($\sigma = 0.187 e/nm^2$) and conductive ($\Psi = 0.5$ V) surfaces. The solid lines are the water oxygen atoms profiles, while the dashed lines are water hydrogen atoms profiles. The black lines represent the profiles in slit-like channels of conductors, while the light-blue lines are in non-polarizable surfaces. The z -coordinate is defined with respect to the middle plane between the two surfaces.

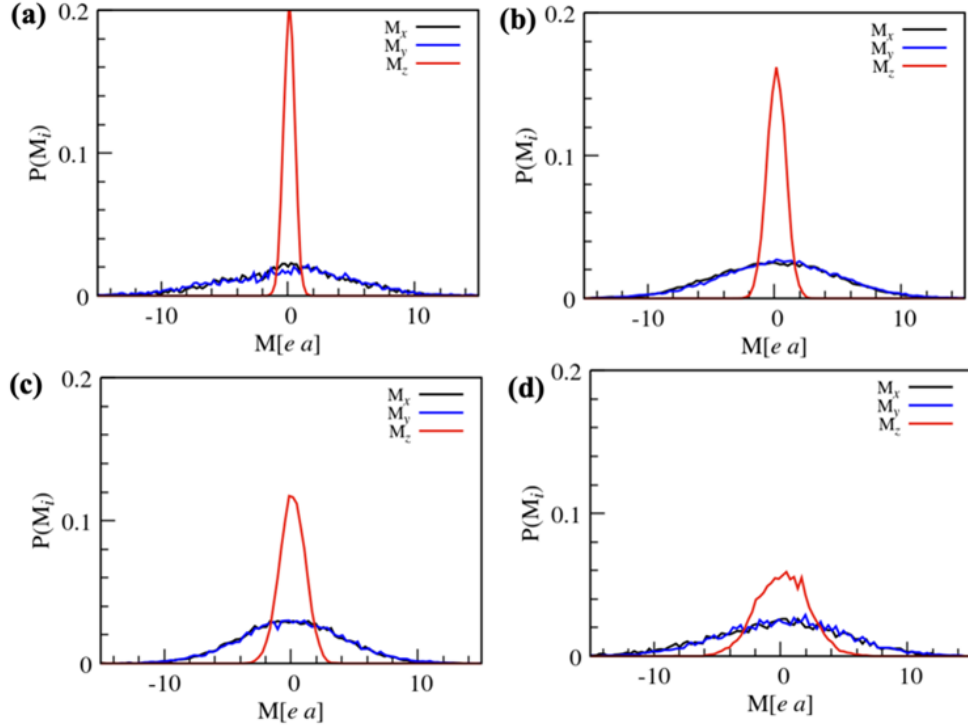


Figure 3.4. Dielectric response of confined water and an electrolyte solution. Probability distribution of the total dipole moment components M_i , $i = x, y, z$ of water between two (a) non-polarizable and (b) polarizable surfaces, and an electrolyte solution between (c) non-polarizable and (b) polarizable surfaces. The surfaces' separation is $h = 0.97$ nm.

The hydrogen and oxygen density profiles are symmetric when the surfaces are un-gated (see Figure 3.3c). When the surfaces are gated, the water molecules orient, and the negative surface preferentially adsorbs hydrogen atoms (see Figure 3.3d). Due to the water dipole moment and high density, the polarization effects from the surface are highly screened. Therefore, the hydrogen and oxygen density profiles are not significantly different when the surfaces are conductors or non-polarizable. However, the dielectric responses and the ions' transport are affected by surface polarization, as we will see next.

We investigate the changes in the dielectric response of water and an electrolyte solution confined by conductors and non-polarizable surfaces. We analyse our results in terms of polarization and the effective dielectric constant. The instantaneous polarization is calculated as $\mathbf{p} = \frac{\mathbf{M}}{V}$, where $\mathbf{M} = \sum_{i=1}^{N_w} \mu_i$ is the dipole moment (μ_i) including all the water molecules in the volume V . The components of the dielectric tensor are given as [55, 56]

$$(3.9) \quad \epsilon_{\parallel} = 1 + \left(\frac{\beta}{2\epsilon_0} \right) [\langle \mathbf{M}_{\parallel}^2 \rangle - \langle \mathbf{M}_{\parallel} \rangle^2]$$

$$(3.10) \quad \epsilon_{\perp}^{-1} = 1 + \left(\frac{\beta}{2\epsilon_0} \right) [\langle \mathbf{M}_{\perp}^2 \rangle - \langle \mathbf{M}_{\perp} \rangle^2]$$

where subscripts \parallel and \perp designate the components in the parallel and perpendicular directions of the slit pore surfaces, respectively; ϵ_0 is the vacuum permittivity, $\beta = 1/(k_B T)$, k_B is the Boltzmann constant, and T is the absolute temperature. The dielectric constant in the parallel direction is proportional to the dipole moment fluctuations (see Eq. 3.9) whereas the component in the perpendicular direction is inversely proportional to the dipole fluctuations (see Eq. 3.10).

We analyse the dipole moment fluctuations of water and an electrolyte solution confined in a slit-like pore of $h = 0.97$ nm. Figure 3.4a shows the probability distribution of the total dipole moment components of water. In the z -direction, the distribution is much narrower than in the x - and y -directions in agreement with the results from the literature [24, 25]. When water is confined by conductors (see Figure 3.4b), the dipole moment probability distributions become broader, and their height decreases with respect

to the non-polarizable surfaces in 4a. The ions have a similar effect as the conductive surfaces by reducing the height and increasing the width of the dipole moment probability distributions (see Figure 3.4c). By placing the electrolyte solution between conductors, the water dipole moment further decreases. The fluctuating total dipole moment of the liquid synchronizes with the induced polarization charge on the surfaces so that the total dipole moment of the system (liquid and polarizable surfaces) is *always* zero.

From the dipole moment fluctuations we obtain the dielectric constant of water using Eq. 3.9 and 3.10. The parallel dielectric constant of water confined by non-polarizable surfaces ($\sigma = 0$) is about $\epsilon_{\parallel} \approx 94.5$. This value is higher than the reported value in bulk for the SPC/E water model. By confining the water between conductive surfaces ($\Psi = 0$), the parallel dielectric constant is about 82. In the presence of ions ϵ_{\parallel} is around 60 when the solution is confined by conductors ($\Psi = 0$) or non-polarizable surfaces (σ). In non-polarizable surfaces, the perpendicular dielectric constant is about $\epsilon_{\perp} \approx 3.5$, which agrees with the measured dielectric constant of water in high confinement⁵. When water is confined by conductors and in the presence of ions, Eq. 3.10 leads to negative values of ϵ_{\perp}^{-1} . This analysis shows that the perpendicular dielectric constant of confined water is significantly lower than in bulk, but in the surfaces' parallel direction can be higher than in bulk. In ultra-thin water layers, the ion-ion interactions mostly occur in the surfaces' parallel direction. Therefore, the interactions are significantly diminished due to the high parallel dielectric constant.

3.3.2. Ion transport in confinement

We investigate ionic transport in the slit channel described in Figure 3.1. To induce the ion transport, we apply an electric field tangentially to the channel surfaces in the x -direction, E_x . The ion current is given as

$$(3.11) \quad I = \left\langle \sum_{i=1}^{N_i} \frac{q_i v_i}{L_x} \right\rangle_{\tau}$$

N_i is the number of free charges (ions) in the system, q_i is the ionic charge, v_i is the instantaneous ion velocity, and L_x is the simulation box size in the x -direction. $\langle \dots \rangle_{\tau}$ means that the average is calculated over the duration time of the simulation, τ . We study the three electrolytes NaCl, CaCl₂, and LaCl₃. The ions' parameters are taken from the AA-OPLS force-field [53]. The compositions of the systems are given in Table S1 in the Supporting Information. We systematically compare the ionic transport in a channel formed by polarizable (conductors) and non-polarizable surfaces.

Figure 3.5 shows the current of NaCl, CaCl₂, and LaCl₃ electrolyte solutions. We observe that the current increases as a function of the applied external electric field E_x and as the cation valence increases. Therefore, at a given electric field different from zero, the lowest current is produced in NaCl and the highest in LaCl₃. Interestingly, the current is systematically higher in channels of conductors than in non-polarizable materials. At all the fields, we observe higher velocities in channels made of conductors than non-polarizable surfaces (for the velocity profiles, see Figure S4 in the Supporting Information). In addition, our data show that the current increases in a non-linear way. The non-linear behavior is enhanced in the slit-like pores made of conductors. The highest

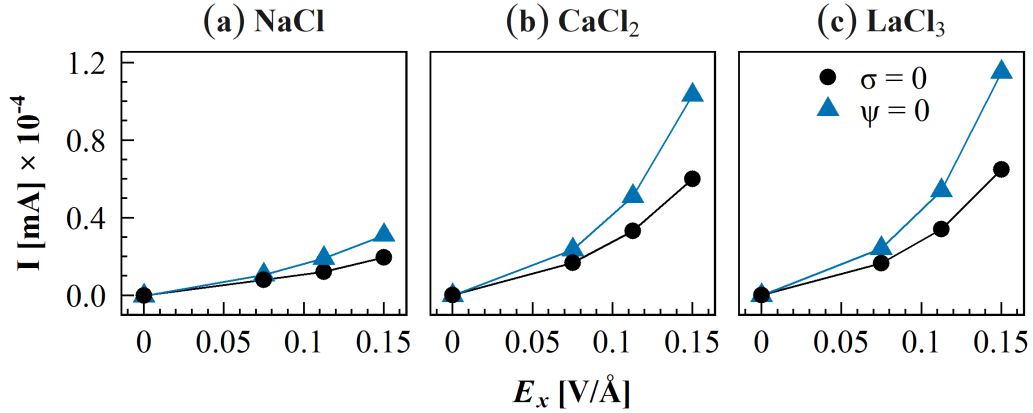


Figure 3.5. Ion transport in a slit-like nanochannel. Average current as a function of the applied external field E_x in electrolytes of (a) NaCl, (b) CaCl₂, and (c) LaCl₃. The electrolytes are confined between non-polarizable surfaces ($\sigma = 0$) and conductors ($\Psi = 0$). The black lines represent the profiles in slit-like channels of conductors, while the light-blue lines are in non-polarizable surfaces. The separation distance between the surfaces is $h = 0.97$ nm. *Note: the error bars in the original publication represented the standard deviation of the data, which is large due to large current fluctuations. Here, the plotted error bars represent the standard error of the current mean, which is quite small.*

field applied in our simulations is 0.15 V/Å (1.5×10^9 V/m), higher than what real systems tolerate [57]. At end of this section, we discuss how equivalent conditions may be created using weaker fields.

Figure 3.6 portrays the contributions to the total current from the two ionic components. In the systems confined by non-polarizable materials, the contribution to the current by both charge carriers, cations and anions, is approximately the same. Similarly, both ions contribute nearly equally to the current in the NaCl electrolyte confined by polarizable surfaces. However, there is a higher contribution from the cation in the CaCl₂ and LaCl₃ systems confined by polarizable surfaces. This phenomenon cannot be

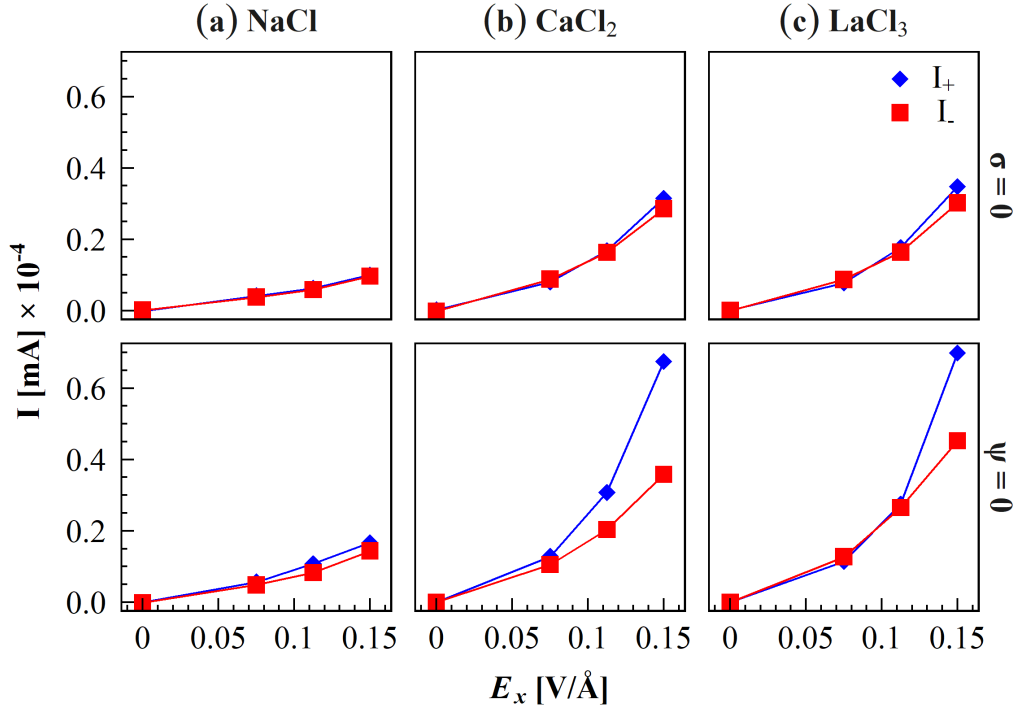


Figure 3.6. Ionic current by components of (a) NaCl, (b) CaCl₂, and (c) LaCl₃. The top panels correspond to slit channels made of non-polarizable ($\sigma = 0$) surfaces whereas the bottom panels are for polarizable surfaces ($\Psi = 0$). Cations contribute to the ionic current more than anions do at high fields and high ion valence. The separation distance between the surfaces is $h = 0.97$ nm. *Note: the error bars in the original publication represented the standard deviation of the data, which is large due to large current fluctuations. Here, the plotted error bars represent the standard error of the current mean, which is quite small.*

understood solely in terms of the higher ionic valence of the cations since it is not observed in non-polarizable systems. Therefore, it is an effect caused by the induced surface polarization.

We investigated the ionic density profiles as a function of the z -coordinate in the channel (see Figure S3 in the Supporting Information). We found that, in general, the cations tend to align at the channel center, whereas the anions are adsorbed on the walls.

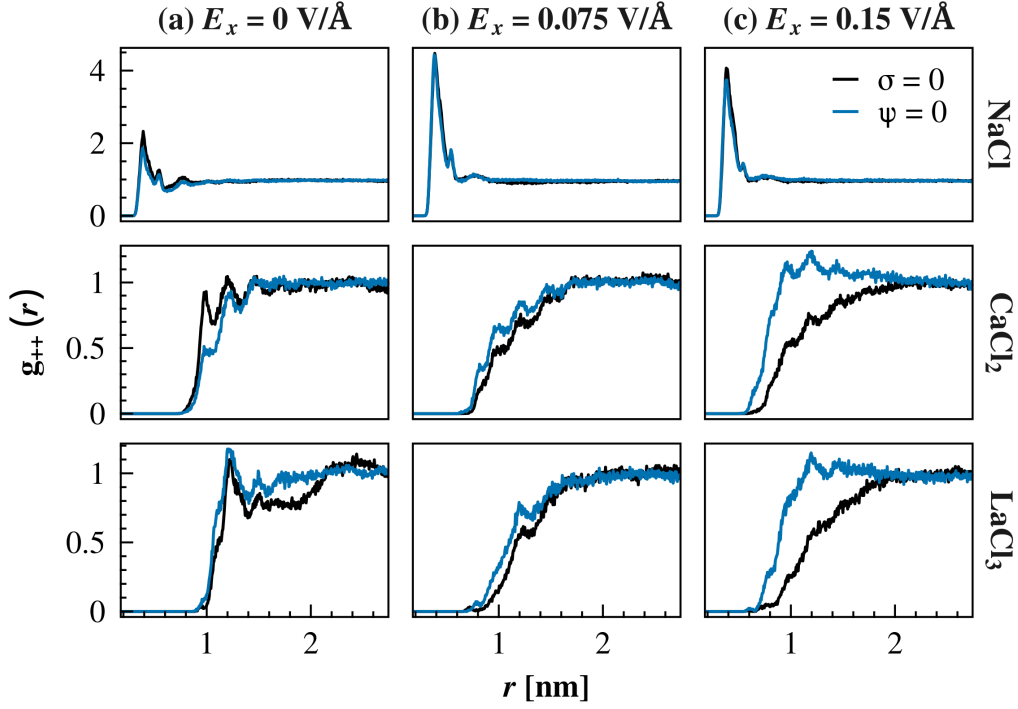


Figure 3.7. Cation-cation pair correlation functions $g_{++}(r)$ in (a) NaCl, (b) CaCl₂, and (c) LaCl₃ confined by slit channels made of non-polarizable ($\sigma = 0$) and polarizable surfaces ($\Psi = 0$). Each row contains the profiles at external fields of $E_x = 0, 0.075,$ and 0.15 V/\AA . The black lines represent the profiles in slit-like channels of conductors, while the light-blue lines are in non-polarizable surfaces. The separation distance between the surfaces is $h = 0.97 \text{ nm}$.

The ionic density profiles slightly change by applying an external field, but these changes are similar in channels made of conductors and non-polarizable surfaces. Therefore, the changes observed in the current cannot be explained in terms of the ionic distributions in the channel.

We look at the pair correlation functions to explain the enhance ionic transport in conductors. The pair correlation functions $g_{+-}(r)$ and $g_{--}(r)$, however, are similar in

polarizable and non-polarizable systems (see Figures S5 and S6 in the Supporting Information). In Figure 3.7, the pair correlations functions between cations $g_{++}(r)$ reveal that only monovalent cations approach other cations at all the fields E_x . The peaks' position implies that the clustering is mediated by the anions. At low fields, divalent and trivalent cations tend to be apart from other cations, however, the tendency to approach between cations increases at high fields in the polarizable systems (In Figure 3.7c, see $g_{++}(r)$ at $E_x = 0.15$ V/Å for CaCl_2 and LaCl_3). Cations continue apart at high fields in the non-polarizable systems.

In terms of the pair correlation function, the potential of mean force between two ions is expressed as $w_{ij}(r) = -k_B T \ln g_{ij}(r)$. The mean force between the two ions is given as $f(r) = -\frac{\partial}{\partial r} w_{ij}(r) = \frac{1}{g_{ij}(r)} \frac{\partial}{\partial r} g_{ij}(r)$. Therefore, a negative slope of a pair correlation profile implies an attractive mean force between the ions. Figure 3.7 shows a region ($1 \text{ nm} < r < 2 \text{ nm}$) where the slope of the $g_{++}(r)$ profiles of divalent and trivalent cations between conductors is negative at the highest electric field. This implies an induced attractive force between the cations confined between conductors, whereas the cations confined between non-polarizable surfaces repel strongly. The attraction between the cations is a cooperative effect caused by the screening of the interactions by the conductors' polarization charge that reduces the repulsion between equally charged ions. The increased capability of cations to approach other cations when they are confined in polarizable surfaces allows them to transport the charge more efficiently.

We studied the ions' transport at surface potentials and charges different from zero. However, the ionic current does not change significantly with respect to the zero-charge and zero-potential conditions (see Figures S7 and S8 in the Supporting Information). This

could result from the polarization charge fluctuations being unaffected at different applied fields and potentials.

Our study shows that changes in surface material induce a difference in ion transport properties at strong electric fields. However, the phenomena described here are difficult to observe in molecular simulations at electric fields lower than 0.05 V/\AA because the dielectric response of water dominates. Effectively, the magnitude of the field experienced by any charge in the system $|\mathbf{E}|$ is smaller than an external field $|\mathbf{E}_{\text{ext}}|$. The attenuation of the applied electric field is due to the induced polarization field that opposes the external field. Hence, the effective electric field is given as $\mathbf{E} = \epsilon^{-1}\mathbf{E}_{\text{ext}}$, where ϵ is dielectric tensor, which has components ϵ_{\parallel} and ϵ_{\perp} greater than 1.

The polarization occurs via the water molecules' orientation and the ions' arrangement at timescales shorter than 10^{-9} s. In water, a strong effective electric field \mathbf{E} may occur (even when \mathbf{E}_{ext} is not too strong) at a timescale faster than the system relaxation time when the components of ϵ are still low. Such conditions can be created using a fast-oscillating AC external field. The effects observed here may also be relevant under weaker fields at lower temperatures or when the transport is induced by a combination of electric field and pressure gradients.

3.4. Conclusions

We studied water and electrolyte solutions confined in nanometre-scale slit-like channels. By comparing slits made of conductors and non-polarizable surfaces, we showed that the surface polarization decreases the repulsion between equally charged ions and is further decreased for multivalent ions. The decreased repulsion between multivalent ions

allows them to move collectively, leading to a more efficient ion transport. While confinement and the surface polarization charges induced in conductors affect the dielectric responses in the confined fluids, it is not enough to explain the increase of the ion conductivity by conductors. Nanochannels formed by conductive electrodes are promising for designing highly efficient energy storage devices, ion removal processes, and bioinspired functions. Tunability of the ionic conduction and dielectric properties is desirable in some applications. Our results show that the conduction and the dielectric response of the confined liquid can be tuned by the dielectric and conductive properties of the confining surfaces.

Gaussian distribution of the polarization charge on the atoms of the conductors could serve to model the screening from electrons. For that, in the future, we will establish the relationship between the width of the Gaussian distribution (η^{-1}) and the electrons' screening correlation length (λ_{TF}) from quantum mechanical calculations.

Acknowledgements: F. J.-A. and M. O. d. l. C. conceived the idea and designed the research. F. J.-A. and A. E. performed the simulations and the data analysis. The three authors contributed to the discussions and drafting of the manuscript.

This work was funded by Award 70NANB19H005 from U.S. Department of Commerce, National Institute of Standards and Technology as part of the Center for Hierarchical Materials Design (CHiMaD) and by the Sherman Fairchild Foundation.

CHAPTER 4

Confined ion current modulation by slit material and polarization plane location

The previous chapter explored the ionic conductivity of specific salts in a conductive nanoslit in water with atomic resolution. However, this system is quite complex: external electric fields reconfigure water in ways that impact the ion-ion interactions and the ions' hydration shell also mediates these interactions. To isolate the electrostatic contribution of the slit wall polarization, the work presented in this chapter models coarse-grained ions in implicit solvent confined to very narrow slits, which are made of materials such that the interfaces are either non-polarizable, insulating dielectric, or constant potential. We also note that, when calculating the induced charge on an interface, it's not always clear where this charge should be relative to the excluded volume of the polarizable wall. This idea will also be discussed and explored. For the simulation and analysis in this paper, Alexandre Pereira dos Santos developed the methods referred to as FSCC and PGF, Felipe Jiménez-Ángeles ran and analyzed simulations of constant potential slits with explicit polarization, and I ran and analyzed simulations of insulating dielectric slits with explicit polarization.

The following was originally published in the Physical Review Research in 2023. It is reproduced here with permission of Alexandre Pereira dos Santos, Felipe Jiménez-Ángeles, Monica Olvera de la Cruz, and the American Physical Society.

Supplementary material associated with this chapter can be found in Appendix B.

Modulation of ionic conduction using polarizable surfaces

Alexandre Pereira dos Santos,* Felipe Jiménez-Ángeles,* Ali Ehlen, Monica Olvera de la Cruz

* equally contributing first authors

Reprinted with permission from:

Physical Review Research **5**, 043174, DOI: 10.1103/PhysRevResearch.5.043174

[https://journals.aps.org/prresearch/abstract/10.1103/PhysRevResearch.](https://journals.aps.org/prresearch/abstract/10.1103/PhysRevResearch.5.043174)

[5.043174](https://journals.aps.org/prresearch/abstract/10.1103/PhysRevResearch.5.043174)

ABSTRACT: Hybrid ionic-electronic conductors have the potential to generate memory effects and neuronal behavior. The functionality of these mixed materials depends on ion motion through thin polarizable channels. Here, we explore different polarization models to show that the current and conductivity of electrolytes is higher when confined by conductors than by dielectrics. We find non-linear currents in both dielectrics and conductors, and we recover the known linear (Ohmic) result only in the two-dimensional limit between conductors. We show that the polarization charge location impacts electrolyte structure and transport properties. This work suggests a mechanism to induce memristor hysteresis loops using conductor-dielectric switchable materials.

4.1. Introduction

Switchable conductance is desirable for designing densely interconnected (neuromorphic) systems for information storage, performing complex logic operations, and executing neural network algorithms [58–60]. To emulate neural activity, such as voltage spiking [5,

61] and synaptic plasticity [62, 63], researchers use different materials considering switchable ionic or electronic conduction [64, 65]. For example, the gate resistance tunability has been explored for neuromorphic circuits using monolayer MoS₂ multi-terminal memtransistors [65]. To expand functionality and flexibility of device design, integration of ionic and electronic conduction is an attractive option as it may allow for imitating synaptic potentiation, emulating plasticity [66, 67], and achieving neural interfacing. The coupling between ionic and electronic transport is promising for leveraging other applications such as biosensing, energy storage, and responsive materials.

Mixed ionic-electronic conductors are materials that conduct both ions and electronic charge carriers (electrons and/or holes)[68]. Recent developments combine electronic and ionic conductor materials into alternating layers of nanometric dimensions where the ionic and electronic conduction occur simultaneously [69]. The close proximity of ionic and electronic charge carriers in these devices means that the conduction behavior of one influences the other. These materials' electronic properties can be modified by the stoichiometry [70, 71], gate biasing [65, 72], and structural changes [69]. The coupled ionic and electronic interactions and transport need special understanding beyond the comprehension of their independent behavior.

Despite numerous technological applications envisioned by using mixed ionic-electronic conduction, the lack of fundamental understanding impedes rational materials design. One essential component of mixed conduction is the effect of induced electronic polarization on ionic conduction. Previous work showed that the electronic properties of surfaces affect the nearby ions, specifically via the induced polarization charges due to dielectric

mismatch on the material-electrolyte interface [14, 17, 73, 74]. A recent formalism employs the Thomas-Fermi model [50] to consider polarization effects on the ions' transport in strong confinement by dielectrics and conductors [17]. However, the formalism is derived only for ions constrained to move in two dimensions. Using two different approaches, here we study ion conduction in strong confinement in a slit-like channel and we recover some aspects of the two-dimensional behavior predicted by the Thomas-Fermi model.

Frameworks and models that integrate the interfacial electronic polarization of materials and electrostatic molecular interactions are essential for exploiting the properties of interfaces in nanometer slit confinement [14, 44, 74]. As illustrated in Fig. 4.1(a), the electrostatic potential generated by a charge in the center of a narrow slit-like channel is highly dependent on the polarizability of the channel. Whereas the range of the potential is increased by dielectric confinement, the potential in strong conducting confinement is so screened that it can be considered short range. Here, we study ionic conduction in strongly confining slit-like channels and show that the ionic conductivity and the ionic adsorption are significantly impacted by changes in the confining material polarization (from dielectric and conductor), the confining distance, and the location of the polarization charges. Results from density functional theory show that the polarization plane location is a material- dependent property [75]. Hence, by adjusting the polarization plane location we consider materials of different electronic properties.

The paper is organized as follows. First, we develop an efficient method for treating ionic interactions in strong confinement by conductors and define the system parameters. We then find a nonlinear ionic conduction response, which is a prerequisite for neuromorphic behavior. Finally, we demonstrate that the location of the polarization

charge impacts the ionic distribution and transport through the channel. The placement of the polarization charge offers a mechanism for modeling material-dependent properties of polarizable surfaces.

4.2. Green's Function Methods and System Parameters

We consider a system consisting of a 1:1 electrolyte with N_+ cations and N_- anions of diameter d confined between two polarizable surfaces placed parallel to the x - y plane and separated by a distance L in the z -direction. The (periodic) box has side lengths L_x and L_y in the x and y directions. Each region has a uniform dielectric constant, which is ϵ_w and ϵ_c for the electrolyte and confining material, respectively. To investigate the ions' transport, we apply an external field \mathbf{E} in the direction parallel to the confining walls. The setup is shown in Fig. 4.1(b).

The ion-ion electrostatic interaction that accounts for the polarization of the confining conducting surfaces is derived from the method developed in Ref. [76]. It circumvents explicit calculation of induced surface charge, applies to strong confinement ($1 < L/d < 2$), and consists of a single term for $1 < L/d \lesssim 1.5$. The method takes advantage of the short-ranged ion-ion electrostatic interaction in strong confinement by conductors, which allows us to use the minimum image convention rather than Ewald summation methods to compute the electrostatic interactions. This significantly accelerates molecular simulations, so we refer to the method as the *fast strong conducting confinement* (FSCC) method. To derive it, we consider a single confined charge q_i at $\mathbf{r}_i = (0, z_i)$, on the z axis of the cylindrical coordinate system, see Fig. 4.1(b). The polarizable infinite planar surfaces are placed at $z = 0$ and $z = L$. The Poisson equation was solved for this setup

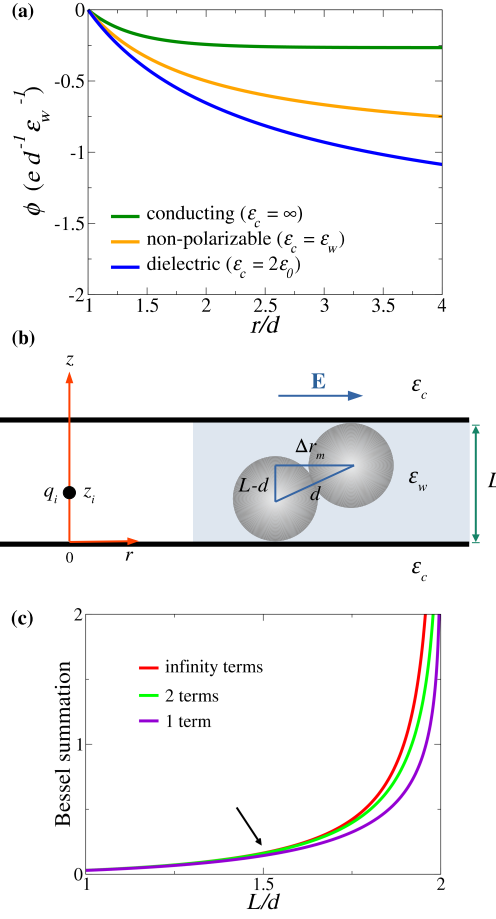


Figure 4.1. Ions strongly confined by polarizable surfaces. (a) Electrostatic potential in the radial direction (r) for $\varepsilon_w = 5\varepsilon_0$, from an ion at the center ($z = L/2$, where $L = 1.475d$) of two conducting, non-polarizable, or dielectric surfaces. We use a $1/r$ potential for non-polarizable confinement and the traditional method of images for the dielectric and conducting confinements. To aid visualization, the potential is set to zero at $r/d = 1$. (b) The cylindrical coordinate system used to derive the FSCC model, and the setup employed in molecular simulations; z and r are the axial and radial coordinates, respectively, and Δr_m is the minimal ion-ion radial separation; \mathbf{E} is the external electric field applied to investigate the ions' transport in the direction parallel to the surfaces. (c) Convergence of the Bessel summation $\sum_{n=1}^{\infty} K_0(\frac{n\pi\Delta r_m}{L})$ in Eq. (4.1) for various interplane distances L at the minimum ion-ion separation $\Delta r_m = \sqrt{L(2d - L)}$. The black arrow indicates the superior limit we consider the function is converged using just one term in sum.

in the context of confined ionic liquids [76]. The electrostatic potential at an arbitrary position \mathbf{r} , generated by the ion q_i is given by

$$(4.1) \quad \phi(\mathbf{r}) = \frac{4q_i}{\varepsilon_w L} \sum_{n=1}^{\infty} \sin\left(\frac{n\pi z}{L}\right) \sin\left(\frac{n\pi z_i}{L}\right) K_0\left(\frac{n\pi \Delta r}{L}\right),$$

where K_0 is the modified Bessel function of order 0 and $\Delta r = \sqrt{(x - x_i)^2 + (y - y_i)^2}$. For strong confinement, meaning L of order of d , just the first term ($n = 1$) of the summation in Eq. (4.1) is necessary because the minimal separation between two ions in the radial direction is $\Delta r_m = \sqrt{L(2d - L)}$, see Fig. 4.1(b). This condition implies that the argument of the modified Bessel function is at least $n\pi\sqrt{(2d/L - 1)}$, leading to a fast convergence of sum. Considering $L = 1.475d$, this gives $K_0(n\pi\sqrt{0.356}) \approx 0.13, 0.01, 0.001$, for $n = 1, 2, 3$, respectively. For the systems studied in this work, we use just the first term, $n = 1$, leading to simple expressions, derived below. For larger L , $1.5 < L/d < 2$, one needs to consider more terms in the summation, see Fig. 4.1(c).

The force between two ions q_i and q_j at positions \vec{r}_i and \vec{r}_j , converting to Cartesian coordinates, is:

$$F_x^{(i,j)} = \frac{4\pi q_i q_j (x_i - x_j)}{\varepsilon_w L^2 \Delta r} \sin\left(\pi \frac{z_i}{L}\right) \sin\left(\pi \frac{z_j}{L}\right) K_1\left(\pi \frac{\Delta r}{L}\right),$$

$$F_y^{(i,j)} = \frac{4\pi q_i q_j (y_i - y_j)}{\varepsilon_w L^2 \Delta r} \sin\left(\pi \frac{z_i}{L}\right) \sin\left(\pi \frac{z_j}{L}\right) K_1\left(\pi \frac{\Delta r}{L}\right),$$

$$F_z^{(i,j)} = -\frac{4\pi q_i q_j}{\varepsilon_w L^2} \cos\left(\pi \frac{z_i}{L}\right) \sin\left(\pi \frac{z_j}{L}\right) K_0\left(\pi \frac{\Delta r}{L}\right),$$

where $F_x^{(i,j)}$, $F_y^{(i,j)}$ and $F_z^{(i,j)}$ are the x , y , and z components of electrostatic force and K_1 is the modified Bessel function of order 1.

The self-electrostatic interaction describes the interaction between an ion and the surface charge it induces. It would be computed by Eq. (4.1) as $r \rightarrow 0$, but K_0 diverges in this limit. In this case, we consider the integral based method [76], which gives

$$\phi_{self}(z_i) = \frac{q_i}{\varepsilon_w} \int_0^\infty \frac{2e^{-2kL} - e^{-2kz_i} - e^{2kz_i-2kL}}{(1 - e^{-2kL})} dk .$$

The self-force acting on charge q_i in the z direction is $F_z^{self} = -\frac{q_i}{2} \frac{\partial}{\partial z_i} \phi_{self}(z_i)$, which can be written

$$(4.2) \quad F_z^{self} = \frac{q_i^2}{4L^2\varepsilon_w} \left[\psi^{(1)}(1 - z_i/L) - \psi^{(1)}(z_i/L) \right] ,$$

where $\psi^{(1)}$ is the polygamma function of first order.

To study ionic transport in confinement by conductors, we incorporate the FSCC method into molecular dynamics simulations. Additionally, we consider the case of confining dielectric walls using the method of periodic Green function (PGF) [13]. While both Green function methods (FSCC and PGF) agree for conducting surfaces, the FSCC method is around two orders of magnitude faster.

We investigate a 1 : 1 electrolyte under two confinement widths, $L = 1.1d$, confining the ions almost exactly to a plane, and a larger value $L = 1.475d$. The dielectric constant within the slit is $\varepsilon_w = 5\varepsilon_0$ to represent an organic solvent or strongly confined water [23]. We set $N_+ = N_- = 10$, and each ion has a charge $q_+ = e$ or $q_- = -e$ located at its center, where e is the positive elementary charge. The lateral dimensions of the simulation box are $L_x = 11.9d$ and $L_y = 12d$, which were chosen based on surface discretization that will be relevant in Section IV. The ions' excluded volume is represented with a truncated Lennard-Jones potential (also known as the Weeks-Chandler-Anderson potential) using

an energy scale ϵ_{LJ} , with $\sigma_{\text{LJ-ion}} = d$. The walls confine the ions via a truncated Lennard-Jones potential, with $\sigma_{\text{LJ}} = 0.8353d$ and ϵ_{LJ} . The wall-ion interaction is calculated using the Lorentz-Berthelot mixing rule. The centers of the confining walls are located at $z = -0.5\sigma_{\text{LJ}}$ and $z = L + 0.5\sigma_{\text{LJ}}$. The values for the energy, mass, and distance scales are $\epsilon_{\text{LJ}} = k_B T$ where $T = 298$ K, the ion mass set to the mass of sodium $m = 22.98$ amu, and $d = 0.425$ nm, a typical size of a hydrated ion. We assume symmetry of ion mass and diameter to focus on the effect of polarization charge on ion transport. Effects due to asymmetry of other ion properties will be explored in future work. We study the ionic currents by applying an electric field $\mathbf{E} = E\hat{x}$ tangentially to the surfaces, see Fig. 4.1(b), and compare the results for conducting ($\epsilon_c \rightarrow \infty$), dielectric ($\epsilon_c = 2\epsilon_0$), and non-polarizable surfaces.

We perform molecular dynamics simulations using the Langevin method with a damping parameter of 100 fs and periodic boundary conditions in x and y directions. We consider 100000 MD steps for equilibration and 100 MD steps of space between 10000 uncorrelated samples created for further analysis.

4.3. Effects of confinement and material polarizability

We analyze the ionic density profiles, the current I , the radial distributions, and the conductivity of the confined ions. Fig. 4.2(a) shows that the ions are more adsorbed to conducting surfaces and more repelled from dielectric surfaces than they are from non-polarizable surfaces. This behavior is expected since the ionic interactions with dielectric or conducting surfaces can be understood in terms of equally or oppositely charged images, respectively [77]. Fig. 4.2(b) shows the pair correlation functions between oppositely

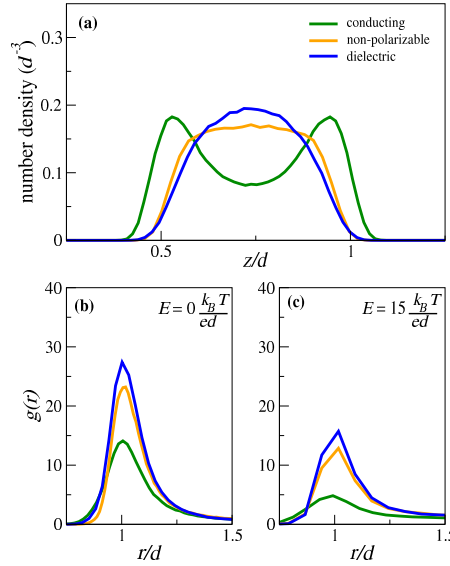


Figure 4.2. Results for 1 : 1 electrolyte for various surface polarization conditions for $L = 1.475d$. (a) The ionic concentration profiles. (b) Cation-anion radial distributions with no applied electric field. (c) Cation-anion radial distributions with applied electric field $E = 15 k_B T e^{-1} d^{-1}$.

charged ions, $g(r)$, which is related to the potential of mean force between ions $w(r)$ as $g(r) = e^{-w(r)/k_B T}$. Therefore, Fig. 4.2(b) shows that the effective interaction between oppositely charged ions is modified by the properties of the confining walls. The ion pairing is seen as a peak in the anion-cation radial distribution function at $r/d \approx 1$. The peak decreases by a factor of ≈ 2.5 for conducting surfaces compared to dielectric surfaces (see Fig. 4.2(b)), signifying that the formation of pairs is less favorable between conducting surfaces than dielectrics. The decrease in pair formation in conducting confinement occurs due to the difference in ion-ion interactions near dielectric and conducting surfaces. An ion q_i interacts with an oppositely charged ion q_j and with q_j 's equally charged image charges near a dielectric material, *but* mostly with the q_j 's opposite image charges near a conducting material. An external electric field \mathbf{E} (applied in the channel's surface

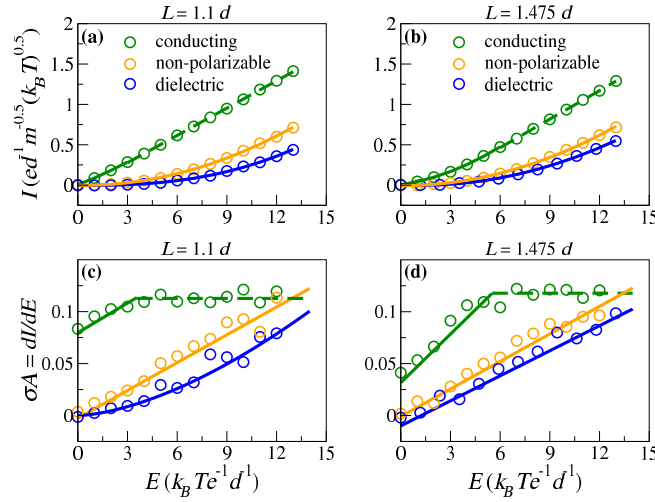


Figure 4.3. Results for 1 : 1 electrolyte for various surface polarization conditions. Current as a function of applied electric field for separation (a) $L = 1.1d$ and (b) $L = 1.475d$. The electrolyte conductivity σA as a function of applied electric field for separation (c) $L = 1.1d$ and (d) $L = 1.475d$. The two regimes for conducting cases can be observed for each curve with dashed and full lines, which are fits of current curves. The current is calculated as $I = \langle \sum_{i=1}^{N_+ + N_-} q_i v_{ix} / L_x \rangle$, where q_i and v_i are the charge and the velocity of particle i .

parallel direction) decreases the effective anion-cation attraction, but the effect due to the confining walls' polarization persists (see Fig. 4.2(c)).

Fig. 4.3(a) and (b) show that the currents obtained with confining conductive surfaces are much higher than those obtained with dielectric surfaces. The applied electric field and the current are related as $I = A\sigma E$, where σ is the conductivity and A is the slit's cross-sectional area. A field-dependent conductivity (non-linear I - E relationship) is essential in *memristors* [63], which are the basis of memory systems. The three I - E curves and their corresponding conductivities in Fig. 4.3 exhibit diverse regimes, depending on separation between surfaces and polarization. In the field range studied here, for a given value of L , the ionic current and conductivity are higher between conductors than

between dielectric or non-polarizable surfaces. At the separation distance of $L = 1.1d$ between conductors, the current is linear in almost the entire range of studied electric fields. Under such strong confinement, ions are constrained to move nearly on a plane, so the Ohmic behavior in our simulations is consistent with the two-dimensional model between conducting surfaces [17]. The ionic current between conductors at the larger separation distance ($L = 1.475d$) shows a non-linear trend for fields below $E \sim 6 k_B T e^{-1} d^{-1}$. For non-polarizable and dielectric surfaces, the I - E curves present a quadratic form, which reflects the linear curves for the conductivity. The exception occurs for dielectric confinement at short separations, which data are best fitted with a $E^{2.6}$ function, which gives a $E^{1.6}$ dependence for conductivity. Combining results using conductor to non-conductor switchable materials suggests a mechanism for inducing hysteresis loops [63] in memristors.

The current nonlinear behavior can be understood in terms of the Onsager's ion pairing theory [5, 78]. According to this theory, the ions form pairs that last for a time τ_d and stay free for a time τ_a . Ion pairs have zero net charge, meaning they do not contribute to the current. Hence, a larger number of ionic pairs between dielectrics than between conductors decreases the overall current. With the increase in electric field the ion pair's duration time τ_d decreases (reflected as a decrease of the radial distribution peak in Figs. 4.2(b,c)) and the current increases. Due to the weaker attraction in confinement by conductive surfaces, τ_d is shorter than between dielectric and non-polarizable surfaces. Therefore, in confinement by conductors the ions tend to move dissociated as an electron gas (Ohmic behavior) whereas in confinement by dielectric and non-polarizable surfaces the ion pairs persist in a broader range of electric fields. At high enough E -fields all

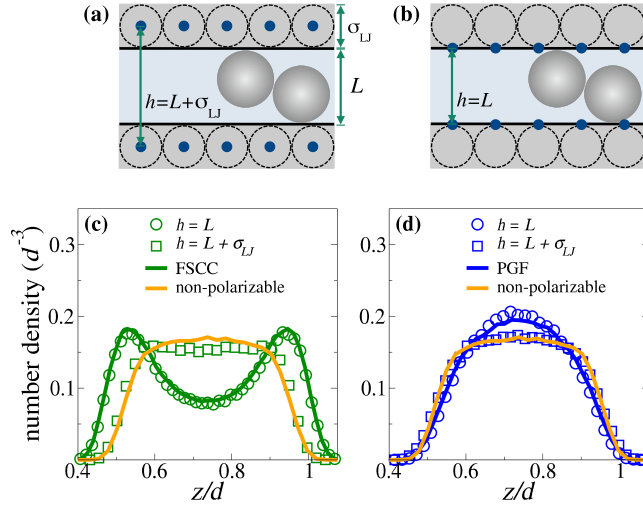


Figure 4.4. Two models for charge placement, using different charge separation distances h : (a) $0.5\sigma_{LJ}$ *inside* the surfaces ($h = L + \sigma_{LJ}$) and (b) exactly on the *surface* of the material ($h = L$); Ion number density profiles for both charge placement models, compared with exact polarizable and non-polarizable results for (c) conducting and (d) dielectric surfaces. In both figures, *inside* charge placement causes the ions to behave almost as if the surfaces were non-polarizable.

confining materials give an Ohmic response. This variety of behaviors show that the particle-particle interaction strongly influences the ionic current revealing the modulation of surface properties to be a tool for tuning ionic behavior.

4.4. Effects of the polarization plane placement

The Green function methods apply to planar confinement. For other geometries, such as conical channels suggested for current rectification [79, 80], other methods are necessary. *Explicit polarization* methods incorporate the surface polarizability into ion-ion interactions by calculating the induced charge in a way that is not restricted to a specific geometry [7, 45]. Conductors are implemented by imposing a uniform surface potential $\psi(\mathbf{s}) = \text{const}$. In dielectrics with no free surface charges, the electric field

boundary conditions at the interface between two media are given by $\varepsilon_w \mathbf{E}_{w,n} = \varepsilon_c \mathbf{E}_{c,n}$ and $\mathbf{E}_{w,t} = \mathbf{E}_{c,t}$, where the subscripts w and c refer to the ions' solvent and confining material, respectively, and n and t indicate the perpendicular and tangential electric field components.

The electrostatic boundary conditions define the polarization plane (image plane) which represents the location of the polarization charges. In early density functional theory studies, Lang and Kohn found that the image plane at metallic surfaces is located at the centroid of the induced charge profile [75]. Later work shows that the induced polarization charge peak resides in a range from tenths of an angstrom inside the surface nuclei to a few angstroms outside, depending on electron density of the material, external electric field, and other factors [81]. More recently, it has been suggested that the image plane location affects the adsorption of charged peptide species on gold [82] and shown that the double layer capacitance of silver and graphite surfaces depends on image plane placement [83].

In classical molecular simulations, however, the induced polarization charge is frequently placed at the center of the beads forming the surface [7, 74]. For conducting surfaces, and extending the concept to dielectrics, we study the impact of this choice by placing the polarization charges (1) *inside* the channel walls ($h = L + \sigma_{LJ}$, Fig. 4.4(a)) or (2) on the *surface* ($h = L$, Fig. 4.4(b)). Because our methods require explicit surface charge to be represented on a discrete mesh, we locate the polarization charges on a hexagonal graphene structure with an average nearest-neighbor distance of $0.332d$ on the x - y plane. All the other parameters are the same as described in Section II. We perform molecular dynamics simulations for only the case of $L = 1.475d$ using the polarization

methods implemented in LAMMPS [8]. In conductors, a constant surface potential is maintained using the Gaussian charge model [38, 39, 45]. For dielectrics, the electrostatic boundary conditions are considered using a boundary element method [7]. Further details of the wall and conductor models are supplied in the Supplemental Material [84].

Fig. 4.4(c) and (d) show the ion density profiles for conductive and dielectric surfaces, respectively. The figures include the profiles at the polarization charge locations of $h = L$ and $h = L + \sigma_{LJ}$. For comparison, we include the results from the Green function methods (FSCC and PGF) and for non-polarizable systems. Placing the polarization charges on the walls' *surface* ($h = L$) leads to conductive surfaces adsorbing the ions and dielectric surfaces repelling them. For both dielectrics and conductors, the effect of surface polarization is significantly dampened when the polarization charges are located inside the surface. Placing the polarization charges *inside* the surfaces causes the profiles of polarizable systems to converge towards those of non-polarizable systems, while placing the polarization charges on the *surface* results in profiles that overlap with the Green function methods. Similarly, the ionic current in polarizable models is close to that of non-polarizable system (see Fig. 4.5(a) and (b)), when the polarization plane is *inside* the surfaces. When the polarization plane is placed on the walls' *surfaces*, the current is similar to that from the Green function methods. We attribute the slight discrepancy between the two methods at high fields to the discrete mesh employed in the *explicit polarization* models (see Fig. B.2 in the Supplemental Material [84]). The pair correlation functions in Figs. 4.5(c) and (d) explain the current behavior. The systems with *surface* charge placement indicate decreased ion clustering (lower peak) for conductive surfaces and enhanced ion clustering (higher peak) for dielectric materials, aligning with the Green

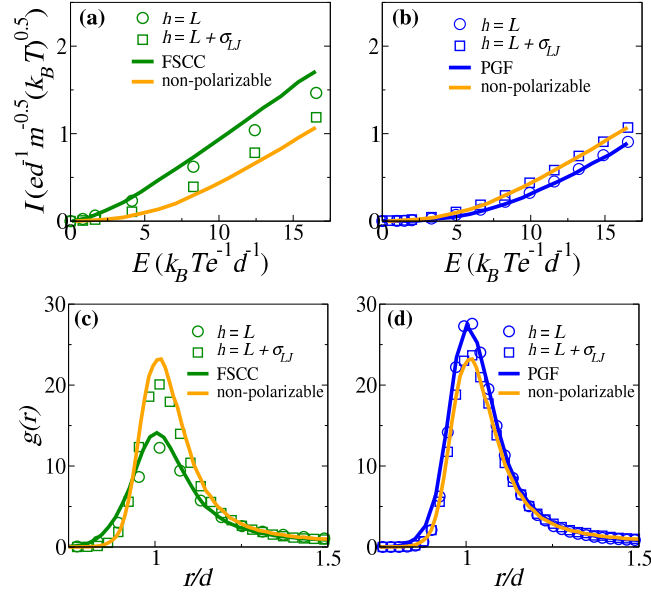


Figure 4.5. Ionic current for confining (a) conducting and (b) dielectric surfaces. Cation-anion radial distribution for (c) conducting and (d) dielectric surfaces, with no applied electric field. Analogously to Fig. 4.4, ion current is much more significantly impacted by changing surface material for *surface* charge placement.

function methods. Our findings demonstrate that both the surface polarization and the polarization plane placement modulate the ion conductance.

4.5. Conclusions

We study the adsorption, interactions, and current of ions confined in slit-like channels made of polarizable surfaces. The ionic current is non-linear and shows different behavior in channels made of conductors, dielectrics, and non-polarizable surfaces. Strong confinement and polarization effects lead to non-Ohmic ionic currents whereas the two-dimensional transport between conductors tends to be linear. The ionic current modulation and non-linear trend (essential for designing memristors) are caused by the screened or

enhanced ionic clustering that is different for each type of confining material. We demonstrate that location of the polarization plane and the confining distance significantly affect the confined fluid properties. Considering the surface of materials with different electronic properties is crucial for studying hybrid ionic/electron coupling in numerous fields such as materials with neuromorphic applications, energy harvesting, and water desalination. In quantum-mechanical calculations, however, considering the coupling between ions transport and the electrons of a surface is challenging due to the differences in time and length scales. Here, we employ the polarization and the polarization plane location to overcome that difficulty in a consistent way with density functional theory.

Acknowledgements: A.P.d.S. thanks the Department of Materials Science and Engineering at Northwestern University for appointing him Eshbach Visiting Professor. A.P.d.S. also thanks FAPERGS and CNPq. F.J.-A., A.E., and M.O.d.l.C. acknowledge the support of NSF through the Northwestern University MRSEC grant number DMR-2308691.

A. P. dos Santos and F. Jiménez-Ángeles contributed equally to this work and both are equal first authors.

CHAPTER 5

Geometry effects

Many of the applications described in Chapt. 2 depend on ions interacting with rough surfaces. For example, supercapacitors have higher energy density when rough electrodes are used to increase the surface area with which the ions can interact. This is also the reason that curved graphene sheets show an improved energy density relative to flat ones: flat graphene can stack in solution, which excludes prevents ions from being near surfaces, and curves in the sheets decrease the likelihood this will happen [2]. In these devices, the surfaces are not just walls but electrostatically responsive materials and therefore will interact with the ions via surface polarization.

We know that curves in a surface impact induced surface charge. As discussed in Chap. 2, if the relative dielectric constant of the wall ε_w is lower than that of the solvent ε_s , then the induced surface charge is repulsive (same sign as the inducing ion), and attractive in the case that $\varepsilon_w > \varepsilon_s$. Because the induced charge is related the component of the inducing electric field that is perpendicular to the dielectrically mismatched interface:

$$(5.1) \quad \hat{n} \cdot (\varepsilon_s \vec{E}_s - \varepsilon_w \vec{E}_w) = 0$$

$$(5.2) \quad \hat{n} \cdot (\vec{E}_s - \vec{E}_w) = \sigma_{\text{ind.}}$$

where \hat{n} points from the wall into the solvent (if there were any fixed surface charge density σ_f , there would be an addition σ_f on the right-hand side of both equations). Together

these imply that the stronger the mismatch between ε_s and ε_w , the greater the difference in components of electric fields \vec{E}_s and \vec{E}_w normal to the surface and therefore the greater the total induced surface charge. Therefore, if a surface is curved inward toward an ion, there will be not only more larger normal components of the inducing electric field, but each side of the curved surface will "see" some component of the electric field due to the other side. Solis and Olvera de la Cruz [19] described the impact of both dielectric mismatch and surface curvature mathematically, as have Duplantier, et al. [18], and Wu et al. showed that, for curved surfaces, the effects of dielectric mismatch (for $\varepsilon_w < \varepsilon_s$) are enhanced in a trough and diluted over a peak [20].

However, two questions arise from these. First, we've shown qualitatively in Fig. 2.2 that, for polarizable walls that can "see" each other (i.e. their surface normals have some component normal to another polarizable interface), they enhance each other's surface polarization charge for the repulsive condition ($\varepsilon_w < \varepsilon_s$) and dampen it for the attractive condition ($\varepsilon_w > \varepsilon_s$). When the surface is curved, there is competition between enhanced surface charge due to surface curvature and dilution of the dielectric effect by the same curvature, especially in the attractive case. Second, almost all of the motivating applications mentioned in Chapt. 2—supercapactors, transistors, or other iontronic devices—involve an external electric field perpendicular to dielectric surfaces, so it is important to understand how the electrostatics already studied are impacted by the presence of this external field. We begin to tackle these two questions in this chapter.

5.1. System setup and wall polarizability

For this work, we study a 2:1 electrolyte between two walls. One is undulating sinusoidally following $z = A \cos(kx) + z_0$, where $A = 1$ and $k = 2\pi/10$, all in units of ion diameter a . They are placed $20a$ apart (measured from the flat wall to the peak of the cosine, so $z_0 = -1$). We chose this setup to focus on the effects of surface curvature, though with the package developed by Nguyen, et al. in [7], arbitrary geometry is possible, and we would like to explore this in future work. The dielectric constant of the solvent ϵ_s is equal to 80, as the water in this system is not strongly confined, and we apply an electric field perpendicular to the surfaces by inserting charged plates of uniform surface charge outside of both walls. This setup (without the ions) is shown in Fig. 5.1a.

To study the effect of wall polarizability, we simulate three conditions: the wall dielectric constant $\epsilon_w = 80$ (non-polarizable interfaces), $\epsilon_w = 2$ (repulsive condition), and $\epsilon_w = 200$ (attractive condition, which could represent a high dielectric constant semiconductor like those mentioned in [85]). Note that the wall undulation and salt are approximately the same as the system simulation by Wu, et al. [20], by our ion concentration is twice as high (approximately 100 mM divalent salt or 300 mM actual particle concentration when converted to real units).

To apply the electric field, we determined a electric field magnitude of about $0.0112 \frac{e}{4\pi\epsilon_0 a^2}$ (lower than the dielectric breakdown voltage of water) and keep that constant between conditions. Because the wall dielectric constant ϵ_w is different in different conditions, that means the wall surface charge must be scaled to keep the electric field value E_z constant. The electric field in a parallel plate capacitor is related to its surface charge

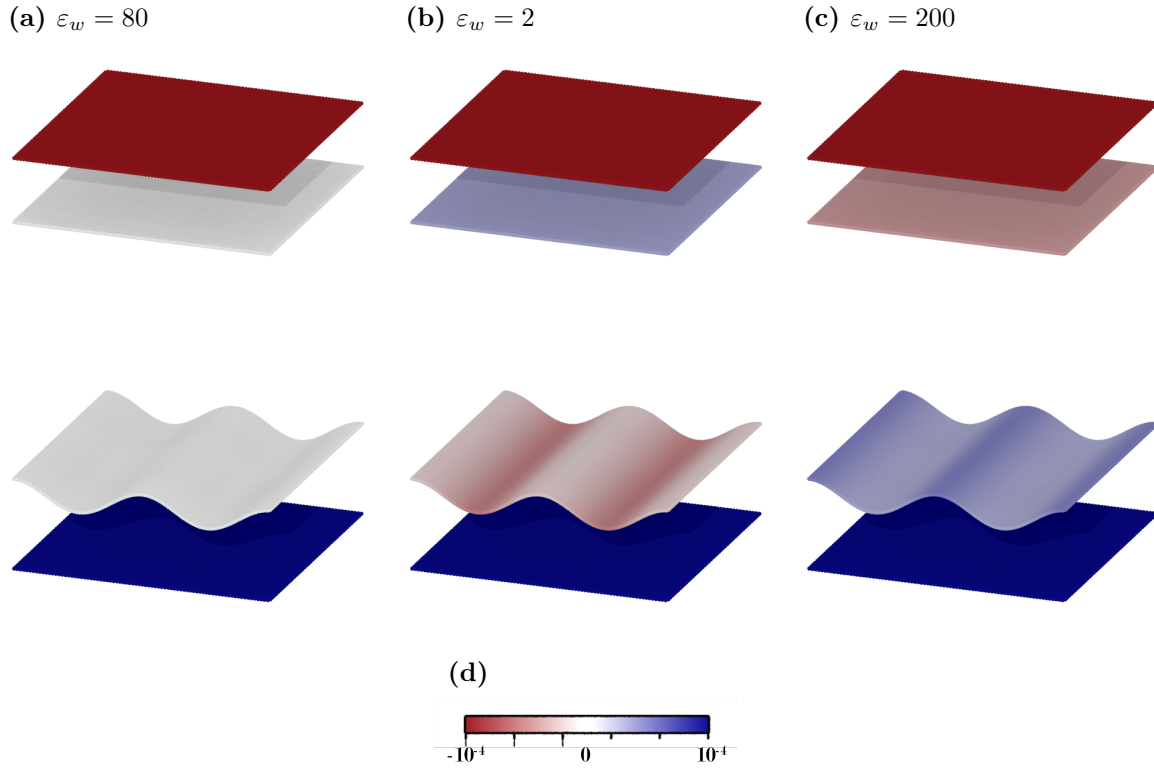


Figure 5.1. The induced polarization charge on polarizable confining walls due to the pictured exterior charged plates (in this case with the electric field pointing up). All systems have a solvent dielectric constant $\epsilon_s = 80$ and different wall dielectric constants ϵ_w . The induced charge on the oscillating surface is non-uniform. Note that the color bar limits are set such that the polarization charge is visible. The charge on the charge plates is much stronger than the induced charge, and therefore appears the same in each part, even though values are different. The charge density on each plate has been adjusted in each case so that the external field E_{ext} is constant despite different values of ϵ_w .

and dielectric constant:

$$(5.3) \quad \vec{E}_{\text{cap}} = \frac{\sigma_{\text{surf}}}{\epsilon_0 \epsilon_r}$$

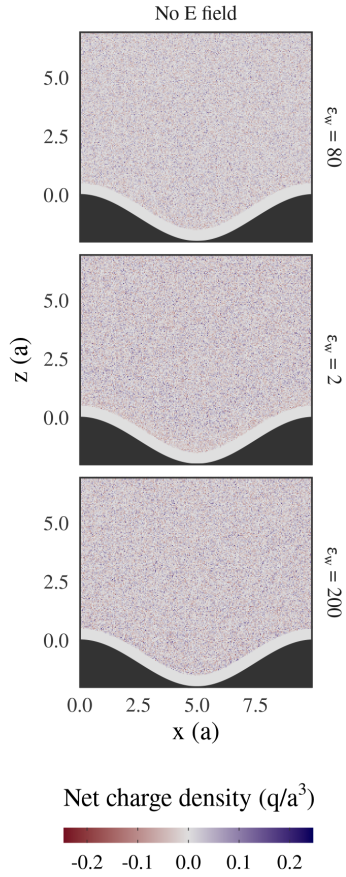
the surface charge must be adjusted in each dielectric constant to maintain comparable fields:

$$(5.4) \quad \vec{E} = \frac{\sigma_1}{\epsilon_0 \epsilon_1} = \frac{\sigma_2}{\epsilon_0 \epsilon_2}$$

$$(5.5) \quad \sigma_1 = \frac{\epsilon_1}{\epsilon_2} \sigma_2$$

While the two walls are far enough apart that the type of mutually induced surface charges due to ions relevant in Chapt. 3 and 4 won't play a large role in the resulting ion distribution, the fact that both walls are polarizable does matter. Both surfaces have substantial area perpendicular to the applied electric field; therefore, both will develop a permanent induced charge, and because this creates an effectively infinite sheet of charge (undulating or not) that produces a constant electric field, the presence of each surface impact the other. These combined effects can be seen in Figs. 5.1b ($\epsilon_w = 2$, repulsive condition) and 5.1c ($\epsilon_w = 200$, attractive condition). The induced charge is significant and opposite in each case, as expected. The induced charge on the undulating surface is non-uniform and concentrates at the surface peak or trough, depending on the value of ϵ_w . Note that the magnitude of the induced charge is on the order of $10^{-5}e$, and the color bar in Fig. 5.1 is quite limited. Therefore, the charged plates look "fully saturated" and uniform between conditions because their surface charges are outside of the range of the color bar. In reality, their surface charges vary according to Eq. 5.5, and they are on the order of 10^{-4} , 10^{-3} , and $10^{-2} e/a^2$ for $\epsilon_w = 200$, $\epsilon_w = 80$, and $\epsilon_w = 2$, respectively.

(a) No external electric field



(b) With external electric field

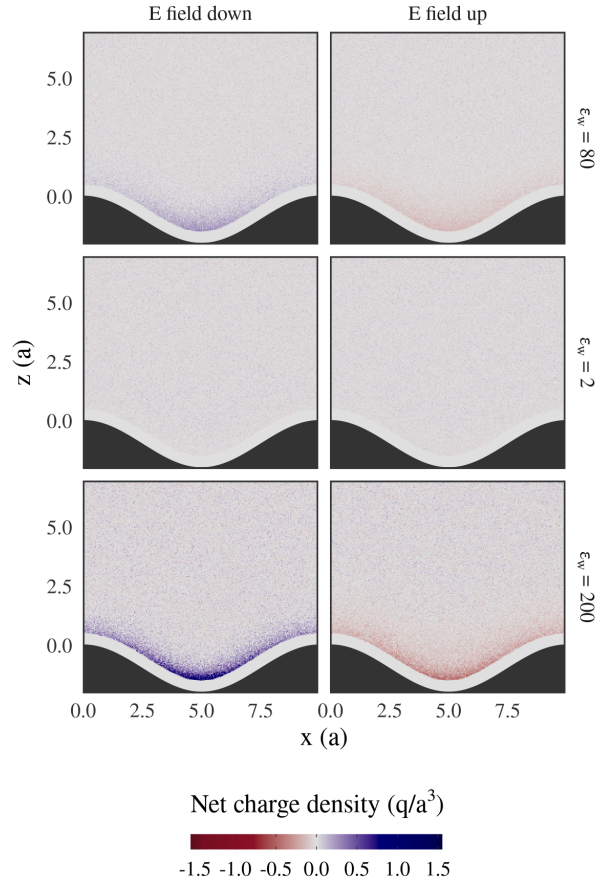


Figure 5.2. Net charge density for different wall dielectric constants and electric field values cE_z where $c \in \{-1, 0, 1\}$. Solvent dielectric constant is always $\varepsilon_s = 80$. Using conversions to real units in [20], $a = \ell_B = 0.714$ nm, the amplitude of the cosine wave is 0.714 nm.

5.2. Initial results

Preliminary results of this work are shown in Fig. 5.2, which give the net ion charge density in units of charge q per a^3 . The dimensions of the actual simulation box in $x \times y$ are $20a \times 20a$, to include two cosine periods. These have been wrapped and averaged into one period in Fig. 5.2. The cases with no applied electric field (Fig. 5.2a) are separated

from the cases with applied electric field (Fig. 5.2a) because the scales are so different. It is clear from these images that the electric fields alter ion distribution significantly, particularly in the trough, in the case of $\varepsilon_w = 80$ and $\varepsilon_w = 200$ —and very little in the case of $\varepsilon_w = 2$.

A more quantitative view of this can be seen in Fig. 5.3, which shows the same net charge density as in Fig. 5.2, but this time plotted specifically for z values above the peak or the trough. The first noticeable effect is that the ion distribution is significantly changed by the electric field in reasonable ways for $\varepsilon_w = 80$ and $\varepsilon_w = 200$. For an upward electric field, the divalent cations are pulled up and the monovalent anions are pulled down, leaving a net negative charge near the surface. Of course, the opposite occurs for downward-pointing electric fields. This effect is much stronger for $\varepsilon = 200$ (note the difference in y axis limits), as the dielectric contrast enhances the external electric field. Somewhat surprisingly, the trough still sees a larger difference between electric field values despite the permanent induced charge being stronger at the peak. This may be due to the ions "falling down" the sides of the undulations, which means that the difference in electric field due to the induced charge between the peak and trough is not strong enough to compete with the overall effect of the external field. There is also an asymmetry in the peaks between the electric field directions is due to the asymmetry of the ions.

For $\varepsilon = 2$, however, the effect is dramatically smaller, and there is never a net positive charge near the surface. Additionally, there may be more of a difference between electric field directions near the peaks than the troughs. This is less surprising when recalling Fig. 5.1b, because this is a reminder that the dielectric induced charge on the surface creates a field opposing the external one and therefore cancels its effect significantly.

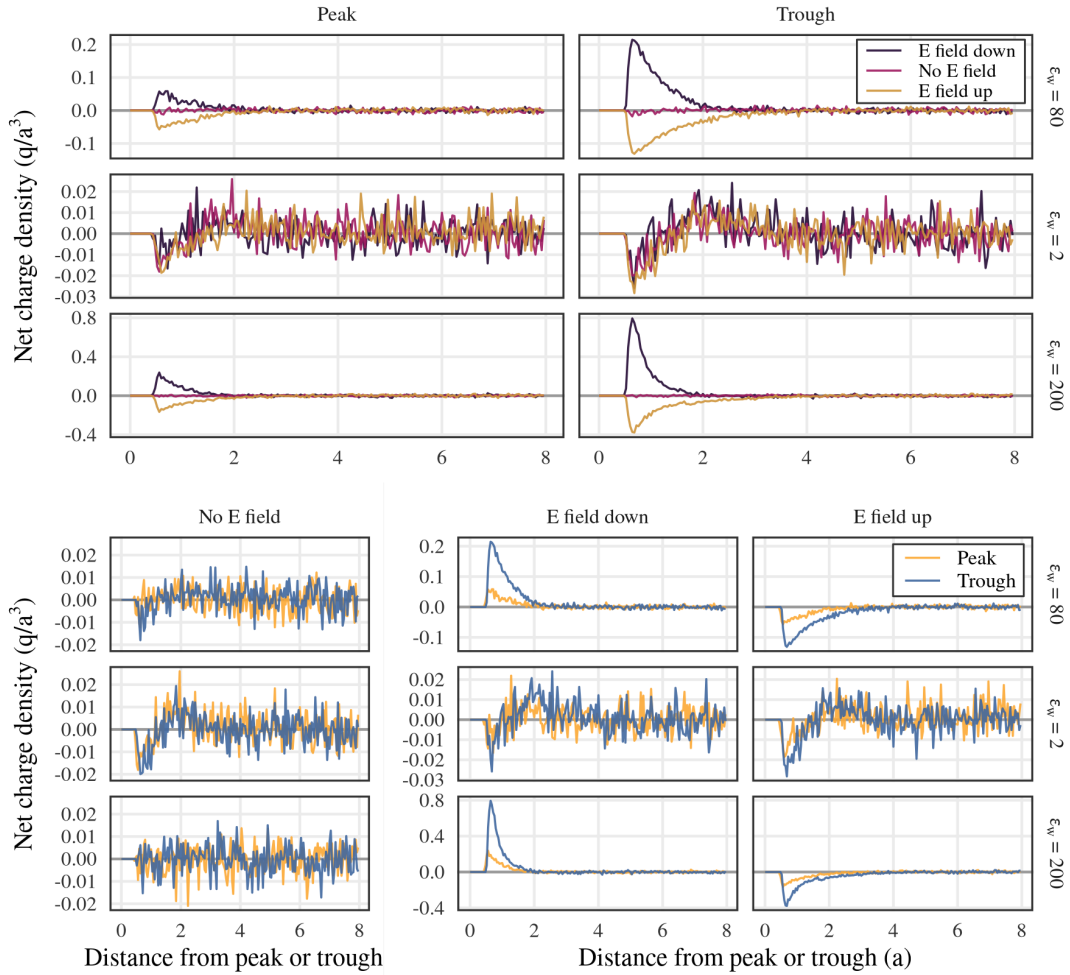


Figure 5.3. Net ion charge density as a function of distance from the surface at either the peak or trough, for different electric fields and values of wall dielectric constant ϵ_w , plotted either by electric field or by position. The solvent dielectric constant ϵ_s is always 80.

It may be the case that, because of the stronger induced charge in the troughs, the cancellation is stronger and therefore the effect of the external field is even weaker.

The takeaways from these results are twofold: first, we can use electric fields to tune the charge patterning near the surfaces of undulating interfaces, and this can be controlled by the type of undulation. Second, any time an external field is applied with some component

perpendicular to a polarizable surface, the effect of enhancing or dampening the electric field is very strong and cannot be ignored. This will be important to keep in mind when designing iontronic devices that depend on charge patterning. Our group will continue to work on these effects, including exploring the effect of changing the undulating surface's wavelength.

Note: even the $\varepsilon = 2$ case for zero electric field shows little difference between the peak and trough. We have been able to reproduce a difference of a larger magnitude than that showed in Wu, et al. in [20]. The results shown here are more subtle than that. This may be due to our higher concentration (more of a push towards the wall due to asymmetric pushes from other ions as discussed in Chapt. 2) or the fact that we have not collected sufficient samples. We are continuing to run the simulations to verify which during this time. We may be able to observe the effect more strongly for a lower solvent dielectric constant ε_s or a lower concentration of electrolyte ions.

CHAPTER 6

Conclusion: outlook and future direction

Chaps. 4 and 5, which interrogated ionic current in channels of different materials and ionic structure near a structured interface bring up many new questions. Our group has continued to develop theories around ions near undulating surfaces [86], and a natural next step is to analyze ionic current in channels with undulating surfaces. The modulation of the surface will result in not only a modulation in the surface's response to a nearby ion, but also charge patterning on the surface, due to the presence of an external field at a polarizable boundary. We have already started work in this area.

It is easy to imagine using these properties to precisely design a device in which the position and concentration of ions influences the material around them, which in turn influences ion mobility or distribution in another portion of the material. These could be cleverly constructed into neuromorphic-type devices, such as those hinted at by the Bocquet group [5, 63] and others [87, 88]. This could include organic components, such as electrically conductive polymers activated by the presence of ions [4]. The potential for devices based on just these components is intriguing, and there is much to do to develop theories—and test those theories with simulation—to posit designs. Additionally, understanding the electrostatic interactions at interfaces can hopefully help us understand and improve the design of energy devices that rely on ion configuration, like supercapacitors.

Of course, in order to improve and design real devices, other details would be required such as atomic roughness and interactions of the solvent and surface. Those details will

also be necessary for addressing some questions about the ion hydration shells' response to external electric fields brought up in Chap. 3. At some point, it will become necessary to include quantum effects and higher orders of feedback between ionic and electronic charges [22, 89], though for now there is still quite a bit of interesting work to do simply with the effects of induce polarization charge.

Part 3

Symmetry in crowded environments: colloidal
crystal metallicity

CHAPTER 7

Introduction

While much of the complexity of electrolyte systems is derived from long-range electrostatic interactions, other systems are complex due to much shorter-range effects. Functionalized nanoparticles have been shown to self-assemble into many interesting nanoscale structures, and their assembly is due to many layered interactions: electrostatic attraction or repulsion of the nanoparticles and their polymer coatings, excluded volume interactions and associated entropic effects, and thermal noise that allows for diffusion and rearrangement of both the particles and their grafted polymers. In this part, we will strip out the electrostatics and focus on thermal, steric, and short-range interactions to examine one specific behavior of self-assembled nanoparticle structures and why these structures may be interesting for nanoparticle applications as well as providing insight into strange atomic structures.

7.1. Properties of assembled nanoparticles

Nanoparticles—particles with nanometer dimensions, which can be made of metallic, semiconducting, polymer, protein, or other materials—can be functionalized by grafting polymers onto their surfaces, which is pictured as a simulation snapshot in Fig. 7.1, taken from [90]. Functionalized nanoparticles in solution can be induced to self-assemble into various three-dimensional ordered structures, the type of which will be discussed in the next section. These structures, though, depending on the material of the nanoparticle core

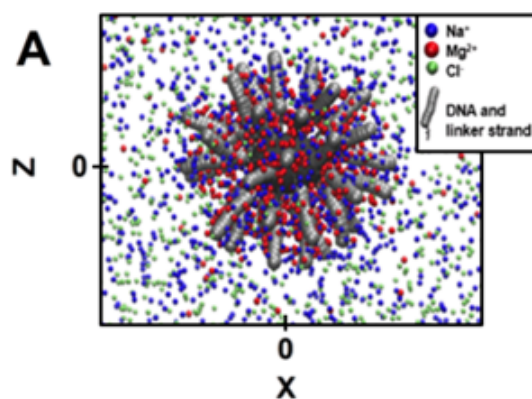


Figure 7.1. Cartoon of a polymer-grafted nanoparticle in an electrolyte solution. In this case, the polymer is a coarse-grained representation of DNA. Reprinted with permission from *Krishnamoorthy, Kewalramani, Ehlen, Moreau, Mirkin, Olvera de la Cruz, Bedzyk. "Enzymatic degradation of DNA probed by in-situ"X-ray scattering." ACS Nano 13, no. 10, 2019.* Copyright 2019 American Chemical Society. This appears at Fig 5 in the original [90].

as well as the grafted polymer, can be used for sensing, magnetic, plasmonic, catalytic, or other applications [91–93]. Functionalizing the nanoparticles with specific polymers allows for control over how the nanoparticles self-assemble in solution. Changing the type of polymer can make the interactions between nanoparticles attractive or repulsive, alter the effective radius of the nanoparticle, and more.

7.2. Colloidal crystals

Motivated by the wide array of potential applications for self-assembled nanoparticle structures, there has been substantial effort put into understanding how the microscopic properties of nanoparticles and their grafted polymers impact the final assembled structure. An example of the diversity of self-assembled structures is shown in Fig. 7.2, originally from Macfarlane et al. [94]. This figure shows that DNA-functionalized nanoparticles will

self-assemble into different crystals based on their size and the number and length of their grafted DNA strands. It also shows that binary nanoparticle structures (two distinct types of nanoparticles in solution, which can differ by core size, grafted polymer number, and grafted polymer length) are also possible and tunable by similar parameters. While this work focuses on the energetic benefit of maximizing attractive interaction between polymers (in this case DNA base pairing), it has also been shown that entropy can play a role in determining the final structure [95]. Quite a bit of work has been done to characterize these nanoparticle crystal assemblies; a few varied examples can be found in [91, 96–100].

7.3. Colloidal crystal metallicity

Until 2019, all crystals assembled from functionalized nanoparticles had "ionic" structures, an analogy to the ionic bonds in an ionic crystal: once the crystal is assembled, each nanoparticle remains at its position in the lattice. However, in 2019, Girard et al. reported a new phenomenon: they showed in simulation and experiment that in binary DNA-functionalized nanoparticle assemblies, if the smaller nanoparticle type was small enough, these smaller particles would start to roam the lattice, delocalized, while the large particles maintained their ordered positions in the crystal [101]. Instead of ionic bonding, the analogous bonding in atomic systems is "metallic," where metal nuclei remain in a lattice while electrons explore the lattice, delocalized. The two cases are pictured in Fig. 7.3.

This discovery opened up many interesting questions and possible applications. In the analogy to metallic bonding, delocalization is a quantum behavior. How can classical

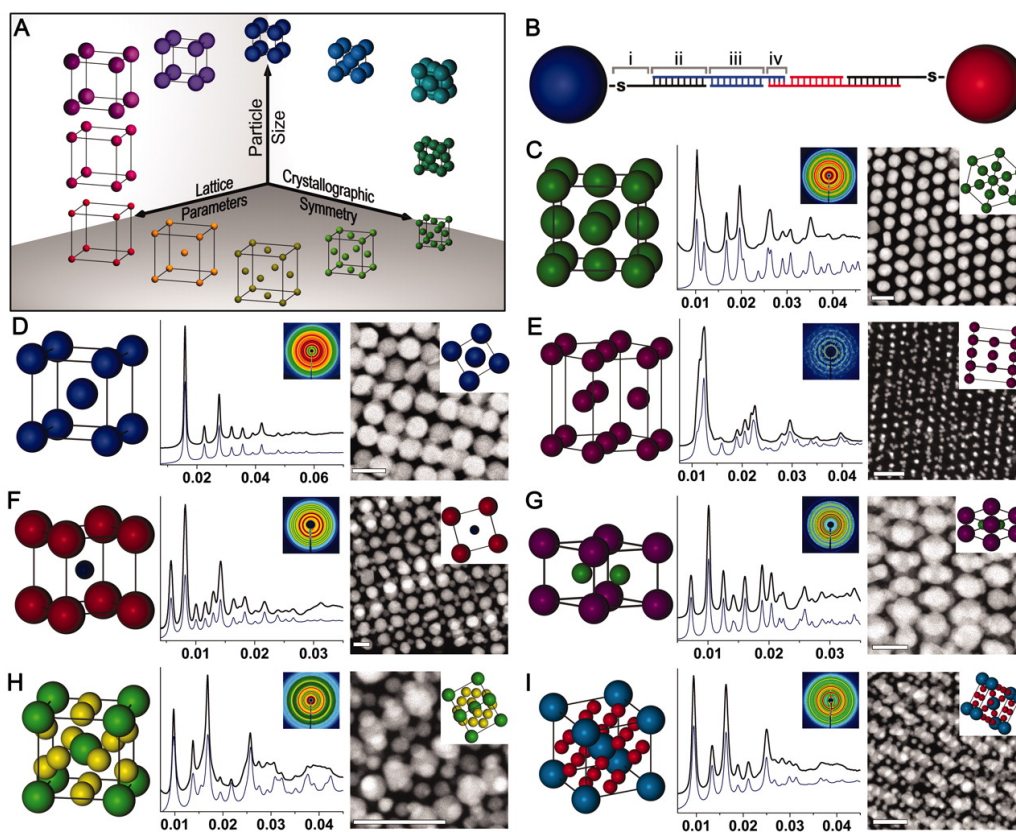


Figure 7.2. A wide array of colloidal crystal assemblies. In this case, the functionalizing polymer is DNA. From *Macfarlane, Lee, Jones, Harris, Schatz, and Mirkin. "Nanoparticle Superlattice Engineering with DNA." Science 334, no. 6053, 2011.* Reprinted with permission from AAAS. This appears at Fig. 1 in the original [94].

nanoparticles exhibit this same effect? Is delocalization a phase transition? Is nanoparticle delocalization a phenomenon specific to DNA-grafted nanoparticles or can other polymers produce this same behavior? Potential applications are also intriguing. If we can understand what conditions produce delocalization in colloidal crystals, producing an assembly in which the diffusion of one species can be manipulated might enhance ways in which these objects can be used for sensing or catalysis.

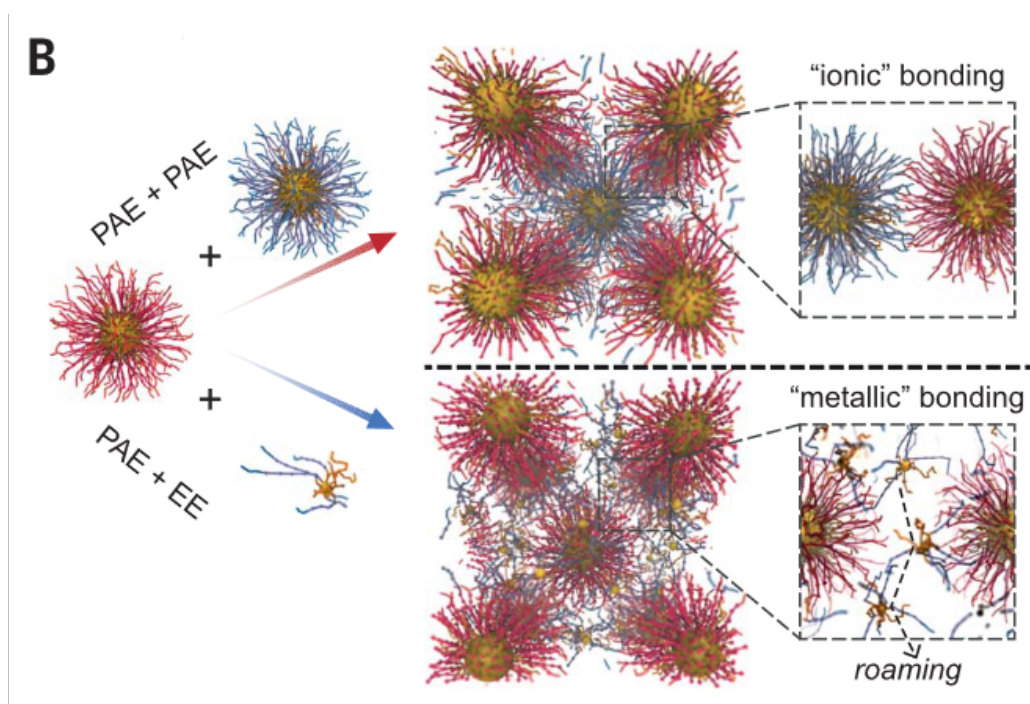


Figure 7.3. Transition from ionic to metallic bonding in a colloidal crystal. Originally Fig. 1b in [101]. From Girard, Wang, Du, Das, Huang, Dravid, Lee, Mirkin, and Olvera de la Cruz. "Particle analogs of electrons in colloidal crystals." *Science* 364, no. 6446, 2019. Reprinted with permission from AAAS. This appears at Fig. 1b in the original [101].

Finally, there is another analogy between delocalized colloidal crystals and atomic ionic structures to be made, which relates to materials called superionics. Superionic materials are ionic crystals which exhibit a sublattice melting transition (at a certain temperature, one ionic species delocalizes), and they are both fundamentally interesting and also under exploration for use in stable, safer batteries [102–104]. While representing an atomic ionic system with classical nanometer-scale particles will not allow study of all aspects of the atomic material, there are advantages to drawing this analogy and studying complex atomic structures by synthesizing their nanoparticle counterparts, as described

in [105]. For this reason, we were also interested to learn more about colloidal crystal delocalization to enhance our understanding of superionic materials.

With these varied motivations, we embarked on a pair of projects that explored the properties of highly size-asymmetric binary colloidal assemblies, which are presented here. In Chap. 8, we looked at 6:1 systems (6 small particles for each large particle), understanding the transition to delocalization as not a phase transition but a smooth change. In Chap. 9, we expand our study to different number ratios and find a wide variety of crystal types and transitions.

CHAPTER 8

BCC assembly and transition to "metallic" state

To begin to address some of the questions raised by Girard et al. when they published their work on colloidal crystal metallicity [101], we noted that they had found BCC, FCC, and A15 crystals in simulations that included a fair amount of detail of the gold nanoparticle cores and grafted DNA strands. We wanted to know whether the delocalization they observed was specific to that system and, if not, how general the transition from "ionic" to "metallic" bonding was. For this reason, we developed a very coarse grained, general model of size-asymmetric binary colloidal particles and used to delve deeply into the delocalization transition of BCC crystals found in 6:1 systems (6 small particles for every large particle). For the simulation and analysis in this paper, Hector Lopez Rios and I contributed equally to the simulation and analysis of all systems.

The following was originally published in the Journal of Physical Chemistry C in 2021. It is reproduced here with permission of Hector Lopez-Rios, Monica Olvera de la Cruz, and the American Chemical Society.

Supplementary material associated with this chapter can be found in Appendix C.

Delocalization Transition in Colloidal Crystals

Hector Lopez-Rios,* Ali Ehlen,* Monica Olvera de la Cruz

* equally contributing first authors

Reprinted with permission from:

Journal of Physical Chemistry C 2021, **125**, 1, 1096-1106, DOI:

10.1021/acs.jpcc.0c09730. Copyright 2021 American Chemical Society.

<http://pubs.acs.org/articlesonrequest/AOR-8UNXPU6QS5KATYESGAJA>

ABSTRACT: Sublattice melting is the loss of order of one lattice component in binary or ternary ionic crystals upon increase in temperature. A related transition has been predicted in colloidal crystals. To understand the nature of this transition, we study delocalization in self-assembled, size asymmetric binary colloidal crystals using a generalized molecular dynamics model. Focusing on BCC lattices, we observe a smooth change from localized-to-delocalized interstitial particles for a variety of interaction strengths. Thermodynamic arguments, mainly the absence of a discontinuity in the heat capacity, suggest that the passage from localization-to-delocalization is continuous and not a phase transition. This change is enhanced by lattice vibrations, and the temperature of the onset of delocalization can be tuned by the strength of the interaction between the colloid species. Therefore, the localized and delocalized regimes of the sublattice are dominated by enthalpic and entropic driving forces, respectively. This work sets the stage for future studies of sublattice melting in colloidal systems with different stoichiometries and lattice types, and it provides insights into superionic materials, which have potential for application in energy storage technologies.

8.1. Introduction

Binary colloidal systems, which have interspecies attraction and intraspecies repulsion, have been shown to self-assemble into a wide variety of binary lattices [99, 106–109]. Generally, if the two colloid species are of sufficiently different sizes, the larger colloids will form a lattice while the smaller colloids occupy interstitial sites [101, 110–112]. In these size asymmetric colloidal systems, many cubic and non-cubic crystals have been detected, including a Frank-Kasper phase [101]. However, under certain conditions, the small particles may delocalize and roam around the crystal while the large particles remain in lattice sites; this is called sublattice melting. Previously, this behavior had been seen primarily in atomic systems, in materials termed superionics [103, 113, 114], where one ionic species delocalizes while the other stays fixed in a lattice. However, recent work has demonstrated sublattice melting in assemblies of hard spheres under pressure [111, 112], oppositely charged colloids with a Debye-Hückel potential [115], and colloids functionalized with sticky DNA chains [101]. The surprising loss of order of only the sublattice also resembles behavior found in metals. In this analogy, the small particles map to delocalized electrons and the large particles to fixed nuclei. Given the unique physical nature of this phenomenon in colloidal systems and the seeming generality of the colloidal crystals that exhibit it, we seek to understand the origin of colloidal sublattice melting using a simplified molecular dynamics (MD) model, which can provide insight into a range of systems.

To calculate reliable thermodynamic and physical quantities of delocalized systems, we developed a scalable MD model. This simplified model enables us to generalize previous work that predicted delocalization in systems of DNA-functionalized gold nanoparticles [101], where the interactions between colloid species were due to DNA hybridization, which is directional and specific. However, the experimental design also included additional free DNA chains that may have acted as depletants. To avoid complications related to DNA hybridization and to explore the generality of the phenomenon, the pairwise interactions in our model are isotropic and short-range.

The generality of this model also enables us to apply it to a wide variety of systems. This encompasses, for example, nanodots with thiols and end terminal attractive groups [116, 117], functionalized nanoparticles with light activated interactions [118, 119], and nanocomposite tectons [120–122]. In fact, nanocomposite tectons would be an ideal system for experimental verification of this study, because the parameters of the system reported in the present work can correspond to metallic nanoparticles functionalized with hydrocarbon chains with short ranged and strong complementary molecular binding pairs. Lastly, with this model, we can start to address questions that have been posed about sublattice melting in superionic materials [123, 124] such as the origin of the sublattice melting transition. However, superionic materials are constrained by the requirement of charge neutrality per unit cell, but colloidal crystals (and this model) have no such constraint.

In this paper, we study the localized-to-delocalized transition in functionalized, size asymmetric colloidal crystals. We explore the order of this transition with respect to temperature and by varying the number of chains per small particle (4, 6, 8, and 10

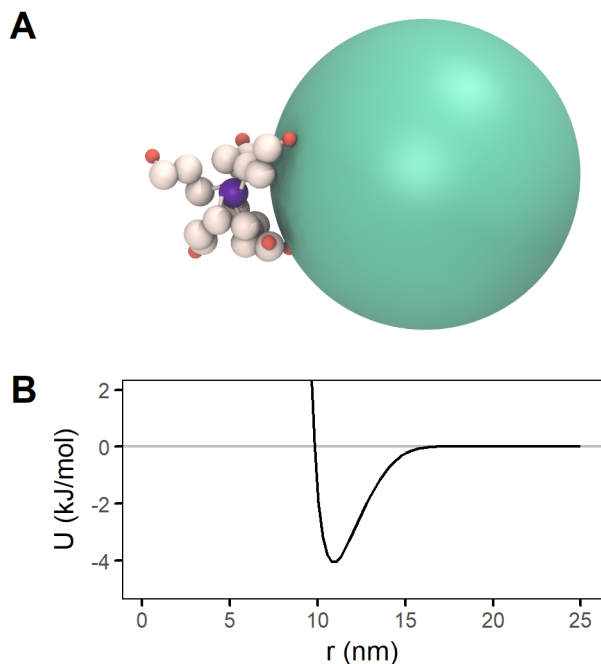


Figure 8.1. The simplified model. **(A)** The smaller colloid (purple) functionalized with chains (white) and larger colloid (turquoise) in our system, to scale. All beads have excluded volume based on their radii, and there is an attractive interaction between the large particles and the interactive ends of the small particle chains (orange). **(B)** Pair potential $U(r)$ between the centers of the large particles and the interactive chain ends. The high-energy region $r < 10$ nm represents excluded volume interactions, and the small potential well accounts for the attractive interaction. The value of U at the minimum is -4.1 kJ/mol.

chains per small particle). We focus on a system composition of 6 small particles per large particle ("6:1 ratio"), because at this composition, the large particles form a stable body centered cubic (BCC) lattice over a wide temperature range. Though other compositions exhibit interesting symmetry changes with temperature and number of chains, we use the 6:1 ratio to study the nature of the localized-to-delocalized transition without the added complexity of a change in the large particle lattice.

An image of the model is shown in Figure 8.1A. The larger colloidal species is represented by a single sphere (shown in turquoise). The smaller species is represented by a small sphere (shown in purple) grafted with a variable number of self-avoiding chains (shown in white). The only interactions in the system are excluded volume between all beads, using a Weeks-Chandler-Andersen (WCA) potential, and a generalized, attractive potential between the large particles and the interactive ends of the chains (shown in orange, referred to here as "interactive ends"); see Figure 8.1B. There is asymmetry in the interaction potential, as the range of the attractive potential is half of the diameter of the large particles. We chose to further simplify the system by representing the large species as spheres without explicit functionalized chains. This choice is consistent with colloidal systems that have previously shown sublattice melting, because these systems' large particles were either spherical [111, 115] or densely enough grafted with polymer chains [101] that a spherical potential is a reasonable approximation. However, the small particles cannot be modeled as spheres due to their higher curvature and therefore lower packing density of grafted chains. When chains are omitted and the interaction potential between small and large particles is modelled with spherical potentials, mostly FCC crystals are obtained [111, 115]. This may be because explicitly representing grafted chains on the small particles also enables spatially anisotropic interactions between the small and large particles. These can occur when chains bundle together in configurations analogous to hybridization electron orbitals present in covalent bonding called skyrmions [121, 125]. The concept of skyrmions has proved useful in explaining the appearance of non-close packed functionalized colloidal crystal structures.

With this model, we find that both size and interaction range asymmetries are needed for delocalization to occur. The passage from localized-to-delocalized small particles is fully continuous, closely related to diffusion of the small particles, and enhanced by the vibrational entropy of the large particle lattice. This continuous behavior arises from a competition between enthalpic and entropic driving forces. Here enthalpic contributions can be understood through analysis of the interaction energy landscape between the large particles and interactive beads of the small particles. Entropic contributions arise from the vibrations of the large particle lattice.

The rest of the paper is organized as follows. We begin by describing the MD simulations, as well as a theoretical model used for the free energy analysis of these crystals. We continue with a symmetry and energy analysis of relevant aspects of the BCC sublattice and its energy landscape. We then describe an analysis of the temperature-dependent thermodynamic and physical properties such as lattice parameter and specific heat per particle. We conclude by analyzing the importance of lattice vibrations as the driving force for both delocalization and lattice expansion for these crystals.

8.2. Methods

8.2.1. General description of the MD model

There are two types of pair interactions between the beads in the system. First, all beads have excluded volume interactions with each other through the WCA potential. Second, there is an attractive interaction between the interactive end of the chain and the large particles. That interaction is in the form of a Gaussian potential and is shown graphically

in Figure 8.1B and mathematically here:

$$(8.1) \quad U_{\text{pair}}(r) = \begin{cases} U_{\text{WCA}}(r) + U_{\text{Gaussian}}(r) & r \leq r_{\text{cutoff}} \\ 0 & \text{otherwise} \end{cases}$$

where

$$(8.2) \quad U_{\text{WCA}}(r) = 4 \left(\left(\frac{\sigma}{r} \right)^{12} - \left(\frac{\sigma}{r} \right)^6 \right) - 4 \left(\left(\frac{\sigma}{2^{1/6}\sigma} \right)^{12} - \left(\frac{\sigma}{2^{1/6}\sigma} \right)^6 \right) \quad \text{for } r \leq 2^{1/6}\sigma$$

$$(8.3) \quad U_{\text{Gauss}}(r) = -\varepsilon e^{-\frac{1}{2} \left(\frac{r}{\sigma_{\text{gauss}}} \right)^2} \quad \text{for } r \leq r_{\text{cutoff}}$$

where r is the distance between the centers of the large particle and the interactive end bead of the small particle chains; $\sigma = \sigma_{\text{large}} + \sigma_{\text{int. bead}}$, the sum of the radii of the large particle and the interactive bead; ε is a (positive valued) parameter that determines the strength of an individual large particle-interactive bead interaction; and σ_{gauss} is a parameter that determines the range of $U_{\text{Gauss}}(r)$. As usual, the WCA potential is cut off at $2^{1/6}\sigma$ and shifted such that U_{WCA} is zero at the cutoff, that is $U_{\text{WCA}}(r = 2^{1/6}\sigma) = 0$. The value for r_{cutoff} was selected such that $U_{\text{Gauss}}(r)$ has safely decayed to near zero by $r = r_{\text{cutoff}}$. We also used the HOOMD-blue `xplor` option which adds a subtle smoothing near r_{cutoff} such that the U_{Gaussian} decays smoothly to zero.¹

These parameters can be adjusted such that the system resembles interactions between two colloid species of choice. Additional parameters may vary are: particle size, number of chains on each small particle, temperature, system composition (ratio of small:large

¹See `md.pair.pair` documentation:

<https://hoomd-blue.readthedocs.io/en/stable/module-md-pair.html>

(a)		(b)	
Parameter	Value	Parameter	Value
$\sigma_{\text{large particle}}$	10.5 nm	small:large particle ratio	6:1
$\sigma_{\text{small particle center}}$	1.0 nm	temperature	$k_B T = 0.8 - 2$ kJ/mol
$\sigma_{\text{chain bead}}$	1.0 nm	# chains/small particle	4, 6, 8, 10
$\sigma_{\text{interactive chain end bead}}$	0.5 nm		
ε	70 kJ/mol		
σ_{gauss}	4.8 nm		
r_{cutoff}	8.4 nm		
# non-interactive beads/chain	3		

Table 8.1. Parameters used in the present study. **(a)** Fixed parameters (σ is radius). With these, the system resembles a binary system of weakly interacting chain-grafted colloids. **(b)** Variable parameters. Changing these allows us to explore properties of the system.

colloids in the simulation box), and length and stiffness of the chains on the small particles. The properties chosen for the study in this paper are listed in the next section.

8.2.2. Parameters and simulation scheme

We chose parameters for the interaction of our particles to generalize the short ranged attractive potential found in self-assembled DNA functionalized colloidal crystals[96, 126–128]. DNA functionalized colloids interact by forming hydrogen bonds between the single stranded DNA at the ends of the grafted chains. Using the parameters in Table 8.1A, at $T^* = 1$, the potential well shown in Figure 8.1B has a depth of $-4.1 k_B T$, which is approximately the binding energy of hydrogen bonding in single-stranded DNA (3

- $6 k_B T$ [96, 128]). However, given the general nature of our model, other forms of interactions found in functionalized colloidal crystals, such as dispersion interactions, can be represented with this model. Additionally, we fixed a particle size asymmetry that is in the regime in which binary solids form interstitial solid solutions (ISSs), where the smaller species occupies interstitial sites of the large species lattice. For example, in metallic binary alloys, one of the Hume-Rothery rules[129] require atomic size asymmetries where the smaller species size is ≤ 0.4 the size of the larger species in order to form ISSs. For functionalized binary colloidal particles, it was experimentally demonstrated[101] that ISSs were formed only for particle diameter ratios of 10 to 1.4 nm, while they were not formed when the smaller particles were larger.

For this study, we ran simulations of colloidal systems at different temperatures and number of grafted chains per small particle, as detailed in Table 8.1B. Varying both temperature and number of chains allows us to explore a wide range of system states. Changing the number of chains per small particle changes the total attraction strength between small and large particles, as well as the symmetry of available chain configurations. Additionally, because the attractive interaction is simple (Equation (8.3)), the system's behavior is determined by the ratio $\varepsilon/k_B T$. Therefore, by varying temperature, we are also effectively examining the range of behavior that would appear if we instead varied interaction strength.

All simulations were run using HOOMD-blue version 2.5.1[130, 131] in the NPT ensemble with periodic boundary conditions at near-zero pressure (207 Pa, which is $\sim 2\%$ of atmospheric pressure). Using a pressure very close to zero enables us to attribute the observed crystal assembly to the interactions between colloids, rather than an external

pressure [101]. Additionally, during the NPT portion of the run, the box was allowed to fluctuate in size and shape, which enabled lattices that were initialized in one crystal structure to relax into another if it was favorable to do so.

The full simulation scheme is as follows: we started the simulations in various initial lattice configurations (BCC, SC, FCC, BCT) with 6x6x6 unit cells in the simulation box. The simulations were then equilibrated, thermalized, and depressurized to their final pressure. This initial sequence lasted 312 ns. Then, the simulations were run in the NPT ensemble for an additional 8.44 μ s. For analysis, the first 1.38 μ s were considered to be an equilibration period and not included in calculation of properties. Therefore, analysis of the simulations was conducted on the last 7.37 μ s.

System topology for the simulation was built using Hoobas, [132] analysis was done in Python using MDAnalysis [133, 134] and R, visualization of the simulation was done in VMD [135] with the GSD plugin² using the internal Tachyon ray-tracing library [136] (see Figure 8.1A), and scientific plotting and calculation of isosurfaces and 3-dimensional densities (see Figures 8.3 and 8.6) was done in Mayavi [137].

8.2.3. Theoretical free energy of the exact soluble model

The theoretical model described in Section *Vibrational entropy drives lattice expansion* is derived by calculating the energetic environment of one interactive bead in one unit cell

²See HOOMD-blue GSD plugin for VMD at <https://github.com/mphoward/gsd-vmd>

of a fixed BCC lattice of large particles. That is:

$$\begin{aligned}
 Z(a, T) &= \int \int e^{-U_{\text{end}}(\vec{r}, \vec{p}; a)/k_B T} d\vec{r} d\vec{p} \\
 (8.4) \quad Z(a, T) &= (2\pi m k_B T)^{3/2} \int e^{-U_{\text{potential}}(\vec{r}; a)/k_B T} d\vec{r}
 \end{aligned}$$

where $U_{\text{end}}(\vec{r}, \vec{p}; a)$ is the energy associated with the particles in one unit cell with lattice parameter a and an interactive end with position \vec{r} and momentum \vec{p} . The position of the interactive bead \vec{r} is integrated over one unit cell and its momentum $d\vec{p}$ is integrated over all real numbers (this Gaussian integral is known from the ideal gas partition function).

The integral has been simplified using the definition of energy U_{end} as:

$$\begin{aligned}
 U_{\text{end}}(\vec{r}, \vec{p}; a) &= \frac{\vec{p}^2}{2m} + U_{\text{potential}}(\vec{r}; a) \\
 U_{\text{potential}}(\vec{r}; a) &= \sum_n U_{\text{pair}}(|\vec{r} - \vec{R}_n|; a) + \sum_{j < k} U_{\text{WCA}}(|\vec{R}_j - \vec{R}_k|)
 \end{aligned}$$

where $U_{\text{pair}}(\vec{r}; a)$ is the pair potential between a large particle and an interactive bead, as defined in Equation 8.1, and the sum is taken over all large particles that could influence the energy of an interactive bead at \vec{r} (\vec{R}_n indicates the position of the n th large particle). In this case, we include 15 large particles: all 9 pictured in the BCC cell in Figure 8.2A, plus the large particles in the center of all 6 non-diagonal adjacent unit cells. The range over which $U_{\text{pair}}(r; a)$ is nonzero in this model is short enough such that this captures all interactions. $U_{\text{WCA}}(r)$ is the WCA potential between large particles; this term becomes important when a approaches the diameter of the large particles.

We then numerically integrate Equation 8.4 to find the partition function, and we can set up equations to calculate any statistical mechanical quantity that can be found with

that result. For example, to calculate the average interaction energy between small and large particles, we numerically evaluate the following (assuming a is large enough that $U_{\text{WCA}}(r)$ can be neglected):

$$(8.5) \quad \langle U_{\text{potential}}(a, T) \rangle = \frac{1}{Z(a, T)} (2\pi m k_B T)^{3/2} \int \left(\sum_n U_{\text{pair}}(|\vec{r} - \vec{R}_n|; a) \right) e^{-U_{\text{potential}}(\vec{r}; a)/k_B T} d\vec{r}$$

The partition function is also used to calculate free energy using:

$$F(a, T) = -k_B T \ln(Z(a, T))$$

This model enables us to understand how the BCC energy landscape impacts system behavior, despite its simplicity. For example, it does not include lattice fluctuations. However, the lack of lattice fluctuations impacts the variance but not the mean of predicted energy values (we have seen this trend when comparing the mean and variance of the interaction energy between the fixed and fluctuating lattice cases).

Additionally, this model does not include particles other than the lattice and a single interactive bead. This is a sufficient approximation because the interaction between the small and large particles is more significant than the interaction between small particles. That is particularly true when small particles have fewer chains, because the small particles interact with 4 large particles when they sit at BCC tetrahedral sites. When there are 4-6 chains on each small particle, each chain is, on average, attracted to one of the 4 nearby but physically separated potential wells (see Figures 8.2B and 8.2C). Therefore, their excluded volume interactions don't substantially impact their average energy values, and agreement between theory and simulation is stronger for systems with fewer chains

per small particle. However, as described later, the theory's lack of bond constraints does matter. In simulation, the bonds in small particle chains don't allow interactive beads to access the lowest-energy part of the unit cell's potential wells. However, this appears to simply scale the average energy of the interactive beads, especially, as noted, for systems with fewer chains.

Lastly, note that the lattice parameter and temperature are both inputs to this partition function. It is possible that this formulation could predict some lattice expansion as a function of temperature. However, because of the differences in average location of the interactive bead between theory and simulation (due to bond constraints), we do not believe that this will be a quantitative prediction for properties of a fluctuating lattice simulation. Despite this, this theory can provide a sense of how much the lattice vibrations contribute to certain properties of a system where they are present.

8.3. Results and Discussion

8.3.1. 6:1 systems form BCC lattices with small particles localized at tetrahedral sites

For each value of chains per small particle, 6:1 systems form BCC lattices over a wide temperature range. This is consistent with findings of Girdard, et al. [101] with respect to their 6:1 systems. At temperatures below this range, we observe formation of other crystal lattice types, and at higher temperatures, we observe liquid or gas phases; see SI for more information on determining BCC stability. At lower temperatures within the BCC range, the large particles sit at BCC lattice points and the small particles localize at the BCC tetrahedral sites, also known as 12d Wyckoff positions; these are shown in Figure 8.2A.

The location of the tetrahedral sites means that each small particle can interact with four large particles simultaneously.

An analysis of the symmetry and energy associated with the tetrahedral sites reveals why small particles localize there. The potential energy of interaction between large particles and the interactive bead at the end of each chain can be seen in Figure 8.2B. Dark red indicates negative interaction energy and defines the areas most favorable for the interactive ends to occupy. Conversely, the lighter areas indicate an interaction energy of approximately zero. There are four nearly zero energy sites per face, visible in the (001) plane image in Figure 8.2B. These are the tetrahedral sites. This suggests that the small particle centers localize at the tetrahedral sites because this enables the interactive ends to access the most energetically favorable regions of the unit cell. Tetrahedral structures have also been observed experimentally. The formation of distorted tetrahedral structures between size asymmetric colloids has been reported within a specific size asymmetry range (which does not include the dimensions of our system)[138]. The experimental tetrahedral clusters, mediated by short ranged but strong potentials (both electrostatic and DNA hybridization), were explained using entropic principles. Here, enthalpy seems to be the predominant driving force for the formation of these BCC crystals.

The energy landscape show in Figure 8.2B is a good predictor of the locations of particles in simulation. Figure 8.3A shows the probability density of the small particle centers in a single BCC unit cell at low temperature. The small particles are clearly localized at the tetrahedral sites. Additionally, Figure 8.2C shows the probability density of the interactive ends in a low temperature simulation. The location of the highest density regions aligns well with the lowest energy positions in Figure 8.2B. A notable exception

is that the limited reach of the chains in simulation does not allow the interactive beads to reach the bottom of each potential well.

Lastly, the 6:1 number ratio between small and large particles allows the tetrahedral sites to be exactly filled. This is because there are 2 lattice points (large particles) and 12 tetrahedral sites (small particles) per BCC unit cell. A lower ratio would produce vacancies in tetrahedral sites; in those cases, we observe hopping of small particles between sites. A larger ratio results in more small particles than available tetrahedral sites; in those cases, interstitial defects are prominent and full localization is not possible. Studying the 6:1 system allows us to focus on the properties of the localized-to-delocalized transition by avoid confounding factors introduced by vacancy hopping or symmetry change.

8.3.2. The localized-to-delocalized transition is smooth and its onset depends on interaction strength

Figure 8.3 shows the average visitation frequency of the small particle centers in one BCC unit cell, when localized and when delocalized. Though the system pictured has 6 chains per small particle, we see similar behavior for all values of chains per small particle: when localized, small particles occupy the tetrahedral sites, and when delocalized, they occupy a much larger volume. Even when delocalized, the small particles concentrate around the tetrahedral sites and form a pattern in which the additional volume occupied by the small particles is roughly along the edges of the BCC's Wigner-Seitz cell. This permits the small particles to move between nearest tetrahedral sites along an energetically-favorable path, equidistant to multiple neighboring lattice points.

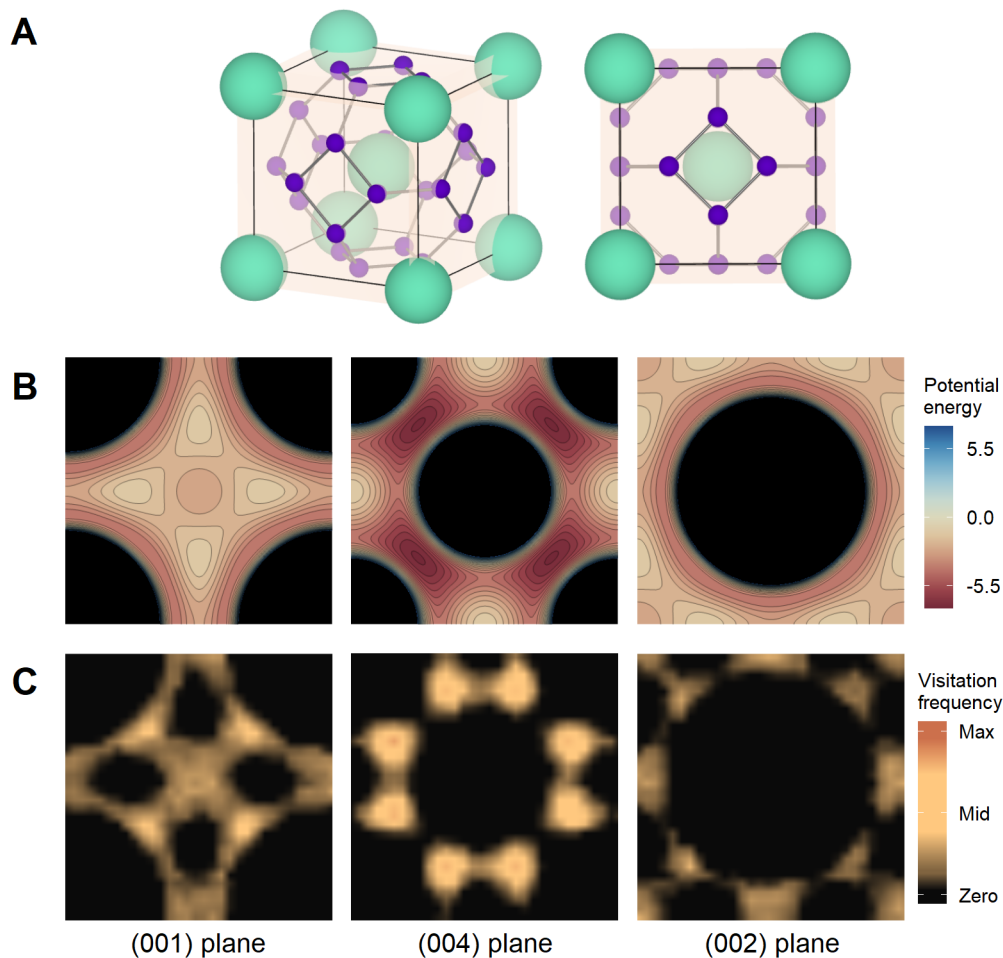


Figure 8.2. **(A)** BCC lattice sites (turquoise) and tetrahedral interstitial sites (purple) of an ideal BCC lattice. Connections between nearest-neighbor tetrahedral sites are shown as visual guides. **(B)** The potential energy landscape in different planes of one interactive end, based on its interaction potential with the large particles, in one BCC unit cell. Deeper red indicates negative values (more favorable energetic interaction), yellow indicates values around zero, and dark blue indicates positive values (unfavorable interactions; the location of large particles is shown in black). **(C)** The probability distribution of the interactive beads on different planes for the case of 6 chains at $T^* = 0.9$. Comparing this to (B), interactive bead probability is highest in areas with the most favorable energetic interactions.

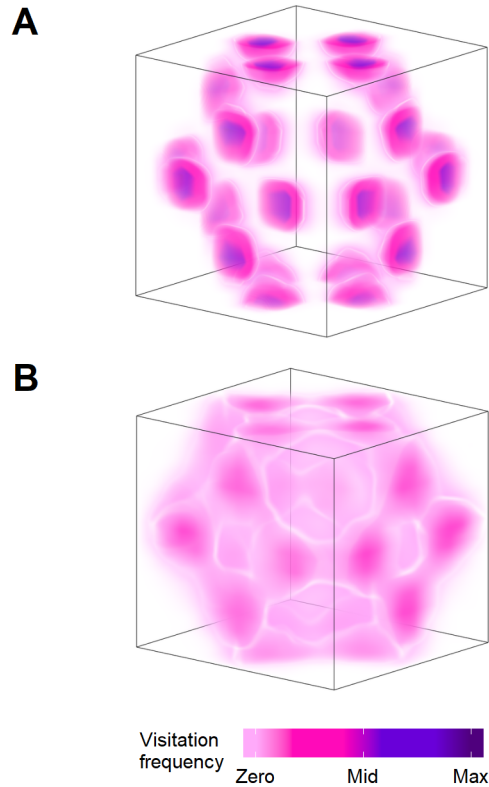


Figure 8.3. Visitation frequency of (centers of) small particles in one unit cell of localized and delocalized systems. Small particles have 6 chains, and the maximum of the visitation frequency is 0.0115. **(A)** $T^* = 0.9$. Small particles are localized on the tetrahedral sites of the BCC lattice. **(B)** $T^* = 1.6$. Small particles are delocalized. They favor the tetrahedral sites of the BCC lattice but also roam around the crystal.

We observe a smooth change from localized-to-delocalized behavior in all cases. Both the onset of delocalization T_{deloc} and the overall melting temperature of the lattice T_{melt} are higher with more grafted chains per small particle; see Table S1. In these systems, the total strength of interaction between the small and large particles scales with the number of grafted chains. Therefore, we use the number of grafted chains per small particle and interaction strength interchangeably throughout this paper. Additionally,

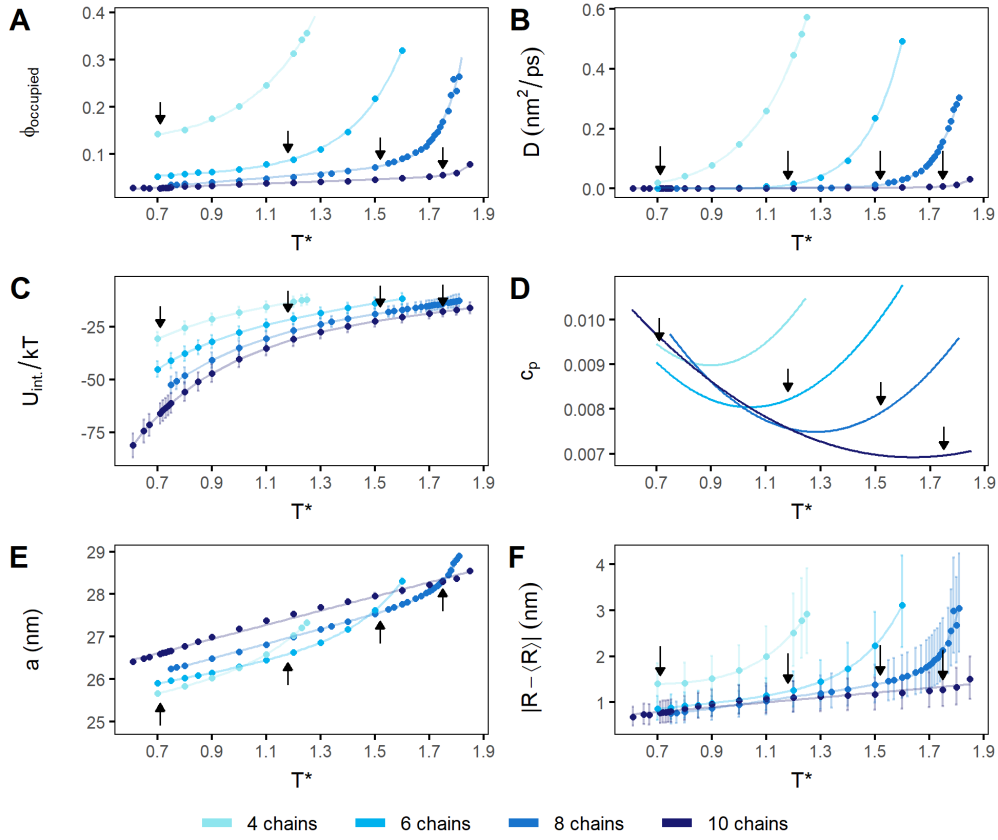


Figure 8.4. Lattice properties as a function of temperature, for all systems studied. Fits are included as visual guides. Black arrows indicate T_{deloc} , the onset of delocalization for each system; see SI for how these are identified. Note that all properties change linearly with temperature below and exponentially above T_{deloc} , with the exception of U_{int} . **(A)** Approximate volume fraction occupied by 70% of the small particles' probability ϕ_{occupied} . This is a qualitative measure of delocalization. **(B)** Diffusion constant D of the small particles. **(C)** Average interaction energy between small and large particles U_{int} , per small particle. **(D)** Specific heat at constant pressure $c_p = C_p/N$ (N is the total number of particles) of the system. These curves were calculated by fitting spline curves to mean values of enthalpy and differentiating those curves with temperature. **(E)** Average BCC lattice parameter a . **(F)** Lattice fluctuations, measured by the median displacement of large particles from their average positions. Uncertainty bars here indicate first and third quartiles, rather than standard deviation, due to the skewed nature of the underlying distribution.

T_{deloc} approaches T_{melt} with increasing interaction strength, which means that we observe a range of behavior. In systems with 4 chains per small particle, T_{deloc} is very low, and the sublattice is delocalized at almost every reported temperature. For 6 and 8 chains per small particle, T_{deloc} is higher and the system is localized at low temperatures and delocalized at high temperatures. For 10 chains per small particle, T_{deloc} is almost equal to T_{melt} , and the small particles exhibit almost no sublattice delocalization until just before crystal melting.

In Figure 8.4, we plot structural and thermodynamic properties of the crystals to characterize their transition. These properties and their importance are listed below.

- Occupied volume fraction of the small particles, ϕ_{occupied} (Figure 8.4A), is a qualitative metric that directly measures delocalization. It represents the approximate volume occupied by 70% of the small particles' probability, as a fraction of the total available volume (see Supplementary Information for more information). In a previous study [101], delocalization was quantified using metallicity, a parameter associated to the Shannon entropy of the sublattice. Here we use a more direct parameter to measure the filling of space by small particles in the sublattice.
- Diffusion coefficient of the small particles, D (Figure 8.4B), has been used to categorize the order of superionic transitions [103]. We have observed that the localized-to-delocalized change is associated with both static properties like ϕ_{occupied} and dynamic properties like D .
- Average interaction energy of a small particle, U_{int} (Figure 8.4C), is capable of reflecting structural changes.

- Specific heat capacity, c_p (Figure 8.4D), provides insight into the order of phase transitions.
- Lattice parameter, a (Figure 8.4E), had been shown to reflect a first order phase transition in previous work in charged colloidal systems [115].
- Median lattice fluctuations (Figure 8.4F) are essential for quantifying melting through the Lindemann criterion.

All properties are plotted as a function of reduced temperature T^* , which is the value of $k_B T$ in energy units. In each panel in Figure 8.4, a black arrow indicates the approximate T_{deloc} for each system. This temperature is estimated from the diffusion properties of the sublattice; see SI for more information about how this was calculated.

Many of the properties in Figure 8.4 exhibit two trends, one during and another before delocalization. The occupied volume fraction ϕ_{occupied} , diffusion coefficient of the small particles D , the lattice parameter a , and the lattice fluctuations (Figures 8.4A, 8.4B, 8.4E, and 8.4F) all increase linearly below T_{deloc} and exponentially above, until the lattice melts. These phenomena appear correlated; particles begin to both diffuse and occupy a larger volume at the same temperatures, which is also the point at which lattice expansion and lattice fluctuations begin to increase dramatically. These ties will be explored in later sections.

The smooth increase in ϕ_{occupied} , a , and other properties suggests that the change from localized-to-delocalized small particles is not a phase transition. This is corroborated by the behavior of the specific heat of the system, c_p , shown in Figure 8.4D. We observe that c_p of all systems is continuous and convex, indicating that no phase transition occurs during

the process of delocalization. This is expected because the change from localization-to-delocalization does not reflect a change in the BCC symmetry imposed by the large particles and so the small particles' energy landscape is not qualitatively impacted.

Even though the c_p curves do not exhibit evidence of a phase transition, they provide information about the underlying energy landscape of the system. We explain the convexity of the c_p curves with the deactivation and activation of degrees of freedom into which energy can be distributed. The low temperature negative slope of these curves relates to the flattening of the local minima of the energy landscape. This flattening decreases the interactive ends' available configurational phase space, decreasing c_p . This is also why the slope is more negative for systems with higher interaction strength. At higher temperatures, new energy modes are enabled in the form of diffusion of the small particles and lattice vibrations. This eventually leads to delocalization, and c_p continues to increase until the lattice fully melts.

Notably, while the ϕ_{occupied} and a change rapidly above T_{deloc} , the interaction energy does not. Figure 8.4C shows the average "binding energy" (the energy of interaction between the large particles and interactive ends, relative to when they are infinitely far apart) per small particle in the system as a function of temperature. That this quantity increases only linearly even above T_{deloc} indicates that entropy plays an important role in delocalization. This will be discussed in Section *Vibrational entropy drives lattice expansion*.

8.3.3. Lattice fluctuations are essential for delocalization

To determine the importance of lattice fluctuations to delocalization, we ran additional simulations in which the large particles were fixed on their lattice points and not allowed to vibrate. The lattice parameter used for a given "fixed lattice" run was the mean value calculated from the unconstrained simulation with the same temperature and number of chains per small particle (Figure 8.4E). We found that without lattice vibrations, the small particles are not able to fully delocalize. This can be seen in the average visitation frequency plots in Figure 8.6. This is quantified by a large reduction in occupied volume fraction and a slight decrease of the diffusion coefficients relative to the unconstrained cases. This is similar to the finding by Schommers [113], who saw diffusion in molecular dynamics models of superionic α -AgI only when the iodine ion lattice was allowed to vibrate.

Based on these results, delocalization is driven by both lattice vibrations and diffusion. We posit that vibration-driven delocalization occurs when lattice deformation either shifts the energy landscape sufficiently such that small particles can more easily diffuse, or that large particles pull small particles between tetrahedral sites while vibrating. Vibration-driven delocalization is fully suppressed in the fixed lattice simulations; this can be seen in Figure 8.5A. However, some delocalization remains due to small particle diffusion. As can be seen in Figure 8.5B, diffusion is still present in the fixed lattice simulations and appears to primarily depend on temperature and the lattice parameter, because they determine the flatness of the energy landscape.

Analysis of the fixed lattice simulations demonstrates that delocalization is fully achieved only when both lattice vibrations and diffusion are present. The similarity

between c_p curves for the fixed and fluctuating lattice runs, shown in Figure 8.5D for the 4 chain system, underscores the importance of diffusion. With or without lattice vibrations, c_p is continuous. Both c_p curves exhibit an initial decrease characteristic of the flattening of the energy landscape but differ at higher temperatures. This is due to the lack of lattice vibrations in the fixed lattice simulations. As stated in the previous section, energy modes associated to the lattice vibrations are what drive the increase of c_p after the flattening of the energy landscape. Therefore, c_p for the fixed lattice simulations continues to decrease, whereas, the unconstrained simulations' c_p increases.

8.3.4. Vibrational entropy drives lattice expansion

Having established that lattice vibrations are crucial for delocalization, we turn to address the exponential expansion shown in Figure 8.4E. The exponential lattice expansion appears to be highly correlated with delocalization, but the reason that it occurs is unclear. To gain a better understanding, we performed a free energy analysis of our system using the same simplified theoretical model that predicted the energy landscape of a BCC unit cell in Figure 8.2B, and which is described in Section *Methods*. This theoretical model describes one interactive end in a fixed (non-fluctuating) BCC unit cell of large particles. The energy of one lattice configuration based on the temperature, lattice parameter, and position of the interactive end $U_{\text{end}}(\vec{r}, \vec{p}; a)$ is found in Equation 8.5, and is based on Equation 8.1 and Figure 8.1A. Using these definitions and a and T from simulation, we calculated the partition function $Z(a, T) = \int e^{-U_{\text{end}}(\vec{r}, \vec{p}; a)/k_B T} d\vec{r} d\vec{p}$ by numerically integrating over a unit cell. From this, we could calculate all relevant thermodynamic properties. See Section *Methods* for more information.

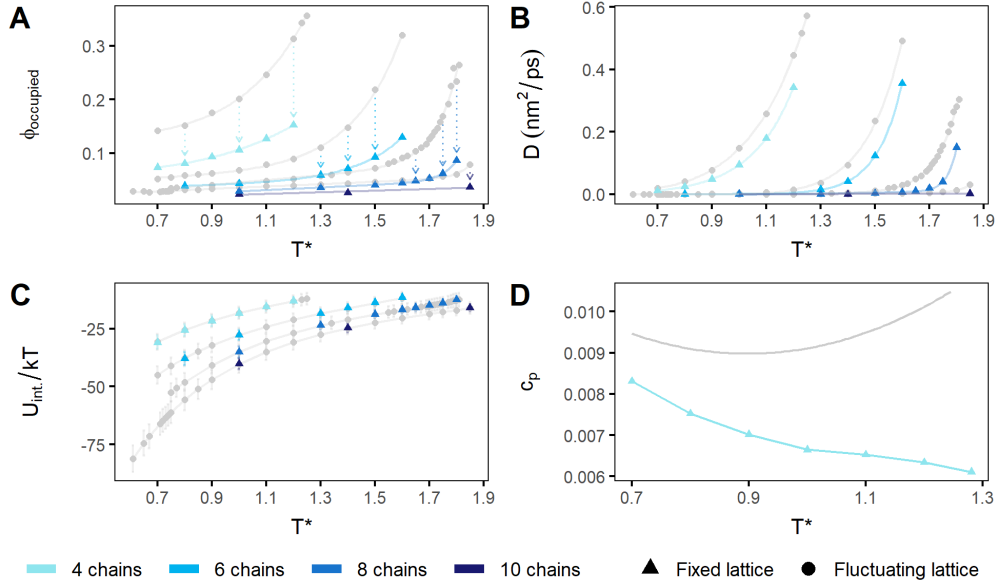


Figure 8.5. Lattice properties as a function of temperature, for fixed lattice runs (compared to unconstrained runs). Data from the main runs (also in Figure 8.4) is shown in grey circles, and data from the fixed lattice runs is shown in blue triangles. Removing lattice fluctuations substantially suppresses delocalization and minorly suppresses diffusion. **(A)** Approximate occupied volume fraction ϕ_{occupied} . Arrows connect fixed and fluctuating lattice simulations with the same number of chains per small particle as a visual guide. **(B)** Diffusion constant D of small particles. **(C)** Average interaction energy U_{int} of small particles with large particles. Because corresponding fixed and fluctuating lattice runs have the same average lattice constant, the average interaction energy of the small particles does not change, though the fluctuations of U_{int} do. **(D)** The specific heat at constant pressure c_p of the system with 4 chains per small particle.

We employed this model to explain why the lattice expands so rapidly at the onset of delocalization. To do this, we compared two cases: *(i)* exponential expansion, which is the observed behavior of the lattice, and *(ii)* linear expansion, in which the lattice expands only linearly over the entire temperature range. We ran fixed lattice simulations of both cases and compared those to theory.

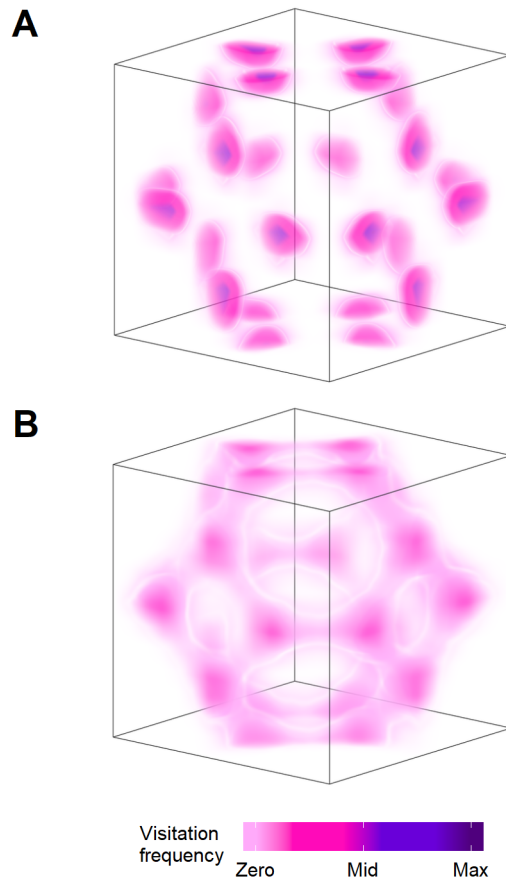


Figure 8.6. The average visitation frequency of the small particle centers in a fixed lattice system with 6 chains per small particle. The maximum of the visitation frequency is 0.0250. Without lattice fluctuations, the small particles in the delocalized case occupy less volume than when lattice fluctuations are present. Note that the unit cells of these lattices are actually different sizes, but the images have been scaled such that the two are comparable. **(A)** $T^* = 0.9$. Small particles are localized on the tetrahedral sites of the BCC lattice. This is similar to the unconstrained lattice case. **(B)** $T^* = 1.6$. Small particles are delocalized. Again, they favor tetrahedral sites but also diffuse between sites.

Figure 8.7A shows the average interaction energy per small particle in the exponentially and linearly expanding cases, for simulation (points) and theory (solid line). We

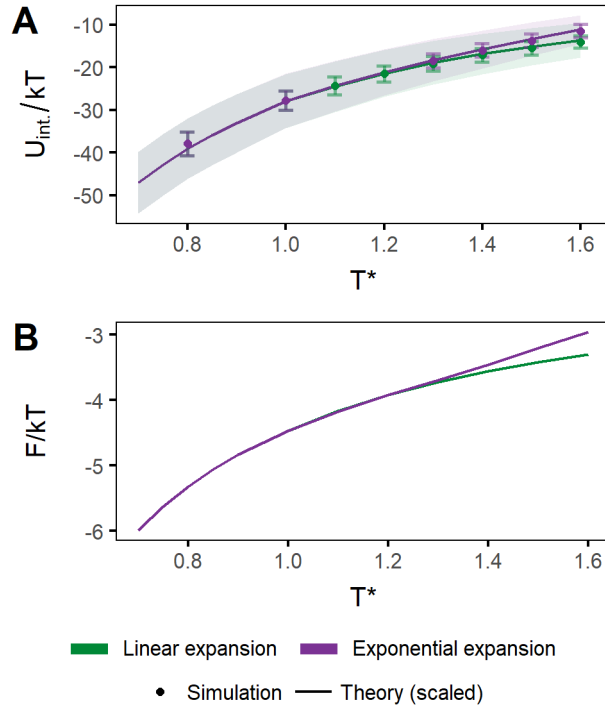


Figure 8.7. Comparison between theory and simulation (6 chain system). **(A)** Interaction energy between small and large particles. Line represents scaled theory results; points represent simulation results. **(B)** Theoretical prediction of the free energy of the systems with exponentially expanding lattice (main cases) and linearly expanding lattice. The free energy of the linear case is lower, indicating that something outside the theory must explain why the lattice expands exponentially.

find that the theoretical model accurately predicts the energy in both cases up to a multiplicative factor. In the theoretical model, the interactive energy of a single interactive end is $\langle U_{\text{potential}} \rangle = \frac{1}{Z(a,T)} \int U_{\text{potential}}(\vec{r}; a) e^{-U_{\text{end}}(\vec{r}, \vec{p}; a)/k_B T} d\vec{r} d\vec{p}$ (a summary of Equation 8.5). Because the result of this integral is the potential energy of one interactive end, we multiply $\langle U_{\text{potential}} \rangle$ by the number of chains per small particle to estimate the total energy of a small particle. For example, Figure 8.7 shows simulation results for runs with 6 chains per small particle. If the theoretical model were exact, we would multiply $\langle U_{\text{potential}} \rangle$ by

6. However, the theoretical model overestimates the average energy per small particle relative to simulation. This is due to the fact that, in simulation, the limited reach of the chains does not allow the interactive end to fully explore the lowest energy portions of the cell's potential wells (this can be seen in the comparison between Figures 8.2B and 8.2C). The result is that the interactive end's energy is about 20% lower in simulation than in theory. Therefore, the theoretical results shown in Figure 8.7A are scaled by a factor of 0.82 (this factor differs by a few percent for the case of 4 chains per small particle). Additionally, excluded volume interactions of more densely grafted chains can impact the possible configurations of the interactive ends. This effect is not observed for small particles with 4 and 6 chains, because the average energy per chain is independent of the number of chains. Meanwhile, excluded volume interactions affect particle energy to a minor extent in systems with 8 and 10 chains per small particle.

The close correspondence between small particle potential energy in simulation and that predicted by theory indicates that the theoretical model can predict differences in properties between the exponentially and linearly expanding cases. Therefore, we used this model to compare the free energies of the two cases, to understand why one is favorable. Using the partition function, we calculated the Helmholtz free energy, $F = -k_B T \ln Z$, which is plotted in Figure 8.7B. According to the theoretical model, the free energy of the linearly expanding lattice should be *lower* than the free energy of the exponentially expanding lattice, so exponential expansion should be not favorable. We conclude, therefore, that at least one of the few interactions missing from the theoretical model must be what drives the observed exponential expansion. There are three pieces missing from the

theoretical model: *(i)* excluded volume interactions due to the presence of the other particle types, *(ii)* bond constraints, and *(iii)* lattice vibrations. We have already established that excluded volume interactions do not greatly impact the average energy of the small particles. Therefore, excluded volume should not contribute to the difference between the exponentially and linearly expanding cases, especially with 4 and 6 chains per small particle. We also can account for the bond constraints by scaling the potential energy by about 0.8, as mentioned above. Additionally, bond constraints limit the reach of the interactive ends and therefore are likely to make rapid lattice expansion less energetically favorable. Therefore, it must be vibrational entropy that drives the exponential lattice expansion. Additionally, large lattice fluctuations have already been seen to stabilize BCC crystals around their melting temperatures [139], which is possible due to BCC crystals' non-close packed structure and low coordination number. Vibrational entropy becomes dominant only above a certain temperature that depends on the number of chains per small particle. This is why we see exponential expansion and delocalization at different temperatures depending on the interaction strength. Based on this analysis, we can see that lattice vibrations determine both the degree of delocalization and the thermal expansion of the lattice.

8.4. Conclusion

In summary, we have seen that the localized-to-delocalized transition in 6:1 (BCC) binary colloidal systems is continuous, dominated by lattice vibrations, and tunable by number of chains per small particle. Our results suggest that the delocalization of the sublattice in this system is not a phase transition. This is supported by the fact that

the symmetry of neither particle type changes during the transition; at all temperatures, the large particles form a BCC lattice and the small particles favor the BCC tetrahedral sites, even when delocalized. The lack of a phase transition is also evidenced by the fact that c_p is continuous for all systems. Moreover, delocalization is highly tied to vibrational entropy. Using simulations in which lattice vibrations were prohibited, as well as a free energy analysis with a simplified theoretical model, we conclude that most delocalization is driven by lattice vibrations, and that vibrational entropy is what causes the lattice to expand so rapidly above T_{deloc} . We can also see that the temperature range associated with the localized-to-delocalized transition is dependent on the number of chains per small particle, a proxy for interaction strength. The nature of the transition does not change as the number of chains per small particle does, but the presence of many chains suppresses delocalization almost entirely. Additionally, the validation between the theoretical model and simulation results reveals that the potential energy landscape of a single interactive end within a BCC unit cell is a faithful representation of the simulated system, even though we have not included other particles within the theoretical model. This is accurate because of the asymmetry of range of interactions imposed by the size asymmetry of the particles.

Based on our analysis, we can identify additional conditions that appear to be favorable for sublattice delocalization. Our findings show that delocalization tends to occur at temperatures such that the small-large particle binding energy per chain is $\sim 3 - 5 k_B T$. Per Figure 8.4C, delocalization occurs when the total interaction energy is around $22 k_B T$ /particle, distributed between all chains. This can be tuned by the number of chains

grafted to the small particles. Additionally, we posit that, for the possibility of delocalization, the small particle size must be comparable to the fluctuations of the lattice and an asymmetry of interaction ranges must exist. The attraction range between small and large particles must be greater than the repulsion range between small particles because small particles must sit at and travel between interstitial sites that are closer together than lattice points. This asymmetry is present in our model, and it can also be achieved with charged colloids given a disparity in charge magnitudes between the small and large particles [115, 140]. Note that increasing the range of repulsion between small particles may change the nature of the transition by adding correlations between small particles; however, we have not tested that here.

Under those conditions, similar analysis and conclusions may be generalized to other colloidal systems, with or without chains, but with certain caveats. For example, a more complex energy landscape with local energy minima at different interstitial symmetry points could change the nature of the transition. This could enable the small particles to transition through different symmetry points at different temperatures [123], which would be reflected in the order of the transition. This may be why previous work on charged colloidal systems [115] found a discontinuity in certain physical parameters like the lattice constant. Additionally, other compositions produce different crystal types, and a phase transition between two crystal lattices can occur as a function of temperature. This can also impact the order of the localized-to-delocalized transition. Finally, the scaling of interaction strength with number of chains per small particle may not hold at system compositions that form non-BCC crystals, because the symmetry of collective

chain configurations (impacted by the number of chains present) can affect the favorability of different interstitial points and crystal structures.

Concerning the comparison between superionics and delocalized colloidal crystals, a continuous transition has also been reported between ionic and superionic states for some superionic crystals [141]. Therefore, drawing on the superionics literature can help us understand colloidal crystal delocalization and vice versa. For example, soft vibrational modes, which are high amplitude vibrations, are reported to be important for the presence of superionic conduction, most commonly a mobile cationic interstitial within an anionic lattice. Soft vibrational modes are stabilized by non-close packed crystals already seen in superionics [123, 124] as well as in these BCC colloidal crystals. The mechanism of this phenomenon is still not fully understood in superionic materials. However, it may be possible to use results reported here by drawing an analogy between the electron density's role in the stability of the crystal and that of the potential energy landscape of our system. The two may be compared by assuming polar covalent bonding between the static and mobile species. If true, then our findings using these colloidal systems would translate to superionic materials which are relevant to applications for the improved design of solid-state batteries for energy storage [142–144].

8.5. Supporting Information

Supporting information contains: the pair distribution functions over the studied temperature range; details of the determination of T_{deloc} ; the calculation method for occupied volume and the heat capacity; and an analysis of nearest neighbor interactions (PDF).

Videos of rotating unit cells of a localized and delocalized sublattice for both unconstrained and fixed lattice simulations are also available (.mp4 videos).

Acknowledgements: This work was supported by the Center for Bio-Inspired Energy Science, an Energy Frontier Research Center funded by the US Department of Energy, Office of Science, Basic Energy Sciences under Award DE-SC0000989. H.L.-R. thanks a fellowship from Fulbright-Garcia Robles and A.E. thanks a fellowship from the National Science Foundation under grant DGE-1450006. M.O.d.l.C. thanks the computational support of the Sherman Fairchild Foundation.

CHAPTER 9

Metallicity transition in other crystal types

After having explored the 6:1 system thoroughly, we wanted to understand how changing the number ratio of small to large particles would influence the favorability of different crystal types, as well as the nature of the transition to delocalization. We expanded the use of our coarse grained model to conduct an extensive study of the crystals formed by our size-asymmetric system. For the simulation and analysis in this paper, Hector Lopez Rios and I contributed equally to the simulation and analysis of all systems.

The following was originally published in *Physical Review Materials* in 2021. It is reproduced here with permission of Hector Lopez-Rios, Monica Olvera de la Cruz, and the American Physical Society.

Supplementary material associated with this chapter can be found in Appendix D.

Metallization of colloidal crystals

Ali Ehlen,* Hector Lopez-Rios,* Monica Olvera de la Cruz

* equally contributing first authors

Reprinted with permission from:

Physical Review Materials 2021, **5**, 115601, DOI: 10.1103/PhysRevMaterials.5.115601

[https://journals.aps.org/prmaterials/abstract/10.1103/](https://journals.aps.org/prmaterials/abstract/10.1103/PhysRevMaterials.5.115601)

PhysRevMaterials. 5. 115601

ABSTRACT: Colloidal crystals formed by size-asymmetric binary particles co-assemble into a wide variety of colloidal compounds with lattices akin to ionic crystals. Recently, a transition from a compound phase with a sublattice of small particles to a metal-like phase in which the small particles are delocalized has been predicted computationally and observed experimentally. In this colloidal metallic phase, the small particles roam the crystal maintaining the integrity of the lattice of large particles, as electrons do in metals. A similar transition also occurs in superionic crystals, termed sublattice melting. Here, we use energetic principles and a generalized molecular dynamics (MD) model of a binary system of functionalized nanoparticles (NPs) to analyze the transition to sublattice delocalization in different co-assembled crystal phases as a function of temperature (T), number of grafted chains on the small particles, and number ratio between the small and large particles $n_s:n_l$. We find that $n_s:n_l$ is the primary determinant of crystal type due to energetic interactions and interstitial site filling, while the number of grafted chains per small particle determines the stability of these crystals. We observe first-order sublattice delocalization transitions as T increases, in which the host lattice transforms from low-

to high-symmetry crystal structures, including $A20 \rightarrow BCT \rightarrow BCC$, $A_d \rightarrow BCT \rightarrow BCC$, and $BCC \rightarrow BCC/FCC \rightarrow FCC$ transitions and lattices. Analogous sublattice transitions driven primarily by lattice vibrations have been seen in some atomic materials exhibiting an insulator-metal transition also referred to as metallization. We also find minima in the lattice vibrations and diffusion coefficient of small particles as a function of $n_s:n_l$, indicating enhanced stability of certain crystal structures for $n_s:n_l$ values that form compounds.

9.1. Introduction

Binary colloids of size-asymmetric particles have been shown to co-assemble into a diverse set of binary crystals [106, 110, 145–150]. These crystals are compounds akin to atomic ionic crystals because the smaller particles occupy interstitial sites of a lattice formed by the large particles. Recently the exploration of binary colloidal crystals with highly size-asymmetric functionalized NPs has yielded the observation of crystal assemblies where the small NPs delocalize, rather than remaining fixed at interstitial sublattice sites [101, 151, 152]. This phenomenon was also observed in simulations of colloidal crystals of oppositely charged, highly size-asymmetric, and highly charge-asymmetric nanoparticles with screened Coulomb interactions [115, 153]. In all these systems, the delocalized and diffusive small particles keep the large particles in fixed lattice positions, as electrons do in crystalline metals. The result is a metal-like colloidal crystal.

The degree of sublattice delocalization was quantified using a normalized Shannon entropy, termed metallicity, by Girard and Olvera de la Cruz [101, 154]. They used simulations of co-assembled DNA-functionalized NPs that were highly asymmetric in size and

grafting density of complementary linkers. These showed that sublattice delocalization, and consequently metallicity, increased with T , changing the crystal from ionic to metallic. Furthermore, Girard and Olvera de la Cruz discovered a minimum in metallicity as a function of the ratio of the number of small NPs (n_s) to the number of large NPs (n_l) in the crystal. They used simple band structure construction concepts from solid state physics to explain the observed minimum in metallicity and equated metallicity to conductivity in metals [154]. In this analogy, the value n_s/n_l is the "valency," and the metallicity, akin to conductivity, decreases with increasing n_s/n_l as interstitial sites are filled until it reaches a minimum at the compound values of the lattice, when the interstitial sites are saturated (*i.e.*, $n_s/n_l = 6$ for a body-centered cubic (BCC) crystal). Upon further increase of n_s/n_l , the metallicity increases as the conductivity does in atomic systems with increasing number of electrons in the conduction band. They also highlighted that the minimum in metallicity becomes sharper with an increase in the interaction energy between the small and large NPs, achieved by increasing the number of linkers on the small NPs. They also suggested that the localization-delocalization transition in colloidal crystals can be described as a classical analog to a Mott-like insulator-metal transition (IMT) in atomic systems.

Interestingly, sublattice delocalization is also observed in non-metallic atomic systems, specifically superionic materials [103], and the transition to superionic sublattice delocalization is often termed "sublattice melting." A canonical superionic material is AgI, in which the larger atomic species I forms a BCC host lattice through which Ag ions diffuse. The Ag ions have been identified as diffusing between neighboring BCC tetrahedral

sites [113, 155], and diffusion has been seen to be strongly coupled to the dynamics of the host lattice [141, 156].

Recently, we have observed similar behavior in colloidal systems by using a generalized MD model of a binary, size-asymmetric system of functionalized NPs with $n_s:n_l = 6:1$. We reported the formation of stable colloidal BCC crystals with a diffusive sublattice of small particles translating between neighboring tetrahedral sites [151]. Similar to AgI, we observed a strong correlation between diffusion and lattice vibrations as a function of T , but we noted that the transition to sublattice delocalization is described by a smooth change, rather than a true phase transition. This suggests that phonons play an important role in the delocalization transition, and that an atomic analog to this classical localization-delocalization transition should include the effect of the interactions of the phonons with metallic electrons as in the Peierls IMT.

Here, we study the transition to sublattice delocalization at different values of the number ratio $n_s:n_l$, as a function of T and the number of grafted chains per small particle, and we examine the origin of the delocalization transition. We highlight the similarities with the IMT and with superionic sublattice melting and analyze the effect of the phonons in the localization-delocalization transition. We use the MD model established in [151] in the NPT ensemble at near zero pressure to ensure that the resulting assemblies are due to interactions between small and large particles alone. The model, consisting of mutually attractive and size-asymmetric NPs, is visually depicted in Fig. 9.1. The turquoise sphere is a coarse-grained representation of a large particle with either densely grafted chains or a functionalized surface. The small particle is represented by a central sphere (purple) and explicitly modeled grafted chains (white), each of which has an interactive terminus

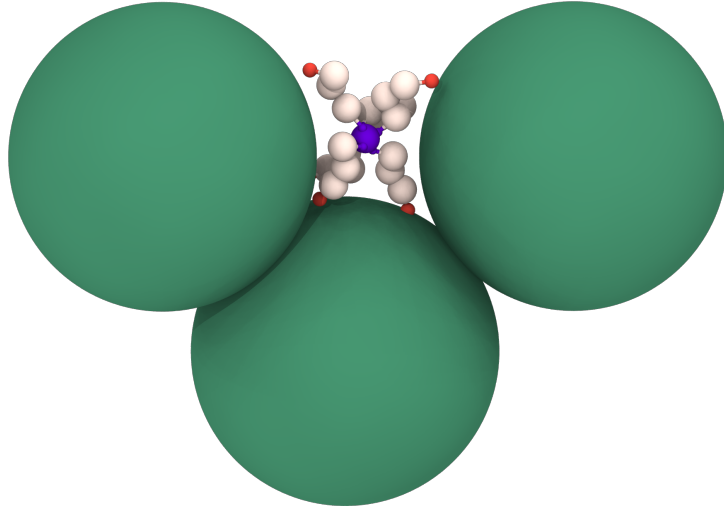


Figure 9.1. Graphical representation of the MD model. All beads have excluded volume interactions with each other, and there is an attractive interaction between the large particles (turquoise) and the interactive end of each chain (orange), as described in [151]. Note that there is no attractive interaction between large particles. Therefore, assemblies of these particles are held together exclusively by the attraction between the small particles' interactive beads and the large particles. Because the large particles represent densely grafted large particles, some overlap is permitted.

(orange) that is radially attractive only to large particles. The generality of the model implies that we can represent a variety of experimental systems [147, 148, 157–160], and the tunability of NPs enables us to find a rich variety of lattices and multiple types of delocalization transitions.

Using this model, we find that the crystal structure is determined by $n_s:n_l$ and the lattice stability is determined by the number of grafted chains per small particle. We observe a variety of crystals, including A20 and body-centered tetragonal (BCT) lattices, and we confirm that the low T (localized sublattice) positions of the small particles can be understood by analyzing their potential energy landscape. Almost all studied systems undergo a transition to sublattice delocalization with increasing T , and the type

of transition is also determined by $n_s:n_l$ based on energetic interactions and interstitial site filling. For some $n_s:n_l$ ratios, the sublattice smoothly delocalizes without undergoing a phase transition. This occurs for cubic lattices with nearly or completely full sublattice sites, near 6:1 and 10:1. For other number ratios, we observe a first-order sublattice delocalization transition accompanied by a first-order host lattice transition to a crystal of higher symmetry with inherent sublattice vacancies. This is seen in transitions from A20 to BCT, BCT to BCC, and BCC to face-centered cubic (FCC), which all occur upon increasing T . We present evidence that these transitions are entropic and driven by lattice vibrations, similar to the metallization of atomic materials driven by phonons, as in the Peierls IMT [161]. Finally, we identify minima in the lattice vibrations and diffusion coefficient of the small particles as a function of $n_s:n_l$. Crystals at the minima are those whose interstitial sites are saturated with small particles, except the high- $n_s:n_l$ FCC crystals.

This article is organized as follows. In the next section, we will describe the range of crystal lattices observed in our parameter space of 4, 6, 8, and 10 grafted chains per small particle and number ratios $n_s:n_l$ between 3:1 and 10:1, over a wide range of temperatures. We will then further detail the three delocalization behaviors we observe and discuss the implications of the diffusion coefficient minima.

9.2. Results

9.2.1. Determining crystal structure by number ratio $n_s:n_l$

At low temperatures, the large particles form a variety of lattices with the small particles localized at interstitial sites. These sites are always Wyckoff positions, which have a unique set of symmetry operators associated with the host lattice. The location of the

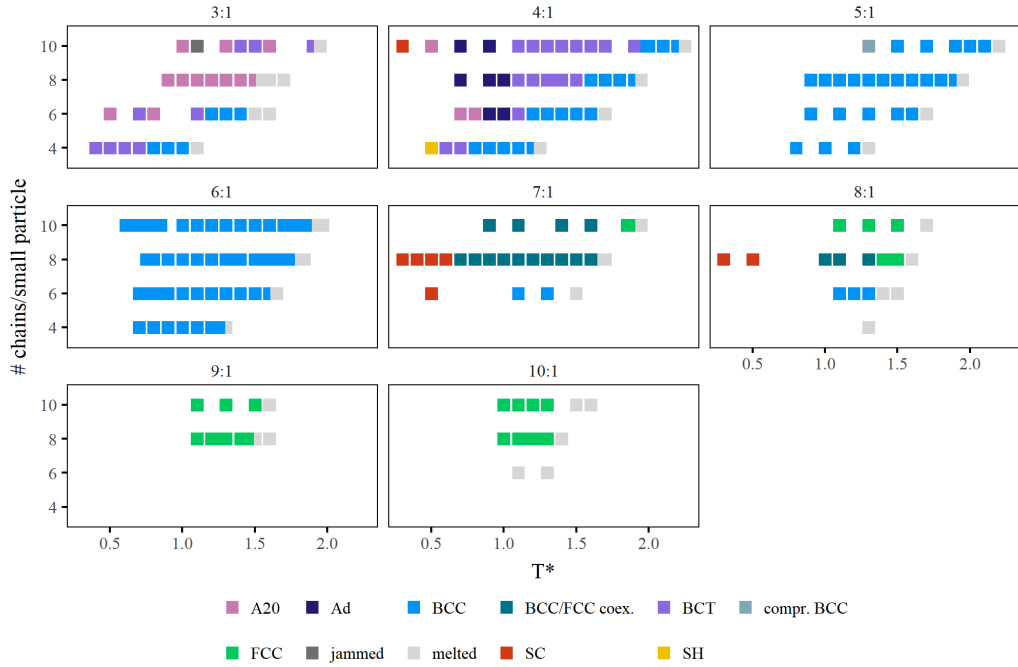


Figure 9.2. Phase diagrams of different $n_s:n_l$ values, as a function of reduced temperature T (see 9.4) and number of chains per small particle. “Coex.” stands for “coexistence” and 129a is an unknown crystal type in space group 129 defined in the Supplemental Material, Section D.2.1. The crystal structures observed only once are not analyzed in detail here. For the higher ratios where no data is shown for 4 or 6 chains, it is because no stable lattices were found. All data plotted in this paper is taken from simulations represented in these phase diagrams.

small particles at these interstitial sites is dependent only on crystal type. We find that the symmetry of the resulting lattices depends on $n_s:n_l$, and the stability of the lattice depends on the number of chains per small particle.

Table 9.1 shows the most common crystals observed in our systems and the number ratios $n_s:n_l$ that produce them, and Figure 9.2 shows a phase diagram of all simulations studied in this work. The phase diagrams demonstrate visually that $n_s:n_l$ determines crystal structure, and the crystal properties in Table 9.1 help explain trends present in

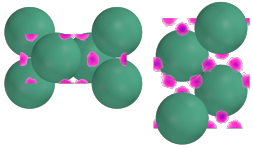
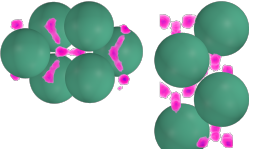
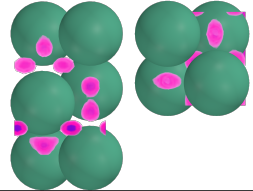
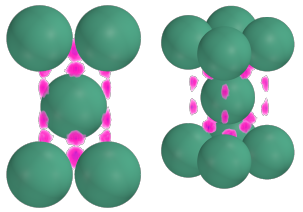
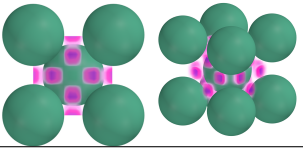
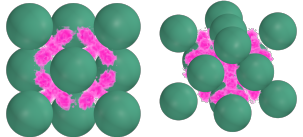
Lattice type, space group		# lattice pts/unit cell	Wyckoff position (# NNs/site)	$n_s:n_l$ ratios that result in this lattice
A20 63 Cmc \bar{m}	<div style="display: flex; flex-direction: column; align-items: center;"> <div style="margin-bottom: 10px;">(3:1) </div> <div>(4:1) </div> </div>	4	16h, 4c (3:1 systems) or 16h, 8g ($\times 2$) (4:1 systems) (all 5 NNs)	3:1 and 4:1, resulting in different parameter ratios
A _d 129 P4/nmm		4	2c ($\times 2$), 4f, 8j (4-5 NNs)	4:1
BCT 139 I4/mmm		2	4d (4 NNs) 4e (5 NNs)	4:1 (with $c/a = 2$, as shown here)
BCC 229 Im $\bar{3}m$		2	12d* (4 NNs)	5:1, 6:1
FCC 225 Fm $\bar{3}m$		4	32f (3 NNs), 8c* (3 NNs)	9:1, 10:1

Table 9.1. Observed lattices, defined by large particles at lattice points and small particles at interstitial sites, and arranged by the $n_s:n_l$ at which they are observed with a localized sublattice. Lower symmetry lattices appear in lower $n_s:n_l$ systems, and the $n_s:n_l$ ratio at which we observe a crystal type corresponds to: #Wyckoff positions/#lattice points, on a per-unit cell basis (for example: $12/2 = 6$ for a BCC). In lower-symmetry lattices, small particles sit at Wyckoff positions with more nearest large particle neighbors (NNs) than those in higher-symmetry lattices. *12d positions in BCC crystals and 8c positions in FCC crystals are tetrahedral sites.

the phase diagrams. For example, the value of $n_s:n_l$ at which a crystal structure is observed is consistent with the ratio of the number of lattice points (large particles) to the number of interstitial points associated with Wyckoff positions (small particles) of the unit cell. Explicitly, column 4 = column 3 divided by column 2 (5:1 and 9:1 cases both contain interstitial vacancies). Note that some Wyckoff positions in A20 lattices are degenerate based on the observed lattice parameter ratios, so the A20 16h Wyckoff positions map onto 8 unique points instead of 16 and one 8g set maps onto 4 points. Table 9.1 also demonstrates that the number of large particle nearest neighbors (NNs) interacting with each small particle decreases with increasing lattice symmetry and $n_s:n_l$ ratio. This is also an important approximation to the average potential energy interactions U_{int} between the two species. In summary, the findings demonstrated in Table 9.1 and Fig. 9.2 show that decreasing $n_s:n_l$ results in lower-symmetry lattices with small particles sitting at lower-energy interstitial points.

The most common lattices are A20, A_d , high symmetry BCTs, BCC, and FCC, though simple hexagonal (SH) and simple cubic (SC) are also observed. The non-cubic nature of BCT, A_d , and A20 requires a larger set of defining lattice parameters than the cubic crystals, and we observe multiple parameter ratios for each structure. For example, most BCT lattices with $n_s:n_l = 4:1$ shown in Fig. 9.2 have the lattice parameter ratio $c/a = 2$. This is the configuration shown in Table 9.1, and it creates favorable conditions for 8 small particles in the unit cell, each of which interacts with 4 or 5 large particles depending on the site. However, some 3:1 and 4:1 BCT crystals in which the small particles have only 4 chains have $c/a = \sqrt{\frac{2}{3}}$ (not shown in Table 9.1 for simplicity). We hypothesize that the interstitial sites in the more elongated BCT structure that allow for interactions with

5 large particle nearest neighbors require the small particles to have at least 5 chains. Therefore, small particles with only 4 grafted chains cannot stabilize those elongated structures. This is supported by a Fig. D.3 in the Supplemental Material, which shows that small particles with 4 chains rarely interact with 5 large particles at once. Generally, BCT crystals only take discrete c/a ratios corresponding to lattices of higher symmetry. For more details, see the Supplemental Materials, Section D.2.1 and Section D.2.2.

A_d lattices are also tetragonal and can be visually compared to BCT lattices in which an additional symmetry is broken because the conventional unit cell's central particle is not body-centered. The A_d unit cell is defined by parameters a and c (similar to BCT) and z , which determines the offset of the central particles. When $z = 0.5$, BCT symmetry is recovered. For all observed A_d crystals $c/a = 2$. However, there is a continuous increase of the z parameter with T , from $z \sim 0.4$ at low T to $z = 0.5$ at the transition to BCT lattice with $c/a = 2$. These local spatial changes as a function of temperature indicate the capacity for these colloidal crystals to be used as reconfigurable materials.

A20 crystals are orthorhombic and yet lower symmetry and more complex than the BCT or A_d crystals. Their unit cells are defined by the ratios between a , b , and c , as well as a parameter y that determines the lattice point placement within the unit cell. We observe two A20 crystal types with different lattice parameter ratios as a function of $n_s:n_l$. All 3:1 A20s have a consistent set of parameters c/a , c/b , and y , while the 4:1 A20 have another. Each parameter set results in different numbers of interstitial sites for the small particles. Additionally, due to the low symmetry of the A20 lattice, its parameters can be tuned to produce other lattices of higher symmetry. These include those observed at

other values of $n_s:n_l$ and temperatures in this study, such as BCC and FCC. More details on all common lattices found in this study can be found in the Supplemental Material.

For almost all crystals listed in Table 9.1, a simple analysis of the potential energy landscape of a unit cell demonstrates why each lattice type is favorable at a given $n_s:n_l$ ratio. The landscapes were calculated with pairwise potentials between the large particles and one interactive chain bead, using the same method as described in [151]. The potential energy of a given point in a unit cell is the sum of the pairwise potential energy between a test particle (one interactive bead) located at that point within the unit cell and all large particles in the current and surrounding unit cells that contribute to the test particle's energy. This method only accounts for interactions between the large particle lattice and one interactive bead, and therefore does not take into account any small particle-small particle interactions or lattice vibration. However, even with these simplifications, the calculated energy landscapes can shed light on the spatial distribution of the particles. Each energy landscape shows potential energy wells (the most favorable locations for the interactive beads) and potential energy plateaus near zero (the least favorable locations for the interactive beads). For almost every lattice, the simulation results show that when the sublattice is localized, the interactive ends spend the most time in the energy wells, and the centers of the small particles spend the most time on the energy plateaus. This means we can predict the location of small particles once we know the unit cell of the large particle crystal, by identifying the location of the energy plateaus. The existence of these energy wells and their non-spherically symmetric distribution around the energy plateaus also highlights the importance of separation between the attractive component of the small particles and their cores, which in this case is due to the grafted chains.

The fact that an analysis of a static energy landscape calculated with only small particle-large particle interactions can accurately identify the locations of the small particle centers indicates that the small particles do not substantially interfere with each other. A more detailed analysis of the BCC case can be found in Lopez-Rios *et al.* [151], and a visual comparison between the energy landscape of a unit cell and the location of small particles can be found in the Supplemental Material. There is one important exception: the FCC energy landscape shows plateaus at the octahedral and tetrahedral sites (Wyck-off positions 4b and 8c, respectively). However, we observe the small particles localizing at the 32f sites, where the energy plateaus are much smaller. In our systems that result in FCC crystals, small particles never localize at the octahedral sites, and they localize at the tetrahedral sites only once the 32f sites are full (at ratios higher than $n_s:n_l = 8:1$). We hypothesize that this is because the distance from the 32f sites to the large particles is shorter than the other sites which is needed to maintain a stable crystal with our system of short-range interactions. Additionally, there are fewer 4b and 8c sites in an FCC, and for the $n_s:n_l$ ratio that would have filled those sites (3:1), there are more energetically favorable crystals available.

Finally, as the number of small particles in the lattice increases (larger $n_s:n_l$ ratios), the energetic interaction between each small particle and the surrounding large particles becomes weaker and the packing density of large particles decreases. This can be seen in Fig. 9.3, which shows the average small particle-large particle interaction energy and system density for each of the common crystal lattices observed in our system. Almost all simulations shown in Fig. 9.2 are included. The number of large particles with which

each small particle can interact decreases with increasing lattice symmetry; see the Supplemental Materials for corresponding simulation data. For example, a BCT lattice with $c/a = 2$ has 8 interstitial sites, at which the small particles can interact with 4 or 5 large particles. Meanwhile, a BCC unit cell contains 12 interstitial sites, and a small particle at any of those sites can interact with 4 large particles. Because BCT and BCC unit cells each contain 2 lattice sites, the favorable sublattice sites are fully occupied at a 4:1 number ratio for a BCT and at 6:1 for a BCC. If there are more small particles than can fit in the BCT interstitial sites, then the system's equilibrium lattice cannot be a BCT and it will instead form a BCC. This pattern holds across all number ratios: systems with larger $n_s:n_l$ ratios form crystals containing interstitial sites that are greater in number but less energetically favorable.

9.2.2. Sublattice delocalization transition entropy and dependence on interstitial site filling

We observe a transition to sublattice delocalization with increased T for almost all assembled crystals. For some values of $n_s:n_l$, the transition to sublattice delocalization is a phase transition accompanied by a change in symmetry of the large particle lattice. For others, sublattice delocalization occurs as a smooth change rather than a phase transition. In the subsequent subsections, we detail the signatures of each observed transition behavior and corresponding lattice properties.

For all values of $n_s:n_l$, we see two overarching trends. First, there is strong evidence that the transition to sublattice delocalization is driven by entropy. This is expected based on the form of the Gibbs free energy $\Delta G = \Delta H - T\Delta S$, the minimization of which

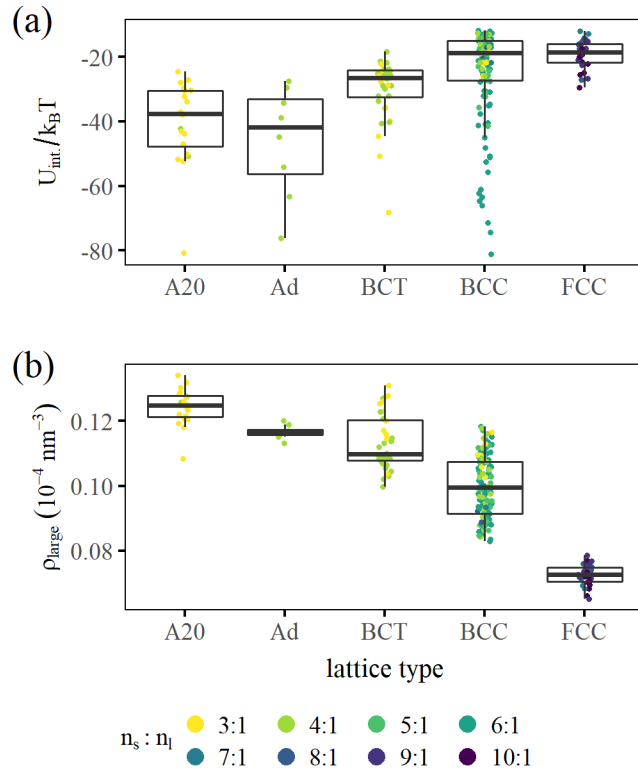


Figure 9.3. (a) Average interaction energy $U_{\text{int.}}/k_B T$ per small particle, which quantifies the potential energy due to small particle-large particle interactions, and (b) number density of the large particles ρ_{large} for each simulation that resulted in the most common crystals (A20, A_d, BCT, BCC, and FCC), arranged by crystal lattice type and colored by the value of $n_s:n_l$ to emphasize the effect of number ratio on lattice structure. Each data point represents a simulation under different conditions (temperature, number of chains, $n_s:n_l$), and the data shown comes from nearly all simulations in Fig. 9.2 that resulted in these common crystals. One very low temperature simulation with an A20 structure ($U_{\text{int.}}/k_B T < -100$) has been removed for clarity. Values of temperature and number of chains per small particle are not distinguished here.

determines the equilibrium crystal phase. ΔG is dominated by enthalpy ΔH at low T and entropy ΔS at high T . Entropic effects have also been experimentally shown to induce phase transitions of binary size-asymmetric colloidal crystals from energetically to

entropically favored phases [108]. In our systems, we see this for all types of transition to sublattice localization.

Second, increasing the chains per small particle increases the temperature at which the entropic transition occurs, effectively increasing the stability of the lattice. Crystal transition and melting temperatures increase approximately linearly with the number of chains per small particle for each value of $n_s:n_l$. Therefore, the addition of chains in most cases simply scales up the magnitude of the interaction between the large and small particles. There are a few exceptions to this rule, which will be discussed in following sections.

Note that the phenomenon of sublattice delocalization has been quantified using metallicity [101] and occupied volume fraction [151]. However, these metrics are difficult to use for comparison between crystal phases due to convergence and normalization issues. We have previously found that sublattice delocalization is highly tied to small particle diffusion and lattice vibrations quantified as median lattice displacement [151], both of which can be calculated more easily and are experimentally measurable. Therefore, we use these properties as measures of the degree of sublattice delocalization.

9.2.2.1. Phase transitions driven by lattice vibrations. For systems at low values of $n_s:n_l$, we observe a phase transition with increasing T from a localized, low-symmetry lattice to a delocalized, higher-symmetry one, specifically BCT \rightarrow BCC and A20 \rightarrow BCT. This is illustrated by a sharp increase in our two descriptors of sublattice delocalization, the diffusion coefficient (Fig. 9.4(a)) and lattice vibrations (Fig. 9.4(b)). The diffusion constant D is calculated as the slope of the mean squared displacement of the small particles, which increases linearly at long time scales. Lattice vibrations $|R - \langle R \rangle|$ are

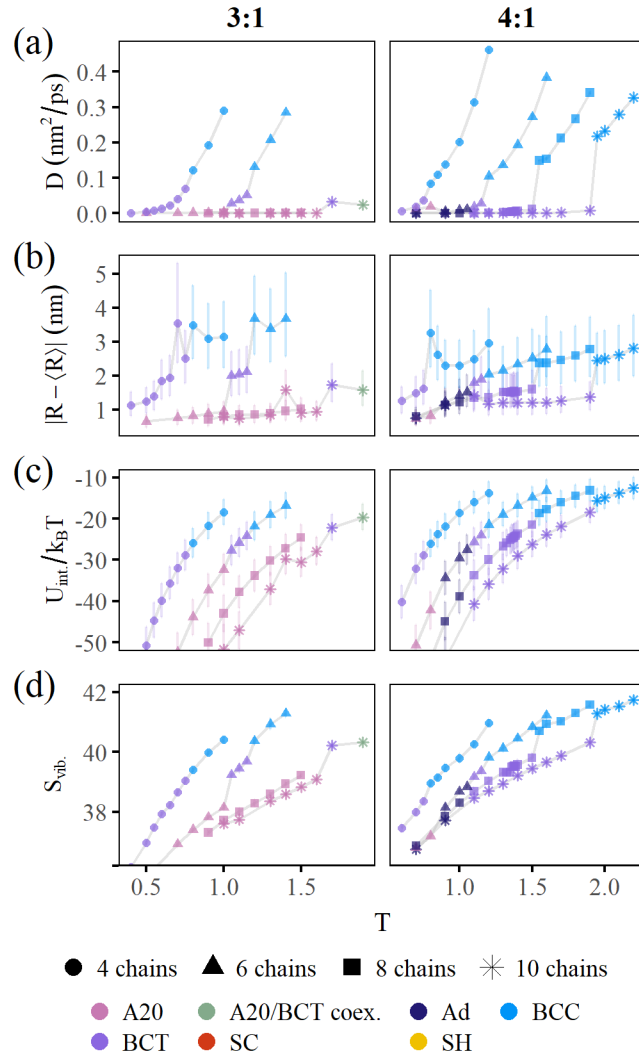


Figure 9.4. Lattice properties of 3:1 and 4:1 systems with 4, 6, 8, and 10 chains per small particle as a function of reduced temperature T (see Section 9.4). All BCT crystals shown have lattice parameters $\frac{c}{a} = 2$ except when the small particles have 4 grafted chains. (a) Diffusion constant, calculated as the slope of the mean squared displacement of the small particles in their linear (diffusive) regime. (b) Lattice fluctuations, quantified as the median displacement of large particles from their mean positions. *Post-publication note: the error bars show the fluctuations' first and third quartile. The fluctuations are not only larger, but have a larger spread, once the crystals have transitioned to BCC.* (c) Average interaction energy $U_{\text{int.}}/k_B T$ per small particle. (d) Average lattice vibrational entropy of the large particles (as they occupy the crystal's lattice points). All quantities show a jump around the phase transition to BCC crystals. Some vary low- T points not relevant to the transition have been removed for clarity.

quantified as the median of the magnitude of the displacement of large particles from their mean positions. Both of these properties increase suddenly at the temperature of a crystal lattice transition, particularly a change to BCC. It is also interesting to note that increasing the number of chains per small particle affects only the temperature at which this change occurs and does not impact the nature of the transition. That indicates that the addition of chains effectively increases the energetic interaction between the small and large particles, stabilizing the lattice against sublattice delocalization and melting. The exception to this is some systems with 4 grafted chains per small particle, which will be discussed later in this section.

The observed transitions appear to be driven by entropy, and this is consistent with the observation that crystals lose energetic interactions while gaining entropy when transitioning to a BCC with a delocalized sublattice. Fig. 9.4(c) shows the average interaction energy per small particle in each system, as a function of T . As temperature increases, the interaction energy tends closer to zero, meaning that energetic interactions become weaker and less favorable. There is also a small jump at the transition to BCC to weaker energetic interactions. This may occur for two reasons. First, the high-temperature BCC lattice is generally less dense and therefore contains weaker interactions than the low-temperature BCT lattice. Additionally, all BCTs shown in Fig. 9.4 with more than 4 grafted chains per small particle have the lattice parameter ratio $\frac{c}{a} = 2$. As indicated in Table 9.1, small particles interact with 4 or 5 neighboring large particles in this type of BCT crystal, but with only 4 in a BCC, so some lose favorable interactions transitioning to a BCC. Finally, delocalized small particles also occupy regions between interstitials

which also decreases the number of interactions with neighboring large particles, as seen in Supplemental Material, Fig. D.3.

Vibrational entropy shows a similar signature. Fig. 9.4(d) shows the lattice (large particle) vibrational entropy per large particle S_{vib} , as a function of T , with clear jumps at the transition temperature. The vibrations of the large particles in a BCT with $\frac{c}{a} = 2$ are more constrained parallel to the (001) planes due to denser packing in those planes. When the crystal transitions to a BCC, the overall density of the system decreases and vibrations can be larger and more isotropic and contribute more to the entropy of the crystal (see the Supplemental Material, Section D.3.2., for details). Other forms of entropy are larger in the BCC phase, as well. Delocalized small particles can occupy a larger volume than localized ones and therefore contribute to a larger entropy. Finally, BCCs with $n_s:n_l = 3:1$ or $4:1$ contain an average of 6 and 4 interstitial vacancies per unit cell, respectively, and therefore their sublattices also have more configurational entropy as not all sublattice sites are filled. This is because, as indicated in Table 9.1, the sublattice of a BCC is filled at $n_s:n_l = 6:1$. However, having more interstitial vacancies should increase the lattice entropy, and the stability of the crystal will be negatively impacted as the melting temperature will be decreased.

The nature of the transition can be further characterized by examining the behavior of the entropy of the system. Here, we consider S_{vib} to be representative of the total system entropy, as we know from previous work that lattice vibrations are highly tied to the other significant contributor to entropy, small particle delocalization, and it is more straightforward to calculate following [162], see the Supplemental Material, Section D.3.6. A first order phase transition occurs at a discontinuity in the first derivative of the free

energy, such as entropy. In Fig. 9.4(d), there is a sharp jump in S_{vib} at the transition to sublattice delocalization when the number of grafted chains per small particle is greater than 4, strongly hinting at a discontinuity that would indicate the presence of a first order phase transition between a localized BCT and a delocalized BCC. This is consistent with Landau *et al.* [163], who state that a first order phase transition is expected between crystal phases when the curve of an appropriate order parameter connecting two phases of differing symmetry is not continuous. While the large particles of a BCT with $\frac{c}{a} = 2$ can change continuously into a BCC, this does not appear to be possible for the small particles, based on their interstitial positions. Therefore, it appears that the transition from BCT with $\frac{c}{a} = 2$ and a localized sublattice to a BCC with a delocalized sublattice is first order. Additionally, estimates of the specific heat capacity corroborate these conclusions and are given in the Supplemental Material, Section D.3.1.

To further confirm the nature of this transition, we look to the phonon-driven IMT in vanadium dioxide (VO_2). The sudden change from an insulating to a conducting state in VO_2 as a function of T is enabled by a phase transition to a more symmetric and entropic crystal phase, in which a strong metallic electron-phonon correlation was detected consistent with a Peierls IMT [161]. Budai *et al.* identified the electron-phonon correlations using the phonon density of states, which narrows towards lower vibrational frequencies in the metallic phase, and anharmonic vibrational modes impeding the filling of lower energy orbitals only in the metallic phase. In our systems that appear to exhibit a first-order sublattice transition, we also find a bias towards lower vibrational modes in crystals with a delocalized sublattice. There is also evidence of anharmonic modes due the expanding lattice parameter of the metallic BCC crystals as a function of temperature. Finally, we

calculate a greater momentum exchange in crystals with a delocalized sublattice, which is most likely due to small particles being more homogeneously distributed throughout the crystal. See the Supplemental Materials for the vibrational density of states (following Dickey *et al.* [164]) and the momentum cross-correlation (following Verdaguer *et al.* and Ishida [165–167]) for the case of a system that exhibits a first-order sublattice transition.

The exception to this discussion is the cases in which the small particles have 4 grafted chains. In those cases, the entropy in Fig. 9.4(d) appears to be continuous but with a change in slope at the transition, indicating a discontinuity in the specific heat capacity, rather than entropy. According to Landau *et al.* [163], a discontinuity in the specific heat is to be expected for continuous phase transitions, specifically between crystal types that can continuously change into one another. While we would need more data to confidently determine the classification of this phase transition, it is also consistent with our intuition that the phase transition for 4 grafted chains per small particle be continuous. This is because the low temperature BCT crystals have $\frac{c}{a} = \sqrt{\frac{2}{3}}$ when the small particles have only 4 grafted chains. As discussed in Section 9.2.1, we believe that small particles with only 4 grafted chains cannot stabilize a BCT with $\frac{c}{a} = 2$. However, for BCT with $\frac{c}{a} = \sqrt{\frac{2}{3}}$, the interstitial sites appear to be such that it is possible for both the small and large particles to continuously change to their BCC lattice sites. Note that the 3:1 system with 4 chains per small particle also transitions through an unclassified BCT; see Fig. D.1 in the Supplemental Material for more information.

Finally, other low-temperature transitions between crystal types are shown in Fig. 9.4, for example $A_{20} \rightarrow \text{BCT}$ and $A_d \rightarrow \text{BCT}$. These transitions exhibit interesting changes in

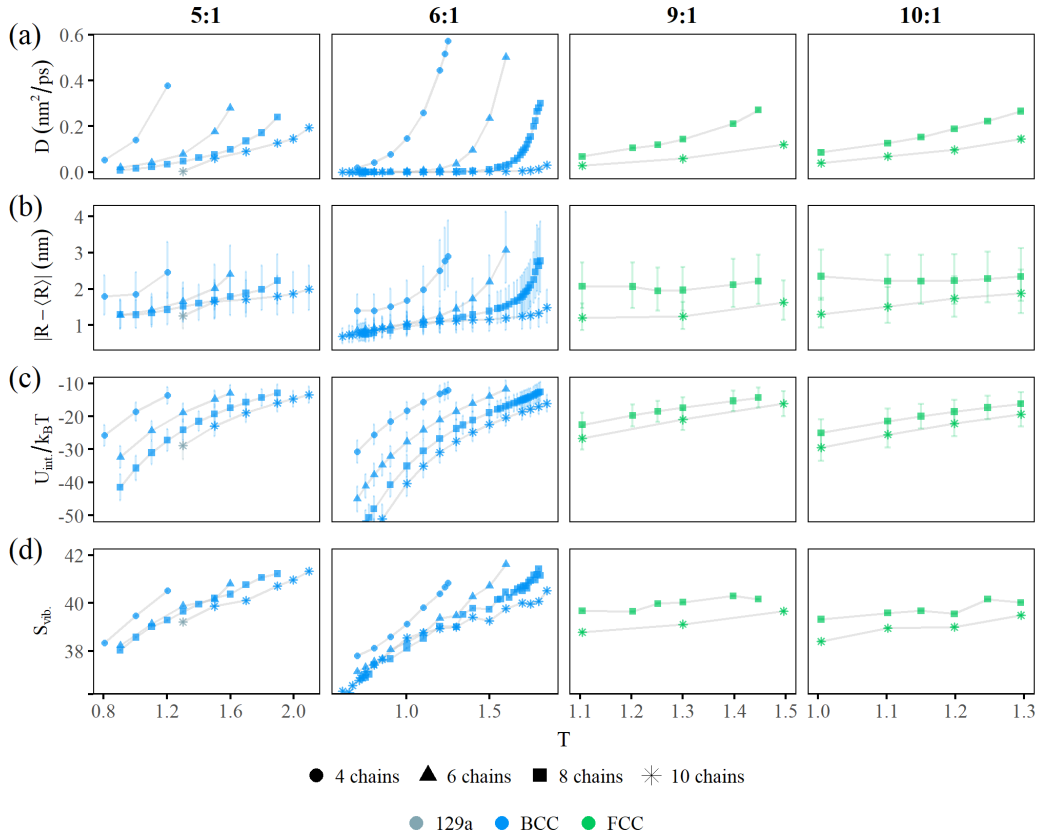


Figure 9.5. Lattice properties of 5:1, 6:1, 9:1, and 10:1 systems with 4, 6, 8, and 10 chains per small particle as a function of reduced temperature T (see 9.4). Data from the 6:1 system is taken from [151] and included for comparison. (a) Diffusion constant. (b) Lattice fluctuations. (c) Average interaction energy $U_{\text{int.}}/k_B T$ per small particle. (d) Average lattice vibrational entropy of the large particles. All show a smooth increase in diffusion and lattice vibrations, indicating a change to delocalization similar to that explored in the 6:1 system.

symmetry; however, we do not study those changes here because they are not accompanied by a change in sublattice delocalization.

9.2.2.2. Smooth change to sublattice delocalization driven by stoichiometry.

At $n_s:n_l$ near the stoichiometric values for BCC crystals (6:1) or FCC crystals (10:1), the transition to delocalization of the small particles is gradual and not a true phase

transition. In these cases, the sublattice delocalizes slowly over a range of temperatures and the large particle lattice never changes structure. This can be seen in Fig. 9.5. Note that, again, as T increases, diffusion and vibrational entropy of the large particles increase at the expense of the magnitude of the interaction energy. We hypothesize that this is because the BCC and FCC lattices are the most symmetric and stable crystals available to systems at lower and higher $n_s:n_l$ ratios, respectively. Specifically, BCC lattices are entropically stabilized at high T [139, 168], so we do not expect a BCC to transition to another crystal with increasing T as long as the number of small particles does not exceed the number of interstitial sites (*i.e.* a number ratio greater than 6:1). At higher number ratios, which would otherwise result in BCC lattices with interstitial defects, FCC crystals are stable simply based on stoichiometry. This will be discussed further in the next subsection.

The 6:1 system is an exemplar of this behavior and has been studied in detail by Lopez-Rios *et al.* [151]. The conclusions of that study were that lattice vibrations and sublattice delocalization are strongly tied, and the temperature of the onset of both is dependent on the number of chains per small particle. We have found this to be true in general for systems that do not exhibit a lattice transition with temperature.

9.2.2.3. Phase transition driven by interstitial defects. For systems with $n_s:n_l = 7:1$ and $8:1$, between the stoichiometric number ratios for BCC and FCC, we observe a stable two-phase coexistence between a localized BCC and delocalized FCC. Coexistence is an indication of a first-order transition between the two phases, and an example is in Fig. 9.6. Experimental evidence of a BCC/FCC mixture in colloidal crystals was reported

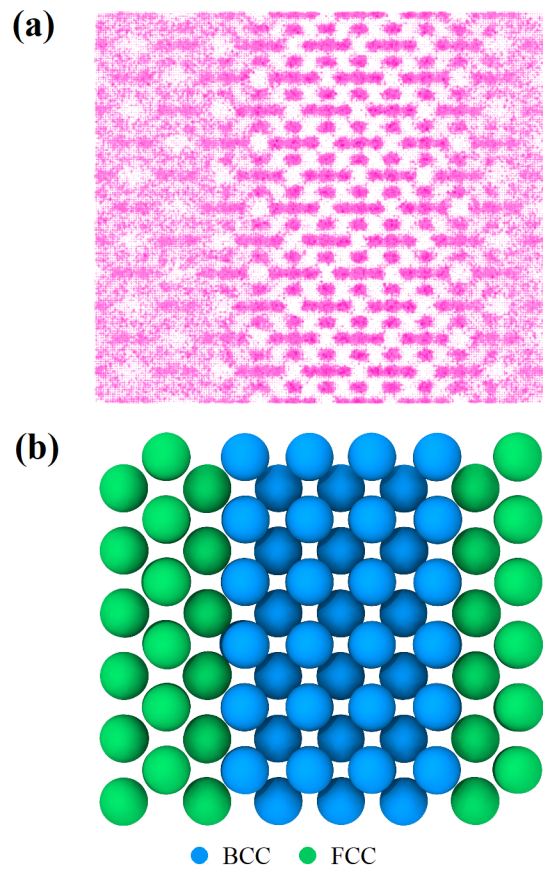


Figure 9.6. BCC/FCC coexistence in a simulation with $T = 1.6$, 8 chains per small particle, and $n_s:n_l = 7:1$. Stable localized BCC and delocalized FCC portions can be seen in (a) a snapshot of the locations of the small particle centers and (b) the averaged positions of the large particles, colored by crystal phase.

at a small particle-large particle number ratio between those required for fully BCC or fully FCC crystal structures [101].

FCC lattices in these systems appear only at high number ratios (7:1, 8:1, 9:1, 10:1), as can be seen in Table 9.1. This is also consistent with Girard *et al.* [101], who observed FCC lattices when the concentration of small particles in solution was high. In our 7:1 and 8:1 systems, the FCC phase appears to be the result of interstitial defect attraction. It has

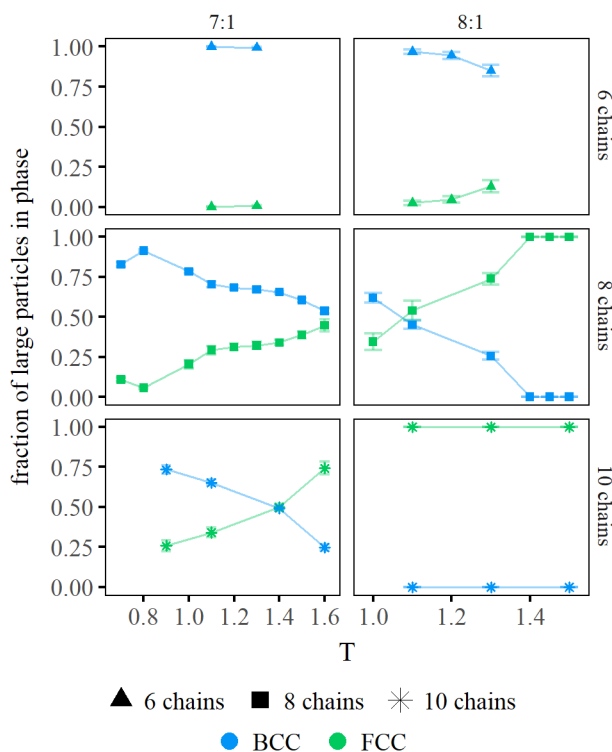


Figure 9.7. Fraction of large particles in the simulation in the BCC and FCC phases for 7:1 and 8:1 systems. The small portion of particles in neither phase is not shown. Increasing both reduced temperature T and number of chains per small particle increases the percentage of the delocalized FCC lattice. These compositions were tested for stability with annealing techniques and at multiple system sizes.

been established that BCC lattices with small particles localized at the usual tetrahedral sites ($n_s:n_l = 6:1$) are stable. At a $n_s:n_l$ of 7:1 or 8:1, however, a fully BCC system would contain 2-4 interstitial defects per unit cell, which is energetically unfavorable. As has been demonstrated by van der Meer *et al.* [112], interstitial defects in colloidal systems show long-range attraction. Therefore, the defects in the BCC system gather when there are strong small particle-large particle interactions (8 and 10 chains per small particle). At very low temperatures, they collect at a grain boundary; a snapshot of this is shown

in the Supplemental Material, Fig. D.8. At moderate and high temperatures, they collect and expand the lattice, resulting in a FCC phase with a delocalized sublattice coexisting with the BCC phase with a localized sublattice. This is consistent with Fig. 9.7, which shows that 8:1 systems have a higher FCC fraction at a given T and number of chains per small particle.

As can also be seen in Fig. 9.7, increasing T results in an increased fraction of the system in the FCC phase. This indicates that the transition between a localized BCC and delocalized FCC is at least in part driven by entropy. Each small particle interacts with 4 large particles in a BCC lattice when localized and only 3 in an FCC lattice (and even fewer when delocalized due to spending less time at energetically favorable sites). Therefore, the transition from the BCC phase to the FCC phase results in an energy penalty, which is compensated for by a gain in entropy in the form of small particle mobility and lattice vibrations in the FCC phase.

Lastly, increasing the number of chains per small particle results in a higher FCC fraction, which deviates from the general rule that adding chains simply increases lattice stability. We hypothesize that this is due to the difference in the unit cell energy landscape between the BCC and FCC lattices. The energy landscape of the FCC is overall shallower and more homogeneous than that of the BCC, as there is little overlap between the attractive regions around the large particles (see the Supplemental Material, Table D.1, for comparisons). In contrast, the BCC unit cell energy wells are deep and localized in spaces between large particles. Therefore, it may be that small particles interact favorably only with FCC energy landscapes when there are more chains and when those chains are configured more isotropically. This may explain why size-asymmetric binary colloidal

systems composed of spherical particles have only seen FCC lattices [111, 115] and why other crystals such as BCC have been observed only with the existence of flexible chains on the small particles [101, 151].

9.2.3. Stability as a function of number ratio $n_s:n_l$

Overall, crystals are more stable and have lower sublattice delocalization when small particles saturate their interstitial sites. This is highlighted in Fig. 9.8 and Fig. 9.9, which show diffusion and lattice vibrations as a function of $n_s:n_l$ for systems with different T -chain number combinations. For clarity, data is separated by whether there is a crystal phase transition as a function of $n_s:n_l$. A minimum in both quantities appears at 3:1, 4:1, and 6:1 (for the 3:1, 4:1 and 6:1 systems that form BCC, A20 and BCT lattices with a fully saturated sublattice). Meanwhile, the 5:1 (BCC crystals) and 9:1 (FCC crystals) ratios both contain inherent vacancies that diffuse, since BCC and FCC interstitials are fully occupied at 6:1 and 10:1 ratios, respectively. Additionally, according to Table 9.1, FCC lattices and their interstitials are less tightly bound than in BCC lattices and therefore should show more delocalization at a given T . It is not included, but lattice vibrations also show minima at 3:1 and 6:1 ratios.

The predominant appearance of BCC lattices over the entire phase space explored may be due to their stabilization by entropy [139]. Their lattice vibrations are isotropic and this garners them additional structural stability as a function of temperature that enables a larger degree of sublattice delocalization than other lattices. For similar reasons, BCC lattices have been suggested as optimal superionic conductors in atomic systems [123].

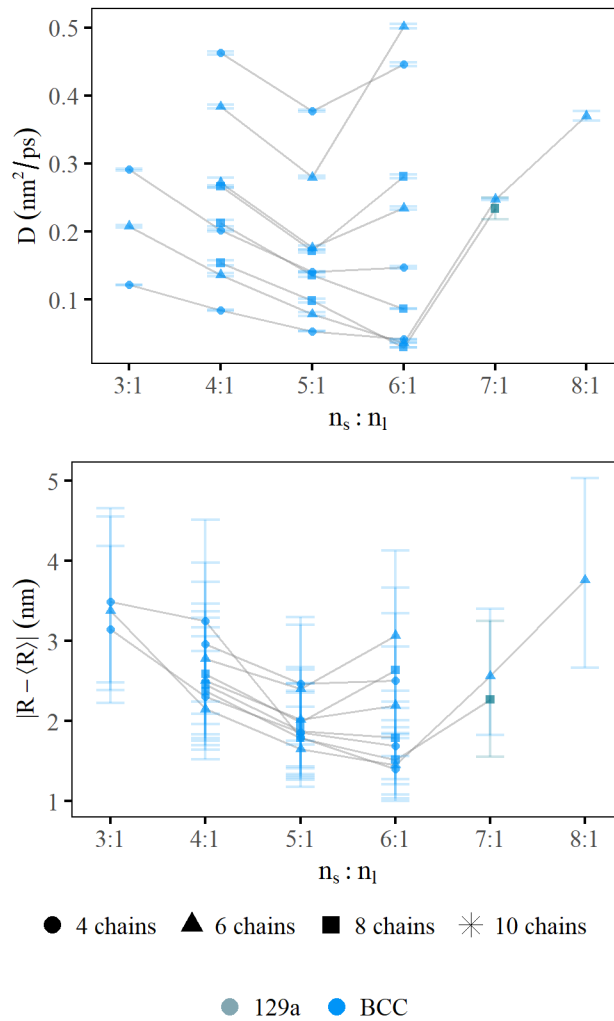


Figure 9.8. (a) Diffusion coefficients D and (b) lattice vibrations as a function of $n_s:n_l$ for simulation groups that do not exhibit a phase transition. Both D and lattice vibrations both show a minimum at 6:1, similar to the metallicity found by Girard *et al.* [101]. Lines connect points with the same value of T and number of chains, and lines are not drawn between non-adjacent points, or if any number of chain- T combination has fewer than 3 data points. Though it is not visually depicted, higher values of D and lattice vibrations for a given number of chains correspond to higher temperatures. *Post-publication note:* The error bars here show the first and third quartiles of D and $|R - \langle R \rangle|$.

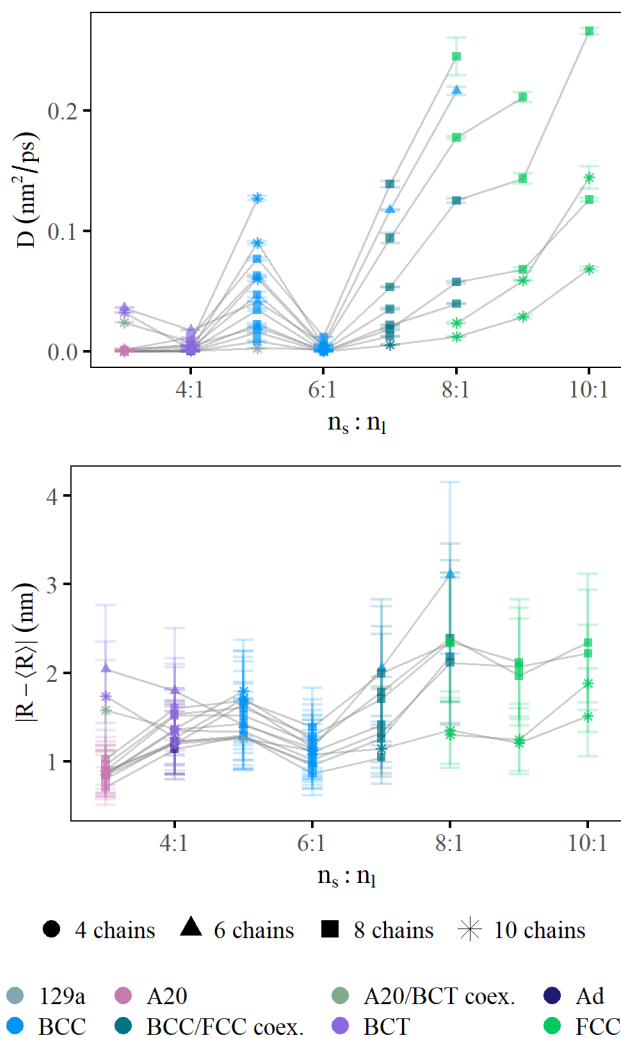


Figure 9.9. (a) Diffusion coefficients D and (b) lattice vibrations as a function of $n_s:n_l$ for simulation groups that do exhibit a phase transition. Both quantities show minima at number ratios corresponding to compound values for BCC and A20 crystals. Lines connect points with the same value of T and number of chains, and lines are not drawn between non-adjacent points, or if any number of chain- T combination has fewer than 3 data points. Though it is not visually depicted, higher values of D and lattice vibrations for a given number of chains correspond to higher temperatures. *Post-publication note: The error bars here show the first and third quartiles of D and $|R - \langle R \rangle|$.*

9.3. Discussion and conclusions

In summary, highly size-asymmetric binary colloids assemble into a variety of crystals that exhibit varying levels of sublattice delocalization. For temperatures at which the sublattice is localized, the crystal structure is determined by energetic interactions between the small and large particles. Crystals with a lower number ratio $n_s:n_l$ form lower-symmetry crystals whose unit cell potential energy landscapes contain many deep wells. As $n_s:n_l$ increases, crystals become more symmetric and the wells become shallower. As a function of T , we observe different types of entropically driven transitions to sublattice delocalization. In some cases, this transition occurs along with a symmetry change of the large particles, always from a lower-symmetry lattice to a higher-symmetry lattice containing more interstitial vacancies. In others, when the lattice is in a cubic configuration (these are entropically stabilized) or already contains inherent vacancies, there is not a phase transition to sublattice delocalization but rather a smooth change.

Additionally, we observe the appearance of different crystal lattices as a function of $n_s:n_l$ at constant T . This is consistent with experiments using DNA functionalized NPs [101, 152] even though hybridization DNA chemistry employed in those studies complicates experiments by including the presence of non-hybridized DNA chains that could act like depletant particles [101, 152]. In particular, the transition we found from BCT to BCC as $n_s:n_l$ increases agrees with Fig. 3 of Cheng *et al.* [152]; note that in [152], "valency" is the number of linkers per small particle and not the number ratio of small ("electron equivalent") particles to large particles as it was defined in [154] and in Fig. S29 in the SI of [101].

We report minima as a function of lattice vibrations and the diffusion constant of the small particles as a function of $n_s:n_l$ in Fig. 9.9 and Fig. 9.8. It is tempting to compare these minima to the minima in metallicity identified by Girard and Olvera de la Cruz [101], which were found for each crystal phase (BCC, FCC, and Frank-Kasper A15) and which correspond to the compound value of $n_s:n_l$ for that phase. The behavior of the lattice vibrations and diffusion constants is similar, indicating that these reflect the same underlying phenomenon. However, we found that it is difficult to compare metallicity values between phases due to normalization and numerical convergence issues; using the more physically measurable values resolves these problems. Plotting indicators of sublattice delocalization in multiple phases on the same axis allows us two additional insights. First, this enables us to compare behavior between phases. We find that there are still minima at the saturation values for some lattices (A20, BCT, and BCC), but that the minimum for FCC found in [101] does not appear because competition between BCC and FCC phases allows for a coexistence not seen in [101]. Second, we see that the studied assemblies are generally more stable in the form of a BCC lattice, whether their sublattice is localized or delocalized. Most of the low-symmetry crystal phases transition to BCC at high temperatures, and BCC only fully transitions to FCC when the number of interstitial defects is very high. BCC's greater structural stability is consistent with observations that BCC crystals are entropically stabilized near their melting point in colloidal assemblies [139] (even without a sublattice). For these systems, the result of BCC lattice stability is that these crystals can maintain a delocalized sublattice for a wider range of temperatures than other crystals. Additionally, Wang *et al.* predicted that superionic materials with a BCC structure should exhibit the highest conductivity [123],

which is of particular interest for applications in solid-state batteries. Our results agree with this for the case of NPs and confirm the stability of BCC colloidal crystals with delocalized sublattices.

It is intriguing to find similar behavior at multiple length scales, from sublattice melting in superionic materials to the insulator-metal transition (IMT) in inorganic materials to sublattice delocalization in colloidal binary crystals. Although colloidal systems are more flexible and tunable due to the lack of any sort of charge neutrality constraint on composition, they exhibit similarities to superionic materials in both structure and dependence on lattice vibrations, explored previously by Lopez-Rios, *et al.* [151]. There are also structural and delocalization transition analogs between colloidal crystals and materials exhibiting an IMT. For example, at low T and 4:1 number ratio, crystal phases resemble the actinide crystal structures, where increasing the number of chains per small particle is analogous to increasing the atomic number. Systems with 4, 6, and 8 chains per small particle assemble into BCT ($c/a = \sqrt{2/3}$), A20, and A_d lattices, which have the same symmetry as protactinium, α -uranium, and β -neptunium, respectively. Increasing T of these and other systems, we observe a transition to sublattice delocalization strongly driven by lattice vibrations. When accompanied by a change of lattice symmetry, this resembles a Peierls IMT, a transition driven by strong correlations between phonons and metallic electrons. For colloidal crystals, this can be thought of as a continuous pumping of momentum of the vibrating large particles to the diffusing small particles. As crystals become more symmetric, lower vibrational frequencies are available, which prolongs the exchange of momentum between the two species given their large vibrational wavelengths. Such tunability as a function of T makes these colloidal crystals possible candidates for

exploration as colloidal photonic crystals [93, 169]. There are other types of IMT, such as the Mott IMT, which is driven by the interactions and correlations between the smaller species. We observe stronger sublattice localization as a function of $n_s:n_l$ with a greater number of grafted chains, which is similar to the behavior of metallicity [154]. This may be seen as a Mott-like transition, where the delocalized lattice may be suppressed by the addition of grafted chains on the small particles as was alluded by Girard *et al.* [154]. However, in some cases, the addition of grafted chains may also change the crystal lattice structure, which complicates this analogy.

There is still more to explore. It is possible that by including the deformability of the large particles, one might increase the range of accessible phases such as the Frank Kasper A15 phase [101]. Furthermore, given that lattice vibrations drive the transition to sublattice delocalization and between host lattices, it would be interesting to consider how impinging acoustic waves or acoustic shock waves would affect the properties of these colloidal crystals for further applications.

9.4. Simulation methods

In the model, as described in Fig. 9.1 (and also in [151]), we change the temperature T , the number of chains per small particle, and the small particle-large particle number ratio $n_s:n_l$. Temperature T is expressed in reduced units, such that $T = \frac{k_B T'}{\varepsilon}$, where T' is the input temperature and ε is the energy unit of the simulation, in our case $T = 1 = 5/3$ kJ/mol.

All simulations were conducted at constant number of particles N , temperature T , and pressure P . The pressure P was the same in all simulations, $P = 2$ Pa (approximately

2% of atmospheric pressure). Simulations at low P simplify the possible contributions to the formation and stability of a crystal such that only two terms remain, energetic and entropic. The pair potential interactions within our model arise from an attractive Gaussian potential between large particles and the termini of the grafted chains $U_{\text{Gaussian}}(r)$ (Eq. 9.1), as well as excluded volume interactions amongst all particles, modeled using the Weeks-Chandler-Andersen (WCA) potential $U_{\text{WCA}}(r)$ (Eq. 9.2). The grafted chains are bonded with harmonic potentials, and no angle or dihedral potential is employed. We also used the HOOMD-blue `xplor` option which prevents artificial discontinuities in $U_{\text{Gaussian}}(r)$ as it decays to zero. Parameters used are shown in Table 9.2.

$$(9.1) \quad U_{\text{Gauss}}(r) = -\varepsilon e^{-\frac{1}{2}\left(\frac{r}{\sigma_{\text{gauss}}}\right)^2} \quad \text{for } r \leq r_{\text{cutoff}}$$

$$(9.2) \quad U_{\text{WCA}}(r) = 4 \left(\left(\frac{\sigma}{r} \right)^{12} - \left(\frac{\sigma}{r} \right)^6 \right) - 4 \left(\left(\frac{\sigma}{2^{1/6}\sigma} \right)^{12} - \left(\frac{\sigma}{2^{1/6}\sigma} \right)^6 \right) \quad \text{for } r \leq 2^{1/6}\sigma$$

where $\sigma = R_A + R_B$ is the sum of the radii of the interacting species.

All simulations were initiated with $6 \times 6 \times 6$ unit cells in the simulation box with either an FCC or BCC lattice with lattice parameter $a = 60$ nm. They were all energetically and thermally equilibrated using NVE integration and later Langevin integration, respectively, then depressurized to their final pressure. This sequence lasted 312 ns. Finally, the simulations were run at their final pressure $P = 2$ Pa for at least 8.44 μs , the first 1.38 μs of which was considered an equilibration period and not used for analysis. Simulation code is available upon request.

Parameter	Value
$R_{\text{large particle}}$	10.5 nm
$R_{\text{small particle center}}$	1.0 nm
$R_{\text{chain bead}}$	1.0 nm
$R_{\text{interactive chain end bead}}$	0.5 nm
ε	70 kJ/mol
σ_{gauss}	4.8 nm
R_{cutoff}	8.4 nm
# non-interactive beads/chain	3

Table 9.2. Parameters used in the present study.

To determine the crystal phase resulting from a simulation of a given set of parameters (T , $n_s:n_l$, number of grafted chains, and initial configuration), we analyzed the pair correlation function ($g(r)$) of the large particles. See the Supplemental Material, Section D.1.1. for details.

While exploring parameter space by changing $n_s:n_l$, it is important to ensure that the crystal configurations we are reporting are equilibrium configurations. To that end, we initialized many $n_s:n_l$ - T -chain parameter combinations in multiple ways, *i.e.* BCC and FCC with an unphysically large lattice parameter, about 3 – 5 times any lattice parameter from an equilibrated lattice structure of this study. If both simulations equilibrated to the same crystal configuration, we considered that configuration to be the lowest free energy state and selected only one to include for analysis in our final set. If the simulations had different results, we annealed both using various techniques described in the Supplemental

Material, Section D.1.1. until both equilibrated to the same configuration. Note that a simulation initialized as an FCC has twice as many particles as one initialized as a BCC (because the FCC unit cell contains twice as many particles), so this procedure of different initialization is also a test for finite size effects.

Sometimes, this annealing process resulted in one version of the simulation with a bulk monocrystal and another in a polycrystal with grain boundaries. It has been observed experimentally that annealing polycrystalline colloids does not always results in a monocrystalline phase, possibly because of the similarity between the melting temperature and the temperature required to remove grain boundaries (see the Supplementary Discussion of [170]). If, after a few rounds of annealing, the two did not converge to exactly the same configuration, we chose to use the simulation resulting in the monocrystal. This is because polycrystals are always higher energy than monocrystals, and the purpose of the current study is the understand bulk crystals based on different parameter sets. Including polycrystals and the added complexity of grain boundaries is outside of these bounds.

Finally, finite-size effects are often associated with seeing two-phase coexistence in an NPT simulation. To test whether simulation size played a role in the existence of two phase in our 7:1 and 8:1 systems, we ran and annealed all points of 7:1 and 8:1 systems in at least two initial configurations (usually BCC and FCC). Simulations of different sizes resulted in very similar BCC to FCC ratios, which are shown in Fig. 9.7. We tested one system (7:1, 8 chains per small particle, $T^* = 1.3$) with 432, 864, and 2000 large particles and saw roughly the same BCC to FCC ratio in all three simulations.

System topology for the simulation was built using Hoobas [132]. Simulations were run with Hoomd-blue [130, 171] and analyzed using MDAnalysis [133, 134]. Images were created with Mayavi [137] (Fig. 9.1 and 9.6(b)) and OvitoVIToteStukowski2010 (Fig. 9.1 and Fig. 9.6(a)). The $g(r)$ functions for determining crystal type were calculated using VMD [135], and some crystal structure determination was done using pymatgen [172] and the AFLOW database [173, 174].

See Supplemental Material at [URL] for all simulation details. An interactive version of the phase diagrams in Fig. 9.2 with pair correlation functions can be found at https://aliehlen.github.io/phase_diagrams/.

Acknowledgements: The authors would like to thank Martin Girard for useful discussions and review of the work. This work was supported by the Center for Bio-Inspired Energy Science, an Energy Frontier Research Center funded by the US Department of Energy, Office of Science, Basic Energy Sciences under Award DE-SC0000989. H.L.-R. thanks a fellowship from Fulbright-Garcia Robles and A.E. thanks a fellowship from the National Science Foundation under grant DGE-1450006. M.O.d.l.C. thanks the computational support of the Sherman Fairchild Foundation.

A.E. and H.L.-R. contributed equally to this work.

CHAPTER 10

Conclusion: outlook and future directions

Since the publication of these two articles presented in Chaps. 8 and 9, there has been interesting development in this area. Others in our group have explored this problem with incorporated electrostatic interactions and found FCC structures that did exhibit a sharp phase transition for specific small to large particle number ratios [115, 175, 176]. Other simulations that use different models have since found similar delocalization in both charged and uncharged systems [177–179], so the evidence is yet stronger that classical delocalization is a generalizable phenomenon. Later experimental and computational work found more colloidal crystals with exhibiting delocalized behavior [180], including SC and BCT structures we predicted.

With the possibility of functionalizing self-assembling nanoparticles of so many materials [92] and shapes [181]—even proteins [182] and core-less functionalized DNA "nanoparticles" [152]—the potential for variety in self-assembled structure and function is wide. It would be interesting to explore other applications: if the small and large particles are each stages in enzymatic or catalytic reactions, then varying the conditions of self-assembled structures will change the transport of one between the other, or the symmetry of the assembly and therefore the number of neighbors each particle is near. From a simulation standpoint, there would be value in a more rigorous focus on equal chemical potential models, where the bulk colloidal crystal assembly is simulated in contact with an actual bulk solvent. This would be useful for closer alignment with experimental conditions.

Part 4

Conclusion

CHAPTER 11

Review and outlook

Throughout this dissertation, we have seen a variety of ways in which nanoscale objects—ions and their larger, more visible counterparts, nanoparticles—respond to their environment and thereby change it.

As has been explored in Chapt. 3 and 4, ions in strong confinement will pack differently due to steric and electrostatic interactions in the presence of confining walls. The polarizability of the confining walls due to a dielectric mismatch will mediate ion-ion and ion-water interactions, which results in both shifting ion density to or from the walls and changing how strongly ions interact with each other. These changes affect the charge density near the walls and the ionic current under an applied field: ions are closer to the walls and move faster when confined by conductors and high dielectric constant materials than when confined by low dielectric constant materials. In electric double layer supercapacitors, this will change the capacitance of the device because the distance between the ion layer and the wall will impact its energy storage potential. In an electric double layer transistor or polymeric-based mixed ionic-electronic devices, proximity of the ion to the wall or polymer will change how efficiently the presence of ions modulates the electronic conduction. Additionally, some of these devices are more efficient when they are made with rough surfaces such as activated carbon or curved graphene, because an increased surface area enables more ion-surface interaction. We saw in Chapt. 5 that the curvature of a surface will change how the ions are attracted to or repelled from the surface,

especially in the presence of an external electric field. As we continue to develop devices that rely on the presence of ions to "dope" a nearby wall with conducting electrons, we will have to understand the interaction between the wall and the ions in more detail to properly predict response time, energy storage, ionic-electronic coupling, and much more.

We can dream bigger. Taking advantage of the feedback between polarizable interfaces and nearby ions, one can imagine the design of all sorts of interesting devices. Robin, et al. have already shown that a confined electrolyte can have memory of previously applied external electric fields [5, 63]. This is because the ion density changes the electrostatic environment, which impacts ion-ion interactions, which in turn changes ion density—and all this is magnified in strong confinement by a dielectric material. They have shown that these systems can be connected into a rudimentary "neuron," which opens the possibility for building networks. There are also materials whose dielectric constant can change in response to external fields [65] and possibly light, which could be used to make these devices' ionic currents switchable.

There is quite a bit of interesting work to do with the dielectric response of curved surfaces. As we saw in Chapt. 5, a sinusoidal surface geometry will result in a sinusoidal geometry of induced charge, which means that a sinusoidal induced electric field is caused by a constant external one. The addition of ions to the system can then result in charge patterning on the surface. Ions may also move differently through corrugated channels, meaning the height of one or both channel walls varies sinusoidally. It will be interesting to understand how the interplay between induced charge enhancement or dampening (based on the sinusoidal surface geometry), geometrical constraints, and ion-ion interaction mediation. Further than this, ionic current through a corrugated channel due to a transverse

applied electric field (along the channel) may be switched on or off by a perpendicular electric field, which would push ions into troughs. When all this is understood, one can imagine designing a device in which the ions in one channel arrange and produce a net electric field that impact the ions in another channel—but this is far outside the scope of the current work. A final, toy idea would be this: a sort of "Brownian ratchet," in which ions are allowed to diffuse over a corrugated sawtooth-patterned surface and subjected to a pulsed perpendicular electric field. The periodic pushing of ions into the sawtooth troughs after intervals of diffusion could result in a net motion of both ion species in one direction. The question would be: could this effect be enhanced by the inclusion of dielectric mismatch? Could it be combined with a transverse electric field to switch whether ions are transported in "current mode" (cations in one direction, anions in the other) or "directed diffusion mode" (all ions move in the same direction)?

The functionalized nanoparticles in Chapt. 8 and 9 react to a crowded environment by assembling into ordered structures. At low temperatures, the attraction between our small and large particles results in crystals of as high symmetry as can host the available small particles. When the number ratio between small particles and large particles is varied, many lattices appear: BCT ($c = 2a$), Ad, and A20 (low ratios), BCC (mid ratios), and FCCs (high ratios). Lower-symmetry crystals are seen at lower number ratios because they are energetically favorable—each small particle can interact with more large particle nearest neighbors. At higher ratios, the number of small particles is larger than the number of favorable interstitial sites in the low-symmetry crystals, which results in higher-symmetry lattices with less favorable interstitial sites.

Then, when the temperature is increased, many of these crystals will delocalize: the small particles leave their fixed interstitial sites and start to roam the lattice, while still holding it together. Meanwhile, the large particle lattice expands and is host to larger vibrations. However, different crystals delocalize differently: symmetric, cubic lattices BCC and FCC show a smooth change to delocalization, as no phase transition is needed for those lattices to host the vibrations required for small particle delocalization. Lower-symmetry lattices (number ratios of 3:1 and 4:1), however, are too strongly bound together; at a certain temperature, these lattices will transition to BCCs and then show signs of delocalization. For number ratios of 7:1 and 8:1, which exhibit two-phase coexistence between a localized BCC and a delocalized FCC, the relative ratios of these phases change with temperature. Both of these latter categories are examples of first order phase transitions.

In part, these findings are interesting because they may shed some light on the sublattice melting transitions of superionic materials. The idea that nanoparticle assemblies can be used as analogs to atomic systems is intriguing [105], as is the ability to see a classical equivalent to atomic quantum transitions. We must better understand these classical transitions by further narrowing which nanoparticle properties allow for delocalization to occur at all. Additionally, the work presented here was all based on bulk crystal simulation, but much more should be done to understand how contact with bulk solution of small particles would impact results.

Finally, the ability to tailor properties of functionalized nanoparticles by changing their functionalizing polymers as well as their core materials can be combined with the findings that delocalization is not specific to DNA- and gold-based system. If the cores

are catalyzing materials or enzymes, is it possible to control the speed of a reaction, or the spread of its products, by controlling the motion of small particles via delocalization? Or, if perhaps the small particles are functionalized with DNA to be delivered to or removed from the large particles, could enhancing or suppressing delocalization could control a particular biochemical process?

In all cases, there is substantial simulation work to do to continue developing understanding of these systems. And, while some of this work has focused purely on one type of interaction in a complex system (i.e. specifically the impact of surface polarization on ionic motion through a channel) it would be worth pursuing experimental verification of these systems, as finer control of 2D materials and associated channels continues to be refined.

Bibliography

- [1] T. Dudev and C. Lim, “Competition among metal ions for protein binding sites: determinants of metal ion selectivity in proteins”, *Chemical Reviews* **114**, Publisher: American Chemical Society, 538–556 (2014).
- [2] C. Liu, Z. Yu, D. Neff, A. Zhamu, and B. Z. Jang, “Graphene-based supercapacitor with an ultrahigh energy density”, *Nano Letters* **10**, Publisher: American Chemical Society, 4863–4868 (2010).
- [3] S. Z. Bisri, S. Shimizu, M. Nakano, and Y. Iwasa, “Endeavor of iontronics: from fundamentals to applications of ion-controlled electronics”, *Advanced Materials* **29**, Publisher: John Wiley & Sons, Ltd, 1607054 (2017).
- [4] B. D. Paulsen, K. Tybrandt, E. Stavrinidou, and J. Rivnay, “Organic mixed ionic–electronic conductors”, *Nature Materials* **19**, Publisher: Nature Publishing Group, 13–26 (2020).
- [5] P. Robin, N. Kavokine, and L. Bocquet, “Modeling of emergent memory and voltage spiking in ionic transport through angstrom-scale slits”, *Science* **373**, Publisher: American Association for the Advancement of Science, 687–691 (2021).
- [6] A. Zangwill, *Modern electrodynamics* (Cambridge University Press, 2013).
- [7] T. D. Nguyen, H. Li, D. Bagchi, F. J. Solis, and M. Olvera de la Cruz, “Incorporating surface polarization effects into large-scale coarse-grained molecular dynamics simulation”, *Computer Physics Communications* **241**, 80–91 (2019).
- [8] A. P. Thompson, H. M. Aktulga, R. Berger, D. S. Bolintineanu, W. M. Brown, P. S. Crozier, P. J. in ’t Veld, A. Kohlmeyer, S. G. Moore, T. D. Nguyen, R. Shan, M. J. Stevens, J. Tranchida, C. Trott, and S. J. Plimpton, “LAMMPS - a flexible simulation tool for particle-based materials modeling at the atomic, meso, and continuum scales”, *Computer Physics Communications* **271**, 108171 (2022).
- [9] Y. Jing, V. Jadhao, J. W. Zwanikken, and M. Olvera de la Cruz, “Ionic structure in liquids confined by dielectric interfaces”, *Journal of Chemical Physics* **143**, Publisher: American Institute of Physics Inc., 194508 (2015).
- [10] J. W. Zwanikken and M. Olvera de la Cruz Monica, “Tunable soft structure in charged fluids confined by dielectric interfaces”, *Proceedings of the National Academy of Sciences of the United States of America* **110**, 5301–5308 (2013).
- [11] D. Bagchi, T. D. Nguyen, and M. Olvera de la Cruz, “Surface polarization effects in confined polyelectrolyte solutions”, *Proceedings of the National Academy of Sciences* **117**, Publisher: National Academy of Sciences, 19677–19684 (2020).

- [12] A. P. dos Santos and Y. Levin, “Electrolytes between dielectric charged surfaces: simulations and theory”, *The Journal of Chemical Physics* **142**, Publisher: AIP Publishing LLC/AIP Publishing, 194104 (2015).
- [13] A. P. dos Santos, M. Girotto, and Y. Levin, “Simulations of coulomb systems confined by polarizable surfaces using periodic green functions”, *The Journal of Chemical Physics* **147**, Publisher: AIP Publishing LLC/AIP Publishing, 184105 (2017).
- [14] A. Schlaich, D. Jin, L. Bocquet, and B. Coasne, “Electronic screening using a virtual thomas–fermi fluid for predicting wetting and phase transitions of ionic liquids at metal surfaces”, *Nature Materials* **21**, Number: 2 Publisher: Nature Publishing Group, 237–245 (2022).
- [15] H. S. Antila and E. Luijten, “Dielectric modulation of ion transport near interfaces”, *Physical Review Letters* **120**, Publisher: American Physical Society, 135501 (2018).
- [16] M. Ma, Z. Xu, and L. Zhang, “Ion transport in electrolytes of dielectric nanodevices”, *Physical Review E* **104**, Publisher: American Physical Society, 035307 (2021).
- [17] N. Kavokine, P. Robin, and L. Bocquet, “Interaction confinement and electronic screening in two-dimensional nanofluidic channels”, *The Journal of Chemical Physics* **157**, 114703 (2022).
- [18] B. Duplantier, R. E. Goldstein, V. Romero-Rochn, and A. I. Pesci, “Geometrical and topological aspects of electric double layers near curved surfaces”, *Physical Review Letters* **65**, Publisher: American Physical Society, 508–511 (1990).
- [19] F. J. Solis and M. Olvera de la Cruz, “Pimples reduce and dimples enhance flat dielectric surface image repulsion”, *The Journal of Chemical Physics* **155**, Publisher: AIP Publishing LLC/AIP Publishing, 104703 (2021).
- [20] H. Wu, H. Li, F. J. Solis, M. Olvera De La Cruz, and E. Luijten, “Asymmetric electrolytes near structured dielectric interfaces”, *The Journal of Chemical Physics* **149**, Publisher: AIP Publishing LLC/AIP Publishing, 164701 (2018).
- [21] Y. Levin, “Polarizable ions at interfaces”, *Physical Review Letters* **102**, Publisher: American Physical Society, 147803 (2009).
- [22] B. Coquinot, L. Bocquet, and N. Kavokine, “Quantum feedback at the solid-liquid interface: flow-induced electronic current and its negative contribution to friction”, *Physical Review X* **13**, Publisher: American Physical Society, 011019 (2023).
- [23] L. Fumagalli, A. Esfandiar, R. Fabregas, S. Hu, P. Ares, A. Janardanan, Q. Yang, B. Radha, T. Taniguchi, K. Watanabe, G. Gomila, K. S. Novoselov, and A. K. Geim, “Anomalously low dielectric constant of confined water”, *Science* **360**, Publisher: American Association for the Advancement of Science, 1339–1342 (2018).
- [24] C. Zhang, F. Gygi, and G. Galli, “Strongly anisotropic dielectric relaxation of water at the nanoscale”, *Journal of Physical Chemistry Letters* **4**, Publisher: American Chemical Society, 2477–2481 (2013).

- [25] F. Jiménez-Ángeles, K. J. Harmon, T. D. Nguyen, P. Fenter, and M. Olvera de la Cruz, “Nonreciprocal interactions induced by water in confinement”, *Physical Review Research* **2**, Publisher: American Physical Society, 043244 (2020).
- [26] John David Jackson, *Classical electrodynamics (third edition)* (1999).
- [27] R. B. Schoch, J. Han, and P. Renaud, “Transport phenomena in nanofluidics”, *Reviews of Modern Physics* **80**, Publisher: American Physical Society, 839–883 (2008).
- [28] J.-L. Barrat and L. Bocquet, “Large slip effect at a nonwetting fluid-solid interface”, *Physical Review Letters* **82**, Publisher: American Physical Society, 4671–4674 (1999).
- [29] S. Buyukdagli, “Nanofluidic charge transport under strong electrostatic coupling conditions”, *The Journal of Physical Chemistry B* **124**, Publisher: American Chemical Society, 11299–11309 (2020).
- [30] A. K. Geim and I. V. Grigorieva, “Van der waals heterostructures”, *Nature* **499**, Number: 7459 Publisher: Nature Publishing Group, 419–425 (2013).
- [31] G. Algara-Siller, O. Lehtinen, F. C. Wang, R. R. Nair, U. Kaiser, H. A. Wu, A. K. Geim, and I. V. Grigorieva, “Square ice in graphene nanocapillaries”, *Nature* **519**, Number: 7544 Publisher: Nature Publishing Group, 443–445 (2015).
- [32] S. Han, M. Y. Choi, P. Kumar, and H. E. Stanley, “Phase transitions in confined water nanofilms”, *Nature Physics* **6**, Number: 9 Publisher: Nature Publishing Group, 685–689 (2010).
- [33] N. Giovambattista, P. J. Rossky, and P. G. Debenedetti, “Phase transitions induced by nanoconfinement in liquid water”, *Physical Review Letters* **102**, Publisher: American Physical Society, 050603 (2009).
- [34] T. Mouterde, A. Keerthi, A. R. Poggioli, S. A. Dar, A. Siria, A. K. Geim, L. Bocquet, and B. Radha, “Molecular streaming and its voltage control in ångström-scale channels”, *Nature* **567**, Number: 7746 Publisher: Nature Publishing Group, 87–90 (2019).
- [35] K. S. Krishnan and N. Ganguli, “Large anisotropy of the electrical conductivity of graphite”, *Nature* **144**, Number: 3650 Publisher: Nature Publishing Group, 667–667 (1939).
- [36] J. Wang, F. Ma, and M. Sun, “Graphene, hexagonal boron nitride, and their heterostructures: properties and applications”, *RSC Advances* **7**, Publisher: Royal Society of Chemistry, 16801–16822 (2017).
- [37] R. Bessler, U. Duerig, and E. Koren, “The dielectric constant of a bilayer graphene interface”, *Nanoscale Advances* **1**, Publisher: Royal Society of Chemistry, 1702–1706 (2019).
- [38] J. I. Siepmann and M. Sprik, “Influence of surface topology and electrostatic potential on water/electrode systems”, *The Journal of Chemical Physics* **102**, 511–524 (1995).

- [39] S. K. Reed, O. J. Lanning, and P. A. Madden, “Electrochemical interface between an ionic liquid and a model metallic electrode”, *The Journal of Chemical Physics* **126**, 084704 (2007).
- [40] V. Jadhao, F. J. Solis, and M. Olvera de la Cruz, “Simulation of charged systems in heterogeneous dielectric media via a true energy functional”, *Physical Review Letters* **109**, Publisher: American Physical Society, 223905 (2012).
- [41] V. Jadhao, F. J. Solis, and M. Olvera de la Cruz, “A variational formulation of electrostatics in a medium with spatially varying dielectric permittivity”, *The Journal of Chemical Physics* **138**, Publisher: American Institute of PhysicsAIP, 054119 (2013).
- [42] G. M. Torrie, J. P. Valleau, and G. N. Patey, “Electrical double layers. II. monte carlo and HNC studies of image effects”, *The Journal of Chemical Physics* **76**, 4615–4622 (1982).
- [43] R. Messina, “Image charges in spherical geometry: application to colloidal systems”, *The Journal of Chemical Physics* **117**, Publisher: American Institute of Physics, 11062–11074 (2002).
- [44] C. Y. Son and Z.-G. Wang, “Image-charge effects on ion adsorption near aqueous interfaces”, *Proceedings of the National Academy of Sciences* **118**, Publisher: Proceedings of the National Academy of Sciences, e2020615118 (2021).
- [45] L. J. Ahrens-Iwers and R. H. Meißner, “Constant potential simulations on a mesh”, *The Journal of Chemical Physics* **155**, Publisher: AIP Publishing LLC AIP Publishing, 104104 (2021).
- [46] L. Scalfi, D. T. Limmer, A. Coretti, S. Bonella, P. A. Madden, M. Salanne, and B. Rotenberg, “Charge fluctuations from molecular simulations in the constant-potential ensemble”, *Physical Chemistry Chemical Physics* **22**, Publisher: Royal Society of Chemistry, 10480–10489 (2020).
- [47] G. Lamoureux and B. Roux, “Modeling induced polarization with classical drude oscillators: theory and molecular dynamics simulation algorithm”, *The Journal of Chemical Physics* **119**, 3025–3039 (2003).
- [48] J. Comtet, A. Niguès, V. Kaiser, B. Coasne, L. Bocquet, and A. Siria, “Nanoscale capillary freezing of ionic liquids confined between metallic interfaces and the role of electronic screening”, *Nature Materials* **16**, Number: 6 Publisher: Nature Publishing Group, 634–639 (2017).
- [49] N. W. Ashcroft and N. D. Mermin, *Solid state physics* (Holt, Rinehart and Winston, New York, 1976).
- [50] E. H. Lieb and B. Simon, “Thomas-fermi theory revisited”, *Physical Review Letters* **31**, Publisher: American Physical Society, 681–683 (1973).
- [51] I.-C. Yeh and M. L. Berkowitz, “Ewald summation for systems with slab geometry”, *The Journal of Chemical Physics* **111**, 3155–3162 (1999).
- [52] H. J. Berendsen, J. R. Grigera, and T. P. Straatsma, “The missing term in effective pair potentials”, *Journal of Physical Chemistry* **91**, 6269–6271 (1987).

- [53] W. L. Jorgensen, D. S. Maxwell, and J. Tirado-Rives, “Development and testing of the OPLS all-atom force field on conformational energetics and properties of organic liquids”, *Journal of the American Chemical Society* **118**, Publisher: American Chemical Society, 11225–11236 (1996).
- [54] J. Xue, J. Sanchez-Yamagishi, D. Bulmash, P. Jacquod, A. Deshpande, K. Watanabe, T. Taniguchi, P. Jarillo-Herrero, and B. J. LeRoy, “Scanning tunnelling microscopy and spectroscopy of ultra-flat graphene on hexagonal boron nitride”, *Nature Materials* **10**, Number: 4 Publisher: Nature Publishing Group, 282–285 (2011).
- [55] D. J. Bonthuis, S. Gekle, and R. R. Netz, “Dielectric profile of interfacial water and its effect on double-layer capacitance”, *Physical Review Letters* **107**, Publisher: American Physical Society, 166102 (2011).
- [56] V. Ballenegger and J.-P. Hansen, “Dielectric permittivity profiles of confined polar fluids”, *The Journal of Chemical Physics* **122**, 114711 (2005).
- [57] M. G. Hogg, I. V. Timoshkin, M. J. Given, M. P. Wilson, S. J. Macgregor, T. Wang, R. A. Fouracre, and J. M. Lehr, “Impulse breakdown of water with different conductivities”, *IEEE Transactions on Dielectrics and Electrical Insulation* **19**, Conference Name: IEEE Transactions on Dielectrics and Electrical Insulation, 1559–1568 (2012).
- [58] J. J. Yang, D. B. Strukov, and D. R. Stewart, “Memristive devices for computing”, *Nature nanotechnology* **8**, 13–24 (2013).
- [59] Y. van De Burgt, A. Melianas, S. T. Keene, G. Malliaras, and A. Salleo, “Organic electronics for neuromorphic computing”, *Nature Electronics* **1**, 386–397 (2018).
- [60] P. A. Merolla, J. V. Arthur, R. Alvarez-Icaza, A. S. Cassidy, J. Sawada, F. Akopyan, B. L. Jackson, N. Imam, C. Guo, Y. Nakamura, B. Brezzo, I. Vo, S. K. Esser, R. Appuswamy, B. Taba, A. Amir, M. D. Flickner, W. P. Risk, R. Manohar, and D. S. Modha, “A million spiking-neuron integrated circuit with a scalable communication network and interface”, *Science* **345**, 668–673 (2014).
- [61] T. M. Kamsma, W. Q. Boon, T. ter Rele, C. Spitoni, and R. van Roij, “Iontronic neuromorphic signaling with conical microfluidic memristors”, *Physical Review Letters* **130**, 268401 (2023).
- [62] D. Kuzum, S. Yu, and H.-S. P. Wong, “Synaptic electronics: materials, devices and applications”, *Nanotechnology* **24**, 382001 (2013).
- [63] P. Robin, T. Emmerich, A. Ismail, A. Niguès, Y. You, G.-H. Nam, A. Keerthi, A. Siria, A. K. Geim, B. Radha, and L. Bocquet, “Long-term memory and synapse-like dynamics in two-dimensional nanofluidic channels”, *Science* **379**, 161–167 (2023).
- [64] B. Cho, S. Song, Y. Ji, T.-W. Kim, and T. Lee, “Organic resistive memory devices: performance enhancement, integration, and advanced architectures”, *Advanced Functional Materials* **21**, 2806–2829 (2011).
- [65] V. K. Sangwan, H.-S. Lee, H. Bergeron, I. Balla, M. E. Beck, K.-S. Chen, and M. C. Hersam, “Multi-terminal memtransistors from polycrystalline monolayer molybdenum disulfide”, *en, Nature* **554**, 500–504 (2018).

- [66] F. Gärisch, G. Ligorio, P. Klein, M. Forster, U. Scherf, and E. J. W. List-Kratochvil, “Organic synaptic diodes based on polymeric mixed ionic-electronic conductors”, *Advanced Electronic Materials* **8**, 2100866 (2022).
- [67] R. Wu, M. Matta, B. D. Paulsen, and J. Rivnay, “Operando characterization of organic mixed ionic/electronic conducting materials”, *Chemical Reviews* **122**, 4493–4551 (2022).
- [68] I. Riess, “Mixed ionic–electronic conductors—material properties and applications”, *Solid State Ionics* **157**, Proceedings of the 6th International Symposium on Systems with Fast Ionic Transport (ISSFIT), 1–17 (2003).
- [69] J. Rivnay, S. Inal, B. A. Collins, M. Sessolo, E. Stavrinidou, X. Strakosas, C. Tassone, D. M. Delongchamp, and G. G. Malliaras, “Structural control of mixed ionic and electronic transport in conducting polymers”, *Nature Communications* **7**, 11287 (2016).
- [70] I. S. Kim, V. K. Sangwan, D. Jariwala, J. D. Wood, S. Park, K.-S. Chen, F. Shi, F. Ruiz-Zepeda, A. Ponce, M. Jose-Yacaman, V. P. Dravid, T. J. Marks, M. C. Hersam, and L. J. Lauhon, “Influence of Stoichiometry on the Optical and Electrical Properties of Chemical Vapor Deposition Derived MoS₂”, *ACS Nano* **8**, 10551–10558 (2014).
- [71] H. Qiu, T. Xu, Z. Wang, W. Ren, H. Nan, Z. Ni, Q. Chen, S. Yuan, F. Miao, F. Song, G. Long, Y. Shi, L. Sun, J. Wang, and X. Wang, “Hopping transport through defect-induced localized states in molybdenum disulphide”, *Nature Communications* **4**, 2642 (2013).
- [72] Y. Wang, T. Seki, X. Liu, X. Yu, C.-C. Yu, K. F. Domke, J. Hunger, M. T. M. Koper, Y. Chen, Y. Nagata, and M. Bonn, “Direct probe of electrochemical pseudocapacitive pH jump at a graphene electrode**”, *Angewandte Chemie International Edition* **62**, e202216604 (2023).
- [73] D. T. Limmer, C. Merlet, M. Salanne, D. Chandler, P. A. Madden, R. van Roij, and B. Rotenberg, “Charge fluctuations in nanoscale capacitors”, *Physical Review Letters* **111**, 106102 (2013).
- [74] F. Jiménez-Ángeles, A. Ehlen, and M. Olvera de la Cruz, “Surface polarization enhances ionic transport and correlations in electrolyte solutions nanoconfined by conductors”, *Faraday Discussions* **246**, 576–591 (2023).
- [75] N. D. Lang and W. Kohn, “Theory of Metal Surfaces: Induced Surface Charge and Image Potential”, *Physical Review B* **7**, 3541–3550 (1973).
- [76] M. Giroto, A. P. dos Santos, and Y. Levin, “Simulations of ionic liquids confined by metal electrodes using periodic green functions”, *Journal of Chemical Physics* **147**, 074109 (2017).
- [77] J. Jackson, *Classical electrodynamics* (Wiley, 1998).
- [78] L. Onsager, “Deviations from Ohm’s Law in Weak Electrolytes”, *Journal of Chemical Physics* **2**, 599–615 (1934).

- [79] J. Gao, A. R. Koltonow, K. Raidongia, B. Beckerman, N. Boon, E. Luijten, M. Olvera de la Cruz, and J. Huang, “Kirigami nanofluidics”, *Materials Chemistry Frontiers* **2**, 475–482 (2018).
- [80] W. Q. Boon, T. E. Veenstra, M. Dijkstra, and R. van Roij, “Pressure-sensitive ion conduction in a conical channel: Optimal pressure and geometry”, *Physics of Fluids* **34**, 101701 (2022).
- [81] N. B. Luque and W. Schmickler, “The electric double layer on graphite”, en, *Electrochimica Acta* **71**, 82–85 (2012).
- [82] H. Heinz, K. C. Jha, J. Luettmmer-Strathmann, B. L. Farmer, and R. R. Naik, “Polarization at metal–biomolecular interfaces in solution”, *Journal of The Royal Society Interface* **8**, 220–232 (2010).
- [83] W. Schmickler, “The electronic response of the metal in simulations of the electric double layer”, en, *Journal of Electroanalytical Chemistry* **856**, 113664 (2020).
- [84] See Supplemental Material at [URL will be inserted by publisher] for details regarding choice of wall softness, Gaussian charge conductor model, and polarization charge surface meshing parameters.
- [85] I. Coropceanu, E. M. Janke, J. Portner, D. Haubold, T. D. Nguyen, A. Das, C. P. N. Tanner, J. K. Utterback, S. W. Teitelbaum, M. H. Hudson, N. A. Sarma, A. M. Hinkle, C. J. Tassone, A. Eychmüller, D. T. Limmer, M. Olvera de la Cruz, N. S. Ginsberg, and D. V. Talapin, “Self-assembly of nanocrystals into strongly electronically coupled all-inorganic supercrystals”, *Science* **375**, Publisher: American Association for the Advancement of Science, 1422–1426 (2022).
- [86] N. Pogharian, A. P. dos Santos, A. Ehlen, and M. Olvera de la Cruz, “Electric fields near undulating dielectric membranes”, *The Journal of Chemical Physics* **160**, 094704 (2024).
- [87] M. U. Khan, J. Kim, M. Y. Chougale, R. A. Shaukat, Q. M. Saqib, S. R. Patil, B. Mohammad, and J. Bae, “Advancement in soft iontronic resistive memory devices and their application for neuromorphic computing”, *Advanced Intelligent Systems* **5**, _eprint: <https://onlinelibrary.wiley.com/doi/pdf/10.1002/aisy.202200281>, 2200281 (2023).
- [88] S. Dai, X. Liu, Y. Liu, Y. Xu, J. Zhang, Y. Wu, P. Cheng, L. Xiong, and J. Huang, “Emerging iontronic neural devices for neuromorphic sensory computing”, *Advanced Materials* **35**, _eprint: <https://onlinelibrary.wiley.com/doi/pdf/10.1002/adma.202300329>, 2300329 (2023).
- [89] M. Lizée, A. Marcotte, B. Coquinot, N. Kavokine, K. Sobnath, C. Barraud, A. Bhardwaj, B. Radha, A. Niguès, L. Bocquet, and A. Siria, “Strong electronic winds blowing under liquid flows on carbon surfaces”, *Physical Review X* **13**, Publisher: American Physical Society, 011020 (2023).
- [90] K. Krishnamoorthy, S. Kewalramani, A. Ehlen, L. Moreau, C. Mirkin, M. Olvera de la Cruz, and M. Bedzyk, “Enzymatic degradation of DNA probed by in situ x-ray scattering”, *ACS Nano* **13** (2019).

- [91] Y. Zhang, F. Lu, K. G. Yager, D. van der Lelie, and O. Gang, “A general strategy for the DNA-mediated self-assembly of functional nanoparticles into heterogeneous systems”, *Nature Nanotechnology* **8**, Publisher: Nature Publishing Group, 865–872 (2013).
- [92] P. A. Gabrys, L. Z. Zornberg, and R. J. Macfarlane, “Programmable atom equivalents: atomic crystallization as a framework for synthesizing nanoparticle superlattices”, *Small* **15**, eprint: <https://onlinelibrary.wiley.com/doi/pdf/10.1002/sml.201805424>, 1805424 (2019).
- [93] Z. Cai, Z. Li, S. Ravaine, M. He, Y. Song, Y. Yin, H. Zheng, J. Teng, and A. Zhang, “From colloidal particles to photonic crystals: advances in self-assembly and their emerging applications”, *Chemical Society Reviews* **50**, Publisher: Royal Society of Chemistry, 5898–5951 (2021).
- [94] R. J. Macfarlane, B. Lee, M. R. Jones, N. Harris, G. C. Schatz, and C. A. Mirkin, “Nanoparticle superlattice engineering with DNA”, *Science* **334**, Publisher: American Association for the Advancement of Science, 204–208 (2011).
- [95] R. V. Thaner, Y. Kim, T. I. Li, R. J. Macfarlane, S. T. Nguyen, M. Olvera de la Cruz, and C. A. Mirkin, “Entropy-driven crystallization behavior in DNA-mediated nanoparticle assembly”, *Nano Letters* **15**, Publisher: American Chemical Society, 5545–5551 (2015).
- [96] P. L. Biancaniello, A. J. Kim, and J. C. Crocker, “Colloidal interactions and self-assembly using DNA hybridization”, *Physical Review Letters* **94**, 1–4 (2005).
- [97] A. V. Tkachenko, “Generic phase diagram of binary superlattices”, *Proceedings of the National Academy of Sciences of the United States of America* **113**, Publisher: National Academy of Sciences, 10269–10274 (2016).
- [98] M. Girard, J. A. Millan, and M. Olvera de la Cruz, “DNA-driven assembly: from polyhedral nanoparticles to proteins”, *Annual Review of Materials Research* **47**, Publisher: Annual Reviews, 33–49 (2017).
- [99] T. Hueckel, G. M. Hocky, J. Palacci, and S. Sacanna, “Ionic solids from common colloids”, *Nature* **580**, Publisher: Nature Publishing Group, 487–490 (2020).
- [100] J. N. Immink, M. J. Bergman, J. J. E. Maris, J. Stenhammar, and P. Schurtenberger, “Crystal-to-crystal transitions in binary mixtures of soft colloids”, *ACS Nano*, Publisher: American Chemical Society, [acsnano.0c03966](https://doi.org/10.1021/acsnano.0c03966) (2020).
- [101] M. Girard, S. Wang, J. S. Du, A. Das, Z. Huang, V. P. Dravid, B. Lee, C. A. Mirkin, and M. Olvera de la Cruz, “Particle analogs of electrons in colloidal crystals”, *Science* **364**, Publisher: American Association for the Advancement of Science, 1174–1178 (2019).
- [102] J. B. Boyce and B. A. Huberman, “Superionic conductors: transitions, structures, dynamics”, *Physics Reports* **51**, Publisher: North-Holland, 189–265 (1979).
- [103] S. Hull, “Superionics: crystal structures and conduction processes”, *Reports on Progress in Physics* **67**, Publisher: IOP Publishing, 1233–1314 (2004).

- [104] Z. Xu and H. Zhu, “Anion charge and lattice volume maps for searching lithium superionic conductors”, *Chemistry of Materials*, Publisher: American Chemical Society (ACS) (2020).
- [105] M. S. Lee, D. W. Yee, M. Ye, and R. J. Macfarlane, “Nanoparticle assembly as a materials development tool”, *Journal of the American Chemical Society* **144**, Publisher: American Chemical Society, 3330–3346 (2022).
- [106] E. V. Shevchenko, D. V. Talapin, N. A. Kotov, S. O’Brien, and C. B. Murray, “Structural diversity in binary nanoparticle superlattices”, *Nature* **439**, 55–59 (2006).
- [107] A. P. Hynninen, C. G. Christova, R. van Roij, A. van Blaaderen, and M. Dijkstra, “Prediction and observation of crystal structures of oppositely charged colloids”, *Phys. Rev. Lett.* **96**, 138308 (2006).
- [108] M. I. Bodnarchuk, M. V. Kovalenko, W. Heiss, and D. V. Talapin, “Energetic and entropic contributions to self-assembly of binary nanocrystal superlattices: Temperature as the structure-directing factor”, *J. Am. Chem. Soc.* **132**, 11967–11977 (2010).
- [109] J. S. Oh, G. R. Yi, and D. J. Pine, “Reconfigurable self-assembly and kinetic control of multi-programmed DNA-coated particles”, *ACS Nano* **14**, 4595–4600 (2020).
- [110] M. E. Leunissen, C. G. Christova, A.-P. Hynninen, C. P. Royall, A. I. Campbell, A. Imhof, M. Dijkstra, R. van Roij, and A. van Blaaderen, “Ionic colloidal crystals of oppositely charged particles”, *Nature* **437**, 235–240 (2005).
- [111] L. Filion, M. Hermes, R. Ni, E. C. Vermolen, A. Kuijk, C. G. Christova, J. C. Stiefelhagen, T. Vissers, A. van Blaaderen, and M. Dijkstra, “Self-assembly of a colloidal interstitial solid with tunable sublattice doping”, *Phys. Rev. Lett.* **107**, 168302 (2011).
- [112] B. van der Meer, E. Lathouwers, F. Smalenburg, and L. Filion, “Diffusion and interactions of interstitials in hard-sphere interstitial solid solutions”, *J. Chem. Phys.* **147**, 234903 (2017).
- [113] W. Schommers, “Correlations in the motion of particles in n-AgI: A molecular-dynamics study”, *Phys. Rev. Lett.* **38**, 1536–1539 (1977).
- [114] M. Tatsumisago, Y. Shinkuma, and T. Minami, “Stabilization of superionic α -AgI at room temperature in a glass matrix”, *Nature* **354**, 217–218 (1991).
- [115] Y. Lin and M. Olvera de la Cruz, “Sublattice melting in binary superionic colloidal crystals”, *Phys. Rev. E* **101**, 032603 (2020).
- [116] M. D. Donakowski, J. M. Godbe, R. Sknepnek, K. E. Knowles, M. Olvera de la Cruz, and E. A. Weiss, “A quantitative description of the binding equilibria of para-substituted aniline ligands and CdSe quantum dots”, *J. Phys. Chem. C* **114**, 22526–22534 (2010).
- [117] R. D. Harris, V. A. Amin, B. Lau, and E. A. Weiss, “Role of interligand coupling in determining the interfacial electronic structure of colloidal CDS quantum dots”, *ACS Nano* **10**, 1395–1403 (2016).

- [118] A. M. Kalsin, M. Fialkowski, M. Paszewski, S. K. Smoukov, K. J. Bishop, and B. A. Grzybowski, “Electrostatic self-assembly of binary nanoparticle crystals with a diamond-like lattice”, *Science* **312**, 420–424 (2006).
- [119] R. Klajn, K. J. Bishop, and B. A. Grzybowski, “Light-controlled self-assembly of reversible and irreversible nanoparticle suprastructures”, *Proc. Natl. Acad. Sci. U. S. A.* **104**, 10305–10309 (2007).
- [120] J. Zhang, P. J. Santos, P. A. Gabrys, S. Lee, C. Liu, and R. J. Macfarlane, “Self-assembling nanocomposite tectons”, *J. Am. Chem. Soc.* **138**, 16228–16231 (2016).
- [121] P. Santos, J., Z. Cao, J. Zhang, A. Alexander-Katz, and R. J. Macfarlane, “Dictating nanoparticle assembly via systems-level control of molecular multivalency”, *J. Am. Chem. Soc.* **141**, 14624–14632 (2019).
- [122] P. J. Santos, T. C. Cheung, and R. J. Macfarlane, “Assembling ordered crystals with disperse building blocks”, *Nano Lett.* **19**, 5774–5780 (2019).
- [123] Y. Wang, W. D. Richards, S. P. Ong, L. J. Miara, J. C. Kim, Y. Mo, and G. Ceder, “Design principles for solid-state lithium superionic conductors”, *Nat. Mater.* **14**, 1026–1031 (2015).
- [124] S. Muy, J. C. Bachman, L. Giordano, H. H. Chang, D. L. Abernathy, D. Bansal, O. Delaire, S. Hori, R. Kanno, F. Maglia, S. Lupart, P. Lamp, and Y. Shao-Horn, “Tuning mobility and stability of lithium ion conductors based on lattice dynamics”, *Energy Environ. Sci.* **11**, 850–859 (2018).
- [125] A. Travesset, “Soft skyrmions, spontaneous valence and selection rules in nanoparticle superlattices”, *ACS Nano* **11**, Publisher: American Chemical Society, 5375–5382 (2017).
- [126] C. Knorowski, S. Burleigh, and A. Travesset, “Dynamics and statics of DNA-programmable nanoparticle self-assembly and crystallization”, *Phys. Rev. Lett.* **106**, 215501 (2011).
- [127] T. I. Li, R. Sknepnek, R. J. MacFarlane, C. A. Mirkin, and M. Olvera de la Cruz, “Modeling the crystallization of spherical nucleic acid nanoparticle conjugates with molecular dynamics simulations”, *Nano Lett.* **12**, 2509–2514 (2012).
- [128] W. B. Rogers and J. C. Crocker, “Direct measurements of DNA-mediated colloidal interactions and their quantitative modeling”, *Proc. Natl. Acad. Sci. U. S. A.* **108**, 15687–15692 (2011).
- [129] W. Hume-Rothery, *The Structures of Alloys of Iron* (Elsevier, Amsterdam, 1966).
- [130] J. A. Anderson, C. D. Lorenz, and A. Travesset, “General purpose molecular dynamics simulations fully implemented on graphics processing units”, *J. Comput. Phys.* **227**, 5342–5359 (2008).
- [131] J. Glaser, T. D. Nguyen, J. A. Anderson, P. Lui, F. Spiga, J. A. Millan, D. C. Morse, and S. C. Glotzer, “Strong scaling of general-purpose molecular dynamics simulations on GPUs”, *Comput. Phys. Commun.* **192**, 97–107 (2015).

- [132] M. Girard, A. Ehlen, A. Shakya, T. Bereau, and M. Olvera de la Cruz, “Hoobas: A highly object-oriented builder for molecular dynamics”, *Comput. Mater. Sci.* **167**, 25–33 (2019).
- [133] N. Michaud-Agrawal, E. J. Denning, T. B. Woolf, and O. Beckstein, “MDAnalysis: A toolkit for the analysis of molecular dynamics simulations”, *J. Comput. Chem.* **32**, 2319–2327 (2011).
- [134] R. Gowers, M. Linke, J. Barnoud, T. Reddy, M. Melo, S. Seyler, J. Domański, D. Dotson, S. Buchoux, I. Kenney, and O. Beckstein, “MDAnalysis: A python package for the rapid analysis of molecular dynamics simulations”, *Proc. 15th Python Sci. Conf.*, 98–105 (2016).
- [135] W. Humphrey, A. Dalke, and K. Schulten, “VMD: Visual molecular dynamics”, *J. Mol. Graph.* **14**, 33–38 (1996).
- [136] J. E. Stone, “An efficient library for parallel ray tracing and animation”, PhD thesis (Computer Science Department, University of Missouri-Rolla, 1998).
- [137] P. Ramachandran and G. Varoquaux, “Mayavi: 3D visualization of scientific data”, *Comput. Sci. Eng.* **13**, 40–51 (2011).
- [138] N. B. Schade, M. C. Holmes-Cerfon, E. R. Chen, D. Aronzon, J. W. Collins, J. A. Fan, F. Capasso, and V. N. Manoharan, “Tetrahedral colloidal clusters from random parking of bidisperse spheres”, *Phys. Rev. Lett.* **110**, 148303 (2013).
- [139] J. Sprakel, A. Zaccone, F. Spaepen, P. Schall, and D. A. Weitz, “Direct observation of entropic stabilization of BCC crystals near melting”, *Phys. Rev. Lett.* **118**, 088003 (2017).
- [140] R. Higler and J. Sprakel, “Doping colloidal BCC crystals-interstitial solids and meta-stable clusters”, *Sci. Rep.* **7**, 1–13 (2017).
- [141] M. Salamon, “Physics of Superionic Conductors”, in , Vol. 15, edited by M. Salamon (Springer-Verlag Berlin Heidelberg, Berlin, 1979), pp. 175–200.
- [142] J. B. Goodenough and K.-S. Park, “The Li-ion rechargeable battery: A perspective”, *J. Am. Chem. Soc.* **29**, 1167–1176 (2013).
- [143] J. C. Bachman, S. Muy, A. Grimaud, H. H. Chang, N. Pour, S. F. Lux, O. Paschos, F. Maglia, S. Lupart, P. Lamp, L. Giordano, and Y. Shao-Horn, “Inorganic solid-state electrolytes for lithium batteries: Mechanisms and properties governing ion conduction”, *Chem. Rev.* **116**, 140–162 (2016).
- [144] T. Famprikis, P. Canepa, J. A. Dawson, M. S. Islam, and C. Masquelier, “Fundamentals of inorganic solid-state electrolytes for batteries”, *Nat. Mater.* **18**, 1278–1291 (2019).
- [145] G.-R. Yi, D. J. Pine, and S. Sacanna, “Recent progress on patchy colloids and their self-assembly”, *Journal of Physics: Condensed Matter* **25**, 193101 (2013).
- [146] M. D. Eldridge, P. A. Madden, and D. Frenkel, “Entropy-driven formation of a superlattice in a hard-sphere binary mixture”, *Nature* **320**, 35–37 (1993).

- [147] I. Cherniukh, G. Rainò, T. Stöferle, M. Burian, A. Travesset, D. Naumenko, H. Amenitsch, R. Erni, R. F. Mahrt, M. I. Bodnarchuk, and M. V. Kovalenko, “Perovskite-type superlattices from lead halide perovskite nanocubes”, *Nature* **593**, 535–542 (2021).
- [148] A. D. Dinsmore, J. C. Crocker, and A. G. Yodh, “Self-assembly of colloidal crystals”, *Current Opinion in Colloid and Interface Science* **3**, 5–11 (1998).
- [149] L. Fillion and M. Dijkstra, “Prediction of binary hard-sphere crystal structures”, *Phys. Rev. E - Stat. Nonlinear, Soft Matter Phys.* **79** (2009).
- [150] A. Travesset, “Nanoparticle Superlattices as Quasi-Frank-Kasper Phases”, *Physical Review Letters* **119**, 115701 (2017).
- [151] H. Lopez-Rios, A. Ehlen, and M. Olvera de la Cruz, “Delocalization Transition in Colloidal Crystals”, *The Journal of Physical Chemistry C* **125**, 1096–1106 (2021).
- [152] H. F. Cheng, S. Wang, and C. A. Mirkin, “Electron-Equivalent Valency through Molecularly Well-Defined Multivalent DNA”, *Journal of the American Chemical Society* **143**, 33 (2021).
- [153] J. Tauber, R. Higler, and J. Sprakel, “Anomalous dynamics of interstitial dopants in soft crystals”, *Proc. Natl. Acad. Sci. U. S. A.* **113**, 13660–13665 (2016).
- [154] M. Girard, “Models and studies of self-assembled systems using high information polymer coated particles”, PhD thesis (Northwestern University, 2018) (available at <http://aztec.tech.northwestern.edu/Images/People%20slides/MartinPhDthesis.pdf>), <http://aztec.tech.northwestern.edu/Images/People%2>.
- [155] W. Schommers, “Structure and dynamics of superionic conductors”, *Phys. Rev. B* **21**, 847–851 (1980).
- [156] T. M. Brenner, C. Gehrman, R. Korobko, T. Livneh, D. A. Egger, and O. Yaffe, “Anharmonic host-lattice dynamics enable fast ion conduction in superionic AgI”, *Physical Review Materials* **4**, 115402 (2020).
- [157] A. F. Demirörs, P. P. Pillai, B. Kowalczyk, and B. A. Grzybowski, “Colloidal assembly directed by virtual magnetic moulds”, *Nature* **503**, 99–103 (2013).
- [158] S. Sacanna, W. T. Irvine, P. M. Chaikin, and D. J. Pine, “Lock and key colloids”, *Nature* **464**, 575–578 (2010).
- [159] Y. K. Lee, X. Li, P. Perdikaris, J. C. Crocker, C. Reina, and T. Sinno, “Hydrodynamic and frictional modulation of deformations in switchable colloidal crystallites”, *Proceedings of the National Academy of Sciences of the United States of America* **117**, 12700–12706 (2020).
- [160] F. Lu, K. G. Yager, Y. Zhang, H. Xin, and O. Gang, “Superlattices assembled through shape-induced directional binding”, *Nature Communications* 2015 6:1 **6**, 1–10 (2015).
- [161] J. D. Budai, J. Hong, M. E. Manley, E. D. Specht, C. W. Li, J. Z. Tischler, D. L. Abernathy, A. H. Said, B. M. Leu, L. A. Boatner, R. J. McQueeney, and O. Delaire, “Metallization of vanadium dioxide driven by large phonon entropy”, *Nature* **515**, 535–539 (2014).

- [162] U. Pinsook, “Molecular dynamics study of vibrational entropy in bcc and hcp zirconium”, *Physical Review B - Condensed Matter and Materials Physics* **66**, 024109–1–6 (2002).
- [163] L. Landau, E. Lifshitz, and M. Pitaevskii, *Statistical Physics. Part 1*, 3rd ed. (Pergamon Press, Oxford, Sept. 1980), pp. 446–516.
- [164] J. M. Dickey and A. Paskin, “Computer simulation of the lattice dynamics of solids”, *Physical Review* **188**, 1407–1418 (1969).
- [165] A. Verdaguer, J. A. Padró, and J. Trullàs, “Molecular dynamics study of the velocity cross-correlations in liquids”, *Journal of Chemical Physics* **109**, 228–234 (1998).
- [166] A. Verdaguer and J. A. Padró, “Computer simulation study of the velocity cross correlations between neighboring atoms in simple liquid binary mixtures”, *Journal of Chemical Physics* **114**, 2738–2744 (2001).
- [167] T. Ishida, “Molecular dynamics study of the dynamical behavior in ionic liquids through interionic interactions”, in *Journal of non-crystalline solids*, Vol. 357, 2 (Jan. 2011), pp. 454–462.
- [168] S. Alexander and J. McTague, “Should all crystals be BCC? Landau theory of solidification and crystal nucleation”, *Phys. Rev. Lett.* **41**, 702–705 (1978).
- [169] M. He, J. P. Gales, É. Ducrot, Z. Gong, G. R. Yi, S. Sacanna, and D. J. Pine, “Colloidal diamond”, *Nature* **585**, 524–529 (2020).
- [170] E. Auyeung, T. I. N. G. Li, A. J. Senesi, A. L. Schmucker, B. C. Pals, M. Olvera de la Cruz, and C. A. Mirkin, “DNA-mediated nanoparticle crystallization into Wulff polyhedra”, *Nature* **505**, 73–77 (2014).
- [171] J. A. Anderson, J. Glaser, and S. C. Glotzer, “HOOMD-blue: A Python package for high-performance molecular dynamics and hard particle Monte Carlo simulations”, *Computational Materials Science* **173**, 109363 (2020).
- [172] S. P. Ong, W. D. Richards, A. Jain, G. Hautier, M. Kocher, S. Cholia, D. Gunter, V. L. Chevrier, K. A. Persson, and G. Ceder, “Python Materials Genomics (pymatgen): A robust, open-source python library for materials analysis”, *Computational Materials Science* **68**, 314–319 (2013).
- [173] M. J. Mehl, D. Hicks, C. Toher, O. Levy, R. M. Hanson, G. Hart, and S. Curtarolo, “The AFLOW Library of Crystallographic Prototypes: Part 1”, *Computational Materials Science* **136**, S1–S828 (2017).
- [174] D. Hicks, M. J. Mehl, E. Gossett, C. Toher, O. Levy, R. M. Hanson, G. Hart, and S. Curtarolo, “The AFLOW Library of Crystallographic Prototypes: Part 2”, *Computational Materials Science* **161**, S1–S1011 (2019).
- [175] Y. Lin and M. Olvera de la Cruz, “Superionic colloidal crystals: ionic to metallic bonding transitions”, *The Journal of Physical Chemistry B* **126**, Publisher: American Chemical Society, 6740–6749 (2022).
- [176] Y. Lin and M. Olvera de la Cruz, “Colloidal superionic conductors”, *Proceedings of the National Academy of Sciences* **120**, Publisher: Proceedings of the National Academy of Sciences, e2300257120 (2023).

- [177] L. A. Padilla, A. A. León-Islas, J. Funkhouser, J. C. Armas-Pérez, and A. Ramírez-Hernández, “Dynamics and phase behavior of two-dimensional size-asymmetric binary mixtures of core-softened colloids”, *The Journal of Chemical Physics* **155**, 214901 (2021).
- [178] I. Q. Matos and F. A. Escobedo, “Self-assembling of nonadditive mixtures containing patchy particles with tunable interactions”, *The Journal of Physical Chemistry B* **127**, Publisher: American Chemical Society, 8982–8992 (2023).
- [179] C. Lionello, C. Perego, A. Gardin, R. Klajn, and G. M. Pavan, “Supramolecular semiconductivity through emerging ionic gates in ion–nanoparticle superlattices”, *ACS Nano* **17**, Publisher: American Chemical Society, 275–287 (2023).
- [180] S. Wang, S. Lee, J. S. Du, B. E. Partridge, H. F. Cheng, W. Zhou, V. P. Dravid, B. Lee, S. C. Glotzer, and C. A. Mirkin, “The emergence of valency in colloidal crystals through electron equivalents”, *Nature Materials* **21**, Publisher: Nature Publishing Group, 580–587 (2022).
- [181] K. Deng, Z. Luo, L. Tan, and Z. Quan, “Self-assembly of anisotropic nanoparticles into functional superstructures”, *Chemical Society Reviews* **49**, Publisher: Royal Society of Chemistry, 6002–6038 (2020).
- [182] Z. Li, S. Wang, U. Nattermann, A. K. Bera, A. J. Borst, M. Y. Yaman, M. J. Bick, E. C. Yang, W. Sheffler, B. Lee, S. Seifert, G. L. Hura, H. Nguyen, A. Kang, R. Dalal, J. M. Lubner, Y. Hsia, H. Haddox, A. Courbet, Q. Dowling, M. Miranda, A. Favor, A. Etemadi, N. I. Edman, W. Yang, C. Weidle, B. Sankaran, B. Negahdari, M. B. Ross, D. S. Ginger, and D. Baker, “Accurate computational design of three-dimensional protein crystals”, *Nature Materials* **22**, Publisher: Nature Publishing Group, 1556–1563 (2023).
- [183] B. Hess, C. Kutzner, D. van der Spoel, and E. Lindahl, “GROMACS 4: algorithms for highly efficient, load-balanced, and scalable molecular simulation”, *Journal of Chemical Theory and Computation* **4**, Publisher: American Chemical Society, 435–447 (2008).
- [184] S. Páll, A. Zhmurov, P. Bauer, M. Abraham, M. Lundborg, A. Gray, B. Hess, and E. Lindahl, “Heterogeneous parallelization and acceleration of molecular dynamics simulations in GROMACS”, *The Journal of Chemical Physics* **153**, 134110 (2020).
- [185] T. Gingrich, “Simulating Surface Charge Effects in Carbon Nanotube Templated Ionic Crystal Growth”, PhD thesis (University of Oxford, 2010).
- [186] W. Cai and W. D. Nix, “Imperfections in Crystalline Solids”, in *Imperfections in crystalline solids* (Cambridge University Press, Cambridge, Sept. 2016), pp. 271–318.
- [187] F. H. Stillinger, “A topographic view of supercooled liquids and glass formation”, *Science* **267**, 1935–1939 (1995).
- [188] P. G. Debenedetti and F. H. Stillinger, “Supercooled liquids and the glass transition”, *Nature* **410**, 259 (2001).

- [189] V. Ramasubramani, B. D. Dice, E. S. Harper, M. P. Spellings, J. A. Anderson, and S. C. Glotzer, “freud: A software suite for high throughput analysis of particle simulation data”, *Computer Physics Communications* **254**, 107275 (2020).
- [190] P. M. Larsen, S. Schmidt, and J. Schiøtz, “Robust structural identification via polyhedral template matching”, *Modelling and Simulation in Materials Science and Engineering* **24**, 055007 (2016).
- [191] A. Stukowski, “Visualization and analysis of atomistic simulation data with OVITO—the Open Visualization Tool”, *Modelling and Simulation in Materials Science and Engineering* **18**, 015012 (2010).

APPENDIX A

Supplementary information for Chapter 3

This appendix contains the supplementary information associated with Chapter 3.

The following was originally published in the Faraday Discussions ("Iontronics: from fundamentals to ion-controlled devices") in 2023. It is reproduced here with permission of Felipe Jiménez-Ángeles, Monica Olvera de la Cruz, and the Royal Society of Chemistry.

Surface polarization enhances ionic transport and correlations in electrolyte solutions nanoconfined by conductors: Supplementary Material

Felipe Jiménez-Ángeles, Ali Ehlen, Monica Olvera de la Cruz

Reprinted with permission from:

Faraday Discussions, 2023, **246**, 576-591, DOI: 10.1039/D3FD00028A

<https://pubs.rsc.org/en/content/articlehtml/2023/fd/d3fd00028a>

A.1. Molecular simulations for ion transport calculations

The simulations for calculating ion transport properties were run in LAMMPS version 23June2022 – Update 2 [8]. All simulations of electrolyte solutions were run in a larger geometry, $L_x = 10.1$ nm and $L_y = 10.2$ nm, with a distance between electrodes of $L_z = 0.97$ nm. Accounting for excluded volume interactions between the carbon atoms of the electrodes and the water, the accessible space in the z -direction was $L_{z\text{-effective}} \approx 0.63$ nm. The number of water and ion molecules included in the simulations is below, with densities calculated using a slit volume of $L_x \times L_y \times L_{z\text{-effective}}$.

Table A.1. Number of ions and water molecules in the transport properties simulations.

	NaCl	CaCl ₂	LaCl ₃
Number of water molecules N_w (water density)	2,264 (1.03 gm/cm ³)	2,192 (1.00 gm/cm ³)	2,264 (1.03 gm/cm ³)
Number of ions N_+, N_- (M cluster, M individual ions)	32, 32 (0.81 M, 1.6 M)	20, 40 (0.51 M, 1.5 M)	16, 48 (0.41 M, 1.6 M)

To simulate ion transport, the initial configurations for NaCl, CaCl₂, and LaCl₃ are generated using GROMACS [183, 184] separately by equilibrating the electrolyte solution

within the slit with a bulk electrolyte solution using the setup shown in Figure A.1. The equilibrated slit region was isolated and replicated 2×2 times in the x - and y -directions. Then, the systems are simulated using LAMMPS with periodic boundary conditions in the x - and y -directions. For the CaCl_2 system, ions stayed within the slit during the equilibration with the reservoir. The system was used as it finalized the equilibration. The NaCl and LaCl_3 systems required adjustment because ions did not easily enter the slit. For the NaCl system, we found the equilibrium concentration of NaCl ions in a separate simulation of a larger slit in contact with a reservoir ($L_z = 12 \text{ \AA}$) equilibrated with bulk electrolyte. We then replaced water molecules in the thinner slit case until they reached this concentration. For the LaCl_3 system, we used the initial configuration of the NaCl system, and changed the identity of ions to match the numbers in Table A.1. We chose to keep the total number of ions roughly constant so that we could compare simulations with different salts without the additional complication of changing the number of ions, which could introduce other effects. We assume that the bulk salt concentrations required to achieve these conditions may be much higher for NaCl and LaCl_3 than for CaCl_2 —though why certain ions more easily enter the slit and under what conditions is another interesting question that we do not explore here.

Interactions between water, electrodes, and ions were modeling using the SPC/E water model and AA-OPLS force field [52, 53] parameters as described in the main text, and charged interactions are calculated using particle-particle-particle mesh solver with a slab correction to account for the quasi-two-dimensional geometry. Additionally, for polarizable electrodes (constant Ψ), the ELECTRODE package in LAMMPS [8, 45] was applied to the carbon atoms of the electrodes to calculate interface polarization charge

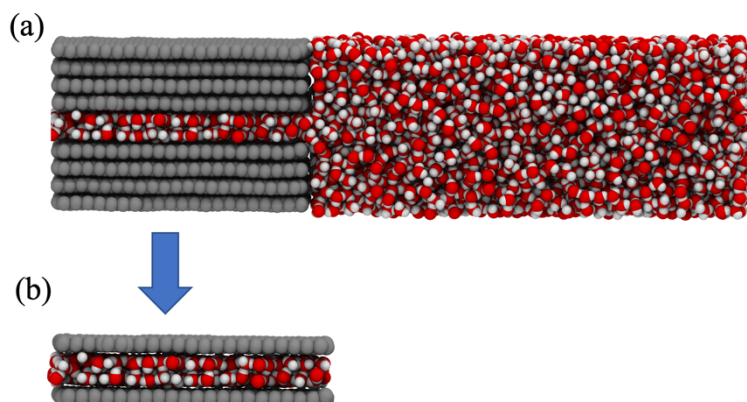


Figure A.1. Equilibration between an aqueous solution confined within a slit-like pore and a bulk solution. (a) Simulation setup consisting of a slit pore region is formed by two surfaces in contact with a bulk aqueous solution. Each surface comprises four graphene layers of $5.05 \text{ nm} \times 5.1 \text{ nm}$. The simulation box dimensions are $L_x = 14.03 \text{ nm}$, $L_y = 5.1 \text{ nm}$, and $L_z = 3.4 \text{ nm}$ in the x -, y -, and z -directions, respectively. The box contains 5484 water molecules. (b) After a simulation equilibration of 10 ns, the slit region is isolated, containing 580 water molecules, approximately. Then, the pore is replicated 2×2 times in the x - and y -directions. The equilibrated slit-like channel is transferred to LAMMPS to perform simulations at constant potential and constant charge.

based on a constant potential constraint. All simulations were run at constant volume for 30 ns at 298 K, and the analysis was performed using the last 28 ns of the trajectory.

A.2. Charge of electrodes

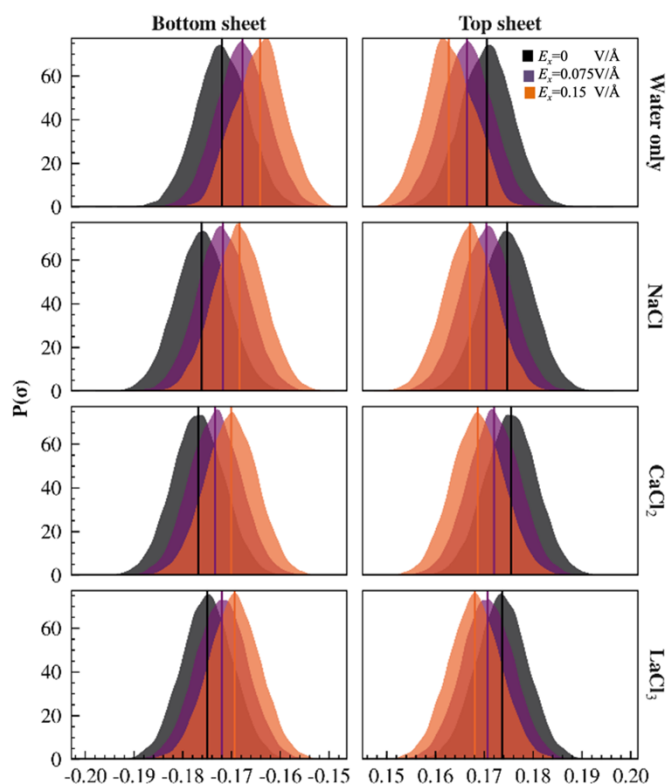


Figure A.2. Histograms of charge densities on each electrode for simulations with polarizable electrodes an applied voltage of $\Psi = 0.5$ V. Each row contains the profiles at external fields of $E_x = 0, 0.075,$ and 0.15 V/Å. The electric field (units of V/Å) is applied parallel to the electrodes impacts the overall induced charge density, as does the ion type. The variance of σ is approximately the same in all simulations. At $\Psi = 0$, the induced charge density fluctuates around zero. The vertical line identifies the mean value of each distribution.

A.3. Ion density in the z direction colored by E field

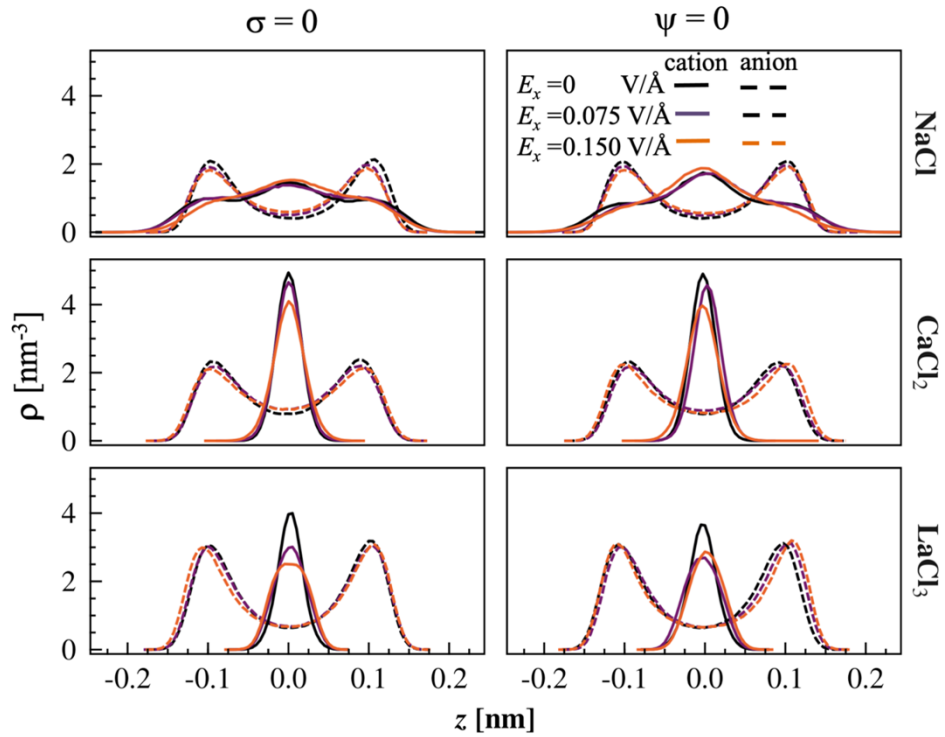


Figure A.3. Ionic number density profiles in the z -direction in ungated channels. The column on the right contains the profiles of non-polarizable channels ($\sigma = 0$) whereas on the left are the profiles of polarizable systems ($\Psi = 0$). Each row contains the profiles at external fields of $E_x = 0, 0.075,$ and 0.15 V/\AA . The solid lines represent the cations' profiles, whereas the dashed lines the anions' profiles. Anions tend to be adsorbed at the electrodes whereas cations remain in the channel's center, regardless of the valence. The effect of increasing electric field strength (units of V/\AA) for higher-valency cations is to broaden their distribution. Ion density profiles and their response to external electric fields are similar for systems of conductors and non-polarizable materials.

A.4. Ionic pair correlation functions in ungated slit-like channels of conductors and non-polarizable surfaces at different E-fields in the surfaces' parallel direction

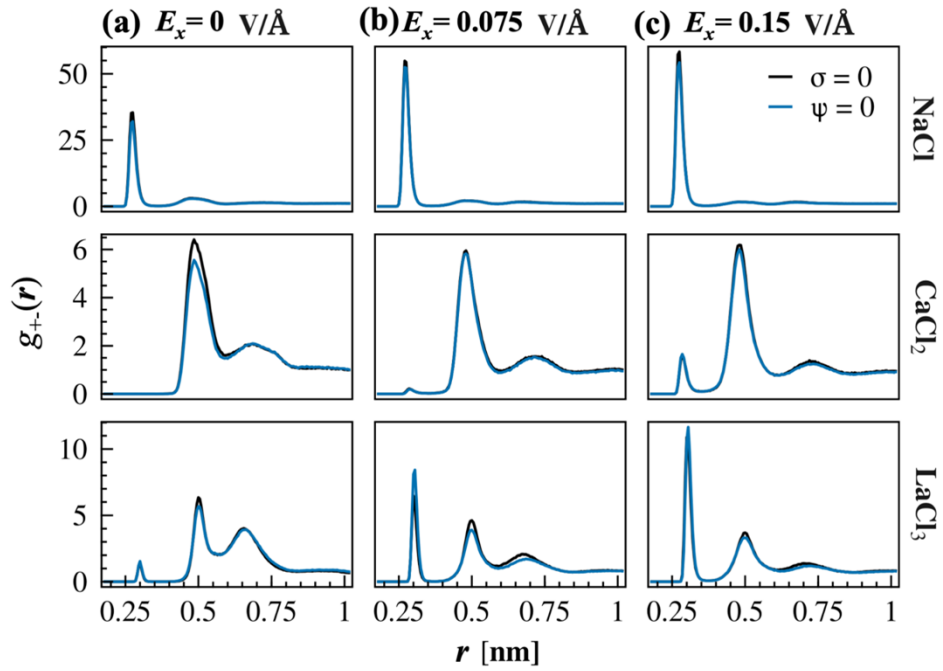


Figure A.4. Cation-anion pair correlation functions $g_{+-}(r)$ of (a) NaCl, (b) CaCl_2 , and (c) LaCl_3 confined by slit channels made of non-polarizable ($\sigma = 0$) and polarizable surfaces ($\Psi = 0$). Each row contains the profiles at external fields of $E_x = 0, 0.075,$ and 0.15 V/\AA . The black lines represent the pair correlation functions in slit-like channels of conductors, while the light-blue lines are those in non-polarizable surfaces. The separation distance between the surfaces is $h = 0.97 \text{ nm}$.

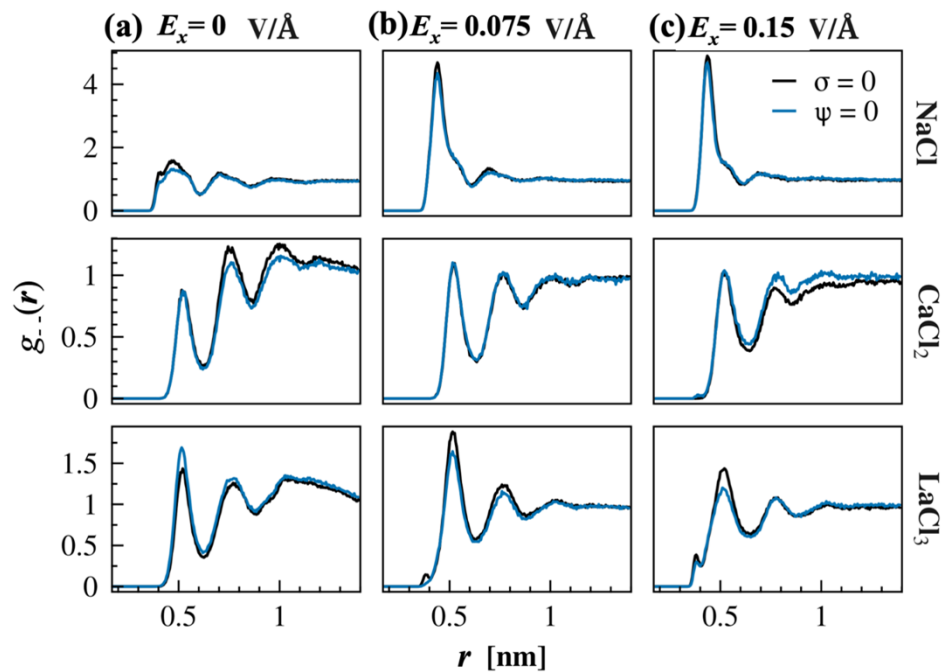


Figure A.5. Anion-anion pair correlation functions $g_{--}(r)$ in (a) NaCl, (b) CaCl₂, and (c) LaCl₃ confined by slit channels made of non-polarizable ($\sigma = 0$) and polarizable surfaces ($\Psi = 0$). Each row contains the profiles at external fields of $E_x = 0, 0.075,$ and 0.15 V/\AA . The black lines represent the pair correlation functions in slit-like channels of conductors, while the light-blue lines are those in non-polarizable surfaces. The separation distance between the surfaces is $h = 0.97 \text{ nm}$.

A.5. Ion transport and density profiles in gated channels

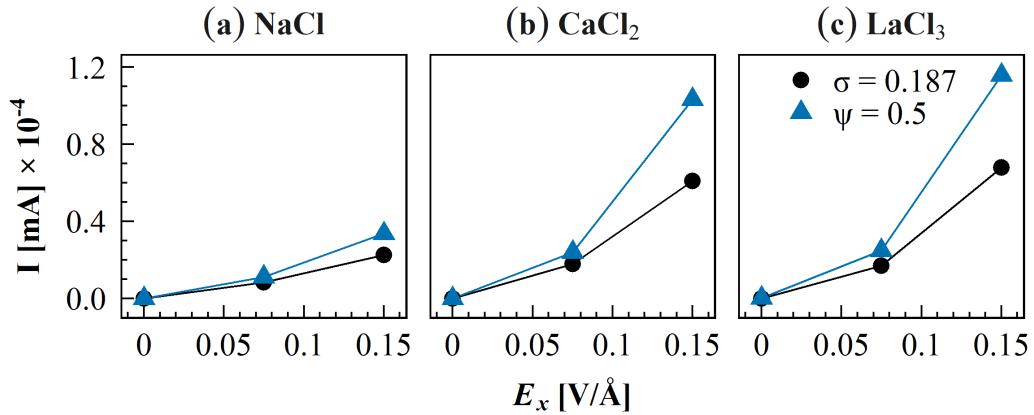


Figure A.6. Ionic current in gated nanochannels. Average current as a function of the applied external field E_x of (a) NaCl, (b) CaCl₂, and (c) LaCl₃ electrolytes. The electrolytes are confined between charged non-polarizable surfaces ($\sigma = 0.187$ e/nm²) and conductors ($\Psi = 0.5$ V, $\Delta\Psi =$ V). The black lines represent the pair correlation functions in slit-like channels of conductors, while the light-blue lines are those in non-polarizable surfaces. The separation distance between the surfaces is $h = 0.97$ nm. *Note: the error bars in the original publication represented the standard deviation of the data, which is large due to large current fluctuations. Here, the plotted error bars represent the standard error of the current mean, which is quite small.*

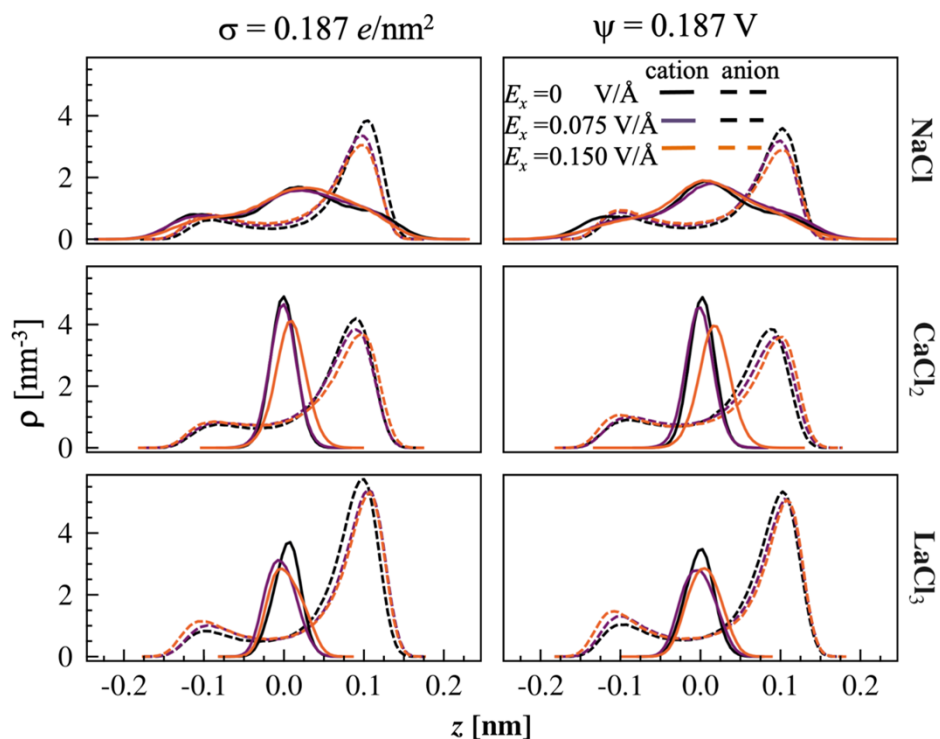


Figure A.7. Number density of ions in the z -direction in gated channels. The solid lines represent the cations' profiles, whereas the dashed lines the anions' profiles. The column on the right contains the profiles of non-polarizable channels ($\sigma = 0.187 \text{ e/nm}^2$) whereas on the left are the profiles of polarizable systems ($\Psi = 0.5 \text{ V}$). Each row contains the profiles at external fields of $E_x = 0, 0.075,$ and 0.15 V/\AA . Anions tend to be adsorbed at the electrodes, whereas cations, regardless of species, tend to remain in the center of the slit. The effect of increasing electric field strength (units of V/\AA) for higher-valency cations is to broaden their distribution. Ion density profiles and their response to external electric fields are similar for systems of conductors and non-polarizable materials.

A.6. Calculation of the Force between two oppositely charged ions at the middle plane between two parallel conductors using the image charge method

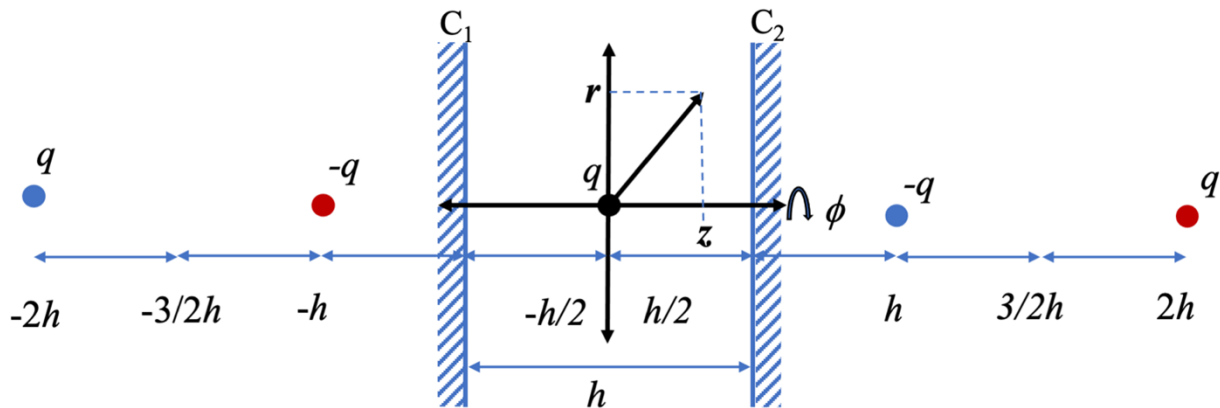


Figure A.8. Schematic representation of two parallel conductors C_1 and C_2 , with perpendicular separation distance h . A point charge q is placed at the middle plane between the two conductors and generates an infinite number of image charges at $z = \pm h/2, \pm h, \pm 3h/2, \pm 2h \dots$ of the same magnitude and with an alternating sign. The positions are designated using a cylindrical coordinate system (r, ϕ, z) placed at the middle plane of the two surfaces.

Consider the system illustrated in Figure A.8 consisting of two planar conductors parallelly placed with a separation distance h . A charge q is placed at the middle plane between the two conductors. The origin of a cylindrical coordinate system is placed at the location of the charge. We model the polarization charge using the image charge method. Due to the interaction of the charge with the conductors and between the conductors, an infinite number of image charges are induced in the system. The electrostatic potential at the position (r, z) , considering the multiple image charges induced by the q , is expressed

as

(A.1)

$$\begin{aligned} \Psi(z, r) = & \frac{1}{4\pi\epsilon_0} \frac{q}{(r^2 + z^2)^{\frac{1}{2}}} - \\ & \frac{1}{4\pi\epsilon_0} \left[\frac{q}{(r^2 + (h - z)^2)^{\frac{1}{2}}} - \frac{q}{(r^2 + (2h + z)^2)^{\frac{1}{2}}} + \frac{q}{(r^2 + (3h - z)^2)^{\frac{1}{2}}} - \dots \right] - \\ & \frac{1}{4\pi\epsilon_0} \left[\frac{q}{(r^2 + (h + z)^2)^{\frac{1}{2}}} - \frac{q}{(r^2 + (2h - z)^2)^{\frac{1}{2}}} + \frac{q}{(r^2 + (3h + z)^2)^{\frac{1}{2}}} - \dots \right] \end{aligned}$$

In a more compact form, the electrostatic potential is written as

(A.2)

$$\Psi(z, r) = \frac{1}{4\pi\epsilon_0} \frac{q}{(r^2 + z^2)^{\frac{1}{2}}} + \frac{1}{4\pi\epsilon_0} \left[\sum_{n=1}^{\infty} \frac{(-1)^n q}{(r^2 + (nh - z)^2)^{\frac{1}{2}}} + \sum_{n=1}^{\infty} \frac{(-1)^n q}{(r^2 + (nh + z)^2)^{\frac{1}{2}}} \right]$$

We take the derivative of the potential with respect to the coordinate z to calculate the electric field in the z -direction, which gives

(A.3)

$$-E_z(r, z) = \frac{\partial \Psi(z, r)}{\partial z} = -\frac{1}{4\pi\epsilon_0} \frac{qz}{(r^2 + z^2)^{\frac{3}{2}}} + \frac{1}{4\pi\epsilon_0} \left[\sum_{n=1}^{\infty} \frac{(-1)^n q(nh - z)}{(r^2 + (nh - z)^2)^{\frac{3}{2}}} + \sum_{n=1}^{\infty} \frac{(-1)^{n+1} q(nh + z)}{(r^2 + (nh + z)^2)^{\frac{3}{2}}} \right]$$

The polarization charge density on the conductor is given as

(A.4)

$$\sigma_p = \epsilon_0 \left. \frac{\partial \Psi(z, r)}{\partial z} \right|_{z=\frac{h}{2}} = -\frac{1}{4\pi} \frac{qz}{(r^2 + (\frac{h}{2})^2)^{\frac{3}{2}}} + \frac{1}{4\pi} \left[\sum_{n=1}^{\infty} \frac{(-1)^n q(nh - h/2)}{(r^2 + (nh - h/2)^2)^{\frac{3}{2}}} + \sum_{n=1}^{\infty} \frac{(-1)^{n+1} q(nh + h/2)}{(r^2 + (nh + h/2)^2)^{\frac{3}{2}}} \right]$$

The total polarization charge q_p on one of the conductors is

(A.5)

$$q_p = \int \sigma_p dA = \int_0^{\infty} \sigma_p 2\pi r dr = -\frac{q}{2}$$

which is exactly one-half of the charge because the polarization charge is distributed symmetrically in the two conductors.

The electric field in the surfaces' parallel direction is given as

$$(A.6) \quad E_r = -\frac{\partial \Psi(z, r)}{\partial z} = \frac{1}{4\pi\epsilon_0} \frac{qz}{(r^2 + z^2)^{\frac{3}{2}}} - \frac{1}{4\pi\epsilon_0} \left[\sum_{n=1}^{\infty} \frac{(-1)^{n+1}qr}{(r^2 + (nh - z)^2)^{\frac{3}{2}}} + \sum_{n=1}^{\infty} \frac{(-1)^{n+1}qr}{(r^2 + (nh + z)^2)^{\frac{3}{2}}} \right]$$

The force on a charge q' located at the middle plane of the two conductors is given as

$$(A.7) \quad F_r(z = 0, r) = q'E_r(z = 0, r) = \frac{1}{4\pi\epsilon_0} \frac{q'q}{r^2} - \frac{q'q}{2\pi\epsilon_0} \left[\sum_{n=1}^{\infty} \frac{(-1)^{n+1}r}{(r^2 + (2nh)^2)^{\frac{3}{2}}} \right]$$

APPENDIX B

Supplementary information for Chapter 4

This appendix contains the supplementary information associated with Chapter 4.

The following was originally published in the Physical Review Research in 2023. It is reproduced here with permission of Alexandre Pereira dos Santos, Felipe Jiménez-Ángeles, Monica Olvera de la Cruz, and the American Physical Society.

Modulation of ionic conduction using polarizable surfaces: Supplementary Material

Alexandre Pereira dos Santos, Felipe Jiménez-Ángeles, Ali Ehlen, Monica Olvera de la
Cruz

Reprinted with permission from:

Physical Review Research **5**, 043174, DOI: 10.1103/PhysRevResearch.5.043174
[https://journals.aps.org/prresearch/abstract/10.1103/PhysRevResearch.
5.043174](https://journals.aps.org/prresearch/abstract/10.1103/PhysRevResearch.5.043174)

Walls model

We use a truncated Lenard-Jones potential to model the interaction between the ions and the wall with an origin z_0 given by $U_{\text{LJ}}(z) = 4\epsilon_{\text{LJ}} \left[\left(\frac{\sigma_{\text{iw}}}{z-z_0} \right)^{12} - \left(\frac{\sigma_{\text{iw}}}{z-z_0} \right)^6 + 1/4 \right]$ for $z \leq z_c \equiv z_0 + 2^{1/6}\sigma_{\text{iw}}$, and $U_{\text{LJ}}(z) = 0$ for $z > z_c$, where $\epsilon_{\text{LJ}} = k_B T$ and $\sigma_{\text{iw}} = (\sigma_{\text{LJ}} + d)/2$, being σ_{LJ} and d the wall's and ion's Lenard-Jones diameters, respectively. We define the wall's surface as z_s , where $z_0 = z_s - \sigma_{\text{LJ}}/2$. Fig. B.1 shows the ion density profile for conductors for different wall softness, modified by the choice of σ_{LJ} . We notice that the ions' distribution is sensitive to the walls' softness, but the qualitative adsorption behavior does not change.

For calculation of induced polarization charges in *explicit polarization* models, we place the polarizable sites at locations $\{\mathbf{R}_i\}$ on a plane at z_0 or z_s in a two-dimensional planar mesh. In the main text, we use a hexagonal (graphene) pattern, but the mesh pattern can affect ion-surface interaction. Ionic currents resulting from changing the mesh type and size are shown in Fig. B.2. Triangular meshes with smaller side lengths give ionic currents

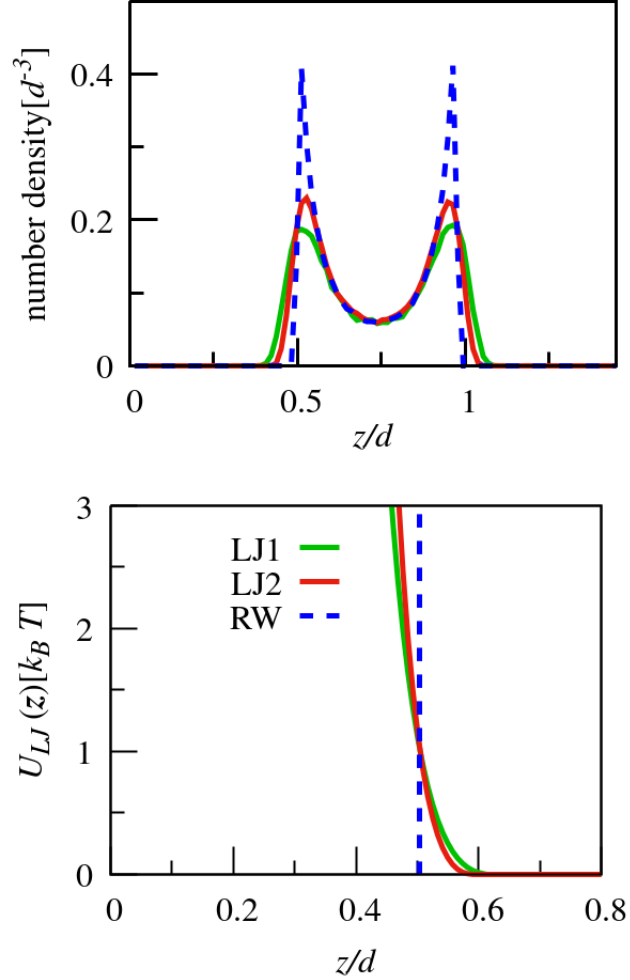


Figure B.1. Effect of the softness (Lennard-Jones energy) of the conducting confining walls, for $E = 0$. (a) Number density profiles as a function of the position in the slit channel using walls of different softness and (b) the corresponding wall interaction potential $u(z)$. LJ1 refers to a Lennard-Jones wall with $\sigma_{LJ} = 0.39$ nm, used in the main text, LJ2 refers to $\sigma_{LJ} = 0.29$ nm, and RW represents a reflective wall, where the z component of the velocity of any ion crossing the wall is instantaneously flipped. The dielectric constant in the space between the two surfaces is $\epsilon_w = 5\epsilon_0$ and $l_B = 26.4d$, as in the main text. Ions adsorb to the confining walls in all cases, but the softness of the walls impacts the quantitative shape of their distribution.

that are closer to those calculated using the Green function method. However, meshing raises the question of whether perfectly smeared or more localized polarization charge better represents a surface in conditions of such strong confinement and small length scales. This is worth further consideration and depends on the system to be studied, as discussed in Section 5.2.2 of [185].

Conductors Model

The electrostatic boundary conditions determine the induced polarization surface charges. In the *polarization* models, we use a grid, consisting of N_g nodes located at $\{\mathbf{R}_i\}$ in a hexagonal (graphene) mesh, to place the polarization charges. For conductors, we assign the polarization charge at each grid point \mathbf{R}_i using a Gaussian distribution [74] as $\rho_i(\mathbf{r}) = q_i \chi_i(\mathbf{r})$ where $\chi_i(\mathbf{r}) = (\frac{\eta^2}{\pi})^{3/2} \exp\{-\eta^2(\mathbf{r} - \mathbf{R}_i)^2\}$. The inverse width of the distribution η is a measure of how tightly bound electrons are to surface nuclei, which affects short-range ion-surface interaction [185]. It is not entirely clear how to select the value of η , which may be material- and configuration-dependent, but some value of η are unrealistic and don't appropriately model a constant potential surface. For a longer discussion of the value of η , see Chapter 5 of [185] (which uses the symbol η for this quantity). We chose η by comparing ion densities between the Green function method (FSCC) and the conducting *explicit polarization* method with *surface* polarization charge placement. Ion densities for varying values of η are shown in Fig. B.3. In our study, we set $\eta=2.8$ ($\eta d = 11.9$) which is the value for which the ion density agrees with the Green function method.

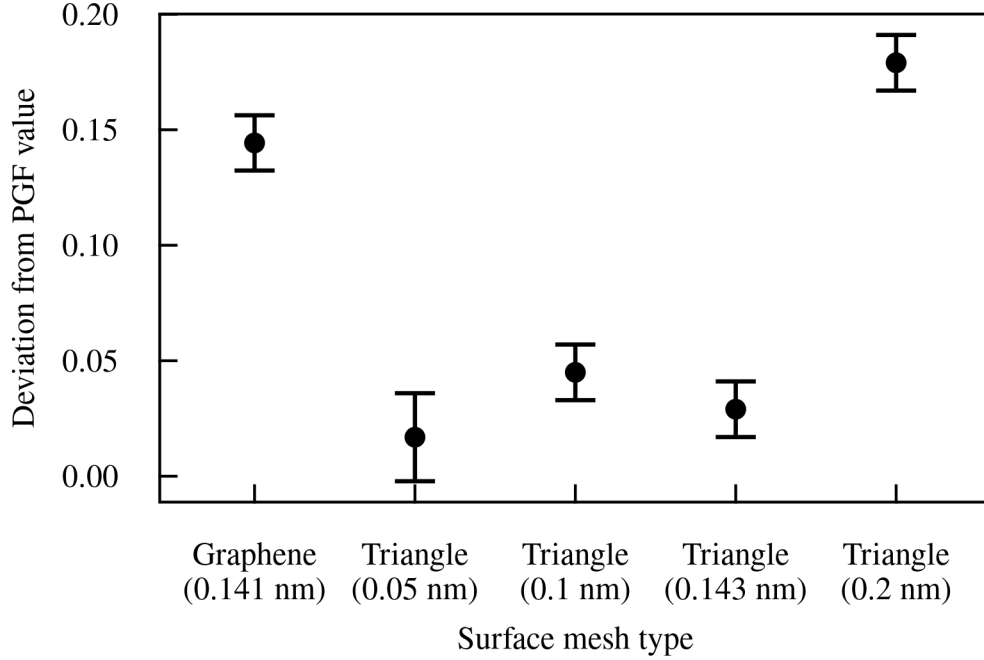


Figure B.2. Analysis of the effect of surface meshing of polarization charge points for *explicit polarization* models. This figure shows the ionic current difference between the PGF and *explicit polarization* models (*surface* placement), for dielectric confinement with $E = 8.275 \text{ k}_B\text{Te}^{-1}\text{d}^{-1}$, as a function of surface mesh type for a fixed box size. Current from the *explicit polarization* models (I_{pol}) is quantified as a deviation from the PGF value (I_{PGF}), which is calculated as: $(I_{\text{pol}} - I_{\text{PGF}})/I_{\text{PGF}}$. Graphene meshing is used in the main text, and thus the graphene point in this plot also appears in Fig. 4. All other points use a triangular mesh, with sizes varying as indicated. All simulations except the 0.05 nm mesh were run for 30 ns. These data indicate that placing polarization charge points on a finer mesh could improve the agreement between models in Fig. 4.

Note: The error bars for the 0.05 nm triangular mesh are larger than the others because this simulation is computationally expensive, and it was run for 13 ns instead of 30. We expect it to fully converge after another 7 ns.

Note that the *explicit polarization* model for dielectric surfaces does not include a similar parameter, because surface charge is distributed as N_g point charges exactly at $\{\mathbf{R}_i\}$.

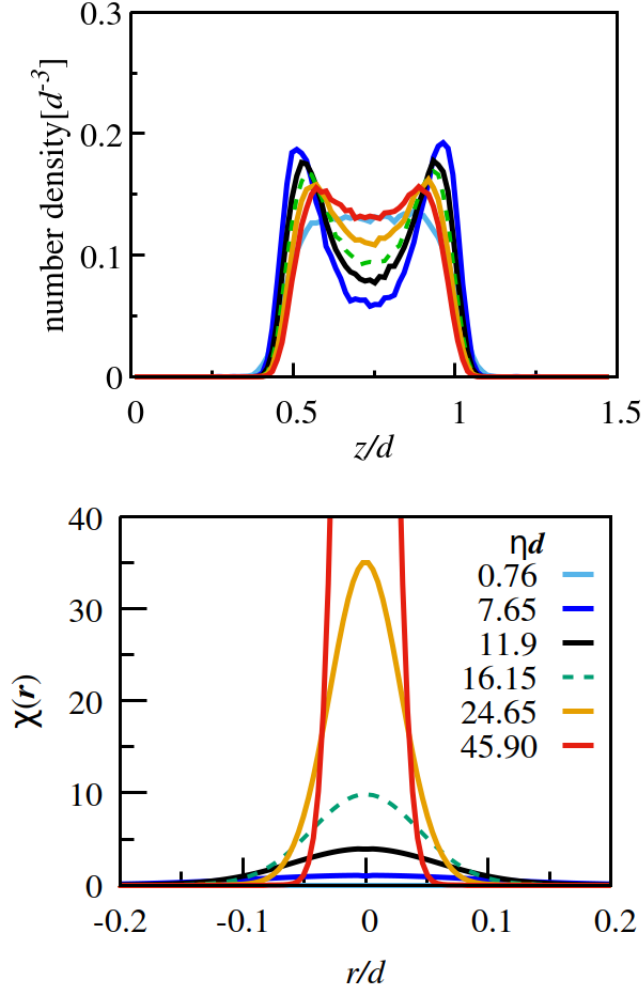


Figure B.3. Effect of the polarization charge distribution width (η) in the *explicit polarization* model for conductors with *surface* charge placement, as implemented in [45]. Here we show how the ion density is modified by changing η . (a) Ion number density profiles as a function of the position in the slit channel at different values of η and (b) the corresponding Gaussian charge distribution, $\chi(r)$. The dielectric constant in the space between the two surfaces is $\epsilon_w = 5\epsilon_0$ and $l_B = 26.4d$, as in the main text.

APPENDIX C

Supplementary information for Chapter 8

This appendix contains the supplementary information associated with Chapter 8.

The following was originally published in the Journal of Physical Chemistry C in 2021. It is reproduced here with permission of Hector Lopez-Rios, Monica Olvera de la Cruz, and the American Chemical Society.

Delocalization Transition in Colloidal Crystals: Supplementary Information

Hector Lopez-Rios,* Ali Ehlen,* Monica Olvera de la Cruz

* equally contributing first authors

Reprinted with permission from:

Journal of Physical Chemistry C 2021, **125**, 1, 1096-1106, DOI:

10.1021/acs.jpcc.0c09730. Copyright 2021 American Chemical Society.

<http://pubs.acs.org/articlesonrequest/AOR-8UNXPV6QS5KATYESGAJA>

C.0.1. BCC Crystal Stability

# chains	T_{\min}	T_{deloc}	T_{\max}	T_{melt}
4	0.7	0.7	1.25	1.28
6	0.7	1.2	1.6	1.65
8	0.75	1.5	1.81	1.82
10	0.61	1.75	1.85	1.9

Table C.1. The (reduced) temperatures of the onset of delocalization (T_{deloc}) and the melting temperature of the crystal (T_{melt}). T_{deloc} is a qualitative measure and roughly corresponds to when the diffusion constant of the small particles is significantly greater than zero. T_{\min} and T_{\max} are the lowest and highest simulation temperatures that produced BCC lattices. T_{melt} is the lowest temperature at which the system is melted.

The thermodynamic stability of the BCC lattice is supported by several trial simulations in which we initialized the 6:1 system with the large particles in different lattice configurations (BCC, FCC, SC, BCT). In those simulations, almost all systems within this temperature range converged to a BCC lattice in equilibrium; this is possible because the simulation box was able to change size and shape during our NPT simulations (see Section *Parameters and simulation scheme*). The range of temperatures used in our simulations for each number of chains per small particle is listed in Table C.1 in columns T_{\min} and T_{\max} . Above the temperature range we report, the simulations show a melted lattice, starting at T_{melt} . Below that temperature range, we see the large particles form other lattices, most of which are SC; this regime requires further study. The values of T_{\max} also demonstrate that crystals are stronger when the small particles have more grafted chains: more chains on the small particles leads to higher melting temperatures. Additionally, in Figure C.1 we show the pair distribution functions, $g(r)$, for all simulations. We observe an ordinary coarsening of BCC peaks as the temperature is increased, without any hallmark for the onset of delocalization.

C.0.2. Determining T_{deloc}

We estimated T_{deloc} for each system as the temperature at which its diffusion increases over a threshold (0.1). Qualitatively, this represents when noticeable diffusion begins. The diffusion coefficient, D , of interstitials can be related to the free energy barrier between interstitial sites as follows [186]:

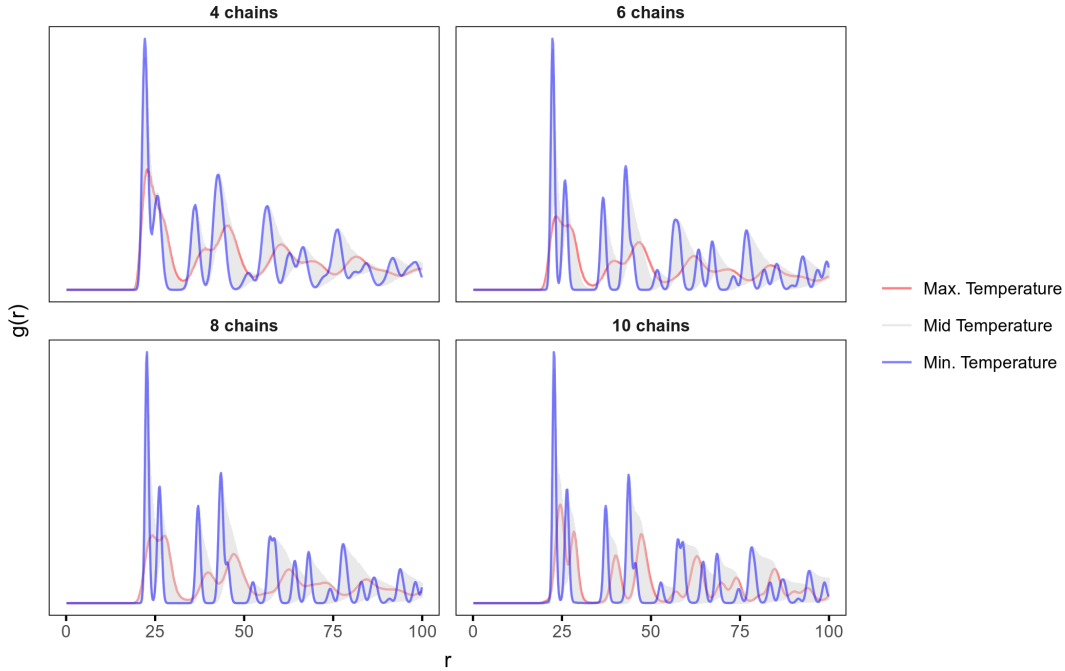


Figure C.1. The pair distribution functions, $g(r)$, for all interaction strengths over their respective temperature range, from T_{\min} to T_{\max} . The pair distribution curves at different temperatures have been color coded. Blue corresponds to T_{\min} , red corresponds to T_{\max} , and all other intermediate temperatures are grey. The coarsening of the BCC peaks is observable over increasing temperature, which is expected.

$$(C.1) \quad D \propto e^{-\Delta G/k_B T}$$

Using this relation, we can fit an exponential curve to the diffusion coefficients in Figure 4B and find the Gibbs activation free energy, ΔG . The resulting fitting parameters, ΔG , are shown in Figure C.2. We can see that the free energy barrier to diffusion increases linearly with the number of chains on the small particles, with a slope of roughly 6.4 kJ/mol-linker. This energy is approximately the enthalpy associated with one interactive

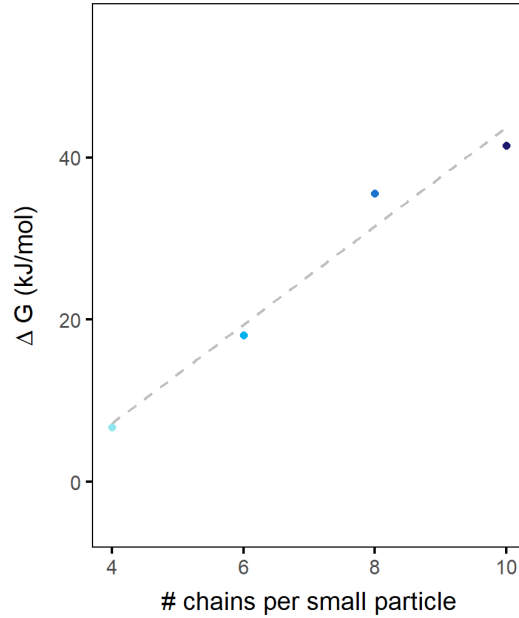


Figure C.2. The fitting parameter ΔG in Equation (C.1). This increases linearly with the number of chains per small particle.

bead localizing in its most energetically favorable volume (darkest red regions in the 004 plane in Figure 2B). This might mean that the contribution of each additional chain is generally enthalpic.

The smooth transition of the diffusing small particles is reminiscent of that of the glass transition curves of enthalpy and volume [187, 188] around the material's glass transition temperature, T_g . Because of the smoothness of the transition, T_g has many definitions. One is the temperature at which the viscosity of the material surpasses a particular value (10^{12} Pa · s). In a similar manner, we defined T_{deloc} as the temperature at which the diffusion coefficient passes a small but specific threshold.

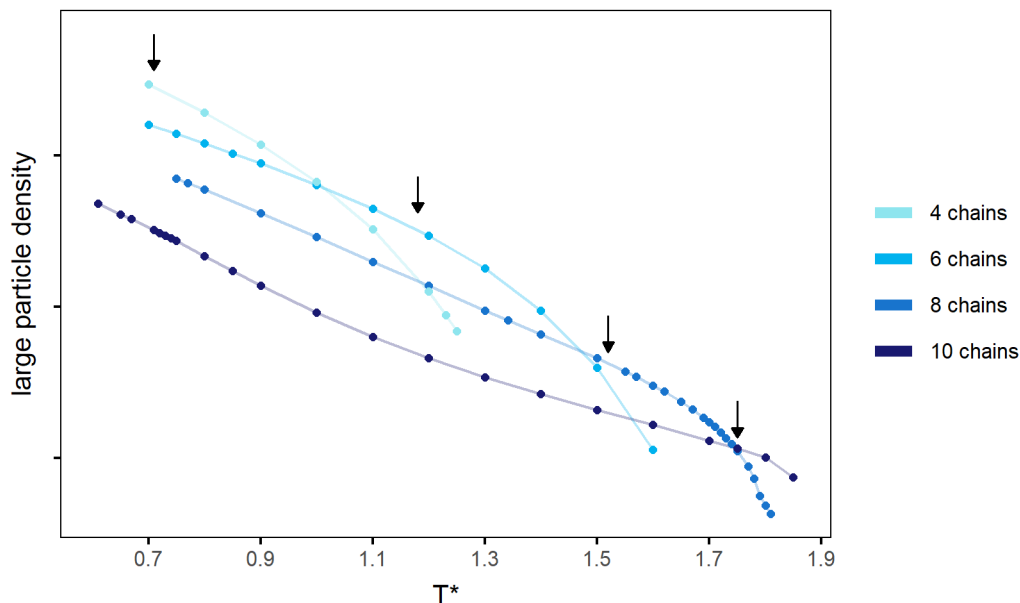


Figure C.3. Lattice density ($1/a^3$) for different cases, as a function of temperature.

This version of T_{deloc} has consistently shown to correlate well with the onset of non-linear behavior of physical and thermodynamical properties as seen in Figure 4 and Figure C.3.

C.0.3. Calculation of occupied volume

The parameter ϕ_{occupied} was inspired by an attribute of delocalization given by the spatial extent of π electrons in aromatic compounds. In these molecules, atomic orbitals conjoin to form hybrid orbitals that span over a carbon based ring backbone. We calculated the volume occupied by the top 70% of small particles' probability in the entire crystal for every simulation, as a fraction of the volume available to the small particles. To do so, we used voxels with side length equal to the diameter of the small particle centers and calculated the small particle centers' probability density distribution (normalized

visitation frequency) for each voxel over all production simulation frames. Then, we ordered the voxels by that probability and summed the probability associated with the first (highest probability) voxels until we reached 0.7. Then, we totaled the volume of all those voxels. Finally, we divided the resulting volume by the available volume, which is the total simulation box volume minus the total volume of the large particles. The resulting fraction is ϕ_{occupied} .

To determine the stability of this metric, we calculated ϕ_{occupied} using different voxel sizes and cutoff values. Occupied volume values using voxel sizes smaller than the diameter of the small particle did not converge with number of frames while the others did. It is understandable for smaller voxels to converge slower than larger ones given that sampling is greatly reduced (by $\sim \delta l^3$, where δl is the difference of side length between different size voxels). This can be corrected with longer simulation times for increased sampling but, that would likely not change the trend obtained with slightly larger voxels. However, it is important to note that using different voxel sizes gives different occupied volume values that vary proportional to the voxel size; bigger voxels equal greater occupied volume values. Thus, this method of calculating ϕ_{occupied} is qualitative, rather than quantitative: changing voxel size does not change the behavior of ϕ_{occupied} with temperature, but it does change the overall value. Larger voxels greatly coarsen space and thus we chose to use voxels that reflect the dimensions of the species under question, meaning side lengths close to the diameter of the small particle. Any value approximating the latter length should all give occupied volume values with similar exponential behavior upon the onset of delocalization.

C.0.4. Calculation of the specific heat c_p

We calculated the specific heat per particle using:

$$(C.2) \quad c_p = \frac{1}{N} \frac{\langle H^2 \rangle - \langle H \rangle^2}{k_B T^2} \quad \text{where, } \langle H \rangle = \langle U \rangle + P \langle V \rangle.$$

The $\langle \cdot \rangle$ operator signifies an ensemble average. In order to calculate the average internal energy, $\langle U \rangle$, of a system, we took into account all known energy contributions of all particles within it, *i.e.* all forms of potential energy (excluded volume interactions and Gaussian bond potentials) and kinetic energy, both translational and rotational. We also calculated c_p employing thermodynamic principles, which should result in the same values if the system is sufficiently large:

$$(C.3) \quad c_p = \frac{1}{N} \left(\frac{\partial \langle H \rangle}{\partial T} \right)_{N,P}.$$

We used cubic spline fitting for $\langle H \rangle$ and calculated its derivative. Both methods give similar results for the unconstrained simulations but they are not identical. A large amount of data is needed to obtain smooth curves from Equation C.2 but they appear to be converging to those values obtained by Equation C.3 for the unconstrained simulations. Additionally, given that the kinetic energy scales linearly with temperature and particle velocity distributions follow that of Maxwell-Boltzmann, we neglected kinetic energy contributions to the internal energy and observed no qualitative change in c_p curves. Therefore, we report c_p curves obtained by Equation C.3 without the kinetic energy contribution to the internal energy for the unconstrained simulations. For the fixed lattice simulations we only employed Equation C.2 to calculate c_p because $\langle H \rangle$ for both sets of

simulations are almost identical and Equation C.3 will not reflect the reduction in energy modes due to fixing the lattice.

C.0.5. Evolution of the number of interacting particles as a function of temperature

Here we show the average number of unique large particles interacting with each the small particle as a function of temperature. The small particles occupy the BCC tetrahedral sites and are functionalized with identically sized chains. Therefore, they must interact with at most four unique large particles at any temperature even when delocalized. Figure C.4 shows that indeed the maximum number of unique large particles interacting with a small one is four for every system. But at temperatures above T_{deloc} , there is a non-negligible fraction of small particles interacting with a lesser amount. This is expected as this parameter is closely related to delocalization. The close relation between delocalization and the ratio of unique interacting large particles to small particles is heightened by both showing continuous behaviour during delocalization. Additionally, Figure C.4 evidences the seeping of probability between nearest neighbor tetrahedral sites without the visitation to other sublattice sites, *e.g.* octahedral (6b Wyckoff positions) sites, which is also clear from Figure 3 and Figure 6.

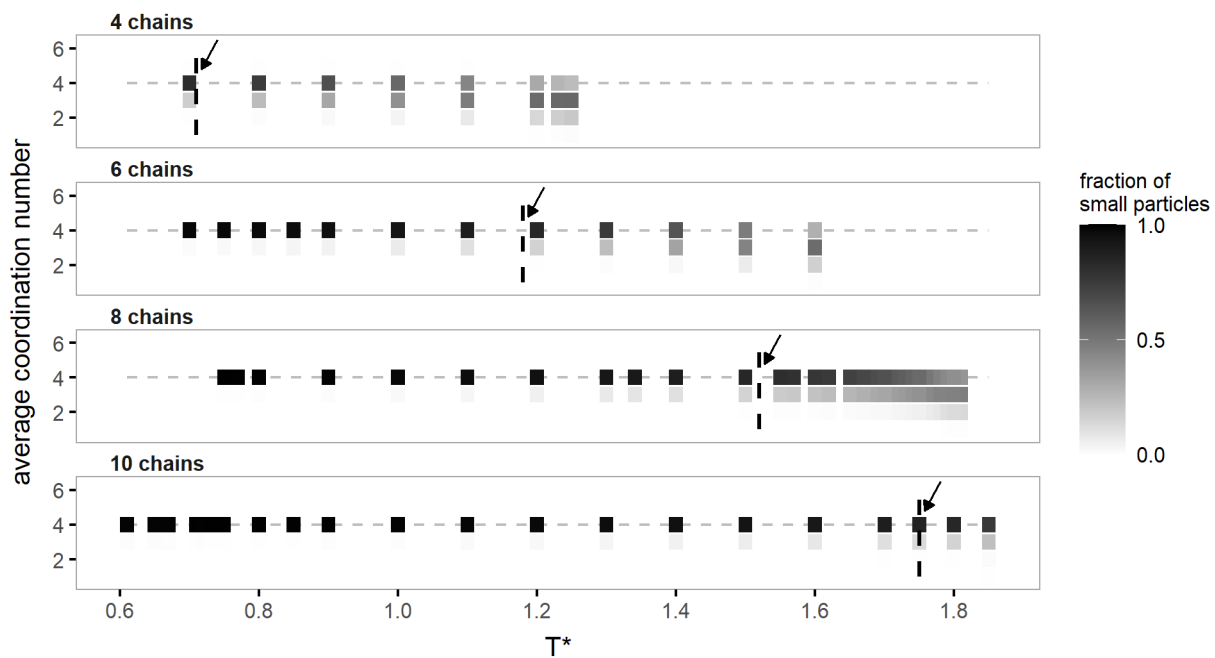


Figure C.4. Distribution of number of large particles interacting with each small particle. The horizontal grey dotted lines indicate interactions with 4 large particles, which is expected for a small particle that is localized at a BCC tetrahedral site. An estimate of T_{deloc} , the onset of delocalization, is marked with an arrow and black dotted line for each system.

APPENDIX D

Supplementary information for Chapter 9

This appendix contains the supplementary information associated with Chapter 9.

The following was originally published in *Physical Review Materials* in 2021. It is reproduced here with permission of Hector Lopez-Rios, Monica Olvera de la Cruz, and the American Physical Society.

Phase transitions in colloidal crystals with sublattice delocalization:

Supplementary Material

Ali Ehlen,* Hector Lopez-Rios,* Monica Olvera de la Cruz

* equally contributing first authors

Reprinted with permission from:

Physical Review Materials 2021, **5**, 115601, DOI: 10.1103/PhysRevMaterials.5.115601

[https://journals.aps.org/prmaterials/abstract/10.1103/](https://journals.aps.org/prmaterials/abstract/10.1103/PhysRevMaterials.5.115601)

PhysRevMaterials. 5. 115601

D.1. Supplementary details on phase diagrams and simulation methods

D.1.1. More detailed simulation methods

More details on annealing, initializing with different configurations and system sizes, and determining crystal type

The majority of points on the phase diagram were simulated using more than one initial configuration. This was done to ascertain the system configuration for production which was later analyzed. Two main initial configurations were used, FCC and BCC. Both configurations began with a lattice parameter of 70σ which is always at least 3 times larger than any stable crystal lattice parameter obtained. With such a large initial lattice parameter, we expect that the equilibrium configuration of each simulation should not be affected or limited given their initial configuration. Therefore, we can assume simulations with different initial configurations, but same physical parameters, are effectively simulations of different system sizes, for example, simulations initialized as a FCC crystal will have two times the number of particles as those initialized as a BCC.

We implemented an annealing protocol for certain kinetically jammed simulations, and for situations in which multiple runs with the same parameter set resulted in different crystals (*i.e.* one initialized as an BCC and the other initialized as an FCC). In the cases where there was initial conflicting information about what the equilibrium lattice was, we annealed both until both simulations resulted in the same lattice. This was also true for systems exhibiting two-phase coexistence. If the percent of the box identified as BCC and FCC (using techniques described in the next section) were vastly different for runs, we also annealed both simulations to test whether they would converge to similar values. They did, and we did not use final values unless all simulations run under the same temperature, $n_s:n_l$, and number of chains per small particle agreed.

Most simulations that required annealing were systems with low composition. As described in the main text, the small particles interact with more large particles at lower small to large particle number ratios. This consequently drives the formation of denser crystals which are prone to kinetically trapped configurations. Different flavors of annealing protocols were employed, but all consisted in raising and lowering the heat bath's temperature albeit in different manners. The temperature ramps followed either an exponentially decaying sinusoidal, a square wave or a sequence of step functions of decreasing value. Additionally, larger simulation systems required higher maximum temperatures for their temperature ramp than smaller simulation sizes. In very unusual cases, only three points of the phase diagram, a barostat ramp was employed followed by a temperature ramp to verify the crystal's stability.

To determine crystal type resulting from a simulation, we analyzed the pair correlation function $g(r)$ of the large particles. The ratios of distances to peaks and relative peak

heights are unique for different crystal types (SC, BCC, FCC, *etc.*). Pair correlation functions were calculated using VMD [135] (without periodic boundary conditions because VMD's tool does not calculate $g(r)$ with periodic boundary conditions in simulation boxes that do not have right angles) and compiled in an online tool we built ¹. If $g(r)$ peak ratios and relative heights matched a known crystal (for example, BCC), we classified the crystal. If not, we used the Python package pymatgen [172] to identify the symmetry of the lattice, then compared to online databases such as AFLOW ² [173, 174], and verified by independently reproducing the $g(r)$ using AFLOW parameters and the python package freud. For example, this is how we identified A20 and A_d crystals. Finally, if the lattice visually resembled a BCT, we used calculations in Mathematica to predict the most likely $g(r)$ peak ratios as a function of c/a (see the Supplementary Materials section on BCT lattice parameters). If peak ratios from simulation matched any predicted value of c/a , we verified by reproducing the $g(r)$ with these parameters using the freud library [189].

D.1.2. Calculations of compositions in the systems exhibiting two-phase co-existence

Polyhedral template matching (PTM) [190] as implemented in OVITO [191] version 3.4 was used to identify which phase particles belonged to. This identification method relies on comparing the distances and graph symmetries of neighboring particles of a central particle with those of a perfect candidate crystal called template. Given the lack of a cut-off distance to identify neighboring particles and the nature of the graph analysis between template and simulation points, this method is more robust against thermal

¹available at [aliehlen.github.io/phase_diagrams](https://github.com/aliehlen/phase_diagrams)

²<http://www.aflowlib.org/>

fluctuations than other lattice identification algorithms like adaptive common neighbor analysis. Although, like any identification algorithm, the minimization and low value of an objective function is what determines the likelihood of whether or not a set of points corresponds to a given phase. It is here where some uncertainty enters this scheme of identification because a bounding value must be considered for the objective function. Here the objective function is a root-mean-square-deviation (RMSD) between two sets of points. One set is obtained from simulation coordinates and the other corresponds to lattice points from a perfect crystal. Here we used a maximum RMSD value of 0.5.

Using PTM we calculated the arithmetic mean of the number of particles in a certain phase over at least 100 uncorrelated frames. We compared data between simulations of different sizes (systems initialized as BCCs and FCCs) and average phase values seemed to be statistically equivalent. This indicates that the average phase values reported are not entirely dependent on system size and physically meaningful.

D.2. Full structure detail: phase diagrams and comparison of energy landscapes and simulations

D.2.1. Full phase diagrams and lattice specification

Here, we include full information about the plotted phase diagrams, including lattice parameters of the various lower-symmetry crystals reported in this paper. This is shown in Fig. D.1. Note that one BCT parameter ratio is still undefined. Below are listed the lattice points and parameter sets for all types of lattice reported.

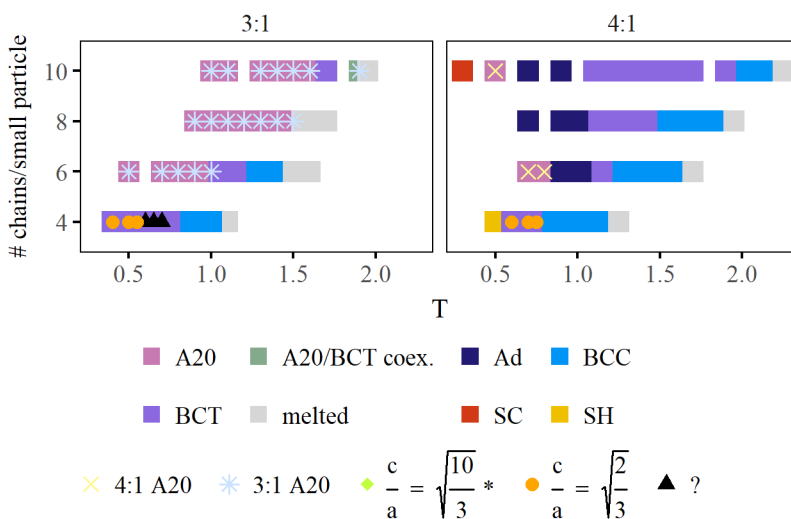


Figure D.1. Phase diagrams for the 3:1 and 4:1 composition systems, also shown in the main paper. These are superimposed with additional detail about the A20 and BCT crystal lattice parameters. Note that all unlabeled BCT points have $\frac{c}{a} = 2$. The parameters differentiating 3:1 A20 and 4:1 A20 crystals are defined in this section.

An interactive version of the phase diagrams, including plots of the pair correlation function of the large colloids in each lattice, can be found at https://aliehlen.github.io/phase_diagrams/.

A20: Orthorhombic, space group 63 (Cmcm)

Parameters: $a \neq b \neq c, y$

Parameter ratios observed: For A20 crystals observed in 3:1 systems, $b/a \sim 2.36$, $c/a \sim 1.44$, $y = 0.14$. For those in 4:1 systems, $b/a \sim 2.5$, $c/a \sim 1.4$ $y = 0.3613$

Basis points in $(\hat{x}, \hat{y}, \hat{z})$ basis:

$$\vec{a}_1 = (a, 0, 0)$$

$$\vec{a}_2 = (0, b, 0)$$

$$\vec{a}_3 = (0, 0, c)$$

Lattice points in $(\vec{a}_1, \vec{a}_2, \vec{a}_3)$ basis:

$$(0, y, 0.25)$$

$$(0, -y, 0.75)$$

$$(0.5, y - 0.5, 0.25)$$

$$(0.5, 0.5 - y, 0.75)$$

Primitive cell convention:

Basis points in $(\hat{x}, \hat{y}, \hat{z})$ basis:

$$\vec{a}_1 = \left(\frac{1}{2}, -\frac{1}{2}b, 0\right)$$

$$\vec{a}_2 = \left(\frac{1}{2}a, \frac{1}{2}b, 0\right)$$

$$\vec{a}_3 = (0, 0, c)$$

Lattice points in $(\vec{a}_1, \vec{a}_2, \vec{a}_3)$ basis:

$$(-y, y, 0.25)$$

$$(y, -y, 0.75)$$

A_d: Tetragonal, space group 129 (P4/nmm)

Parameters: $a = b \neq c, z$

Parameter ratios observed: $a = \sqrt{c}$. Various values of z between 0.4 and 0.5, increasing with higher temperature. When $z = 0.5$, this becomes identical to a BCT with $c'/a' = 2$.

Basis points in $(\hat{x}, \hat{y}, \hat{z})$ basis:

$$\vec{a}_1 = (a, 0, 0)$$

$$\vec{a}_2 = (0, a, 0)$$

$$\vec{a}_3 = (0, 0, c)$$

Lattice points in $(\vec{a}_1, \vec{a}_2, \vec{a}_3)$ basis:

$$\left(\frac{3}{4}, \frac{1}{4}, 0\right)$$

$$\left(\frac{1}{4}, \frac{3}{4}, 0\right)$$

$$\left(\frac{1}{4}, \frac{1}{4}, z\right)$$

$$\left(\frac{3}{4}, \frac{3}{4}, -z\right)$$

129a: Tetragonal, space group 129 (P4/nmm)

Parameters: $a = b \neq c, z$

Parameter ratios observed: $a = 0.94c, z = 0.3$. Note that this lattice is observed only once in our simulations, and this is in a low-temperature 5:1 system. It is visually similar to a BCC, but compressed in one direction in such a way that there are 10 interstitial sites instead of 12. It is also equivalent to an A_d without the first two lattice points.

Basis points in $(\hat{x}, \hat{y}, \hat{z})$ basis:

$$\vec{a}_1 = (a, 0, 0)$$

$$\vec{a}_2 = (0, a, 0)$$

$$\vec{a}_3 = (0, 0, c)$$

Lattice points in $(\vec{a}_1, \vec{a}_2, \vec{a}_3)$ basis:

$$\left(\frac{1}{4}, \frac{1}{4}, z\right)$$

$$\left(\frac{3}{4}, \frac{3}{4}, -z\right)$$

BCT: Tetragonal, space group 139 (I4/mmm)

Parameters: $a = b \neq c$

Parameter ratios observed: $c/a = 2$ (most common), $c/a = \sqrt{2/3}$, and one unclassified parameter set.

Basis points in $(\hat{x}, \hat{y}, \hat{z})$ basis:

$$\vec{a}_1 = (a, 0, 0)$$

$$\vec{a}_2 = (0, a, 0)$$

$$\vec{a}_3 = (0, 0, c)$$

Lattice points in $(\vec{a}_1, \vec{a}_2, \vec{a}_3)$ basis:

$$(0, 0, 0)$$

$$(0.5, 0.5, 0.5)$$

BCC: Cubic, space group 229 ($\text{Im}\bar{3}\text{m}$)

Parameters: $a = b = c$

Parameter ratios observed: N/A

Basis points in $(\hat{x}, \hat{y}, \hat{z})$ basis:

$$\vec{a}_1 = (a, 0, 0)$$

$$\vec{a}_2 = (0, a, 0)$$

$$\vec{a}_3 = (0, 0, a)$$

Lattice points in $(\vec{a}_1, \vec{a}_2, \vec{a}_3)$ basis:

$$(0, 0, 0)$$

$$(0.5, 0.5, 0.5)$$

FCC: Cubic, space group 225 ($\text{Fm}\bar{3}\text{m}$)

Parameters: $a = b = c$

Parameter ratios observed: N/A

Basis points in $(\hat{x}, \hat{y}, \hat{z})$ basis:

$$\vec{a}_1 = (a, 0, 0)$$

$$\vec{a}_2 = (0, a, 0)$$

$$\vec{a}_3 = (0, 0, a)$$

Lattice points in $(\vec{a}_1, \vec{a}_2, \vec{a}_3)$ basis:

$$(0, 0, 0)$$

$$(0.5, 0.5, 0)$$

$$(0.5, 0, 0.5)$$

$$(0, 0.5, 0.5)$$

D.2.2. Types of BCT lattices

The BCT crystals that we have observed have c/a ratios that lead to higher-symmetry arrangements. This can be seen in Fig. D.2. This means that the distance between distinct lattice points are equal. For example, for $c/a = \sqrt{2}$ (when a BCT structure is equivalent to an FCC structure), the distance from the $(0,0,0)$ point in a BCT unit cell to the adjacent corner (a) is equal to the distance to the point at the center of the unit cell ($\frac{1}{2}\sqrt{c^2 + 2a^2}$).

D.2.3. Identification of interstitial sites using unit cell energy landscape

We found that, with the exception of the FCC crystal, the potential energy landscape is a good predictor of the location of the small colloid species. The small particle cores localize at the near-neutral points in the energy landscape, while the interactive beads at the ends of their chains localize at or on the border of the energy wells (this is dependent on the reach of the chains). Here, we show direct comparisons between calculated energy

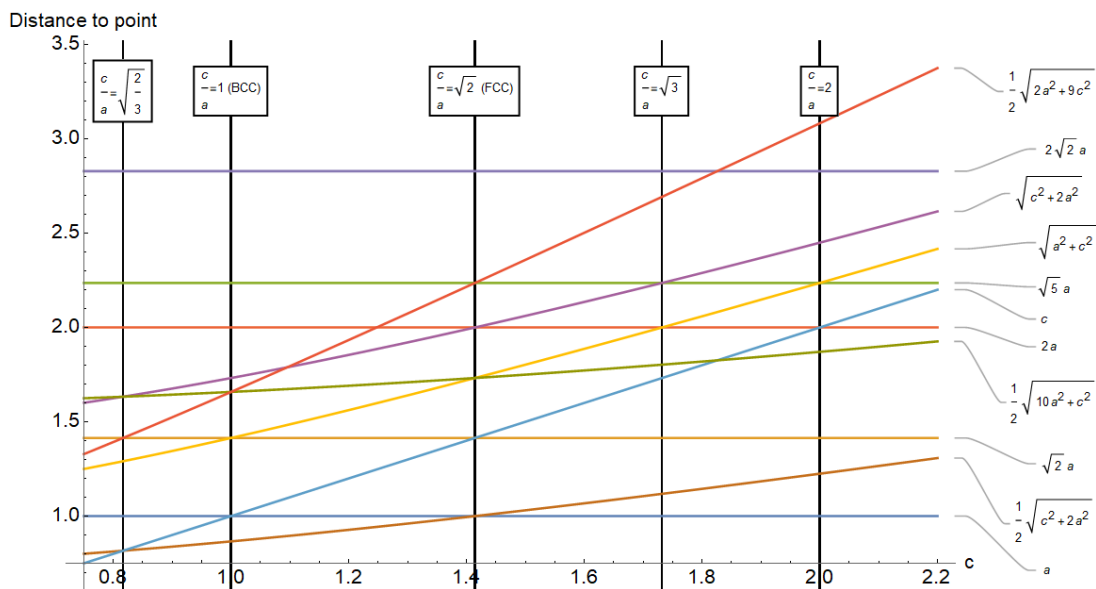


Figure D.2. For a value of $a = 1$, the distance from the point $(0, 0, 0)$ of a BCT unit cell to the 11 nearest points in the lattice, as a function of the value of c . Each line on the plot represents one lattice point. Higher symmetry points (where the lines cross *i.e.* where distances to multiple distinct lattice sites are equal) are highlighted with vertical black lines. These correspond to the c/a ratios seen in BCT lattices observed in this study.

landscapes and simulations results. It is difficult to adequately compare three dimensional structures in two dimensions, so we have included representative two-dimensional slices for each crystal type as an example in Table D.1. Mathematica notebooks showing three dimensional plots of the energy landscapes are available upon request.

D.3. Supplementary simulation results

D.3.1. Nearest neighbor plots for identifying lattices

As we have seen, the local spatial symmetry of the small particles varies as a function of the crystal phase, see Table D.1, this is to be expected. But if the sublattice is delocalized,

A20 (3:1): $\perp \vec{a}_3$		A20 (3:1): $\perp \frac{1}{2}\vec{a}_3$		A20 (4:1): $\perp \vec{a}_3$		A20 (4:1): $\perp \frac{1}{2}\vec{a}_3$	
Simula- tion	Theory	Simula- tion	Theory	Simula- tion	Theory	Simula- tion	Theory
A_d : $\perp \vec{a}_3$		A_d : $\perp \frac{1}{4}\vec{a}_3$		BCT: $\perp \vec{a}_3$		BCT: $\perp \frac{1}{2}\vec{a}_3$	
Simula- tion	Theory	Simula- tion	Theory	Simula- tion	Theory	Simula- tion	Theory
FCC: $\perp \frac{1}{8}\vec{a}_3$		FCC: $\perp \frac{3}{8}\vec{a}_3$		FCC: $\perp \frac{1}{4}\vec{a}_3^*$		Simula- tion	Theory
Simula- tion	Theory	Simula- tion	Theory	Simula- tion	Theory	<i>probabil- ity</i>	$U_{pot.}$

Table D.1. Comparison between simulation results and theoretically calculated energy landscapes. Simulation: visitation frequency of the small particle centers from various simulations in a given slice of the unit cell. Theory: potential energy landscape of a single interactive chain end in the same slice of a unit cell of large particles, calculated using an average lattice parameter from simulation. All slices are taken parallel to the plane formed by \vec{a}_2 and \vec{a}_3 , and at the intersection with \vec{a}_3 indicated by \perp . Note the similarity between the regions of high probability in simulation to regions of near-zero potential energy. The 6:1 case can be found in [151]. *The tetrahedral sites shown here are only filled when the $n_s:n_l > 8:1$, *i.e.* once the 32f sites are full. The other FCC images depict 8:1 systems.

the small particles' coordination number to large particles must be different than when localized. This is due to their exploration of regions that are between their interstitial sites and should be smaller compared to when localized. Therefore, observing the coordination number distribution of the small particles is indicative of the crystal phase, see Figure D.3. Additionally, if there is a large percentage of coordination numbers that is smaller than for a localized sublattice of the same crystal phase, this is a good indication of sublattice delocalization. For example, we know that four is the coordination number of the small particles to large particles in a BCC lattice (hence, the tetrahedral interstitial site nomenclature), therefore, a significant percentage of lower coordination numbers would be indicative of a delocalized sublattice.

D.3.2. Anisotropy of vibrations in BCT lattices

The vibrations of BCT lattices are anisotropic, which can be seen in Fig. D.4. The x , y , and z directions are based on simulation and do not necessarily correspond to lattice directions. The important differences between BCT and other lattice types is that the majority of BCT lattices show vibrations that are not equal in all directions. We hypothesize that the vibrations in the BCT lattices are perpendicular to the (001) planes (direction of \vec{a}_3), because of the spacing in the BCT unit cell. Modeling a BCT ($c/a = 2$) with thermal noise that is larger in the \vec{a}_3 direction produces a pair correlation function that matches that of simulation.

According to the combination of Fig. D.4 and Fig. 4, when a crystal transforms from BCT to BCC, lattice vibrations become more isotropic and greater in magnitude, which is a component of the entropic favorability of the BCC lattice.

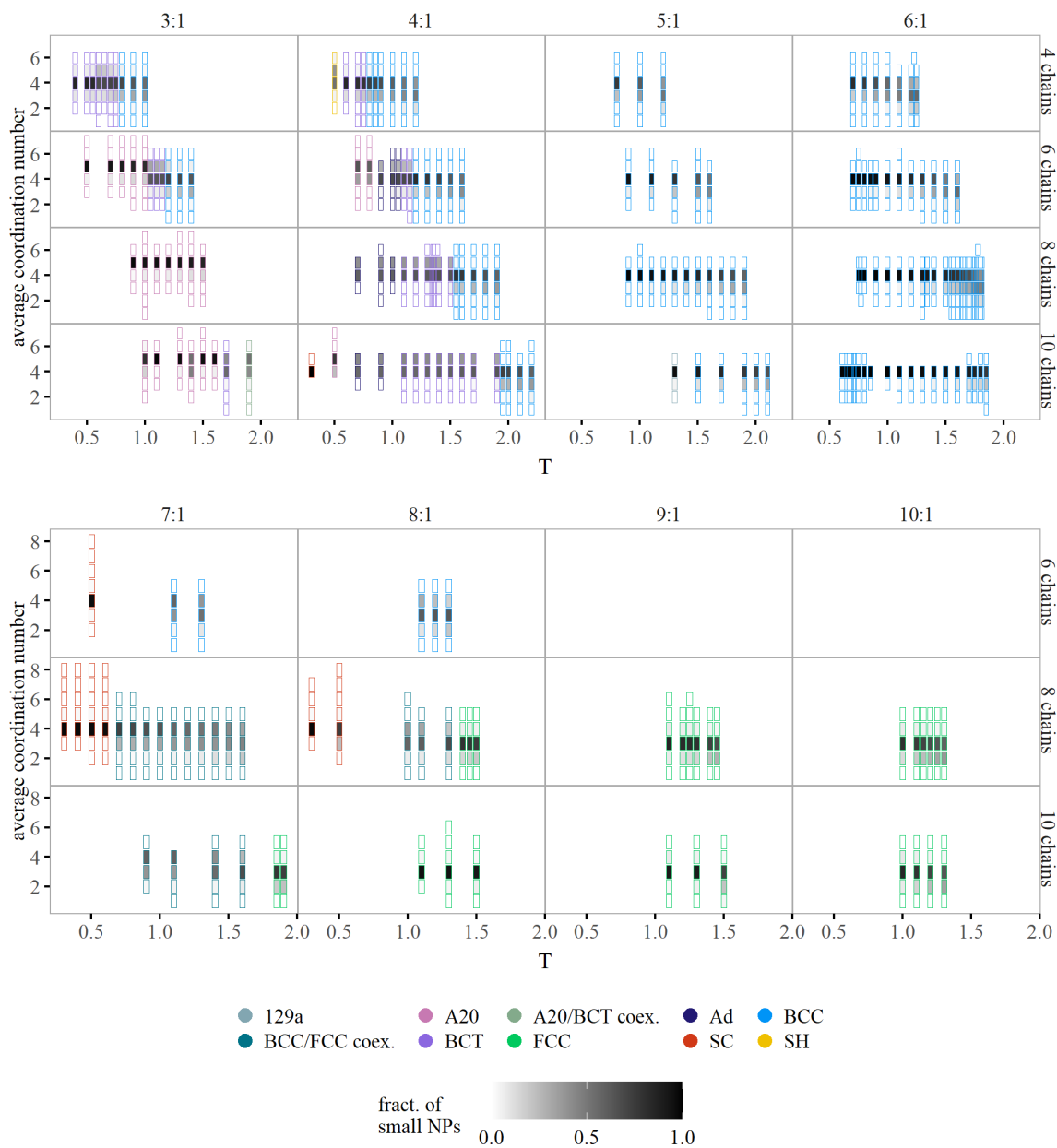


Figure D.3. Histograms of how many large particles each small particle is interacting with as a function of T , for all (non-melted) simulations used in this work. Colors indicate the lattice type. Each lattice type had a unique distribution, which tends toward lower numbers with increasing T . 6:1 data taken from [151] and included for comparison.

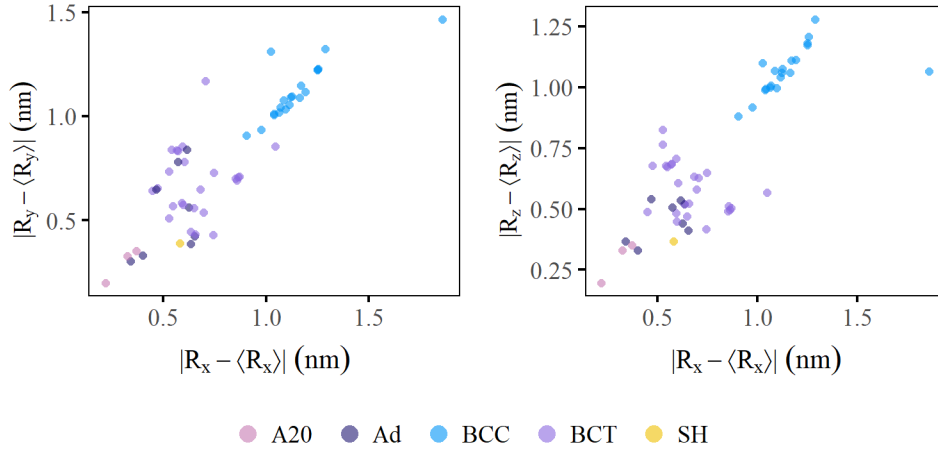


Figure D.4. Lattice vibration components for different types of lattices. Vibrations in BCC and A20 lattices are isotropic because all components are approximately equal. Vibration components of BCT crystals are not equal, indicating anisotropy. Different points correspond to different $n_s:n_l$ ratios, number of chains per small particle, and T .

D.3.3. Lattice density as a function of temperature

Plot of large particle number density (# large particles per volume) as a function of T , $n_s:n_l$, and number of chains per small particle. Density is a more useful metric for comparison than lattice parameter, because some crystal types are characterized by multiple lattice parameters.

D.3.4. Small particle chain end-to-end distance

End-to-end distance of the chains attached to the small particles. This decreases with temperature as chains explore more configurational space, and increases with number of chains per small particle because of excluded volume effects. The crystal lattice configuration also impacts the chain end-to-end distance, as can be seen in the small but consistent change in values between different crystal types.

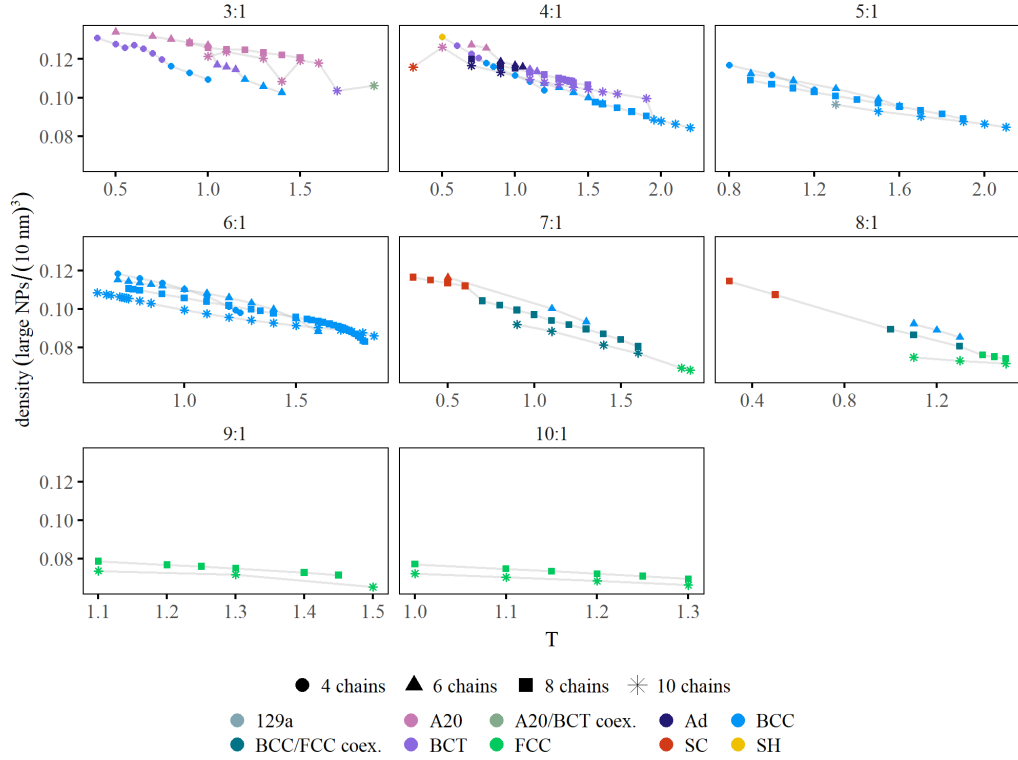


Figure D.5. Large particle number density of all (non-melted) simulations used in this work.

D.3.5. Vibrational Density of States

The vibrational density of states $D(\omega)$ is calculated by normalizing the real part of the Fourier transform of the velocity auto-correlation function (VACF) of the large particles [164]:

$$(D.1) \quad \text{VACF} = \frac{\langle \vec{v}(t) \cdot \vec{v}(0) \rangle}{\langle v^2(0) \rangle}$$

An approximate resolution of 37 ps is used for sampling data points for the construction of the VACF. In the left panel of Fig. D.7 we observe $D(\omega)$ for two different crystals. The left panel shows data for a 4:1 system with 8 grafted chains per small particle at

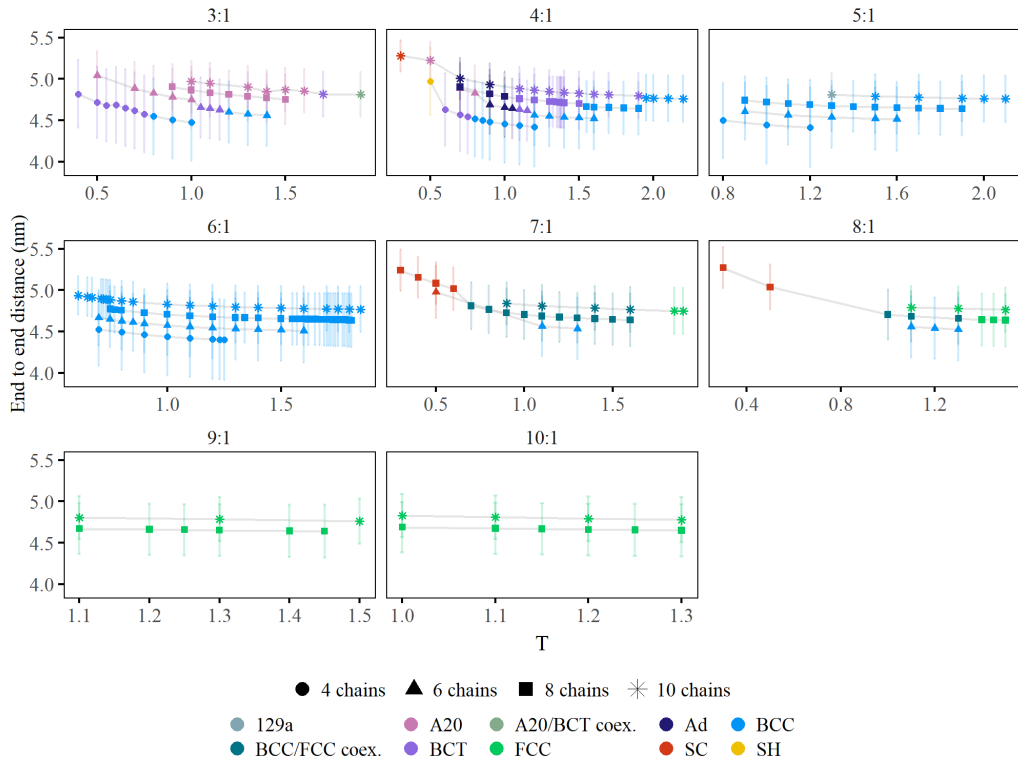


Figure D.6. Average end-to-end distance of the chains grafted on the small particles for all (non-melted) simulations used in this work.

$T = 1.3$ (blue curve, forms a BCT with a localized sublattice) and $T=1.7$ (red curve, forms a BCC with a delocalized sublattice). The lower temperature system has a more complex $D(\omega)$ than the higher temperature one. This is relevant given that a bias towards lower vibrational frequencies at higher T is also observed in the Peierls metallic-insulator transition of VO_2 [161].

The right panel of Fig. D.7 shows $D(\omega)$ for a 6:1 system with 8 grafted chains per small particle at $T = 1.3$ (blue curve, forms a BCC with a localized sublattice) and $T = 1.7$ (red curve, forms a BCC with a delocalized sublattice). There is little qualitative difference in the shape of $D(\omega)$ between two crystals with the same structure but different

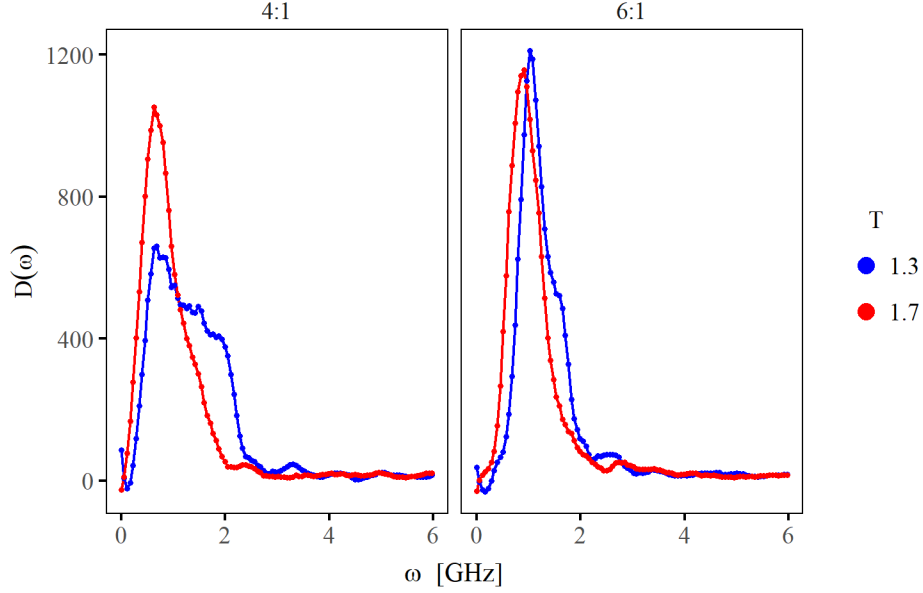


Figure D.7. Vibrational density of states for two systems that exhibit different sublattice transitions. The 4:1 system (left panel) with 8 grafted chains per small particle exhibits a first order sublattice phase transition at which it forms a BCT lattice with a fixed sublattice at $T = 1.3$ and forms a BCC phase with a delocalized lattice at $T = 1.7$. A similar system but with a 6:1 ratio (right panel) remains a BCC lattice when its sublattice is localized at $T = 1.3$ (blue curve) and delocalized $T = 1.7$ (red curve)

degrees of sublattice delocalization, though there is a slight shift toward lower frequencies at higher temperature.

D.3.6. Vibrational Entropy

We calculate vibrational entropy S_{vib} using

$$(D.2) \quad S_{\text{vib}} = 3 \int_0^{\omega_{\text{max}}} d\omega D(\omega) [(n(\omega) + 1) \ln(n(\omega) + 1) - n(\omega) \ln(n(\omega))]$$

where $D(\omega)$ is the vibrational density of states and $n(\omega) = \frac{1}{e^{\frac{\hbar\omega}{k_B T}} - 1}$ is the Bose-Einstein occupation factor. We use a cutoff frequency of $\omega_{\text{max}} = 6$ GHz. This expression for S_{vib}

has been employed with a $D(\omega)$ obtained from either experimental measurements [161] or simulations [162].

D.3.7. Existence of crystals with grain boundaries at 7:1 $n_s : n_l$

As discussed in Section 9.2.2.3 of the main text, we observe the existence of grain boundaries in mostly BCC lattices for 7:1 systems with 8 and 10 grafted chains per small particle at low T . This is shown in Fig. D.8 where the left image corresponds to a mostly BCC lattice with a grain boundary in its diagonal, while the right image corresponds to its sublattice composed of small particles. Interestingly, we do not see the appearance of stable grain boundaries in 7:1 systems with 6 grafted chains per small particles, we posit this is due to the lower enthalpic effects of the small particles that prevents the growth of a stable grain boundary.

D.3.8. Momentum transfer of the lattice to neighboring small particles

In order to quantify the momentum coupling between the lattice and small particles for systems that exhibit a first order crystal phase transition, we calculated the velocity-cross correlation function [165–167]

$$\gamma(t) = \frac{\langle \vec{v}_{s,i}(t) \cdot \vec{v}_{l,j}(0) \rangle_R}{\sqrt{v_s^2(0)v_l^2(0)}}$$

where $\vec{v}_{s,i}$ is the velocity of the i -th small particle, $\vec{v}_{l,j}$ is the velocity of the j -th large particle and $\langle \cdot \rangle_R$ is a restricted ensemble average over pairs whose distance $r = \sqrt{\|\vec{r}_{s,i} - \vec{r}_{l,j}\|^2}$ is within a range R . In this work, we choose $R \in (0, 15.75)\sigma$ where σ is the simulation length unit. $\gamma(t)$ is then interpreted as the momentum imparted by a large particle to

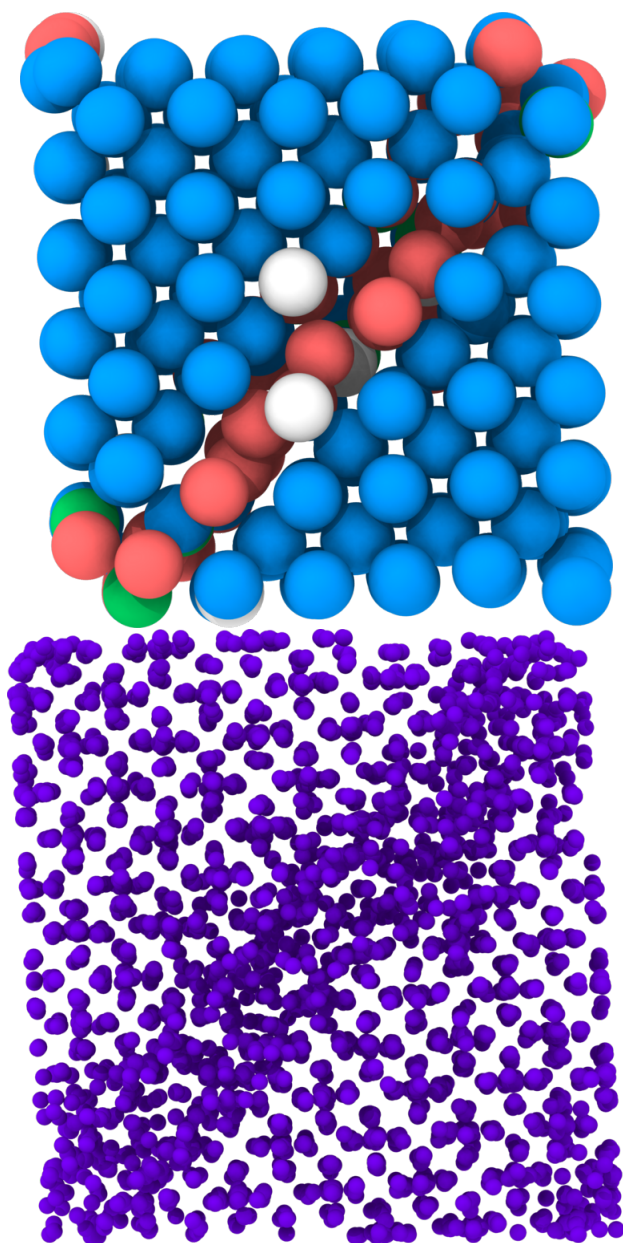


Figure D.8. Formation of grain boundaries in 7:1 systems with mostly a BCC lattice and 8 and 10 grafted chains per small particles at low T . The left image represents a snapshot of only the large particles where the color blue denotes a BCC lattice. The colors green, red, and white represent the HCP, FCC, and no lattice, respectively. The right image is the sublattice of the left image.

small particles within a sphere with radius 15.75σ , and a slower decay of the oscillations of $\gamma(t)$ signify a greater momentum exchange. In the left panel of Fig. D.9, we plot $\gamma(t)$ for a 4:1 mixture with 8 grafted chains on the small particles at two different temperatures. The system at $T = 1.3$ (blue curve) forms a BCT lattice with a localized sublattice, while at $T = 1.7$ (red curve) it has transitioned to a BCC crystal with a delocalized sublattice. Here we see a greater momentum exchange from the large particles to the small particles when the 4:1 system in the sublattice delocalized BCC phase, consistent with a Peierls insulator-metal transition. Meanwhile, for comparison to a system that does not exhibit a Peierls-like transition, the right panel shows $\gamma(t)$ for a 6:1 system with 8 grafted chains per small particles and for the same temperatures as the systems on the left. These crystals are both BCC lattices, but the sublattice is localized at lower T (blue curve) and delocalized at higher T (red curve). We observe no clear difference between the system with a localized sublattice and that with a delocalized one. This is contrasting to the 4:1 case, which had a first order sublattice transition.

D.3.9. Heat capacity c_P

We calculate the heat capacity c_P of all crystal phases using

$$(D.3) \quad c_P = \frac{1}{N} \left(\frac{\partial \langle H \rangle}{\partial T} \right)_{N,P} \approx \frac{1}{N} \frac{\Delta \langle H \rangle_{N,P}}{\Delta T}$$

Where N is the total number of particles in the system, H is the enthalpy of the system, T is the simulation temperature, and P is the simulation pressure. As indicated in Equation 3, we approximate the partial derivative of H with respect to T by calculating the ratio

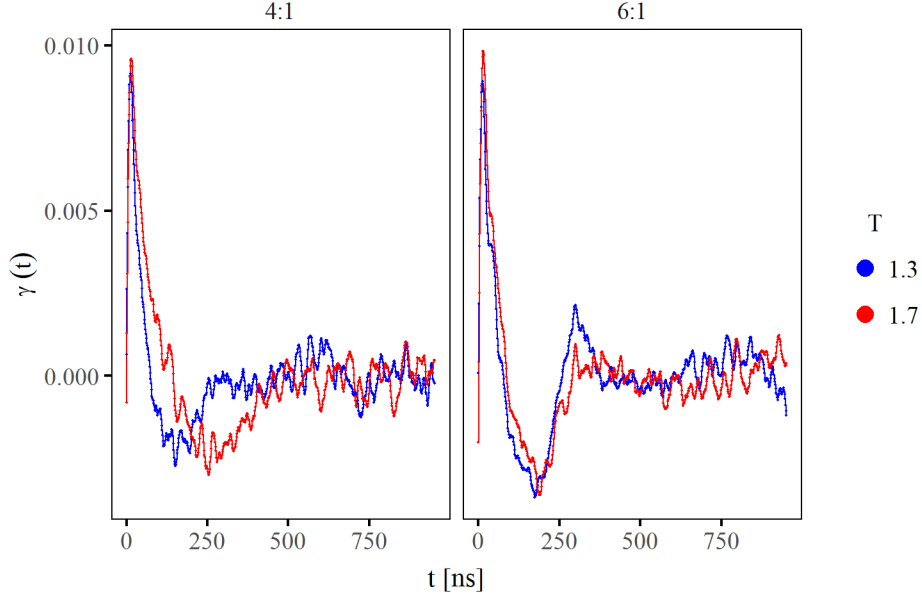


Figure D.9. Velocity cross-correlation function $\gamma(t)$ for a system that has a first order sublattice phase transition and another system that exhibits a continuous change from a localized to delocalized sublattice. The 4:1 system (right panel) with 8 grafted chains per small particle exhibits a first order sublattice phase transition at which it forms a BCT lattice with a fixed sublattice at $T = 1.3$ and forms a BCC phase with a delocalized lattice at $T = 1.7$. A similar system but with a 6:1 ratio (right panel) remains a BCC lattice when its sublattice is localized at $T = 1.3$ (blue curve) and delocalized $T = 1.7$ (red curve)

of differences of H and T between neighboring simulation points of identical physical parameters ordered sequentially by ascending simulation temperatures.

As indicated in the main text, a discontinuity in S indicates a first order phase transition, while the existence of an inflection point could indicate a continuous phase transition. We observe likely signatures of both behaviors in our system, as discussed in Section 9.2.2. of the main text. However, particularly since we are only estimating entropy using $S_{\text{vib.}}$, it is necessary to observe additional signatures within c_P to conclude which type of phase transition if any is present in these systems. To confirm the existence of a first order phase

transition, there must be an undefined point within c_P (corresponding to the discontinuity in S), while a discontinuity or divergence in c_P would be expected for a continuous phase transition. In simulations and in experiments, properly identifying a phase transition is a difficult task due to finite size effects and the amount of data needed to confirm such mathematical points. Our case is no different and thus we can only suggest the presence of these points given a combination of a qualitative understanding of our system, physical arguments by those such as Landau *et al.* [163], and observations in Fig. D.10 and Fig. D.11.

Fig. D.10(b) and Fig. D.11(b) show $S_{\text{vib.}}$, which appears to show a discontinuity at any transition from a non-cubic, localized lattice to a delocalized BCC lattice for systems with more than 4 chains per small particle, and a possible kink for systems with 4 chains per small particle. Fig. D.12 shows no change in lattice type and no such discontinuity in $S_{\text{vib.}}$. The plotted values of c_P show a spike at points of structural transition, indicated by a black circle. This indicates a first order phase transition, and by comparing interstitial and lattice sites and the argument of Landau *et al.*, we expect that for the transition BCT ($\frac{c}{a} = 2$) \rightarrow BCC. If this is the case, this spike should become an undefined point for larger system sizes and with much more dense data.

There are indications of small peaks or discontinuities at other transitions (BCT ($\frac{c}{a} = \sqrt{\frac{2}{3}}$) \rightarrow BCC, $A_d \rightarrow$ BCT ($\frac{c}{a} = 2$)). This may indicate the presence of a continuous phase transition, and with more data and by varying system size, we would be able to distinguish more precisely the behavior of c_P there.

In contrast, Fig. D.12 shows no crystal lattice transition at any temperature, and no peak in c_P . The change in slope of $S_{\text{vib.}}$ for the system with 10 chains per small particle

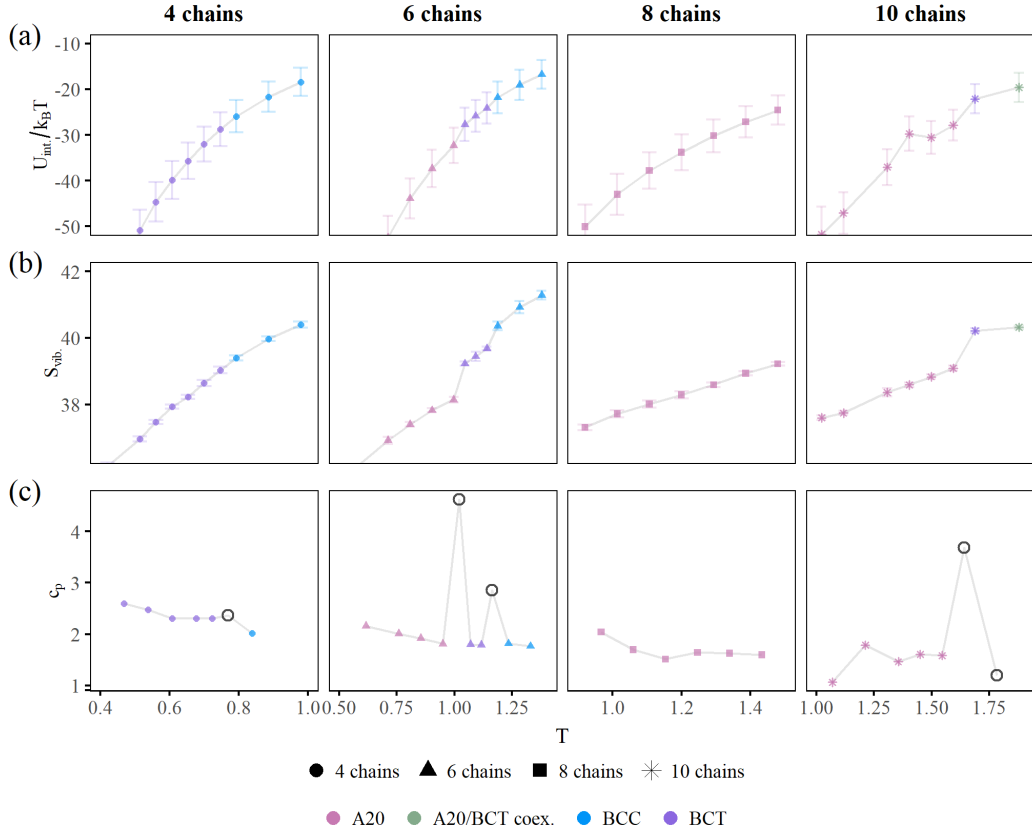


Figure D.10. Thermodynamic quantities of all stable crystal phases for particle number ratio 3:1 ($n_s : n_l$) as a function of simulation temperature. We plot the (a) average interaction energy per small particle $U_{\text{int.}}/k_B T$, (b) lattice entropy $S_{\text{vib.}}$, and (c) c_P , calculated as the slope between simulation points $j, j+1$ using $\frac{1}{N} \frac{H_{j+1} - H_j}{T_{j+1} - T_j}$, per Eq. (D.3). Hollow circles indicate points for which simulations j and $j+1$ resulted in different crystal types. We can see evidence for a first order phase transition for systems with greater than 4 chains. At region where there is a crystal phase transition, we see evidence for a discontinuity in the average interaction energy and lattice entropy, along with a peak in their c_P , indicative of a possible undefined point. For systems with 4 chains, we see evidence for a continuous phase transition in c_P , namely, a possible discontinuity between different crystal structures.

may indicate interesting behavior, but because this does not correspond to a transition to delocalization of the sublattice, it is out of the scope of this paper to explore this further.

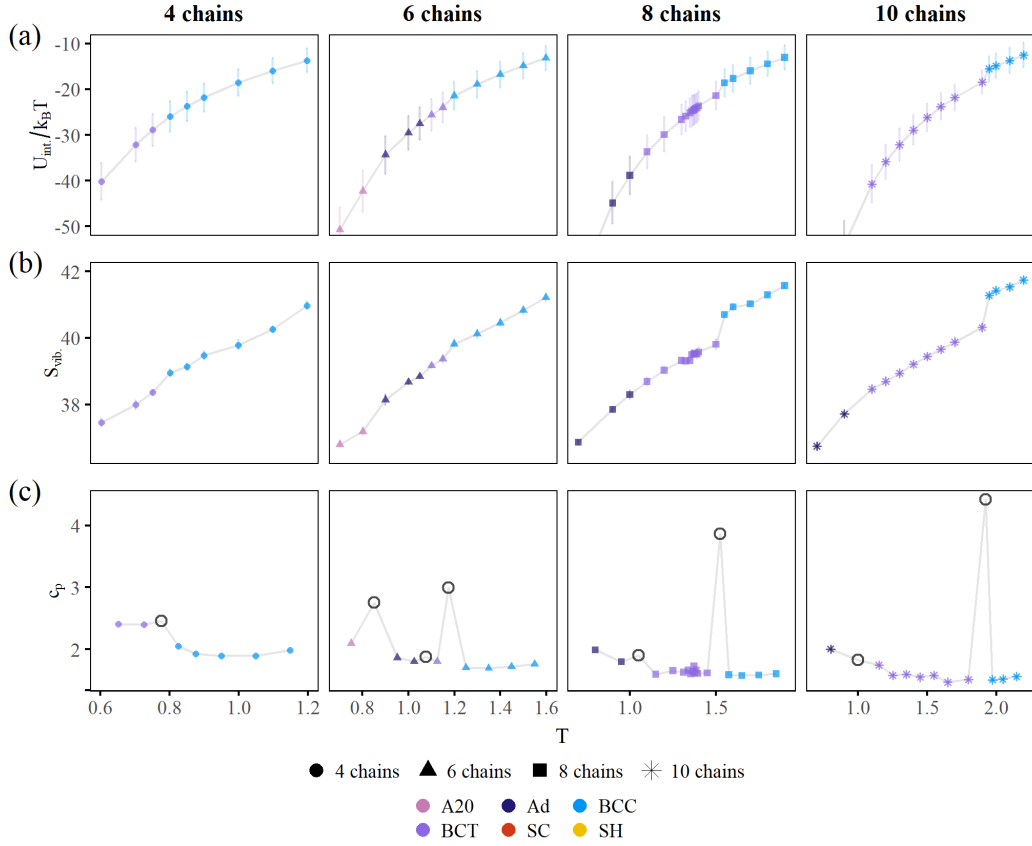


Figure D.11. Thermodynamic quantities of all stable crystal phases for particle number ratio 4:1 as a function of simulation temperature. We plot the (a) average interaction energy per small particle $U_{\text{int.}}/k_{\text{B}}T$, (b) lattice entropy $S_{\text{vib.}}$, and (c) c_P , calculated as the slope between simulation points $j, j + 1$ using $\frac{1}{N} \frac{H_{j+1} - H_j}{T_{j+1} - T_j}$, per Eq. (D.3). Hollow circles indicate points for which simulations j and $j + 1$ resulted in different crystal types. We can see evidence for a first order phase transition for systems with greater than 4 chains. At region where there is a crystal phase transition, we see evidence for a discontinuity in the average interaction energy and lattice entropy, along with a peak in their c_P , indicative of a possible divergence. For systems with 4 chains and for the $A_{\text{d}} \rightarrow \text{BCT}$ transitions, we see evidence for a continuous phase transition, namely, a possible discontinuity in c_P between different crystal structures.

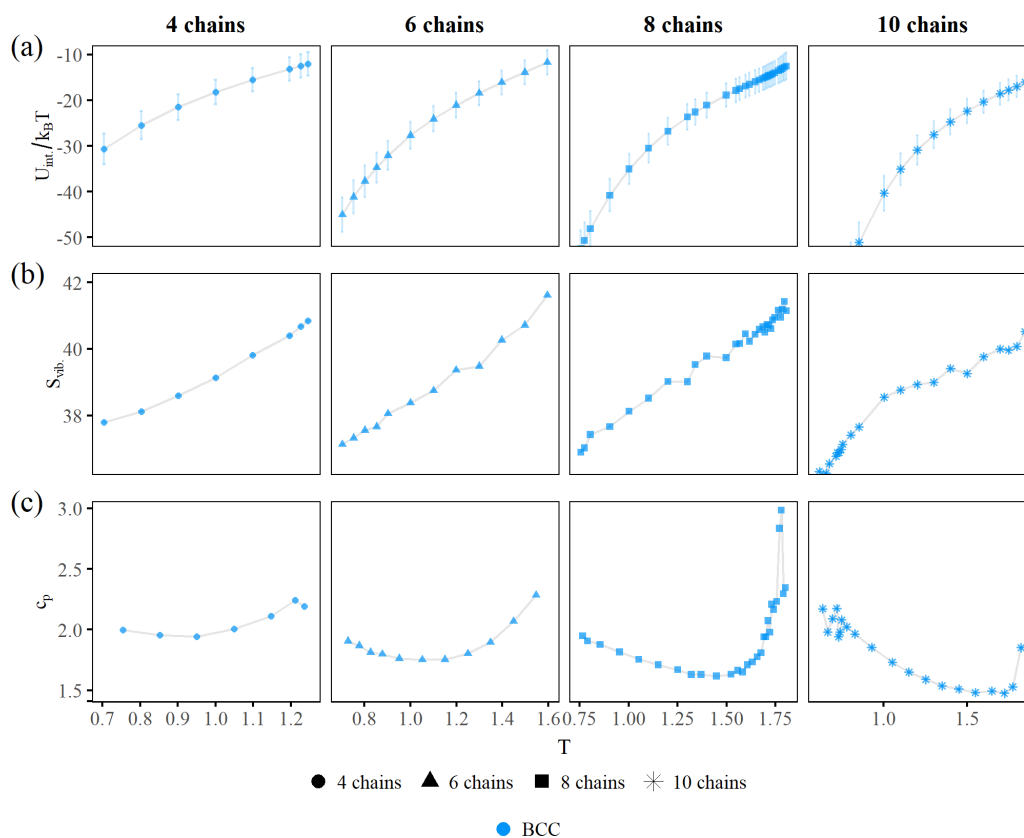


Figure D.12. Thermodynamic quantities of all stable crystal phases for particle number ratio 6:1 as a function of simulation temperature. We plot the (a) average interaction energy per small particle $U_{\text{int.}}/k_B T$, (b) lattice entropy $S_{\text{vib.}}$, and (c) c_P . Invariant of number of chains, we see no evidence for a any type of phase transition due to the continuous nature of all thermodynamic parameters plotted. The lack of hollow circles in c_P is also indicative of a lack of any phase transition occurring in these 6:1 systems.